Faculty of Applied Sciences

Doctoral Thesis

Power Line Conductors, a Contribution to the Analysis of their Dynamic Behaviour

---

Suzanne Guérard

Supervisor: Prof. Jean-Louis Lilien

June, 2011

II

Faculty of Applied Sciences

Doctoral Thesis

Power Line Conductors, a Contribution to the Analysis of their Dynamic Behaviour

---

Suzanne Guérard

Supervisor: Prof. Jean-Louis Lilien

June, 2011

Abstract

All the chapters of this thesis are linked with the concern of aeolian vibration. At locations where the motion of overhead power line conductors is restrained (e.g. at suspension clamps), the presence of aeolian vibration may result in another phenomenon called "fatigue of overhead conductors". The latter being responsible for serious damage to overhead power lines. The first part of the document is devoted to a review of the basic concepts of aeolian vibration and fatigue, of the tools available to model, measure or predict vibrational damage, and what are the remedial measures.

In a second part, a series of experimental studies are related:

- A review of the usual fatigue indicators, based on measurements performed on a 63.5m laboratory test span (chapter 2). The aim is to better understand how to perform a correct vibration risk analysis, knowing e.g. what to measure and at which locations.

- An evaluation of conductor self-damping properties based on real outdoor measurements, using a new type of monitoring device, able to perform continuous measurement on power lines (chapter 3). Unlike laboratory tests, such on-site measurements permit to take into account e.g. the effect of span ends, the spatial and time fluctuations in wind, leading to a more realistic vibration risk assessment.

- A study of the vibratory pattern associated to the failure of a conductor wire[1] (chapter 4). If not detected early, the presence of conductor fatigue may eventually lead to the failure of some conductor wires. This chapter investigates the possibility to detect such an event and eventually to use it as a fatigue indicator.

The third part of the thesis gathers modelling studies, starting with a few basic model validations (chapter 5), which permit to understand some interesting phenomena observed experimentally and to highlight the presence of amplitude fluctuations in the computed time response. The latter are believed to be linked to tension fluctuations. The hypothesis is further developed in chapter 6, comparing the results of constant versus variable

[1] Overhead power line conductors are made out of "twisted" ("stranded") wires

tension models and discussing the potential impact of tension fluctuations, when the vibrational behaviour of a real line is being extrapolated from tests performed on laboratory test spans. The modelling part ends up with the mining of experimental curves measured at University of Liège by A. Godinas [28] (chapter7). Once this input has been adequately processed, the followings have been achieved,

- A formula to compute the self damping per unit length within the conductor has been deduced. The predicted self damping values are consistent with those deduced from the literature, using more complicated measurement techniques,

- The parameters of an equivalent viscoelastic material have been deduced. Once implemented within a non-linear beam element, it permits to model both the conductor variable bending stiffness and self damping properties,

- A new method is proposed to measure the conductor self damping properties. The required test set-up is the one used by Godinas. The proposed method is much simpler than others already published in the literature in the sense that: the load can be applied quasi-statically, only a limited number of measurements is required, the test set-up is simple, simple to operate, less expensive than others... The perspective shown by this work is the following: knowing the conductor properties and the shape of some moment versus curvature cycles, the proposed formula would permit to estimate the conductor self damping in any kind of aeolian vibration without any dynamic testing.

In the last and fourth part of this chapter, the modelling results have been compared to experimental ones. To be more precise, the compatibility between the conductor variable bending stiffness deduced in chapter 7 and other results either published in the literature or measured by the author is checked in chapter 8. Then, chapter 9 illustrates the difficulties faced to reproduce resonance conditions on an experimental test bench. Some of them could be due to tension fluctuations. Last, in chapter 10, an energy balance is used to figure the order of magnitude of the self-damping due to non linearities.

Abstract

Le point commun qui unit les chapitres de cette thèse est le souci des vibrations éoliennes. Aux endroits où le mouvement des conducteurs de lignes aériennes est entravé, la présence de vibrations éoliennes peut engendrer un autre phénomène, appelé "fatigue des conducteurs", et pouvant occasionner d'importants dégâts.

La première partie du document est consacrée à une présentation des concepts de base liés à la fatigue des conducteurs et aux vibrations éoliennes, aux outils permettant de modéliser ces phénomènes ou de les quantifier, ainsi qu'aux mesures "curatives", permettant d'éviter ce phénomène ou de limiter son impact.

Dans la seconde partie, une série d'études expérimentales sont relatées:

- Une étude comparative des indicateurs usuels de fatigue, basée sur des mesures effectuées sur une portée de laboratoire de 63.5m de long (chapitre 2). L'objectif de cette étude étant de mieux comprendre comment réaliser une analyse de risque vibratoire correcte, par exemple en sachant à quelles mesures procéder, et à quels endroits.

- Une étude des propriétés d'auto-amortissement de conducteurs, basée sur des mesures réalisées sur de vraies portées, en environnement extérieur (chapitre 3). Les mesures ont été récoltées à l'aide d'un nouveau type d'appareil, capable d'effectuer des mesures en continu sur des lignes aériennes. Contrairement aux essais réalisés en laboratoire, les mesures sur site permettent de prendre en compte entre autres l'effet des extrémités de portée sur les vibrations, les fluctuations temporelle et spatiale de vent, ce qui conduit à une estimation plus réaliste du risque vibratoire.

- Une étude de la signature vibratoire associée à une rupture de brin [2]. Si le phénomène de fatigue n'est pas détecté à temps, celui-ci peut conduire à la rupture de brins et même du conducteur. Dans le chapitre 4, la possibilité d'arriver à détecter les ruptures de brins est étudiée, avec en point de mire son utilisation comme indicateur de fatigue.

[2] Les conducteurs de lignes électriques aériennes sont constitués de brins toronnés.

La troisième partie du document rassemble différents résultats de modélisation, qui permettent de comprendre certains phénomènes observés expérimentalement, et de mettre en évidence la présence de fluctuations d'amplitudes dans la réponse du conducteur (chapitre 5). Le document prend pour thèse que ce sont des variations de traction qui génèrent ces fluctuations. La thèse est développée plus en détails dans le chapitre 6, où les résultats de simulations à traction variable et constante sont comparés. Ce chapitre discute aussi l'impact potentiel des fluctuations de traction, lorsque des résultats d'essais réalisés sur de courtes portées de laboratoire sont extrapolés pour prédire le comportement de lignes réelles. La partie "modélisation" s'achève sur l'exploitation de courbes exprérimentales mesurées à l'ULg par A. Godinas (chapitre 7). Une fois ces données traitées de manière adéquate, les résultats suivants ont été obtenus:

- Une formule pour calculer la puissance dissipée par unité de longueur dans les conducteurs a pu être déduite. Les valeurs fournies par la formule sont cohérentes avec celles déduites de la littérature, qui se basent sur des techniques de mesure plus complexes.

- Les paramètres d'un modèle de matériau viscoélastique équivalent au conducteur ont pu être déduits. Une fois ce matériau introduit dans un élément de poutre non linéaire, il devrait permettre de modéliser à la fois l'amortissement et la rigidité en flexion variable du conducteur.

- Une nouvelle méthode est proposée pour mesurer les propriétés d'auto amortissement des conducteurs, utilisant le dispositif d'essais de Godinas. La méthode proposée est beaucoup plus simple que d'autres, dans le sens où les essais peuvent être réalisés de manière quasi statique (les autres méthodes requièrent des essais dynamiques), le dispositif d'essais est simple, simple à manipuler, moins cher que d'autres... La perspective offerte par cette nouvelle méthode est la suivante: connaissant les caractéristiques du conducteur et quelques courbes moment en fonction de la courbure, l'auto amortissement du conducteur soumis à n'importe quelle amplitude ou fréquence de vibration éolienne devrait pouvoir être estimé par la formule sans devoir réaliser d'essais dynamiques.

  Dans la dernière et quatrième partie de la thèse, les résultats obtenus par modélisation sont comparés à d'autres résultats expérimentaux. De manière plus précise, la compatibilité entre la rigidité en flexion variable déduite au chapitre 8 et d'autres résultats publiés est vérifiée. Dans le chapitre 9, les difficultés de réaliser l'ajustement entre fréquence d'excitation et de résonance au laboratoire sont illustrées. Certaines de ces difficultées pourraient être attribuées aux variations de traction. Pour finir, au chapitre 10, un bilan énergétique est utilisé

pour estimer l'ordre de grandeur de la puissance dissipée par les non-linéarités.

Contents

List of symbols **1**

Acknowledgements **3**

Introduction **5**

I Bibliography **7**

1 State of the art **9**
1.1 When it all began . . . 9
1.2 Dangerous conditions and aeolian vibration . . . 9
1.3 Fretting damage mechanisms . . . 10
1.4 From friction between strands to damping . . . 10
1.5 Calculation of idealized stresses . . . 11
1.6 Fatigue indicators . . . 13
1.7 Modelling of conductors and its limits . . . 14
1.8 Usual check up . . . 14
1.9 Non dimensional numbers related to self damping . . . 15
1.10 Cable self damping measurement techniques . . . 16
1.10.1 The power method . . . 16
1.10.2 The decay method . . . 17
1.10.3 The ISWR method . . . 18
1.11 Experimental self damping power law and similarity law . . . 19
1.12 The wind power input . . . 20
1.13 Analysis of a span with (a) damper(s) . . . 23
1.14 Cigré recommendations . . . 24
1.15 Vibration recorders . . . 26
1.16 Fatigue curves obtained in laboratory . . . 26
1.17 Cumulated damage from constant amplitude to variable amplitude and frequency . . . 28
1.18 Estimation of conductor lifetime . . . 29

II Experimental approach **31**

2 Evaluation of power line cable fatigue parameters based on measurements on a laboratory cable test span **33**
2.1 Introduction . . . 33
2.2 Presentation of test equipment . . . 34
2.3 Experiments description . . . 36
2.4 Analysis of the results . . . 37
2.5 Relationship between Y_b and fy_{max} . . . 37
2.6 Influence of a suspension clamp on Y_b measured near span end 39
2.7 Comparison between Y_b at the suspension clamp and at the equipment clamp . . . 40
2.8 Conclusions . . . 42

3 Self-damping evaluated in actual conditions **45**
3.1 Introduction . . . 45
3.2 Presentation of test equipment . . . 46
3.3 Self damping evaluated in actual conditions . . . 48
3.3.1 The self-damping power . . . 48
3.3.2 The wind power input . . . 49
3.3.3 Self damping fit with actual observations . . . 49
3.3.4 Wind power input comments . . . 52
3.3.5 Real world approach of power line vibration . . . 54
3.4 Conclusions . . . 54

4 The failure vibratory pattern of a conductor **57**
4.1 Introduction . . . 57
4.2 Description of the set-up and tests . . . 57
4.2.1 The test span . . . 57
4.2.2 Conductors and fittings . . . 58
4.2.3 Test conditions . . . 58
4.2.4 Measurement of the conductor accelerations . . . 58
4.2.5 Measurement of the rotation of the conductor . . . 59
4.3 Analysis of the “noise” signal . . . 60
4.4 Failures . . . 64
4.4.1 Failures of the AAAC conductor . . . 64
4.4.2 Failures of the ACSR conductor . . . 68
4.5 Detection of the failures . . . 70
4.5.1 Overview . . . 70
4.5.2 Eigen frequencies . . . 71
4.5.3 Tracking tools: wavelet transform versus short time Fourier transform . . . 74
4.5.4 Study of the rotational acceleration . . . 76
4.6 Axial acceleration of the conductor . . . 83

4.7 Evolution of the eigen frequencies as the number of failures increases . . . 86
4.8 Conclusions . . . 90

III Modelling **93**

5 Basic model validation **95**
5.1 Introduction . . . 95
5.2 Model description . . . 95
5.3 Shape of eigen modes . . . 96
5.4 Time response with a forced excitation . . . 98
5.5 Parametric study . . . 101
5.6 Reproduction of observed phenomena when in-span line equipment is introduced . . . 103
5.7 Time response . . . 106
5.8 Conclusions . . . 107

6 Tension fluctuations and related consequences **109**
6.1 Introduction . . . 109
6.2 Equations for vertical motion . . . 109
6.3 Figuring the change in tension . . . 110
6.3.1 Simple formulation . . . 110
6.3.2 A more accurate formulation . . . 111
6.3.3 Comparison of the changes in tension computed analytically versus with a finite element model . . . 111
6.4 Tension fluctuations in real spans versus laboratory test spans 115
6.4.1 Changes in tension in a single dead end span versus a section span . . . 115
6.4.2 The axial rigidity of span ends . . . 116
6.4.3 fy_{max} (amplitudes times frequency) and changes in tension in single dead end spans . . . 116
6.4.4 Checking the hypotheses made . . . 117
6.5 The effect of tension fluctuations on amplitudes . . . 118
6.5.1 Resolution of the constant tension problem . . . 118
6.5.2 Resolution of the variable tension problem . . . 124
6.5.3 Comparison of the variable tension problem without damping versus reality . . . 130
6.5.4 Comparison of the variable and constant tension problems without damping . . . 132
6.5.5 Comparison of the variable and constant tension problems versus reality when damping is introduced . . . 133
6.6 Conclusions . . . 133

7 Modelling conductor self-damping and bending stiffness 135
7.1 Introduction . . . 135
7.2 Relationship between curvature and moment versus conductor bending stiffness . . . 136
7.3 The Available data collected by Godinas . . . 138
7.3.1 Presentation of the experiments . . . 138
7.3.2 Moment versus rotation angle curves . . . 138
7.4 Modelling strategy . . . 141
7.4.1 Introduction . . . 141
7.4.2 Viscoelastic model . . . 142
7.5 Deducing moment versus curvature curves from experimental measurements on conductor AMS621 . . . 142
7.5.1 Introduction . . . 142
7.5.2 Finite element model of the test-span . . . 143
7.5.3 The moment value of equation 7.4 . . . 144
7.5.4 How is the conductor tension affected by the tests? . . 145
7.5.5 From rotation angle to curvature . . . 145
7.5.6 The difference between rotation angle and curvature for a vibrating cable . . . 148
7.5.7 The dimensional homogeneity of the relationship between moment and curvature . . . 148
7.6 Formula giving the power dissipated per unit length . . . 149
7.6.1 Introduction . . . 149
7.6.2 The area within the moment versus curvature curve . 149
7.6.3 Energy dissipated in a viscoelastic beam, under harmonic flexural loading . . . 150
7.6.4 Comparison of the self damping deduced from moment versus curvature curves and other results of the empirical power law . . . 151
7.7 Deducing the viscoelastic model parameters from measurements 153
7.7.1 Parameter A (which controls the slope of the hysteresis curve) . . . 153
7.7.2 Parameter B (which controls the self damping via the area of the hysteresis curve) . . . 153
7.8 Dynamic bending stiffness deduced from measurements . . . 159
7.8.1 Slope of the moment versus curvature curve . . . 159
7.8.2 Comparison with K. Papailiou's model . . . 160
7.9 Proposal of a new method for the measurement of a conductor's self damping properties . . . 161
7.10 The implementation of the viscoelastic model . . . 163
7.11 Another interpretation of the self-damping evaluated in actual conditions (chapter 3) in light of the present conductor self damping model . . . 164
7.12 Conclusions . . . 167

IV Model validation **169**

8 Validation of the variable bending stiffness model **171**
8.1 Average bending stiffness values deduced from measurements on Ireq test span . . . 171
8.2 Comparison with other average bending stiffness values given in the literature . . . 173
8.3 Comparison with other variable bending stiffness models . . . 174
8.4 Conclusions . . . 174

9 Experimental attempts to reproduce resonance conditions **175**
9.1 Introduction . . . 175
9.2 About the tests . . . 175
9.3 Phase shift between excitation force and conductor acceleration 176
9.4 Excitation force . . . 181
9.5 Amplitudes at "nodes" of vibration . . . 183
9.6 Amplitudes at antinode of vibrations . . . 185
9.7 Conclusions . . . 187

10 Potential impact of the "non linear damping" in the energy balance **189**
10.1 Introduction . . . 189
10.2 Energy injected within the beam . . . 190
10.3 Energy dissipated within the conductor . . . 190
10.4 Axial strain energy . . . 192
10.5 Conclusions . . . 192

V General Conclusions **195**

11 General Conclusions **197**
11.1 The new multi-tool strategy to assess conductor self damping 197
11.2 Understanding the impact of non-linearities . . . 198
11.3 Superiority of real on-site measurements . . . 199
11.4 Future work . . . 200

VI Appendixes **201**

A Experimental moment versus rotation angle curves recorded by Godinas **203**
A.1 AMS 621 . . . 203
A.2 AMS 298 . . . 205

B Dissection reports **209**
B.1 AAAC conductor 209
B.2 ACSR conductor 211

C Calibration of the Hall sensors **213**
C.1 AAAC conductor (testbench 6) 213
C.2 ACSR conductor (testbench 3) 214

D Data acquisition: matching between the accelerometer axes and the channels of the acquisition system **215**

E Average bending stiffness of the AAAC conductor **217**

F Self damping in mechanical systems **219**
F.1 Introduction 219
F.2 Material damping 219
F.2.1 Viscoelastic damping 219
F.2.2 Hysteretical damping 220
F.3 Structural damping 220
F.4 Fluid damping 220
F.5 Viscous damping 221

List of symbols

Symbol	Description	S.I. Unit
A	Antinode single-peak amplitude of vibration	[m]
A	$A = \beta(C_\star N)^{1/2-\delta}$	$[kgm^2/s^2]$
β	Angle through which the conductor is bent	
β	Self damping parameter	$[kgm^2/s^2]$
c	Damping coefficient	$[Ns/m^2]$
c	Friction parameter (Coulomb model)	
c_m	Mass proportional damping coefficient	
c_k	Stiffness proportional damping coefficient	
C	Damping coefficient or matrix	$[Ns/m]$
C_D	Drag coefficient	[1]
C	$\gamma(C_\star N)^\delta \xi \sqrt{\frac{EI}{N}}$	m
D,d	Diameter	$[m]$
D	Damage parameter	[1]
D	$\frac{2\beta(C_\star N)^{1/2-\delta}}{\gamma(C_\star N)^\delta \xi \sqrt{\frac{EI}{N}}}$	$[kgm/s^2]$
δ_r	Reduced decrement	
ε	Strain	[1]
E	Young's modulus of elasticity	$[N/m^2]$
E^*	Parameter of the viscoelastic model	$[Ns/m^2]$
E	$2y_{max}(\frac{2\pi}{\lambda})^2$	$[1/m]$
f	Frequency	$[Hz]$
H	Horizontal component of conductor tension	$[N]$
I	Area moment of inertia	$[m^4]$
k	Factor used in the power law	
K	Stiffness matrix	$[N/m]$
l	Exponent of the power law	
L	Span length	$[m]$
L	Length base quantity (Dimensional analysis)	
λ	Wave length	$[m]$
M	Bending moment	$[N.m]$

Symbol	Description	S.I. Unit
M	Mass matrix	$[kg]$
M	Mass base quantity (Dimensional analysis)	
m_l	Conductor mass per unit length	$[kg/m]$
m	Exponent of the power law	
μ	Single-to-peak amplitude at the excitation point	$[m]$
n	Cycles of vibration	
n	Exponent of the power law	
n_{wires}	Number of wires	
N	Number of cycles or number of samples	
N	Horizontal component of conductor tension	$[N]$
p	$\sqrt{\frac{H}{EI}}$	$[m^{-1}]$
P	Power per unit length	$[W/m]$
Φ	Phase shift	
Re	Reynolds number	[1]
ρ	Density	$[kg/m^3]$
S_t	Strouhal number	
S	Area	$[m^2]$
Sc	Scrouton number	[1]
σ	Stress	$[N/m^2]$
T	Tension	$[N]$
T	Time base quantity (Dimensional analysis)	
v	Speed	[m/s]
W	Work, energy	$[J]$
w	Weight per unit length	$[N/m]$
ξ	Coefficient	[1]
y	Vertical coordinate	$[m]$
y_0	Initial vertical coordinate	$[m]$
y_{max}	Antinode single-peak amplitude of vibration	$[m]$
Y_b or Y_{b2}	Peak-to-peak bending amplitude measured at 89mm from the last point of contact between the conductor and the clamp	[m]
Y_{b1}	Peak-to-peak amplitude measured at 44.5mm from the last point of contact between the conductor and the clamp	[m]
Y_{b3}	Peak-to-peak amplitude measured at 178mm from the last point of contact between the conductor and the clamp	[m]
ζ	Loss factor	[1]

Acknowledgements

I acknowledge my principal advisor Professor Jean-Louis Lilien. During this thesis, I also received advice from Dr. Pierre Van Dyke, Professor Sylvain Goudreau and Professor Louis Cloutier. I acknowledge IREQ, Henri Pastorel and Dr. Pierre Van Dyke for allowing the use of their outstanding laboratory, Ireq's members for their kindness and in particular the technical team who accompanied me during the tests: Roger Paquette, Martin Gravel and Jacques Poirier. I acknowledge GREMCA laboratory and their team for enabling me to collect remarkable fatigue material. I am grateful to University of Liège which has sponsored most of my travel costs through travel grants and my stay at University as assistant. Many thanks to the Ampacimon [3] team who made the "real outdoor tests" presented in the document possible. Last but not least, I acknowledge my husband and family for their unconditional support.

[3]Research project started at University of Liège in 2003 and initially sponsored by the French Community of Belgium

Introduction

The common thread of this document is aeolian vibration of overhead power lines. This phenomenon is characterized by vibration amplitudes of the order of the cable diameter and frequencies ranging approximately from 3 to 200 Hz [25]. The focus will be drawn to conductor fatigue[4], in particular to fatigue indicators, vibrational risk analysis, prediction of amplitudes, conductor self damping... No fluid aspect will be dealt with.

The input material for the study consists in several experimental measurements:

- Laboratory measurements performed at and supported by IREQ[5],
- Continuous real outdoor span measurements performed by ULg using a new monitoring device developed at the same University, named "Ampacimon",
- Laboratory measurements performed at GREMCA's laboratory (Université Laval, Quebec),
- Original laboratory measurements made by A. Godinas at ULg on 4 meter long cable samples, which have not been exploited yet.

The analysis of these tests has led the author to propose a new non-linear model for overhead power line conductors, based on an existing non-linear beam finite element code and able to deal with both the variable bending stiffness and self damping properties of a conductor. Using a viscoelastic material with adequate parameter values, the moment versus curvature hysteresis curves observed experimentally can be accurately reproduced (the area within the hysteresis represents the conductor self damping and the slope of the hysteresis its variable bending stiffness). All non-linear effects due e.g. to changes in tension are automatically coped with via the non-linearity of the finite element software itself.

[4]The presence of aeolian vibration may result in another phenomenon called "fatigue of overhead conductors". The latter being responsible for serious damage to overhead power lines.

[5]IREQ: Institut de Recherche d'Hydro-Québec, www.Ireq.ca

This model will serve as a basis to interpret and discuss experimental results. Some energy balances will also be produced in order to better quantify the different contributions to vibration amplitudes. Based on these developments, a new formulation for conductor self damping will be proposed, which unlike others is based on the physics behind the phenomenon itself and is dimensionally correct.

Last, some new laboratory and on-site test ideas will be suggested in order to better assess the dynamic behaviour of conductors and hence their potential fatigue level.

Part I

Bibliography

Chapter 1

State of the art

1.1 When it all began

The first papers to address aeolian vibrations as a cause of fatigue of overhead lines were written in the beginning of the twentieth century. The Stockbridge damper, which is one of the first commercial devices to protect overhead lines against the harmful effect of vibrations, appeared around 1925. Lots of developments linked to fatigue have followed and are still ongoing, some of which are summarized in the next paragraphs.

1.2 Dangerous conditions and aeolian vibration

Dangerous conditions for conductor fatigue generally coincide with the presence of Aeolian vibration. Fatigue may also occur from vibration phenomena called galloping or wake-induced vibration [25]. So-called Aeolian vibration on power line conductors is limited to low amplitude high frequency vortex shedding phenomena. Vortex shedding is characterized by vibration frequencies in the approximate range of 3-200 Hz and by amplitudes that can reach the conductor diameter for the lower range of frequencies [25].

As high frequencies are considered, it means that modal shapes have numerous loops along the span. All modes of a power line span have frequencies very close to each other, as the basic frequency is generally a fraction of Hz. Aeolian vibration can occur on almost any transmission line and at any time. Low turbulence wind will favour it [36]. Other parameters selected in [5] to qualify the vulnerability to Aeolian vibration are $\frac{H}{w}$, the ratio between the initial horizontal tensile load H and conductor weight per unit length w and also $\frac{LD}{m}$, the ratio of the product of span length L and conductor diameter D to conductor mass m per unit length in the case of single damped conductors.

1.3 Fretting damage mechanisms

Dynamic stresses in a conductor are only partially due to bending. Since all wires are tensioned, it generates pressure on the layers below. This pressure results in friction during vibrations. At locations where the motion of the conductor is restricted, the curvatures are maximum and some micro-slip or even some sliding may occur. Due to the conductor cyclic motion, the direction of micro-slip is continually reversed, which may lead to the generation of small cracks. Under small vibration amplitudes, the contact pressure may stabilize them but under large amplitudes, some of them will further propagate and eventually cause a wire failure. Strand failures will occur where such singular conditions are created (where the conductor motion is restrained), mainly at suspension clamps but also at a damper, marker or spacer clamp [25]. Two fretting sub-cases are generally distinguished: fretting wear and fretting fatigue [48] but Waterhouse for example splits fatigue damage into three categories : fretting fatigue, fretting wear and fretting corrosion [89, 90]. According to [94], wording "fretting wear" must be used for surface movements induced by external vibration just as "fretting fatigue" must be related to surface movements induced by a cyclic loading of one of the two contacting parts. The development of long cracks is not restricted to fretting fatigue, but occurs also in fretting wear, as demonstrated by Vingsbo and Soderberg [88], Vincent et al. [87, 86, 93].

1.4 From friction between strands to damping

According to Hardy et al [38], most of the damping in the cable transversal motion comes from the friction between strands which takes place at the numerous wire contact interfaces. In other words, structural damping (defined in appendix F according to [80]) plays a preponderant role in cable self damping.

In 1985, Johnson derived an expression for the frictional dissipation per cycle when two materials are in contact [44]. Note that the sliding and therefore frictional damping between two materials in contact only occurs when a certain curvature level is reached (see e.g. [65]). Using this contact mechanics formulation as a basis, several authors have studied analytically the conductor self damping behaviour. In 1998, Goudreau et al [29] derived that the energy loss per vibration cycle is proportional to the cube of the vibration amplitude, inversely proportional to the tension in the cable and inversely proportional to the sixth power of wavelength. In 1999, Hardy et al highlighted the importance of flexural self damping in vibrations [38]. In 2008, Rawlins derived an expression of frictional dissipation at the contacts and extended it to a total dissipation per unit length of conductor [73]. The accuracy of the analytical self damping estimation is limited by the hypothe-

ses made and by the uncertainty associated to some input parameters such as friction coefficients, specific self damping capacity of a material at a given frequency, and also the tension in each wire (function of the load history and the composition of the cable).

1.5 Calculation of idealized stresses

The term "idealized stress" is used because the conductor fatigue mechanisms are so complex that the stress analysis has to be approximate. As an example, which value of bending stiffness should be used to perform a stress calculation? Also, it is difficult to deduce the stress state of a cable from measurement. Therefore, the alternating stress computed at the topmost fibre of a strand is generally chosen as an indicator of the stress state of a cable [25]. In 1936, Sturm published a paper where some simplified formulae to assess the stress in the vicinity of a clamp, and an analysis of the ways to reduce the maximum stresses were shown [82]. Other authors followed up with similar analyses ([58], [46], [76], [79], [12]). It is worth mentioning the formulae that give conductor curvature at the clamp:

- As a function of the angle through which the conductor is bent at the clamp by the vibration, β (see figure 1.1),

$$\frac{d^2y_t}{dx^2}|_{x=0} = \beta\sqrt{\frac{H}{EI}} \tag{1.1}$$

- As a function of the antinode amplitude y_{max}

$$\frac{d^2y_t}{dx^2}|_{x=0} = 2\pi\sqrt{\frac{m}{EI}}fy_{max} \tag{1.2}$$

  It is interesting to note that the conductor tension does not appear in the previous equation. This is due to the fact that the moment is the product of tension times its lever arm and that those two parameters vary in inverse proportion: the higher the tension, the sharper the conductor emerges from the clamp and the smaller the lever arm (see figure 1.1).

- As a function of the amplitude in the vicinity of the clamp

$$\frac{d^2y_t}{dx^2}|_{x=0} = \frac{p^2y}{e^{-px} - 1 + px} \tag{1.3}$$

$$p = \sqrt{\frac{H}{EI}} \tag{1.4}$$

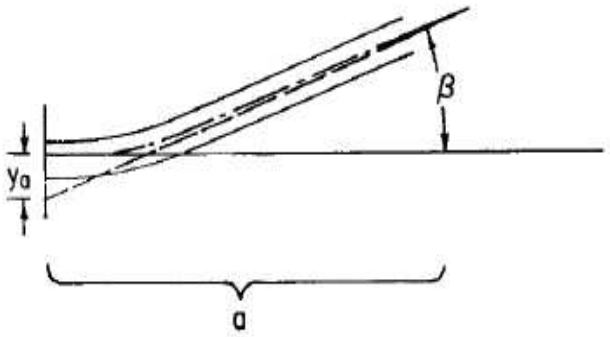

Figure 1.1: Angle through which the conductor is bent at the clamp by the vibration, courtesy of EPRI [25]

This equation is well known as the Poffenberger-Swart formula [68]. The bending moment at the clamp can be obtained by multiplying the conductor curvature by EI. The stress is then obtained by $\sigma = \frac{Mv}{I}$ (where v is half the diameter of the cable). Eventually, the formulae to compute idealized alternating stress in the top surface of a strand at the clamp are obtained [25]:

$$\sigma_a = \frac{dE_a}{2}\beta\sqrt{\frac{H}{EI}} \tag{1.5}$$

$$\sigma_a = \pi dE_a\sqrt{\frac{m}{EI}}fy_{max} \tag{1.6}$$

$$\sigma_a = \frac{dE_a\frac{p^2}{4}}{e^{-px} - 1 + px}Y_b \tag{1.7}$$

The industry standard position to measure y is at x=89mm (3.5 inches) [74] and, when measured at that position, its peak to peak value is called Bending amplitude ($Y_b = 2y$).

In 1997, K.O. Papailiou published a paper where a new model for the variable bending stiffness of conductors is presented. In this model, interlayer friction and interlayer slip during bending are taken into account [65, 64].

1.6 Fatigue indicators

The residual life of a conductor is often determined as a function of some measure of vibration intensity [25]. The usual vibration intensity indicators are listed below:

- fy_{max} , the product of frequency by the free loop (antinode) single-peak amplitude of vibration ([54, 1, 42, 81]),
- β, the angle through which the conductor is bent at the clamp by the vibration ([79, 7, 41]),
- Y_b, the bending amplitude (amplitude of conductor relative to clamp, measured a short distance, generally 89mm, from the last point of contact between the conductor and the clamp [83, 74, 45, 13]),
- ε, the dynamic strain in an outer-layer strand in the vicinity of the clamp, ([92, 59])

Fatigue curves have been developed through tests on laboratory spans using each of these parameters as the measure of vibration intensity.

According to [25], four problems arise in applying such fatigue curves in order to assess vibration of field spans.

- One is that (talking about fy_{max}, β, ε) "The parameter expressing vibration intensity may be inconvenient to measure reliably in the field" and (talking about fy_{max}) "does not do justice to the complicated behaviour found there". Let us review those two arguments, with an engineer and pragmatic point of view. With a monitoring device able to measure the conductor accelerations, provided its position in the span is known, it should be possible to deduce fy_{max} accurately using the wave propagation theory. Considering the second argument, it is true that fy_{max} does not reflect the interstrand fretting fatigue mechanism at the clamp, but indeed, which information is needed? An engineer who is in charge of the maintenance of transmission assets probably wants to know whether a line is at risk or not and whether remedial actions are needed. In this case, fy_{max} is an image of the fatigue risk on a span. If in-span free-loop amplitudes are small, then the amplitudes in the vicinity of a clamped device will generally be small. The opposite is not true: the amplitude measured at a suspension span, where an armour rod may be installed, often behind a vibration damper will not necessarily reflect in-span amplitudes. Also, clamped devices will often be installed in-span (a spacer for example). Therefore, an analysis solely based on the measurement of Y_b at the span ends may fail to detect some vibration risks: Y_b must therefore be measured at any location where the conductor motion is restrained.

- The second problem is that "vibration fatigue tests data are only available for a small fraction of the conductor sizes and types that are in use, and such data are expensive to acquire. Since none of the above parameters is simply related to the fatigue-initiating stresses, results from tests on one conductor size are not necessarily applicable to others".
- The third problem is that "fatigue tests have to be performed with a particular clamp" and it has been found that different types of clamps may yield to quite different fatigue test results.
- Finally, the fourth problem arises when field vibration amplitude is not a constant, "while available fatigue tests are performed keeping the selected amplitude parameter constant".

1.7 Modelling of conductors and its limits

The models which are currently used to model aeolian vibrations are based on the energy balance principle, which states that "the steady-state amplitude of a conductor due to Aeolian vibration is that for which the energy dissipated by the conductor and other devices used for its support and protection equals the energy input from the wind" [25]. The models based on this principle are simple, but are not able to take into account the reality, e.g. the excitation of several frequencies and the variation of wind in time and space. An improvement to the basic energy balance principle is to take into account a turbulent wind through a reduced wind power input [61, 19, 70]. However, this aspect of the problem has not been fully resolved yet and research is still going on. Research is ongoing also on more sophisticated models. These models can be either in time domain [18] or in frequency domain [61]. The target is to be able to model wind variation in space and time and to have a more realistic model of vortex shedding. There are still lots of work to do before those models are ready.

1.8 Usual check up

Most utilities, before stringing their lines or sometimes afterwards, face the difficulty of evaluating the vibration behaviour of a given power line. The difficulty mainly lies in choosing an appropriate stringing tension and evaluating the number of dampers needed (or not needed) to prevent vibration damage and obtain an appropriate lifetime. In order to use the energy balance principle, both a wind power input estimation and an estimation of the power dissipated by the conductor are needed. Conductor self damping and the wind power input are data very difficult to obtain (and indeed very strategic ones to evaluate lifetime based on calculations only). In absence

of data, literature provides values for wind power input and conductor self damping based on laboratory [25, 38], and wind tunnel testing [72]. In the past, it was both expensive and time consuming to perform tests in a laboratory or on a real span to collect representative information on conductor behaviour. In the coming years, the arrival of new commercial energetically autonomous vibration monitoring devices might make field measurements more common, accessible and easy. This should lead to more realistic studies: actual conditions may be quite different from the cases observed in laboratory as long spans are used, fixtures are very different from one case to another and cable behaviour may vary significantly. An on-site measurement may give access to actual maximum amplitude for each of the frequencies after a certain time of observation (see chapter 3). On another side, the maximum observed amplitude may then be used to tune the energy balance either thanks to the wind power input or the self damping (see section 3.3).

1.9 Non dimensional numbers related to self damping

Several authors commonly use the Scruton number in publications related to vibrations of cylindrical structures. This number is a dimensionless combination of variables and gives an image of the damping of the structure. Let us first define the following dimensional variables:

- m_l, the cylinder mass per unit length $[kg/m]$,
- ρ, the fluid density $[kg/m^3]$,
- d the cylinder diameter $[m]$,
- C the system structural damping coefficient$[N * sec/m]$,
- C_c the cylinder system critical damping coefficient $[N * sec/m]$,

The mass ratio and the structural damping ratio, which are dimensionless variables, can be defined as:

$$m^\star = \frac{m_l}{\rho d^2} \tag{1.8}$$

$$\zeta = \frac{C}{C_c} \tag{1.9}$$

Let δ be the logarithmic decrement, which characterizes the free decay of a structure in time domain. In the field of overhead power lines, one can

write $\delta = 2\pi\zeta$ (see section 1.10.2). Then the Scruton number Sc can be defined as a combination of the two previous dimensionless variables:

$$Sc = \delta m^\star \tag{1.10}$$

$$Sc = 2\pi\zeta m^\star \tag{1.11}$$

The Scruton number is therefore an image of the damping of the structure. It is often used in lieu of the reduced damping or reduced decrement

$$\delta_r = 2m\delta/(\rho d^2) \tag{1.12}$$

1.10 Cable self damping measurement techniques

Different methods exist to measure conductor self-damping in laboratory: the power method, the inverse standing wave ratio, the decay method [25]. These are described in documents published by IEEE and EPRI [63, 25]. Self damping measurements are performed in laboratory test spans which length ranges from 30 to 90m. The conductor is held rigidly and strung at the required tension between two very stiff blocks. An electrodynamic shaker excites the conductor at one of its resonance frequencies. An example of such test span arrangement can be seen in figure 2.1.

These tests are carried out at different tension levels in order to account for the impact of tension on the interstrand friction zones. The results are corrected in order to subtract the self damping coming from the interaction between the vibrating cable and still air. Most of the time, these measurements are performed with the Inverse Standing Wave Ratio method (denoted ISWR), with which it is possible to separate the contribution of "in-span" and "span end" losses. Other methods are the power Method and the decay method. All three methods are described hereafter.

1.10.1 The power method

The power method states that the energy introduced in the span by the shaker is entirely dissipated within the conductor ([25], formula 2.3-9):

$$W_{in} = W_{diss} = \pi F \mu \sin(\Phi) \tag{1.13}$$

where Φ is the phase between the excitation force and the displacement, and F and μ represent the amplitudes of respectively the excitation force and displacement.

Note: formula 1.13 can be deduced from the general expression of external work given in chapter 13 of [56] : $W_E = \int_0^\Delta F^t d\Delta^t$, where both F^t (the external force) and Δ^t (the corresponding displacement) are a function of time. The integral value represents the area within the curve of force versus

displacement at the location of the excitation (both quantities are harmonic functions, with a phase shift equal to Φ) .

Let us assume the excitation corresponds to the k^{th} eigen frequency of the span f_k. The power dissipated per unit length of the cable is worth [25]

$$P_{diss} = W_{diss}\frac{f_k}{L} \tag{1.14}$$

where L is the span length.

Let $W_{k,max}$ be the maximum kinetic energy of the cable. Assuming a modal decomposition of the vibration (with a single contribution from the excited mode), the position of the cable as a function of time $y(x,t)$ satisfies:

$$y(x,t) = A_k \sin(\frac{k\pi x}{L})\cos(\omega_k t) \tag{1.15}$$

where A_k is the single-peak antinode amplitude of vibration of the k_{th} mode.

The expression of the $W_{k,max}$ is:

$$W_{k,max} = \frac{1}{2}\int_0^L m_l \omega_k^2 A_k^2 \sin^2(\frac{k\pi x}{L})dx = \frac{1}{4}m_l\omega_k^2 A_k^2 L \tag{1.16}$$

(which is identical to the expression of maximum kinetic energy given in [25], equation 2.3-11).

The damping is often expressed via the following non-dimensional damping coefficient, also called "loss factor"(see [25], formula 2.3-10):

$$\zeta_k = \frac{W_{k,diss}}{4\pi W_{k,max}} \tag{1.17}$$

Applying the power method, one must keep in mind that extraneous dissipation sources (e.g. external sources of damping and end damping) are included in the measurements [25].

1.10.2 The decay method

In the decay method, the cable is forced to vibrate at one of its eigen frequencies, the k_{th} one for example. Then the excitation is stopped and the decay of the cable studied [25]. If $X_{k,i}$ is the amplitude of motion during the decay cycle i (the abscissa where $X_{k,i}$ is measured does not really matter, provided the measurement is performed at the sample place from one cycle to another), the logarithmic decrement δ_k is defined as $\delta_k = \ln(\frac{X_{k,i}}{X_{k,i+1}})$. If $\zeta_k \ll 1$ (which is the case for overhead power lines, where ζ_k has an order

of magnitude of 10^{-3}), the non dimensional damping coefficient is simply given by ([25]):

$$\zeta_k = \frac{\delta_k}{2\pi} \tag{1.18}$$

This second method requires the excitation to be stopped properly so that the shaker is perfectly disconnected from the cable and that no unwanted impulse is induced [25]. It also has the disadvantage of including extraneous losses like end damping in the measurements.

1.10.3 The ISWR method

The third method, called ISWR requires the amplitudes of vibration at some nodes to be measured as well as an amplitude at an antinode. The method is derived from the work of Tompkins et al [85] and is based on the principle that if there were no dissipation within the cable, no motion at nodes would occur (because incident and reflecting waves are equal). The motion that occurs at vibration"nodes" hence reflects the damping within the conductor. The amplitudes at vibration "nodes" are small (a few micrometers), which makes their measurement difficult. Let us suppose the span is vibrating at its k_{th} eigen mode. Let us define the inverse standing wave ratio as

$$S_{k,i} = \frac{a_{k,i}}{A_k} \tag{1.19}$$

where $a_{k,i}$ is the single amplitude of vibration in a node and A_k that at a vibration antinode. From an electromechanical analogy, Tompkins derived that the power flowing through one section of a cable is given by [85]:

$$P_{k,i} = \frac{V_k^2}{2} S_{k,i} \sqrt{T m_l} \tag{1.20}$$

with $V_k = \omega_k A_k$

The power dissipated between nodes i and j distant of n_v half-wave lengths is equal to

$$P_k = P_{k,i} - P_{k,j} \tag{1.21}$$

The power dissipated per unit length of the conductor is then

$$P_{k,diss} = \frac{P_{k,i} - P_{k,j}}{n_v \lambda_k / 2} \tag{1.22}$$

From the definition of the maximum kinetic energy of a cable on the one hand and the expression of frequencies of a string, it can be deduced that the non dimensional self damping coefficient ζ_k is given by:

$$\zeta_k = \frac{S_{k,i} - S_{k,j}}{n_v \pi} \tag{1.23}$$

Provided the amplitudes of vibration at nodes can be measured adequately, the ISWR method permits to withdraw the contribution of span ends and external devices and to consider only the energy dissipation which takes place within the portion of cable under study only.

1.11 Experimental self damping power law and similarity law

The power dissipated per unit length of conductor is often expressed empirically through a power law:

$$P_{diss} = k \frac{y_{max}^l f^m}{T^n} \tag{1.24}$$

Where P_{diss} is the self damping power per unit length $[W/m]$, k is a proportionality factor depending on cable data, y_max is the antinode zero to peak amplitude [m], f the frequency [Hz] and T the tension in the conductor [kN]. The exponents l, m, n may vary significantly but are generally in the range given in table 1.1. Let d [mm] and RTS [kN] be respectively the conductor diameter [mm] and RTS its rated tensile strength [kN]. The k factor satisfies

$$k = \frac{d[mm]}{\sqrt{RTS[kN] * m_L[kg/m]}} \tag{1.25}$$

and is close to 1.5 or 2 for classical conductor material and cross section in SI system [24]. In 1998, a Cigré working group collected information on the coefficient found experimentally by different laboratories around the world [84].

Table 1.1: Range of the exponents l, m, n of the self damping power law

Factor	Range
l	2-2.5
m	4-6
n	2-2.8
k	1.5-2

In [25], the following interesting comment is given: the exponents vary significantly according to the measurement method and the configuration of

span ends. When the power method is used with span ends rigidly fixed, the amplitude exponent is close to 2 and the frequency exponent close to 4. When the ISWR or the power method with pivoted extremities is used, the amplitude and frequency exponents are close to respectively 2.4-2.5 and 5.5. Reminding the discussion of the previous paragraph, this difference is mainly due to span end effects, which can not be withdrawn in the power method with rigidly fixed ends. Self damping coefficients deduced from the ISWR method and power method with pivoted ends therefore give a more accurate value of the self damping which comes exclusively from the conductor.

A comparison of the self damping power computed using coefficients deduced with the same method (ISWR), but by different authors will be shown in chapter 3, section 3.1. It shows important scattering within the results (the self damping values may differ by one order of magnitude).

As mentioned in the previous paragraph, the self damping characteristics of a conductor will depend among others on the wire material (e.g. for a given size and topology, the damping behaviour of an ACSR conductor will be very different from an aluminium alloy conductor), and on the size of the friction zones (and therefore on the size of the conductor and its amount of layers). Self damping power laws are therefore established for one given conductor, characterized by its material, number of wires, mass per unit length... Since the tests required are expensive, one author has studied the possibility to extrapolate the self damping laws to other conductors from the same class and with a similar size. In 1997, Noiseux published generalized similarity laws for near-field (near span ends) and free field (in span) loss factors for ACSR conductors. Once self damping measurements have been performed on a given ACSR conductor, these similarity laws permit to predict self damping for other ACSR conductors with identical constructions but different diameters [62].

1.12 The wind power input

Wind power input data is based on wind tunnel experiments made in the air flow at different reduced velocities. Curves of power as a function of y_{max}/d (single-peak amplitude/diameter ratio, denoted A/d in [25] and the following figure) are then drawn from these test data. The maximum energy input curve is finally determined by the envelope of all the curves.

The tests to evaluate the maximum energy input are made on rigid or flexible cylinders, leading to different results, as can be seen in the following figure. The curves representing the flexible cylinder tests are in [70, 8], while others represent the rigid cylinder tests.

There are several characteristics of wind power input and of the method used to obtain relative curves which are worth being mentioned in the present report. The initiation of aeolian vibrations occurs when the ve-

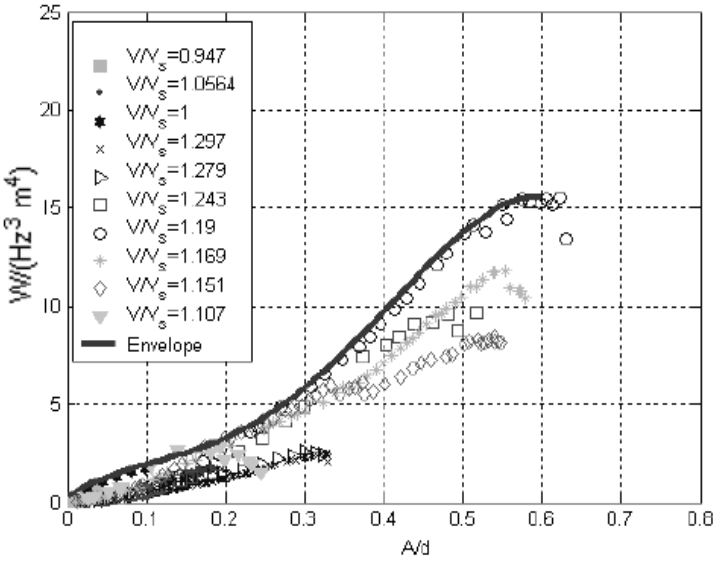

Figure 1.2: Wind power input curves measured for different reduced velocities, courtesy from EPRI (A is the peak-to-peak displacement/2) [25]

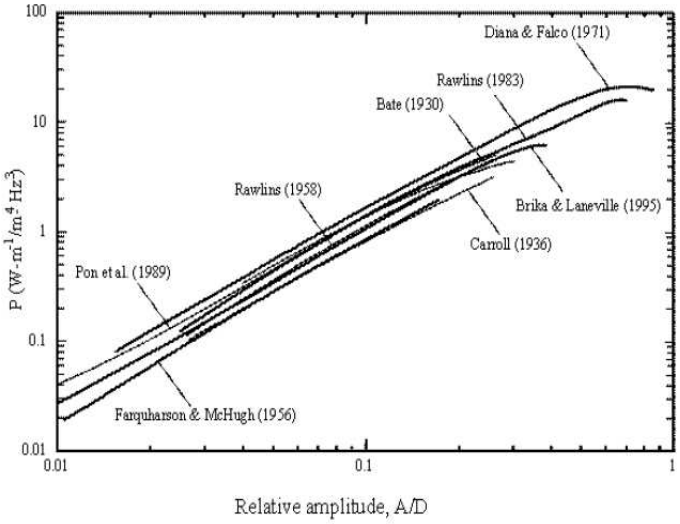

Figure 1.3: Maximum wind power input coefficient in case of a single conductor, A is the peak-to-peak displacement (courtesy from[25], based on [8])

locity of the incoming flow is such that the frequency of the vortices shed in the wake of the conductor approaches a modal frequency of the span. Such a velocity is called onset velocity in the literature [25]. The shedding frequency of the vortices is given by the following relationship:

$$f_{st} = \frac{S_t v}{d} \tag{1.26}$$

where S_t is the Strouhal number, v is the fluid speed $[m/s]$ and d the diameter of the cylinder which is plunged into the flow $[m]$. The Strouhal number may be function of three criteria:

- the Reynolds number (Re) [1]
- the relative surface roughness,
- the aspect ratio.

The effect of the two latter criteria can be considered as small for overhead conductors. Thus the vortex shedding phenomenon can be considered as "governed" by two non-dimensional numbers: the Strouhal number and the Reynolds number. In the range of Reynold's number of interest for aeolian vibrations ($350 < Re < 35000$), the value of the Strouhal number is almost constant and approximately equal to 0.18 [25]. Once aeolian vibrations are installed, in other words for larger amplitudes of vibrations, the vortex shedding frequency may be "locked" by the vibration of the cylinder and aeolian vibration may continue to exist even if the velocity of the incoming flow is slightly changed. Experimentally, it was possible to maintain aeolian vibrations with wind velocities comprised between 90% and 130% of the onset velocity. This phenomenon is called lock-in and has an impact on the method used to deduce wind power input curves. In order to plot wind power input curves, several reduced velocities[2] are considered. Only the maximum values obtained for different reduced velocities are eventually retained to plot wind power input curves. Also, both the oscillation amplitudes and the wind power input show a hysteresis: depending on the initial conditions of excitation, the wake flow pattern can either be a 2P or 2S mode[3] which results in two branches in the wind power input curves [8].

The turbulence of the incoming flow is another parameter which will influence the value of the power imparted by wind to a vibrating conductor. The lower the turbulence, the higher the wind power that can be imparted

[1] Let v be the flow velocity $[m/s]$, ν the kinematic viscosity of the fluid (m^2/s) and d the conductor diameter $[m]$. The Reynold's number is given by the ratio $\frac{Vd}{\nu}$.

[2] a reduced velocity is the ratio of flow velocity on the Strouhal onset velocity

[3] The name of the shedding mode "2P" or "2S" comes from the pattern in the wake of the conductor which can be characterized either by the shedding of two pairs of vortices (2P mode) or two single vortices (2S mode) per cycle of oscillation

to the conductor. Rawlins has published a paper where a model is proposed in order to take into account the turbulence of wind [72].

1.13 Analysis of a span with (a) damper(s)

In 2005, Cigré working group 11 issued a report on Modelling of aeolian vibration of a single conductor plus damper [4]. Other useful information on this topic may be found in [25]. The question which needs to be answered by grid owners is the following: "How much damping needs to be introduced in the overhead power lines in order to keep them safe from vibration damage". To answer this question, several approaches are described in the literature, depending on the possibility to feed the analysis with experimental data. The first step of the procedure is to assess the damping efficiency of the cable plus damper system. Here is how this first step is performed:

- If the damper can not be tested, the first step is to build a model of this equipment. Then the mode shapes of the span plus damper system need to be computed so that a modal solution for the equation of motion can be sought.

- If the frequency response of the vibration damper is known (e.g. if a test on a vibration shaker has already been performed), this input can be introduced in the span model under the form of an equivalent transmitted force. In such a case, the model must be able to simulate the span distortion caused by the damper presence,

- If it is possible to perform self damping laboratory tests of the cable+damper system, then the power dissipated by the damper will be measured at different frequencies of interest for aeolian vibrations and at different amplitudes.

Then, the second step is to estimate the vibration amplitudes which can be expected on-site. Once again, field recordings will provide the most appropriate and complete answer to this question. In their absence, the amplitudes will be estimated thanks to the Energy Balance Principle EBP. The wind power input information can be either modelled (e.g. using [72]), or (advantageously) measured on-site.

The last step is to perform a vibration risk diagnosis. In case the incidence level of fatigue is unacceptable, more damping needs to be introduced and the analysis restarted.

C.B. Rawlins has investigated the vibration damping on long spans [69], characterized by non sine shaped modes and variable loop amplitude along the span. His conclusions mention that the effect of the great length of the span is to reduce the amount of damping needed by 10 % for overland spans and by 25% for span crossings.

1.14 Cigré recommendations

In 1950, a first report was presented by the members of the group "Cigré Comité d'études 6" [16]. The conclusion of this first report was that an adequate conception of clamps should prevent vibration damage. Ten years later, another report was published, based on the statistical analysis of the conductor mechanical tension [17]. The concept of Everyday Stress (EDS) was introduced, which is the stress in the conductor, expressed as a percentage of its tensile strength, at his average temperature and without (mechanical) overload. A maximum EDS was recommended. Nevertheless, failures happened even if the EDS value was very low, e.g. $< 15\%$. This is due to the fact that fatigue depends on several other parameters than EDS (topography, turbulence of wind, type of clamps, manufacturing of the line). Cigré researches posterior to 1960 (mainly those based on conductor self damping) have shown that the ratio of horizontal tension load and the conductor weight per unit length (H/w) was probably a more appropriate parameter than EDS. In 2005, Cigré 22.1, TF4 recommended the H/w values present in figure 1.4 [5].

Terrain category	Terrain characteristics	$(H/w)_{adm}$ (m)
1	Open, flat, no trees, no obstruction, with snow cover, or near/across large bodies of water; flat desert.	1000
2	Open, flat, no obstruction, no snow; *e.g.* farmland without any obstruction, summer time.	1125
3	Open, flat, or undulating with very few obstacles, *e.g.* open grass or farmland with few trees, hedgerows and other barriers; prairie, tundra.	1225
4	Built-up with some trees and buildings, *e.g.* residential suburbs; small towns; woodlands and shrubs. Small fields with bushes, trees and hedges.	1425

Figure 1.4: Recommended Safe Design H/w values for single unprotected conductors, Cigré 22.11 TF4 2005

For damped single conductor, the same working group proposes a new parameter for rating the protective capabilities of dampers [4]. This parameter is $\frac{LD}{\sqrt{Hm}}$(L is the span length, D the conductor diameter, H the horizontal tension and m the mass of conductor per unit length). Since $\frac{H}{w}$ is a commonly used parameter, Cigré then decided to simplify the two parameters $\frac{LD}{\sqrt{Hm}}$ and H/m in $\frac{Ld}{m}$ and H/w. Figure 1.5 shows the design recommendations of Cigré working group 22.11, TF4, 2005. Four sets of curves are presented. Each one is associated to a certain type of terrain category described in the legend.

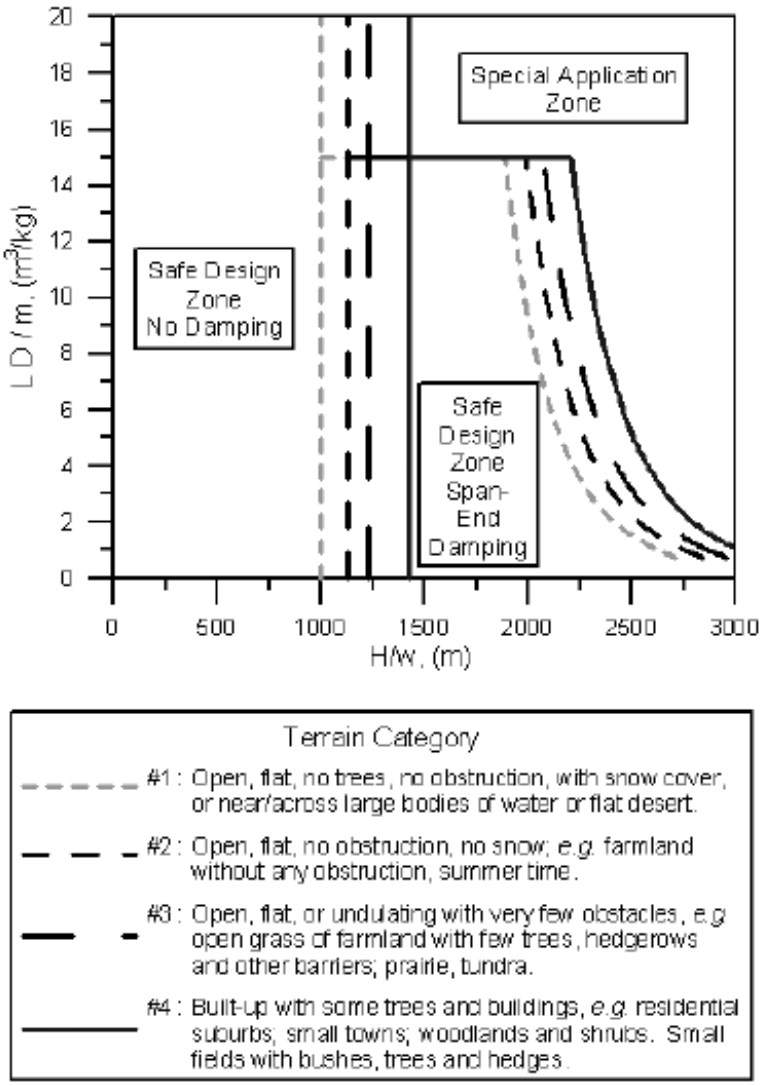

Figure 1.5: Recommended safe design tension for single conductor lines. H: initial horizontal tension; w: conductor weight per unit length, L: actual span length, D: Conductor diameter and m: conductor mass per unit length [5].

1.15 Vibration recorders

Most existing vibration recorders try to measure the bending amplitude of conductors. Vibration recorders designed to measure antinode amplitude are quite recent.

Let us first review the bending amplitude recorders. The oldest bending amplitude recorders are analog devices such as Ontario Hydro recorder (1963). Those devices, developed by Edwards and Boyd [22] contained a clock and were timed to obtain one second recording every 15 minutes. The autonomy of this instrument was about 3 weeks and it was necessary to take it off the line to get the recorded data. Other analog bending amplitude recorders are HILDA and Sistemel.

Digital recorders are micro-processor based, battery-powered, with a memory in which the data are stored under a digital form. Examples of such devices are Vibrec, Pavica, Scolar III and Ribe LVR vibration recorder. The autonomy of these devices is of the order of a few months. The weight of these instruments ranges from 0.5kg (Pavica) to 3.1kg for Scolar III (but 6.1kg with standard fittings) [3]. Since these devices are battery powered, in order to spare energy, these devices are only able to perform intermittent measurements. According to [3], Scolar III can be set up for 1 to 4 seconds every 10 minutes and in general, vibration recorders perform ten seconds recordings every fifteen minutes. Then, the recorders have to perform a data reduction because of storage limitations. The frequency and the amplitude of the vibration cycles are measured by suitable algorithms and stored in a memory matrix according to the procedure suggested by IEEE [74]. The Pavica and Scolar III recorders store the highest amplitude and the average frequency of any sample period. Other recorders like Vibrec400 and Ribe LVR store amplitude and frequency of each individual cycle recorder in the sample period. In paper [3], U. Cosmai stresses that the results obtained with these two procedures can be rather different. In the frame of this thesis, it is also stressed that lots of information is lost when vibrations are recorded only for a few seconds every 10-15 minutes. The occurrence of vibration at a given location is far from obvious. In 2003, University of Liège started a project (named Ampacimon) with the aim to conceive a vibration monitoring device. The particularity of this device is that for the first time, the device is installed in-span, is energetically autonomous and is able to perform continuous vibration measurement.

1.16 Fatigue curves obtained in laboratory

Fatigue curves are generally established relative to fy_{max} or to bending amplitude. The idealized dynamic stress can be calculated using equation (1.)6 or (1.7). Examples of such fatigue curves drawn at constant amplitude

with conductors supported by rigid ends can be found in [25]. Let us consider fatigue curves relative to fy_{max}. One of these is shown in figure (1.6), relative to fy_{max}. Most data used to plot these figures come from Alcoa and Gremca laboratories.

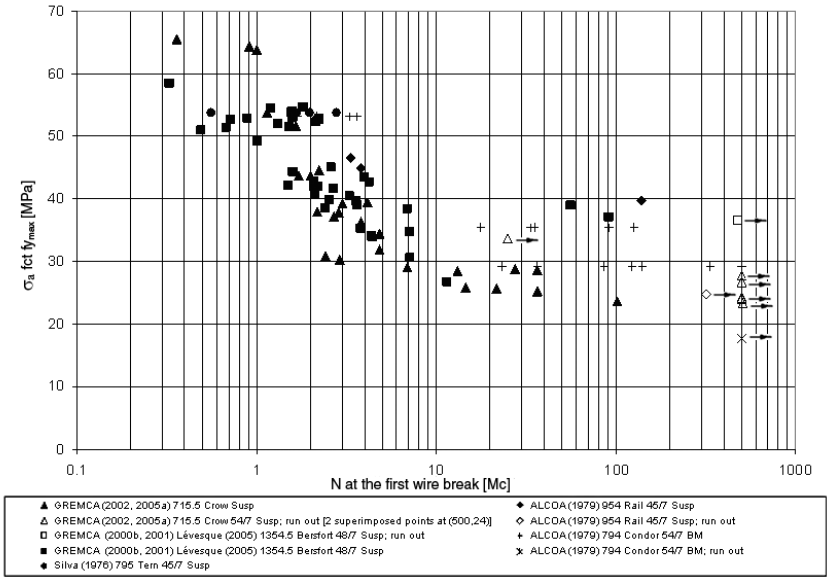

Figure 1.6: Fatigue tests of three-layer ACSR, courtesy from EPRI [EPRI2006].

The number of cycles N leading to a first strand failure at a given amplitude shows a wide scattering rather than a "well defined fatigue curve" [25] (chapter 3). Having examined several of those fatigue curves, the authors of that chapter noticed that:

- Given a conductor and its supporting clamp, the level of tension in the conductor seems to have little effect on the fatigue curve,
- Given a conductor and its supporting clamp, the number of layers appears to have some influence on the fatigue curve,
- The σ_a-N relationship is relatively insensitive to clamp contour.

In case there is no S-N (stress S depending on the number N of cycles to failure) available for a certain conductor, the Cigré safe border line can be used. This curve is derived from various laboratory fatigue measurements. It represents the conservative lower limit of the permissible number of cycles at various stress levels. It is applicable for commonly used aluminium, aluminium alloy and multi-layer ACSR conductors and all types of clamps. The safe border line can be seen in figure 1.7 and is represented by the following equation:

$$\sigma_{bf} = CN^z \tag{1.27}$$

where σ_{bf} is the dynamic limit stress in N/mm^2, N the number of cycles until failure, $C = 450$ and $z = -0.2$ for $N \leq 2 * 10^7$ and $C = 263$ and $z = -0.17$ for $N \geq 2 * 10^7$ [91].

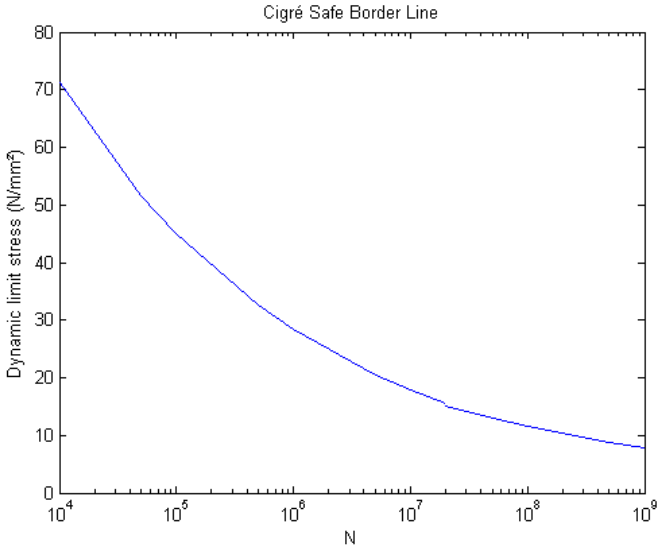

Figure 1.7: Cigré safe border line

1.17 Cumulated damage from constant amplitude to variable amplitude and frequency

As explained in the previous section, fatigue curves are drawn from laboratory tests, considering constant amplitude of vibration. In reality, the conductor will undergo variable amplitudes of vibration. To go from the constant to variable amplitude situation, the usual approach is to consider a "cumulated damage law". One of the simplest cumulated damage law is the Palmgren-Miner one, often denoted Miner's law. Assuming a conductor specimen to be subjected to k stress amplitude levels σ_i, this rule consists in calculating an equivalent damage parameter D as follows [57, 39]:

$$D = \sum_{i=1}^{k} \frac{n_i}{N_i} \tag{1.28}$$

Where

- n_i is the number of cycles at stress amplitude i,
- N_i is the number of cycles to failure if the specimen was subjected to constant amplitude level i.

According to Miner's rule, the failure occurs for $D = D_f = 1$ (D_f is the damage at failure). Nevertheless, one should be aware that Miner's law has two limitations, which have been proven by tests [77]:

- The sequence of occurrence of amplitudes (i.e.: the load history) is not taken into account in the previous law,
- The impact of amplitudes below the endurance limit is not taken into account (for N approaching infinity).

Improvements to this damage law have been proposed in [77], but Miner's rule still remains used because of its simplicity. Its validity for conductor fatigue has been tested to some extent (see for example [30, 31]). In [10], a study of the value of the damage parameter is reported. It appears that D_f is not a constant but rather follows a statistical distribution and extends over at least a 3:1 range. The use of Miner's law has been recommended by Cigré, but with the remark that the critical value of D_f (damage at failure) may vary from 0.5 to 2. If $D = 0.5$, life time is divided by 2 compared to $D = 1$, and if $D = 2$, life time is multiplied by 2 compared to $D = 1$.

1.18 Estimation of conductor lifetime

In [47], one can find a complete description and an example of the procedure to assess a conductor lifetime. This procedure comprises uncertainties and approximations.

First, if the "load history" comes from an old type of vibration recorder, as explained in the paragraph devoted to these devices, because of energy savings, these devices only perform a few seconds of vibration measurements every 10 to 15 minutes. Out of these few seconds of records, one amplitude is saved in memory. Lots of information may then be lost on the real "load history". The recordings may not represent the real conditions. With new energetically autonomous devices, continuous measurement is possible [53].

Second, as mentioned by [20], the local terrain affects the severity of vibration. Even if there has been no systematic study of the variability of vibration severity structure-to-structure in any line, the exposure to fatigue probably varies span-to-span. Choosing a single test structure means taking a single sample out of a population of structures having varied exposure to damage. This should be taken into account when doing a fatigue analysis.

Third, it has also been shown by [23] that the behaviour of the different phases at the same tower can be different.

In the fourth place, the severity of vibration varies with weather conditions, on an hourly and daily basis and as seasons go by [67]. A full year of record should be preferred to account for these seasonal effects [20].

In the fifth place, the recorder, by its presence, can change the variable that is being recorded. The mass of the instrument alters the inertial properties of the support where it is attached. In some cases, a resonance can occur that results in amplification of amplitudes at some frequencies and reduction at others [78, 11, 34, 40].

In the sixth place, the intensity of vibration displays variations in the form of beats. This beating pattern exists because more than one vibration mode may be excited at the same time. All these aspects complicate the problem of interpreting recorded data by means of laboratory data on the fatigue characteristics of conductors [20].

Last, as mentioned in one of the previous sections, fatigue curves are obtained with tests run at constant amplitude. The problem is conventionally dealt with through Miner's rule which also has its limitations: both the sequence of occurrence of amplitudes and amplitudes under the endurance limit are not taken into account (see section 1.13). Moreover, the parameter of damage at failure is not a constant and extends over a at least a 3:1 range.

For all these reasons, estimation of conductor lifetime is an extremely challenging task.

Part II

Experimental approach

Chapter 2

Evaluation of power line cable fatigue parameters based on measurements on a laboratory cable test span

2.1 Introduction

The present chapter describes experiments carried out on IREQ's [1] laboratory cable test bench by Suzanne Guérard (ULg), Roger Paquette, Martin Gravel and Jacques Poirier (IREQ), under the supervision of Pierre Van Dyke (IREQ). Test span arrangement is a 63.15m cable span with termination ends designed to minimize energy dissipation. A shaker provides a vertical alternating force to the conductor. During the experiments, a maximum of information on mode shape is collected: location of nodes, antinodes, relative displacement at 44.5, 89, and 178mm from the last point of contact with the metallic clamp. Several configurations are studied: span equipped with a homogeneous steel cable, span equipped with an ACSR [2] Crow conductor, sometimes in combination with other equipments such as a vibration damper or a local mass, to investigate how the presence of such devices impacts conductor vibrations. It results from these experiments an interesting comparison of two widely used fatigue indicators, the relative displacement Y_b (also called "bending amplitude") [3] and fy_{max} (the product

[1] IREQ: Institut de Recherche d' Hydro-Québec, www.Ireq.ca

[2] Aluminium Conductor Steel Reinforced

[3] Peak-to-peak displacement of conductor relative to the clamp, generally measured at 89mm from the last point of contact between the conductor and the metallic clamp. In this chapter, Y_{b1}, Y_{b2} $(= Y_b)$ and Y_{b3} stand for relative displacement measured respectively at 44.5, 89 and 178mm from the last point of contact between the conductor and the metallic clamp

of antinode amplitude of vibration by frequency).

Recognized vibration intensity indicators are the product of antinode amplitude of vibration by frequency (fy_{max}) [1, 7, 13], angle through which the conductor is bent at the clamp [42, 74, 45], relative displacement (Y_b) [59, 79, 81] and dynamic strain at the surface of an outer-layer strand (usually measured at the top of conductor [43]) in the vicinity of the clamp [83, 92]. Fatigue curves may be obtained through tests on laboratory spans using any of those parameters as the measure of vibration intensity, but it is more common to see fatigue curves drawn as a function of relative displacement, fy_{max} or an equivalent idealized stress [25].

Among those vibration intensity indicators, relative displacement has been used for field measurement for decades [74]. However, nowadays, new technologies are being developed, which allow continuous antinode amplitude monitoring. Given this context, it is interesting to investigate what are the opportunities associated with real time field measurement of antinode amplitude of vibration, in order to perform a vibration risk diagnosis of a line. The tests performed on IREQ test span allow to compare relative displacement and fy_{max} as vibration intensity indicators and to bring interesting arguments in this discussion.

The tests performed also meet the following objectives:

- Collect all the required data to validate the modelling of a conductor vibrating at its natural vibration modes,
- Improve the understanding of conductor behaviour at singularities along the span where the impact of conductor bending stiffness is particularly important. Examples of such singularities are suspension clamps, spacer (damper)/damper clamps, aerial warning markers, real time monitoring devices, etc..
- Improve the understanding of the interaction between parameters Y_b and fy_{max},
- Finally, collected data also enables the assessment of conductor self damping.

2.2 Presentation of test equipment

A sketch of IREQ 63.15m long laboratory test span is shown in the figure 2.1. The conductor is installed into rigid clamps which are part of an extremely stiff concrete block embedded in the rock underground in order to minimize end losses. Conductors are tensioned at least 24h before the beginning of tests, in order to get a final tension value of approximately either 15 or 25% of their RTS (rated tensile strength). An electrodynamic shaker located at

1.69m from the anchoring block provides a vertical alternating force to the conductor.

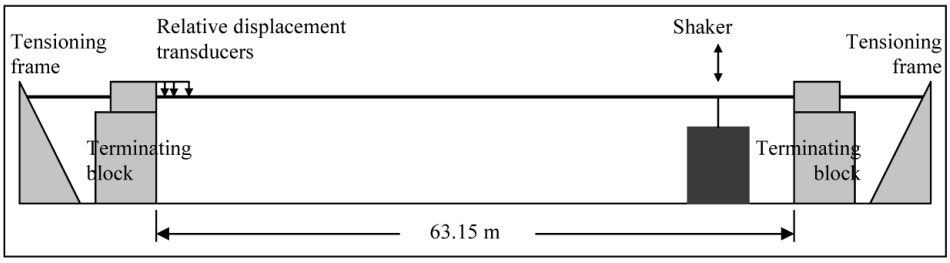

Figure 2.1: IREQ 63.15m long laboratory test span

Two cables have been tested: a ground cable (7 steel wires, diameter: 11.0mm, mass per unit length: 0.577kg/m, rated tensile strength (RTS): 86.7kN) and a Crow conductor (54 aluminium wires over 7 steel wires, diameter: 26.3mm, mass per unit length: 1.369kg/m, RTS: 117.2kN). Other equipments used during the tests include:

- A conventional saddle metal-to-metal suspension clamp, which was installed on the span with a 5 inclination angle relative to horizontal to reproduce the exit angle of the cable in a standard span length,
- An aeolian vibration damper developed by IREQ and commercialized by Helix Uniforme Ltd [21]. Energy dissipation is obtained through an elastomer articulation. The damper is installed at a distance of 1 m from the last point of contact with the clamp. Two non-contact sensors measured the relative displacement of the conductor on each side of the damper clamp, at 89mm from the last point of contact with the conductor.
- A fake vibration damper, with the same geometry and located at the same place as in the previous set-up, but without articulations and thus no energy dissipation.
- A prototype of a real time monitoring device based on vibration measurement. It consists of a micro system array in its aluminium housing. The housing dimensions are 370mmx173mmx255mm and it is fixed on the conductor with a metallic clamp on one side and an EPDM clamp on the other side. The mass of this prototype is approximately 7kg. During the tests, the position of the housing on the span was slightly modified, but remained between 5 and 9m from the suspension clamp. Two non-contact sensors, located at a distance of respectively 89mm and 178mm from the metallic clamp recorded the conductor displacement relative to the device.

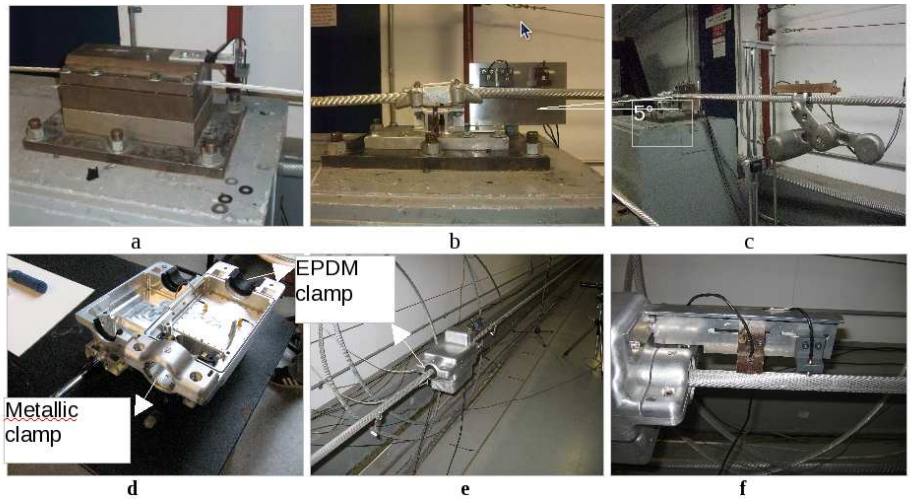

Figure 2.2: (a) Span end opposed to the shaker equipped with a rigid clamp embedded in a concrete block; (b) Span end opposed to the shaker equipped with a suspension clamp; (c) aeolian vibration damper ; (d-e) real time monitoring device; (f) non-contact sensors located at 89 and 178mm from the last point of contact with the metallic clamp in order to measure relative displacements

2.3 Experiments description

For each experiment, excitation frequency has been tuned so as to correspond with one of the natural frequencies of vibration of the conductor and the followings have been measured:

- Conductors excitation frequency.
- Antinode amplitude of vibration (using a Zimmer camera).
- Location and vibration amplitude of 4 nodes on the span (three nodes located near the span end, and one node located near the shaker), so as to deduce conductor self damping. The vibration amplitude of nodes is measured with non-contact sensors.
- Conductor relative displacement, i.e. peak-to-peak displacement amplitude measured respectively at 44.5 (Y_{b1}), 89 (Y_{b2}, frequently simply written Y_b in the literature), and 178mm (Y_{b3}) from the last point of contact with the metallic clamp, using non-contact sensors.
- In case there is some equipment installed on the span, relative displacements at 89mm (Y_b or Y_{b2}) and/or 44.5mm (Y_{b1}), and/or 178mm (Y_{b3}) from the device's clamp is measured.

2.4 Analysis of the results

2.5 Relationship between Y_b and fy_{max}

A steel ground wire and Crow conductors have been tested at several eigen frequencies, comprised respectively between 18 and 113Hz and between 7 and 62Hz. For each frequency, tests were repeated with three different amplitudes which corresponded to fy_{max} values of 40, 80 and 160mm/s. Free-loop amplitudes were measured, as well as "relative displacements" at 44.5, 89 and 178mm from the last point of contact with the clamp. The following figures represent the evolution of the ratio Y_b over fy_{max} as a function of frequency. As can be seen in these figures, for all cases without any particular in-span equipment, the ratio between Y_b over fy_{max} is almost constant with frequency and close to:

- 0.0030s for steel cable equipped with a rigid clamp and tensioned at 25%RTS and for ACSR Crow conductor equipped with a suspension clamp and tensioned at 15%RTS,
- 0.0023s for Crow ACSR conductor equipped with a rigid clamp, whatever its tension.

There is a considerable difference (superior to 20%) between the Y_b/fy_{max} ratio of the Crow ACSR conductor as the span extremity changes from suspension to rigid clamp.

The correlation coefficient between measured data and linear regression is for all cases superior to 0.95, and most of the time very close to unity, even when relative displacements are measured at a distance of 44.5mm or 178mm from the clamp. The ratio between Y_b and fy_{max} tends to decrease slightly with an increase of fy_{max}.

As could be expected, the situation is different when in-span devices such as vibration dampers are installed. Figure 2.3 represents the evolution of the ratio Y_b measured at 89mm over fy_{max} as a function of frequency for three different configurations: A suspension clamp (figure 2.2 b) is installed at the span end remote from the shaker and one aeolian vibration damper (figure 2.2 c) is installed at a distance of 1m from the suspension clamp. The conductor is tensioned at 24%RTS. Same set-up but with a fake (rigid) aeolian vibration damper. Same set-up but with a real-time monitoring device (figure 2.2 c) installed at 5 to 9m from the suspension clamp. One can see in figure 2.3 that there is no obvious relationship between Y_b and fy_{max} whenever some equipment which can be considered as an obstacle to wave propagation is installed in the vicinity of the span end. The correlation coefficients between measured data and a linear regression are low (lower than 0.55), which means that amplitude near the clamp is no longer an image of in-span amplitude (and vice versa).

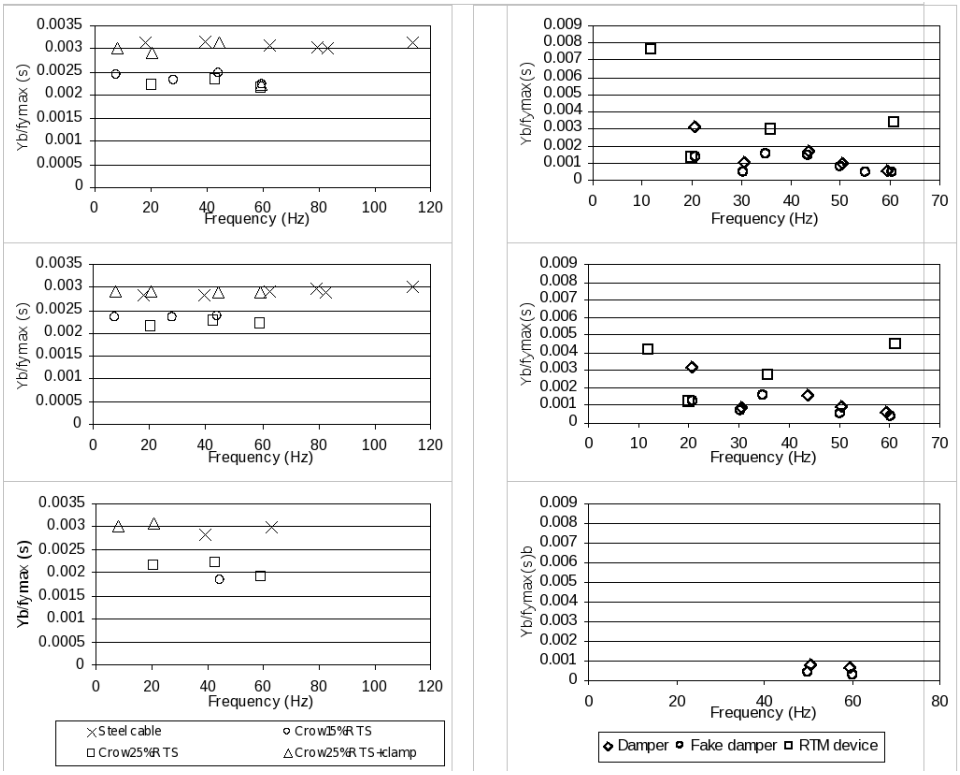

Figure 2.3: Evolution of the ratio of Y_b over fy_{max} as a function of frequency for $fy_{max} = 40mm/s$ (top), $fy_{max} = 80mm/s$ (middle) and $fy_{max} = 160mm/s$ (bottom), left column corresponds to no device installed in-span, right column corresponds to tests with devices installed in-span

2.6 Influence of a suspension clamp on Y_b measured near span end

When a suspension clamp is introduced at the extremity of the span opposed to the shaker (to replace the rigid clamp visible in figure 2.2 a), an increase of 30% in average of relative displacements measured at 89mm from the last point of contact between conductor and clamp is obtained. This phenomenon is illustrated in the following figure.

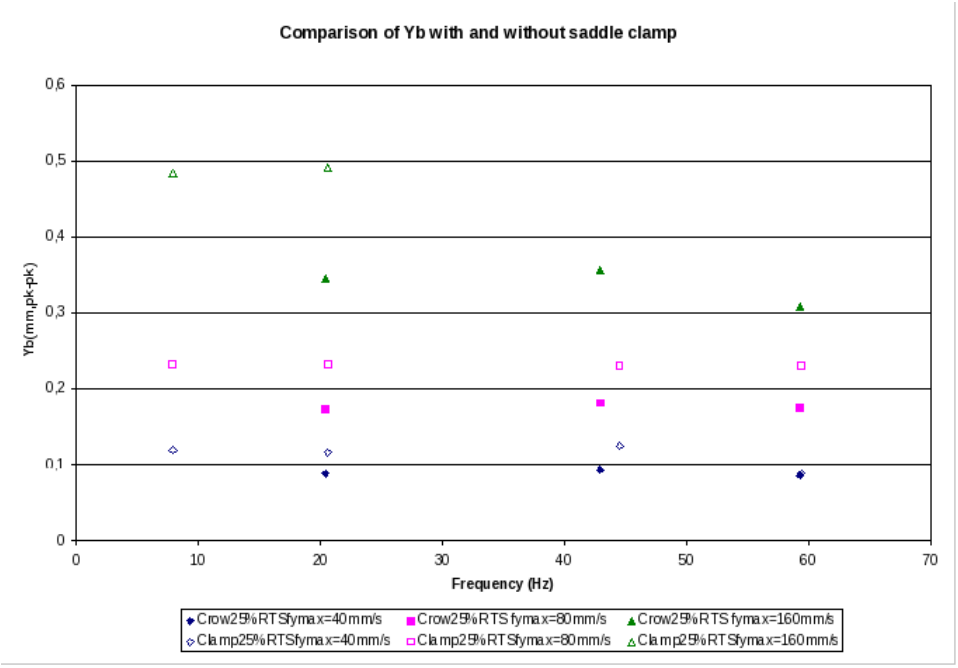

Figure 2.4: Relative displacements (measured at 89mm from the last point of contact between conductor and suspension clamp) at span end with and without the presence of a suspension clamp

This increase in relative displacement measured values is probably due to the fact that with a suspension clamp, the mode shape begins slightly further inside the clamp since the keeper is slightly shorter than the length of the clamp in contact with the conductor. Moreover, there may be some deformation of the saddle clamp itself since it is made of aluminium while the rigid clamp which is thicker, made of steel, and held in place with eight bolts is much more rigid. These results show that the last point of contact between conductor and clamp may not be perfectly still and its behaviour may change with amplitude and frequency. Moreover, while the suspension clamp is held in place on the laboratory span end, in the field, a real suspension clamp may rock at amplitudes depending on the mode excited in the adjacent spans.

Therefore, the relationship between fy_{max} and Y_b is sometime difficult to obtain and it may have an impact on damage and residual lifetime estimation with fatigue curves and cumulative damage law. In the rest of this chapter, a suspension clamp will systematically be present at the span end opposed to the shaker.

2.7 Comparison between Y_b at the suspension clamp and at the equipment clamp

In this paragraph, the introduction of line devices on the span is considered, and a comparison of relative displacements measured at the suspension clamp and at the device clamp is performed. Let us first consider the case of Crow conductor tensioned at 23.8%RTS, with an aeolian vibration damper 1m apart from the suspension clamp. Figure 2.5 compares relative displacements measured on both sides of the damper clamp (one side is oriented towards the suspension clamp and the other one towards the vibration shaker) with relative displacement at the suspension clamp. The highest relative displacements are observed at the clamp of the damper, on the side oriented towards the shaker [4]. The fact that relative displacements may be higher at the damper clamp than at the suspension clamp at some frequencies has already been observed (e.g. by IREQ) during previous measurements made with Stockbridge dampers. Relative displacements at the Aeolian vibration damper's clamp, but on the suspension clamp's side, are significantly less important than the suspension clamp's ones. Let us now consider the case of Crow conductor tensioned 23.8 % RTS, with a suspension clamp and a real time monitoring device in the vicinity of the clamp (note that the metallic clamp of the monitoring device is oriented towards the suspension clamp). Relative displacements are measured at 44.5, 89 and 178mm from the last point of contact with the Slater clamp, and at 89 and 178mm from the last point of contact with the clamp of the monitoring device during a test where excitation is at an eigen frequency of 12Hz.

For most measurements, relative displacements (at 89 and 178mm of the last point of contact between conductor and clamp) at the equipment clamp are inferior to those at the Slater clamp. Nevertheless, there is one exception. When the monitoring device is located at 8.45m from the Slater clamp, for fy_{max} equal to 20mm/s pk, the relative displacement at the monitoring device was more important than at the Slater clamp. This will be further investigated through modelling. It results from this paragraph

[4] When the vibration damper is installed at a distance of 1m from the suspension clamp, it subdivides the initial span in a two portions, a long one (L-1) m and a short one (1m). With regard to propagation of waves created by the shaker, we can say the long portion of span is "before the obstacle to vibrations (the damper)" and the short portion is "after" this same "obstacle".

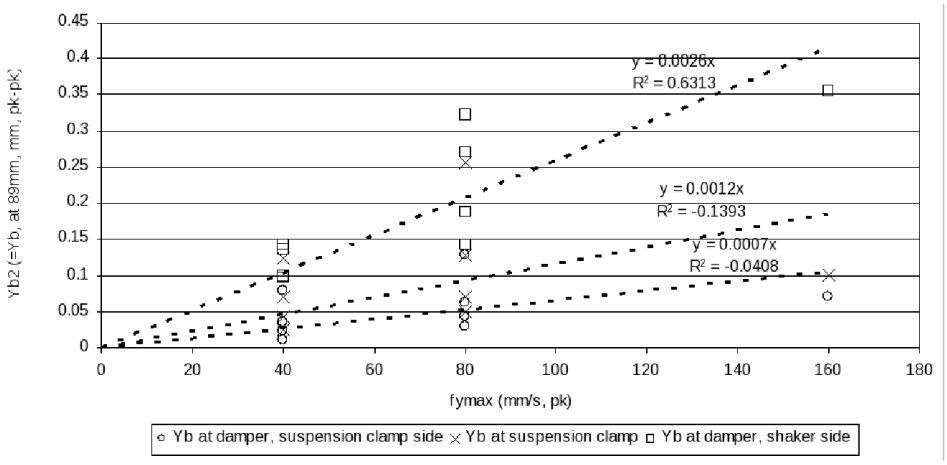

Figure 2.5: Comparison of relative displacements measured at 89mm from suspension and dampers clamp, Crow conductor tensioned at 23.8 %RTS

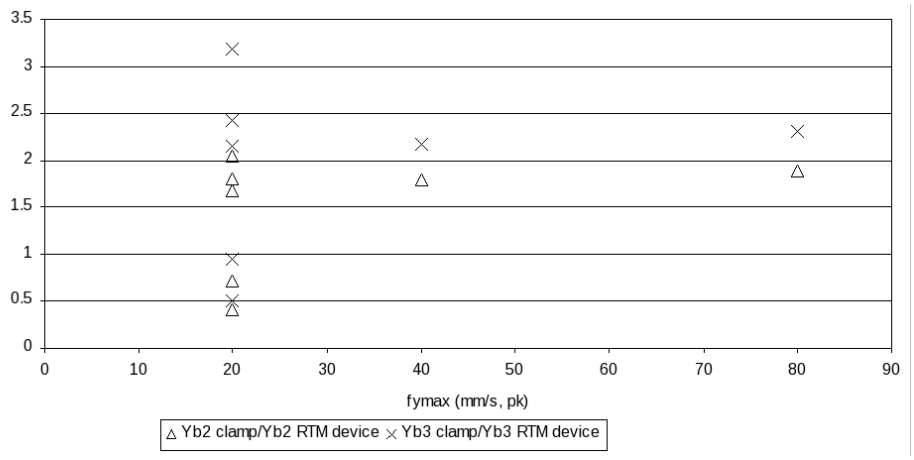

Figure 2.6: Comparison of ratios of relative displacements measured at 89mm and 178mm from the suspension and real time monitoring device clamp, Crow conductor tensioned at 23.8%RTS

that the study of relative amplitudes in the vicinity of suspension clamps is only part of the vibration information. It must be completed by in-span measurements to perform an adequate vibration risk analysis because all span locations where the movement of the conductor is restrained may be at risk (e.g. near the clamp of vibration dampers, air warning markers, spacers).

2.8 Conclusions

When no particular in-span equipment (such as vibration damper, aircraft warning marker, spacer) is installed in a span, fatigue parameters Y_b measured at the extremity of the span and fy_{max} lead to similar information: the ratio between conductor bending stiffness and free-loop amplitude of vibration is almost constant with frequency for all test cases without any particular in-span equipment. It has also been observed that the ratio between Y_b and fy_{max} decreases slightly with an increase of fy_{max}. The situation is completely different when in-span devices such as vibration dampers are installed. Free-loop amplitude of vibration is no more an image of relative displacement at the suspension clamp. Tests have shown that the most important relative displacement may be present at the clamp of in-span devices, particularly when their mass may disturb locally the modal shape of the span. Such case depends on the system location and the ratio mass of the device/mass of the conductor. This appears to be quite disturbing. A fixed point (like a span end) could have been considered at first as more rigid than a moving point, but it has been observed that local mode shape may be significantly affected. Also, it has been observed that resonances may occur when subspans are present (between two systems or between a system and the suspension clamp), and may catch more energy than in the free span situation. In the reality, such high amplitudes may probably occur between the span extremity and some line equipment or between two line equipments such as aircraft warning markers for example. The last point of contact between conductor and clamp may not be perfectly still and its behaviour may change with amplitude and frequency. Moreover, while the suspension clamp is held in place on the laboratory span end, in the field, a real suspension clamp may rock at amplitudes depending on the mode excited in the adjacent spans. Therefore, the relationship between fy_{max} and Y_b is sometimes difficult to obtain and it may have an impact on damage and residual lifetime estimation with fatigue curves and cumulative damage law. The present study will be completed by a modelling of the observed phenomena (see chapters 5-7), but an important conclusion can already be drawn: the study of relative amplitudes in the vicinity of span extremities is only part of the vibration information. It must be completed by in-span measurements to perform an adequate vibration risk analysis because all

span locations where the movement of the conductor is restrained may be at risk (e.g. near the clamp of vibration dampers, air warning markers, spacers, etc.).

Chapter 3

Self-damping evaluated in actual conditions

3.1 Introduction

The leading roles and interactions of aeolian vibration, self damping and fretting damage mechanisms in the fatigue phenomenon have already been underlined in chapter 1 (State of the Art). Conductor self damping needs to be taken into account in describing the aeolian vibration phenomenon. In fact, wind energy input is balanced by conductor self damping (and any additional damping on the line, due to any kind of damper or to the aerodynamic damping). Conductor self damping is very much related to inter-strand friction. As amplitude increases, there is some stick-slip behaviour between the strands of different layers. Such friction is at the origin of energy dissipation. It is thus very much influenced by the frequency (which affects- through the modal shape- the radius of curvature of the vibration for a given amplitude) and by the conductor tension, which has an effect on the inter-layer stickiness.

To date, a method based on the "Energy Balance Principle (EBP)" has often been used to approximate the vibration behaviour of a given power line. It requires for its use wind power input as well as system self damping power values. Up to now, information on conductor self damping generally comes from laboratory measurements, which require a substantial amount of money and time. A state of the art on Wind-Induced conductor motion was published by EPRI in 2006 [25]. Different sets of parameters for self damping computation using the so called "power law" (see section 1.11) are given in the second chapter of that book. The range of variation of these parameters is given in section 1.11 of the present document. Each set of parameters has been measured by an author on a laboratory span which length is comprised between 36 and 92m. Computing the amount of self damping with this information, one may find very different results

according to the selected set of parameters. As an example, for an amplitude of vibration equal to 20mm, a frequency of 5 Hz and a mechanical tension of 30 kN, comparing the self damping power computed using on the one hand the set of parameters given by G. Diana and on the other hand the set of parameters given by Noiseux, one obtains $\frac{P_{Diana}}{P_{Noiseux}}$ ranging from 6 to 30 [1]. This shows an extreme sensitivity to the parameters of the power law (and in particular to the tension exponent n).

Many experiments have been carried out in the area of self damping, but after decades of research, the whole picture is not known yet. The influence of wind direction, large scale wind turbulence, conductor stranding (smooth wire, round wire), the along span effect (tension is not constant, wind spatial coherence) and some other aspects are still under investigation. Measurements are needed to better understand the actual behaviour of power lines in the wind.

This chapter will be focused on continuous observations at a site well known for being prone to aeolian vibration. Aeolian vibration occured during about 30 % of the measurement period. About 10 million cycles were observed on each cable. They covered all frequencies between 2 and 60 Hz but most cycles were located within the range 3 to 30 Hz. This chapter is suggesting new ways to better tune self damping on actual observations on a cable during a few weeks to deduced appropriate laws of dissipation. The aim is to help utilities to improve the design of their lines, in particular to check the need, if any, of dampers and their efficiency after installation.

3.2 Presentation of test equipment

The measurements were performed on a 190 m dead-end span equipped with four different kinds of conductors. Two of them are conventional AAAC conductors (Aster 228 and Aster 570). The two others have Z shaped wires in their external layers (Azalee 261 and Azalee 666, see figure 3.1). Their properties are summarized in table 3.1.

Figure 3.1: Section of an AZALEE666 conductor with Z shaped wires in its external layer

[1] Diana gives l=2, m=4, and n comprised between 1.5 and 3 while Noiseux gives l=2.44, m=5.63 and n=2.76. Taking n=1.5 or n=3 in Diana's set of parameters, one obtains respectively $\frac{P_{Diana}}{P_{Noiseux}} = 6$ or $\frac{P_{Diana}}{P_{Noiseux}} = 30$.

Table 3.1: Conductor properties

Name	Aster 228	Aster 570	Azalee 666	Azalee 261
Area [mm^2]	227.83	570.22	666	261
Diameter [mm]	19.6	31.05	31.5	19.6
Breaking load [kN]	74.05	185.3	211.6	84.9
Linear mass [kg/km]	648	1631	1900	737
Lay direction	left	left	right	right
Round wires				
Wire number	37	61	1+6+12	1+6
Diameter [mm]	2.8	3.45	3.5	2.8
Z shaped wires				
Wire number			18+24	12+24
Thickness [mm]			3.5	2.8

A Lacrosse WS2300 weather station was installed on-site. It permitted among others to continuously measure the wind speed (to be more precise, its average value deduced from 8 seconds of records). In the data sheet of the weather station, the following characteristics are given for the anemometer: wind speed range of 0-50m/s, precision of 0.1m/s and threshold start-up speed of 0.7 m/s. A turbulence value of the order of 20 % was deduced from the measurements. The device used to record vibration amplitudes is a patented Microsystems array (including among others 3D accelerometers) embedded in an aluminium housing (see figure 2.2.d and 2.2.e). It was fixed directly on the conductor. Its location during the first test campaign was about 0.4m away from the span end. During the second test campaign, it was fixed about 9m away from the span end. The mass of the whole measuring system is of the order of 6kg. Further details on the device can be found in [53].

Some calibration tests of the monitoring device have been performed on IREQ's laboratory test span, using a vibration shaker to excite the cable. The main results are given in chapter 2. The tests included not only a study of the influence of the monitoring device, but also a comparative study with the influence of other line equipment such as an aeolian vibration damper or a concentrated mass (which represents the effect of e.g. an "Aerial Warning marker"). Using a vibratory shaker to excite the cable, it has been observed that the introduction of a device in a span (whether it is a monitoring device or a vibration damper or a concentrated mass) was susceptible to modify the vibration amplitudes. It is as if the initial span were subdivided in smaller "subspans" which extremities correspond to the location of some line equipment. There may be as many different amplitudes of vibration in a span as there are "subspans"... In summary, under the test conditions, different amplitudes of vibration may be met on either side of

some line equipments. Nevertheless, a shaker excitation, though extremely helpful for laboratory investigations, differs from a wind-induced one, so that these laboratory calibration results may not serve to predict the effect of the monitoring device on the vibration amplitudes of a real span, under a real wind excitation. Further calibration tests (on a real wind-excited test span) would be required to deal with both the calibration question and the problem of shaker excitation compared to wind-induced excitation.

3.3 Self damping evaluated in actual conditions

To date, the Energy Balance Principle (EBP) has often been used to approximate the vibration behaviour of a given power line (see section 1.7). This principle, as detailed in [25, 84] and many other studies, holds that the steady-state amplitude of vibration is that for which the energy dissipated by the conductor and other devices used for its protection and support equals the energy input of the wind. Most of the time, the expressions of wind power input and self damping needed to apply this principle come from laboratory tests. Caution is taken during those laboratory investigations to remove the aerodynamic damping due to conductor friction in still air, to obtain the "net" wind power input and the "net" self damping to be used in the EBP. During vibration, all aerodynamic effects are included in the net wind energy input. There is no need to re-insert aerodynamic damping in the EBP [70]. Both conductor self damping and wind power input are very strategic data for evaluating lifetime based on calculations only.

3.3.1 The self-damping power

The self-damping power is difficult to measure because extremely low quantities are involved. Also, in a laboratory environment one cannot take into account:

- the sag effect,
- the cable ageing which may affect damping,
- etc.

Furthermore, it is also believed that non linearities play a role in the conductor motion (see chapter 6). Obviously, in real world, span end effects also make their contribution to the global damping on actual span and only on-site measurement would be able to evaluate this accurately.

In laboratory, a series of tests is carried out in still air to determine the conductor self damping (the aerodynamic damping is subtracted from the measurements thanks to an adequate formulation [70, 49]). These tests are needed for any particular conductor, but the range of values may be deduced

from literature as it will be detailed in the following section. As shown in the introduction, the self damping parameters deduced from laboratory tests have a significant scattering in their evaluation.

3.3.2 The wind power input

The wind power input is usually estimated thanks to wind tunnel tests. During those tests, either a flexible or a rigid cylinder is used to simulate a conductor. A set of tests is performed in wind tunnel at different wind velocities to calculate the energy transfer from the wind to the mechanical system. Details on the method used to derive the wind power input curves can be found in [25] and also in section 7.2.4 of the present document. These curves have been produced in the literature and may be used for any case with round conductors. A comparison of eight wind power input curves can be seen in [8]. One of the key information of this comparison is that the wind power input may vary from a factor 2 according to the model chosen for wind power input. Based on these facts, self damping, which is the most uncertain value, will be evaluated from on-site observations.

3.3.3 Self damping fit with actual observations

In the present work, the self damping has been evaluated using the EBP with a wind power input given by Rawlins [72]. Let us first describe Rawlins' model for wind power input. Let P_w be the power imparted to a conductor by the wind. As published in [25], P_w [W/m] can be expressed as a function of the reduced decrement δ_r:

$$P_w = \pi^2 \rho_a f^3 (\frac{y_{max}}{d})^2 \delta_r \tag{3.1}$$

In the previous expression, ρ_a stands for the air density $[kg/m^3]$, f the frequency [Hz], y_{max} the 0-peak antinode amplitude of vibration, d the conductor diameter [m]. In [72], Rawlins proposes a polynomial function to fit the reduced wind power input at a certain turbulence intensity ranging from 1 to 50 %:

$$\delta_r = \sum_{i=0}^{8} b_i (\frac{Y_{max}}{d})^i \tag{3.2}$$

where Y_{max} is the peak-to-peak antinode amplitude of vibration.

The polynomial coefficients required to use this function are given in table 3.2.

It is the latter polynomial fit which has been used as an input for the present work, assuming a wind input turbulence equal to 20 % (as measured on site).

Table 3.2: Test campaign (2007, 550 hours of recording), tension ranges used for the tuning of "n" self damping coefficient

	Turbulence Intensity - percent							
	1	5	10	15	20	25	30	50
b_0	34.168	18.049	13.068	10.368	8.667	7.424	6.460	4.205
b_1	-406.028	-150.250	-110.024	-90.243	-79.443	-71.244	-64.283	-45.629
b_2	2741.457	963.571	701.130	564.503	493.535	441.383	399.244	289.692
b_3	-9899.726	-3460.676	-2436.195	-1915.370	-1656.876	-1472.724	-1332.614	-985.356
b_4	20488.414	7169.112	4879.637	3752.601	3209.715	2833.061	2561.163	1923.147
b_5	-25119.433	-8816.763	-5839.613	-4402.105	-3722.522	-3262.983	-2945.282	-2241.371
b_6	18000.492	6344.838	4119.534	3049.446	2550.008	2220.876	2001.174	1541.440
b_7	-6955.235	-2464.492	-1579.364	-1149.512	-950.860	-823.263	-740.502	-576.682
b_8	1118.049	398.636	253.667	181.697	148.718	128.061	114.978	90.425

Applying the energy balance principle, the wind power input has been assumed equal to the power dissipated per unit length within the vibrating conductor. Referring to section 1.8, the latter amount can be approximated by the "power law" (equation 1.24): $\frac{P}{L} = k\frac{y_{max}^{l} f^{m}}{T^{n}}$ [W/m]. During the observations, there were interesting periods of vibrations covering the whole range of frequencies. For a given wind power input, the best fit in self damping coefficients (l, m and n) can thus be estimated.

The second test campaign included a considerable amount of data, and a wide range of (measured) tension in the conductor. Not only were there temperature changes, but tension was also changed manually from one week to another. Moreover, two different kinds of conductor diameter were tested.

The data collected during this test campaign was used to find a suitable combination of exponents for the self damping power law. In order to do that, as can be seen in table 3.3, recorded data was classified into three classes according to the corresponding conductor tension value.

A tuning operation is performed on the damping coefficient n (see equation (1.24), tension dependency). In the frequency range of interest for aeolian vibration, the amplitudes are reasonably well predicted for the following values of exponent n :

- Aster 228: n=4.4,
- Azalee 261: n=4,
- Aster 570: n=2.6,
- Azalee 666: n=2.7

Figures 3.2 and 3.3 show both measured amplitudes and amplitudes predicted by the self damping power law for conductors Azalee666 and Azalee261, when exponent n is taken equal to 2.7 and 4 respectively. Table 3.4 is a summary of suitable combinations of self-damping coefficients for the different conductors, filled in under the following hypotheses:

Table 3.3: Test campaign (2007, 550 hours of recording), tension ranges used for the tuning of "n" self damping coefficient

	Range [% RTS]	Range [N]
Azalee 261		
Tension range 1	9.4-12	7992-12206
Tension range 2	12-15	10206-12720
Tension range 3	15-17.3	12720-14687
Aster 228		
Tension range 1	11.5-13.2	8526-9773
Tension range 2	13.2-16.4	9773-12127
Tension range 3	16.4-18.1	12127-13408
Azalee 666		
Tension range 1	12.7-14.7	26852-31116
Tension range 2	14.7-16.0	31116-33949
Tension range 3	16.0- 17.3	33949-36680
Aster 570		
Tension range 1	12.6-15.3	23250-28351
Tension range 2	15.3-17.4	28351-32215
Tension range 3	17.4-19.3	32215-35805

Table 3.4: Test Campaign (2007, 550 hours of recording), best coefficient combinations to fit low frequency (lower than 20-30 Hz) amplitudes

Conductor	l	m	n
Aster 228	2.44	5.63	4
Aster 570	2.44	5.63	2.6
Azalee 261	2.44	5.63	4
Azalee 666	2.44	5.63	2.7

- The combinations given in table 3.4 correspond to a fit of low frequency amplitudes of vibration (lower than 20-30 Hz), recorded during the second test campaign,
- Predicted amplitudes are obtained by intersecting wind power input curves from Rawlins and the conductor self damping power law. The wind power input curves cover a range of relative amplitudes (peak-to-peak antinode amplitude/diameter) between 0.05 and 1.4. For a given frequency, when wind power input is (for all amplitudes) higher than the power which can be dissipated by the conductor, the predicted peak-to-peak relative amplitude is taken equal to 1.4.

For Azalee 261 and Aster 228, the values of coefficient "n" (n=4 and 4.4 respectively) are outside the range given in the literature. This is not the case for large diameter conductors (Azalee 666 and Aster 570), where

their evaluation (n=2.7 and 2.6 respectively) is within the top band of the proposed values.

Using data recorded during the first test campaign, it was possible to check whether the coefficients listed in table 3.4 were suitable to predict the amplitudes of vibration on the same test site, but during another test period. The result is given in figure 3.4. For frequencies ranging from 0 to 20 Hz, a good agreement can be seen between the fit and data measured in 2006.

Some "holes" can be noticed (frequency ranges with no corresponding recorded vibrations) in the frequency domain, near 11 Hz, 24 Hz and 32 Hz. As there is no reason not to have seen corresponding wind speeds, these zones are probably related to stronger damping in these areas. The extra damping obviously does not come from the conductor itself. Therefore it must come from outside: mainly from towers.

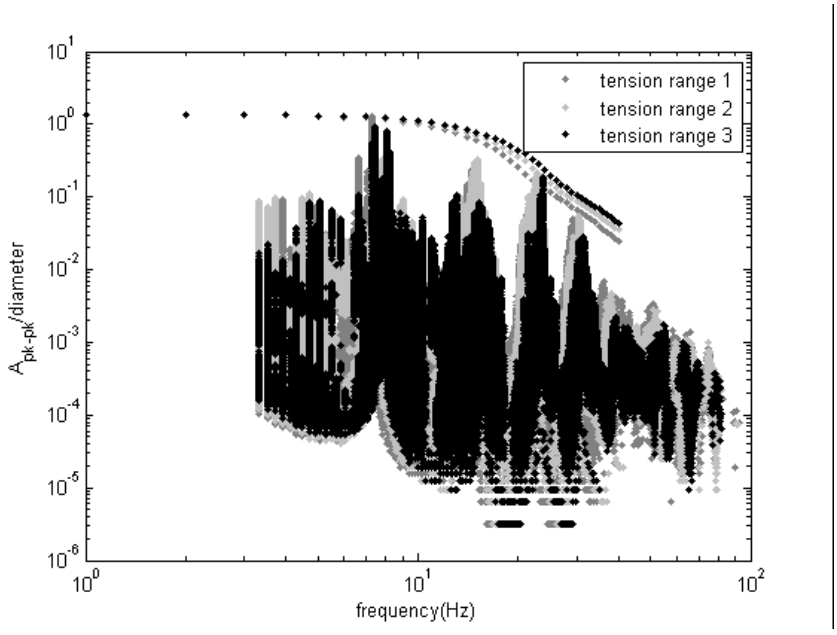

Figure 3.2: Dimensionless anti-node amplitude of vibration vs frequency. AZALEE666. Measured data is classified in three tension ranges (Table 3.3) and is fitted by a value of coefficient n equal to 2.7

3.3.4 Wind power input comments

Figure 3.5 shows 1 % and 20 % turbulence curves of the wind power input together with recorded data converted into self damping power using the best fit coefficient as explained in previous section. The envelope of the curve of the measured values (dots) obviously fits with the 20 % turbulence wind

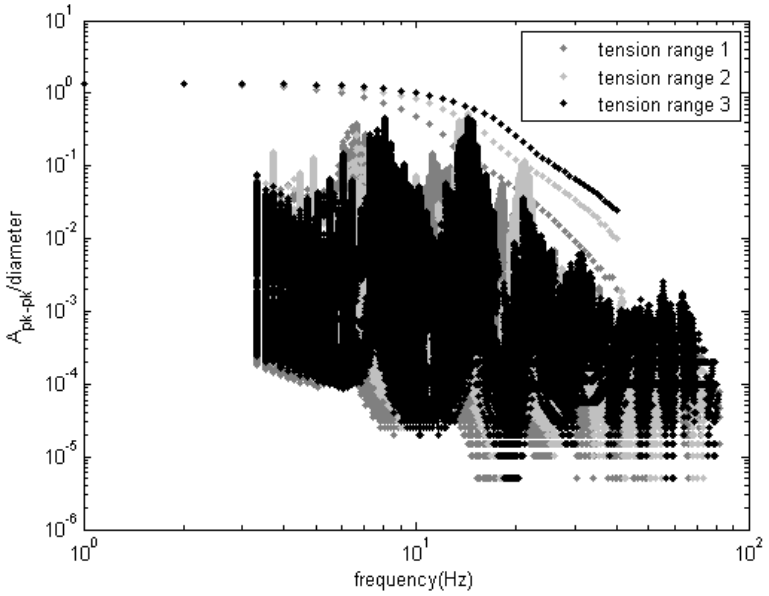

Figure 3.3: Dimensionless anti-node amplitude of vibration vs frequency. AZALEE261. Measured data is classified in three tension ranges (Table 3.3) and is fitted by a value of coefficient n equal to 4

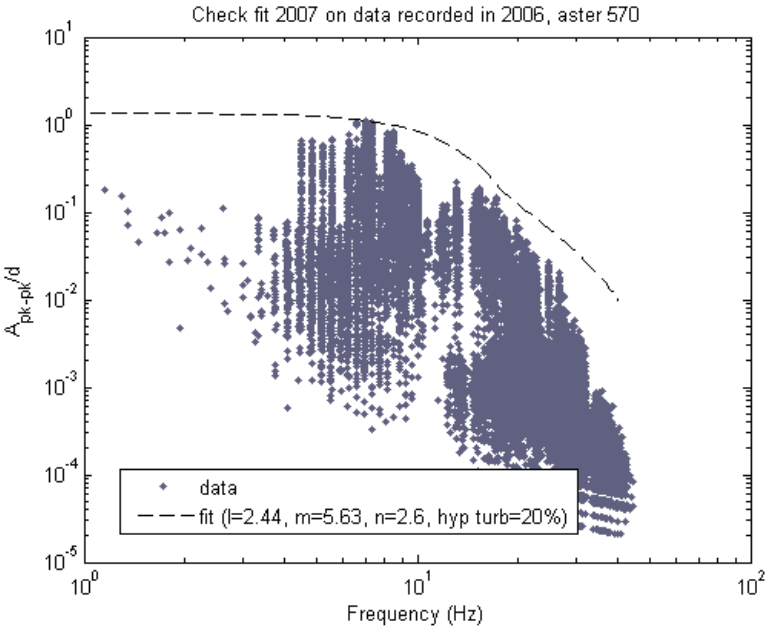

Figure 3.4: Checking of the fit based on data recorded in 2007 as a result of data recorded in 2006 -example of conductor ASTER570.

power input curve. Even though the discrepancies look small, the log-log graph emphasizes a significant difference between 1 and 20 % turbulence.

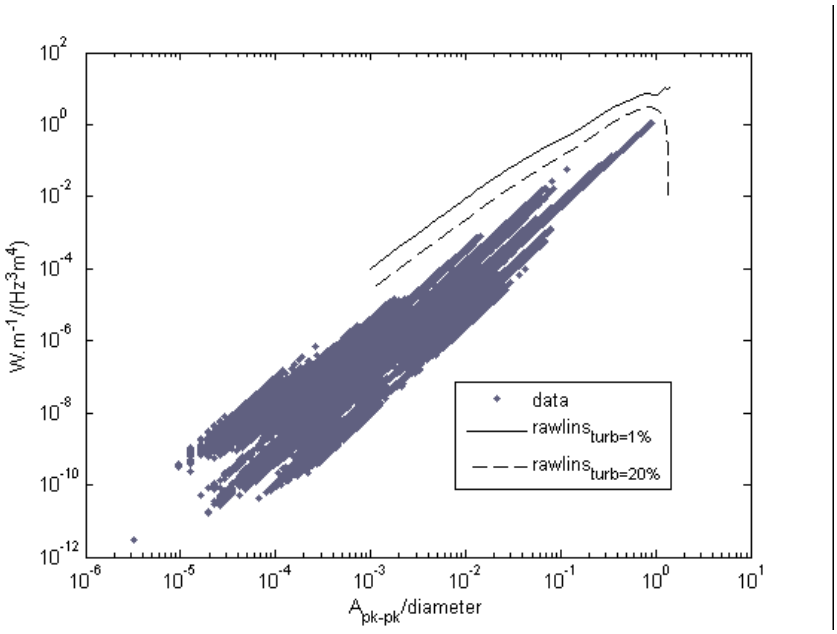

Figure 3.5: Reduced wind power input versus relative anti-node amplitude. In red, experimental dots based on self dissipation obtained using best fit coefficients for dissipation. In dashed and continuous lines, wind power input at 1 and 20% turbulence respectively, following Rawlins [71]

3.3.5 Real world approach of power line vibration

Self damping of conductors is overestimated by some existing heuristic laws available in the literature. This may be quite significant, particularly for smaller diameter conductors. The error in self power damping by existing laws may be as high as a factor of 30 for thin conductors (the actual value being 30 times lower than predicted), but the same factor is much closer to the real world in the case of larger conductor, e.g. between 1.3 and 2.

A few weeks of on-site measurement by appropriate systems might help to accurately evaluate actual self power damping, which could lead to a real world approach and better diagnosis.

3.4 Conclusions

Field experiments with the Ampacimon monitoring device provide interesting information on conductor self damping behaviour. Two periods of measurement have been detailed. The following conclusions may be drawn

from these tests based on four different types of conductor, all sagged at about the same level:

Based on fits of measurements, the best value of the self damping coefficient (tension exponent) n for Azalee 666 and Aster 570 are given in this chapter. The values of this coefficient are well within the range proposed in the literature. The dependence of both conductors, on tension in the dissipation law, was almost the same. To respect the same sag/span ratio, the tension in the smooth conductor has to be higher. All other things being equal, this will induce lower dissipation capacity for smooth conductors.

Based on fits of measurements, the best value of the self damping coefficient (tension exponent) n for Azalee 261 and Aster 228 are given. These values are much higher (about two times) than the values usually proposed by other authors. This means that the self power dissipation of these conductors is much lower than what can be predicted from the literature.

During most of the observations (between 54 % and 98 % of the time), there were high frequency vibrations of small amplitudes. These vibrations (over 20 Hz up to 100 Hz, the maximum detection level) were larger on smooth conductors compared to round wire conductors, but these vibrations had no effect on the fatigue behaviour, as their amplitudes were too small (this sentence results from an estimation of the conductor damage using the method described in sections 1.17 and 1.18). They were, therefore, not taken into account in the self damping power evaluated above.

Another interpretation will be given to these results in chapter 7, in light of other results related to the modelling of conductor self damping.

Chapter 4

The failure vibratory pattern of a conductor

4.1 Introduction

Beyond its scientific interest, the detection of a wire failure may represent some potential for fatigue study. The number of broken wires is a very practical fatigue indicator. An interesting question is: could wire failures be detected in real life processing the conductor accelerations? This chapter represents a first step in order to answer this question by characterizing the vibratory pattern generated by a failure. It describes tests which have been performed in Gremca's laboratories (Université Laval, Quebec), by Suzanne Guérard (ULg), helped by Claude Jolicoeur and under the supervision of Prof. Goudreau (ULaval).

4.2 Description of the set-up and tests

4.2.1 The test span

These tests were carried out on two conductors, at a constant bending amplitude Y_b (see sections 1.4-5 for the definition of this indicator) of the order of 0.7mm peak-to-peak, concomitantly with fatigue tests.

The test bench model can be seen in the following figure, which is extracted from [31].

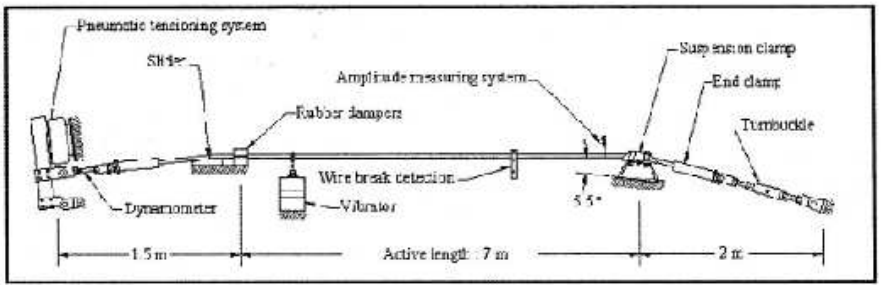

Figure 4.1: Resonance fatigue test bench, GREMCA laboratory

4.2.2 Conductors and fittings

As required by Gremca's laboratory, the brand and exact type of conductors may not be disclosed, but their main characteristics are as follows.

Type	Wires	Ext. ø[mm]	lin. mass [kg/m]	RTS [kN]
ACSR	54(al)/7(steel)	26.3	1.369	117.2
AAAC	61	31.05	1.574	183.6

During the tests, a clamp was installed at the span end opposed to the vibrator, at an angle of 6.5 to 7 degrees with the horizontal. Its model is of current use in France.

4.2.3 Test conditions

The ACSR conductor was strung at about 35kN (20%RTS) and the AAAC conductor at about 30kN (25%RTS).

The tests on the AAAC conductor took place on 05/05/2009, 06/05/2009 and 11/05/2009 and were deliberately carried out during work hours only (the driving system was stopped at 5 pm each day). A bending amplitude Y_b equal to 0.7mm (peak-to-peak) was maintained constant all along that period.

The tests on the ACSR conductor took place from 20/05/2009 until 27/05/2009. The driving system was not stopped between the first and second failure. The tests began at a constant amplitude of $Y_b = 0.65mm$ peak-to-peak. Due to the accelerometers saturation it was decided to reduce this amplitude to $Y_b = 0.6mm$ after the second failure.

4.2.4 Measurement of the conductor accelerations

Conductor accelerations have been measured with tri-axis accelerometers of the MEMS type. Their reference is LIS344ALH and their measurement range can be selected, either +-2g or +-6g. During the first tests these

accelerometers have been used in the +-6g range. For this range of acceleration, the manufacturer of the sensors guarantees a sensitivity of 0.22V/g+-5%. The minimum analogical output of the accelerometers is 0V and the maximum 3.3V.

In general, during the fatigue tests performed at Gremca, the conductors are excited at a frequency which is near their fifth vibration mode. In order to minimize the impact of the excitation signal and the potential saturation of the accelerometers, it was decided to place the accelerometers at the first vibration node near the suspension clamp (note that the wire failures generally occur where the motion of the conductor is constrained, that is to say at the clamp in the present case).

The accelerometers were placed diametrically opposed to each other on the conductor, with a lever arm of 0.1m from the conductor axis.

The different measurement axes are shown in figure 4.2.

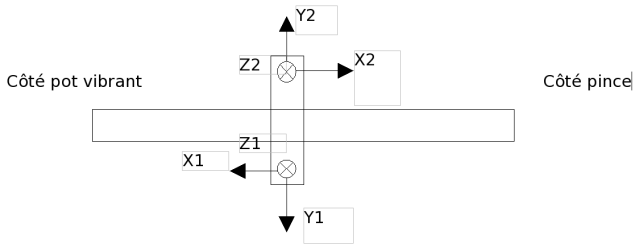

Figure 4.2: The two accelerometers are placed diametrically opposed on the conductor. In the figure, the shaker side is on the left and the clamp side on the right

The matching between those axes and the channels of the data acquisition system is given in appendix D.

4.2.5 Measurement of the rotation of the conductor

Usually, at Gremca's laboratory, a Hall sensor is placed near the clamp to detect a wire failure. In figure 4.3, this sensor can be seen between the span end and the accelerometer system. This Hall sensor is fixed to the ground

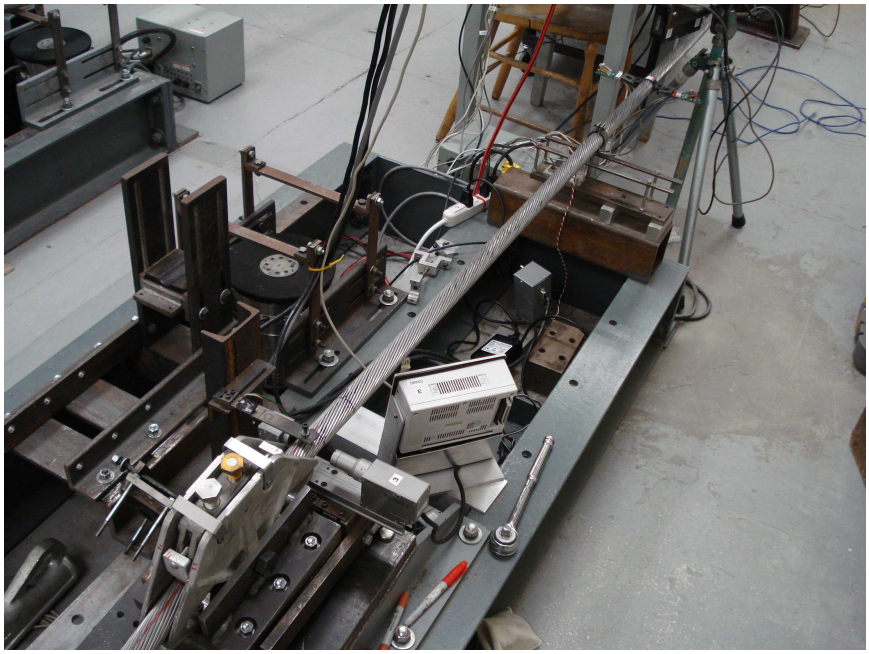

Figure 4.3: View of the test settings on the clamp side of the span, the Hall sensor is located between the clamp and the accelerometers

of the laboratory and has in its line of sight a metallic rod fixed to the conductor. The distance between this target point and the conductor axis is approximately 67mm. Any rotation of the conductor will set in motion the metallic rod fixed to it. The output from the Hall sensor is an image of the distance between the metallic rod and the hall sensor itself. The rotation angle of the conductor can be deduced by trigonometry.

The Hall sensor of the two test benches used have been calibrated respectively on 11/05/2009 (just after the first failure) for test bench 6 and on 27/05/2009 (just after the third detected failure) for test bench 3. The result of the calibration can be seen in appendix C. The error on the knowledge of the rotation angle is of the order of 15 %, which does not enable an accurate measurement but rather an estimation of its order of magnitude and gives some qualitative information on its evolution during the failure.

4.3 Analysis of the "noise" signal

The signal of interest is the failure vibratory pattern. All other contributions to the measured accelerations (such as accelerations generated by the alternate vibration of the conductor) can be considered as "noise". A comprehensive study of the "noise" signal has been performed in a separate document. It permits to highlight that even if the accelerometers are

located at a vibration node, the "noise" level is high. All accelerometers continually measure a harmonic acceleration signal of the order of a few g as well as a harmonic rotation signal. The level of the latter acceleration signal is maximum for the Z_i (vertical) axes. Figure 4.4 illustrates the level of vibration which is continually measured during the tests (data recorded on 30/04/2009 on the AAAC conductor, when $Y_b = 0.7mm$, which is a rather high amplitude). Figure 4.5 is the FFT (fast Fourier transform) of some signals measured during the tests, with a frequency resolution of 0.017Hz (sampling frequency equal to 1000Hz and number of samples equal to 60000). Here are some plausible hypotheses to explain the high level of "noise" and the harmonic content:

- Imperfect excitation. The signal of the vibration shaker may contain some harmonics,
- Changes in tension. The tension continually varies during the tests. Each vibration cycle corresponds to two cycles in tension, which can explain the presence of the second harmonic,
- Due to cable self damping, the amplitudes of incident and reflected waves are not equal. Their sum at a vibration "node" is not zero,
- The accelerometer system is fastened to the cable with a collar which width is not negligible, and may overlap on the up and down vibration loops,
- Changes in tension are parallel to the wires. Because of the angle between the conductor axis and the wires, the changes in tension may generate some rotation of the conductor (the rotation and conductor axes are the same).The rotation generates a tangential acceleration $\omega^2 * r$. The 0.1 m of the lever arm support of the accelerometers, which was chosen with the purpose of amplifying the conductor rotation during a wire failure also amplifies the motion due to changes in tension.

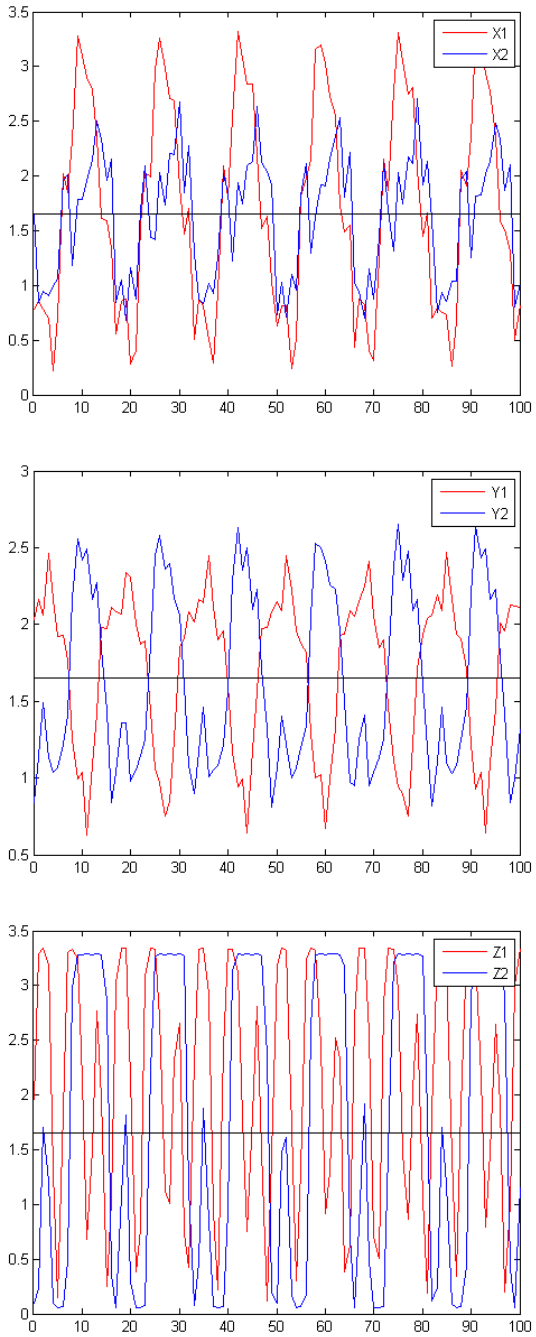

Figure 4.4: Evolution of the X_i, Y_i and Z_i signals (respectively top, middle and bottom), when the AAAC conductor is vibrating with an amplitude Y_b=0.7mm. The vertical axis gives a value in volts [V] and the horizontal one the sample number.

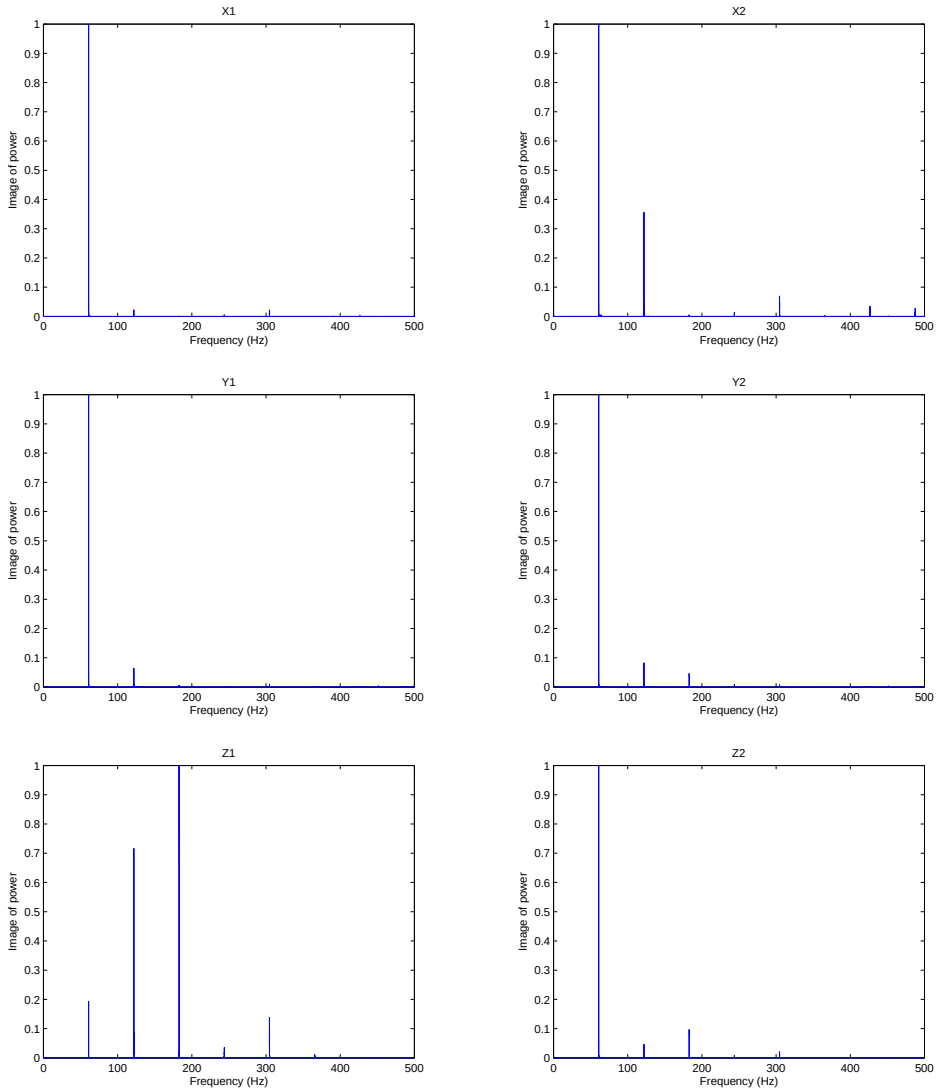

Figure 4.5: Frequency content of the X_i, Y_i and Z_i signals (respectively top, middle and bottom) presented in figure 4.4, when the AAAC conductor is vibrating with an amplitude Y_b=0.7mm. The vertical axis shows a non-dimensionnal image of the signal power.

Table 4.1: Failures on the AAAC conductor

No.	Day	hour	location	noticed
1	2009/05/11	1h22 pm	ext. layer, clamp bottom	during the tests
2	2009/05/18	11h47 pm	ext. layer, clamp top	during the tests
3	2009/05/19	11h39 pm	ext. layer, clamp top	during the tests

Table 4.2: Failures on the ACSR conductor

No.	Day	hour	location	noticed
1	2009/05/22	9h22 am	ext. layer, clamp bottom	during the tests
2	2009/05/25	4h45 pm	ext. layer, clamp bottom	during the tests
3	2009/05/27	2h00 pm	ext. layer, clamp bottom	during the tests
4	N.A	N.A.	inner layer just under ext. layer	during the dissection
5	N.A	N.A.	inner layer just under ext. layer	during the dissection
6	N.A	N.A.	inner layer just under ext. layer	during the dissection

4.4 Failures

All the failures on the AAAC conductor were noticed as the tests were ongoing. For the ACSR conductor, three failures were noticed during the tests but three additional failures were confirmed by the dissection of the conductor. An overview of the failures on both conductors is given in tables 4.1 and 4.2. Detailed information can be found in appendix B (dissection report).

As will be explained in the next sections, the tests permitted to highlight that the behaviour of the AAAC conductor versus the ACSR during a failure was different.

4.4.1 Failures of the AAAC conductor

Before the tests began, a line was drawn on the conductor perpendicularly to its axis so that a wire sliding in the external layer could easily be visualized. The wire pre-stress is decreased after each failure, causing the longest remaining part of the broken wire to move of approximately 5mm towards the centre of the span (figure 4.6).

The following chart shows the data recorded by the Hall sensor during the failure. The sampling frequency is equal to 1000Hz. The time interval shown is therefore equal to 10 minutes. The three failures on the AAAC conductor are characterized by a similar rotational pattern. As an example, considering failure 1, before the failure takes place, the signal oscillates around an average value equal to 0.16V. As the failure moment approaches, one can

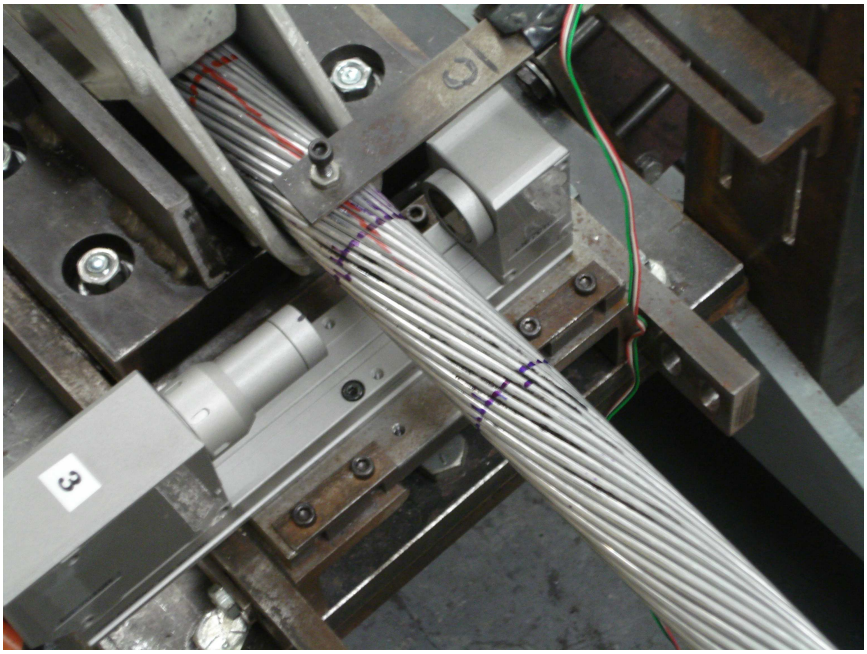

Figure 4.6: AAAC conductor, images of the span after the first failure

see that the signal increases of approximately 0.2V. Then, another phase begins. Let us call it phase 2. It is characterized by a constant rotation speed of $0.13°/s$ and lasts for 1.5s approximately. It is followed by a third phase with a constant rotation speed of approximately $0.03°/s$. Finally, a counter rotation begins (phase 4). It is characterized by a decreasing rotation speed. The signal levels between failures 2 and 3 are consistent: about 0.4V at the end of failure 2 and before failure 3 arises. The difference in signal levels between failures 1 and 2 can be explained by the fact that the position of the hall sensor was modified manually on 11 May 2005 (just after the first failure) to perform a calibration. Also, one can see some regularly spaced "noise" events (every 25 seconds approximately) in the figure. According to Prof. Goudreau, this "noise" may not be attributed to the control system of the test bench (which regularly needs to adjust the excitation amplitude to maintain both Y_b and fy_{max}). So far, the origin of this "noise" remains unexplained. The failure event is automatically followed by the switch off of the vibrator a few tens of seconds afterwards.

The dissection of the conductor confirms that the number of broken wires is limited to 3. The complete dissection report is provided in appendix B. Failures 2 and 3 coincide with the last point of contact of the conductor with the cap of the clamp. The conductor grease was seeping and unlike in the ACSR conductor, the conductor wires had a tendency to untie themselves.

Some typical rupture faces can be seen in the figure 4.8 (courtesy from

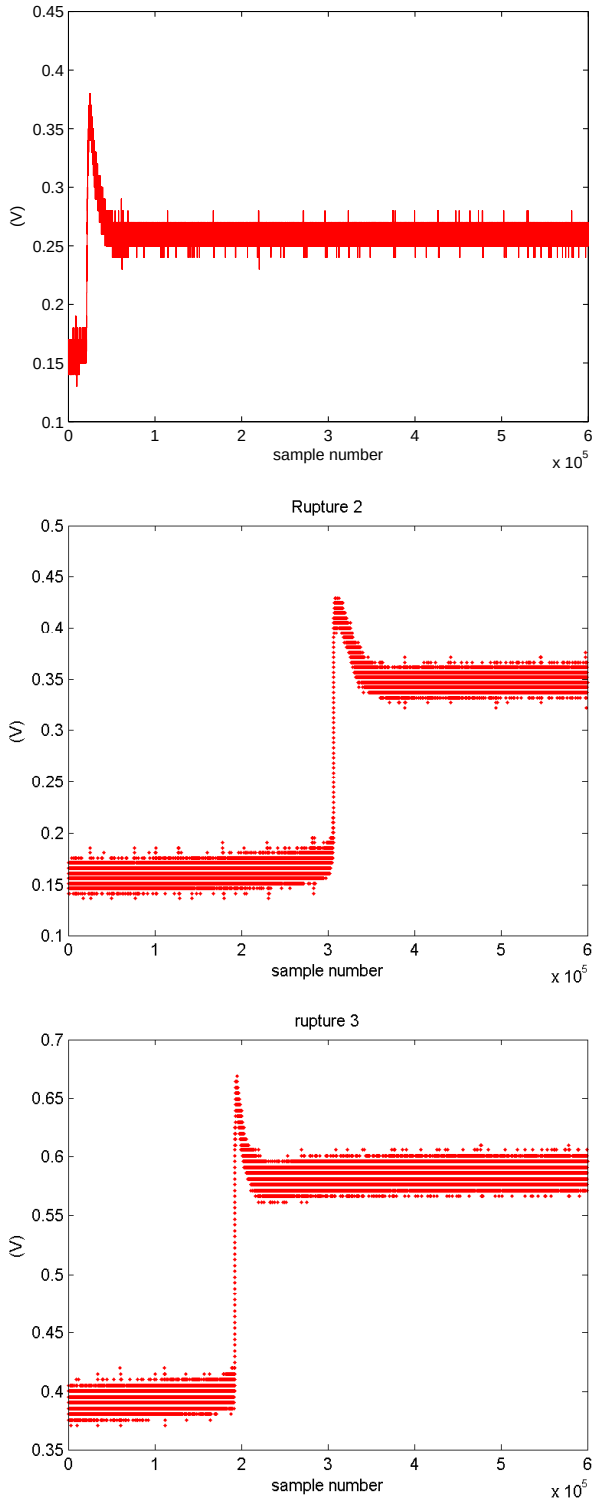

Figure 4.7: AAAC conductor, signal recorded by the Hall sensor during the first failure (top), second failure (middle), third failure (bottom)

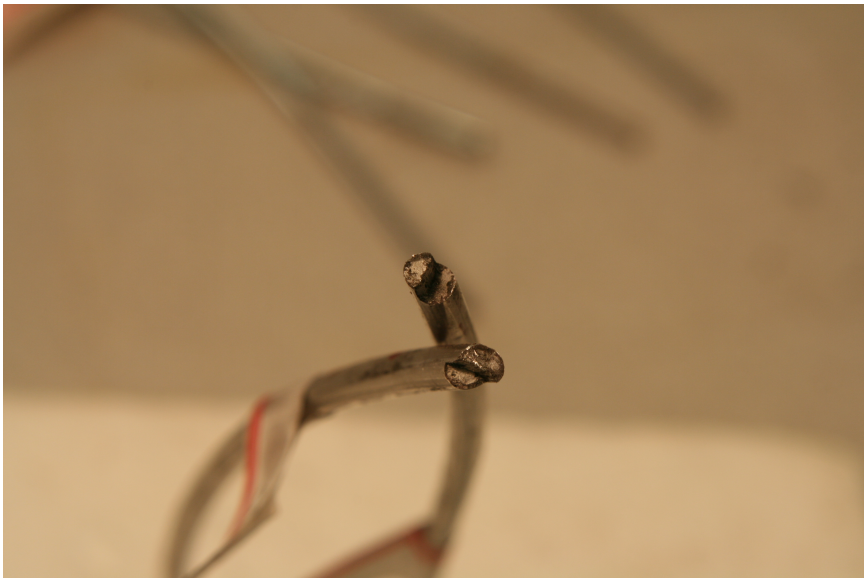

Figure 4.8: AAAC conductor, faces of the second failure (courtesy from Claude Jolicoeur)

Claude Jolicoeur). The section is always composed of a smooth area and a rough one. The smooth area corresponds to the failure propagation. The repeated cycles have caused the caulking of this area. The reduced section of the conductor plasticized and eventually broke leaving the rough area. The sharp change in level was created during the plasticizing of the reduced section.

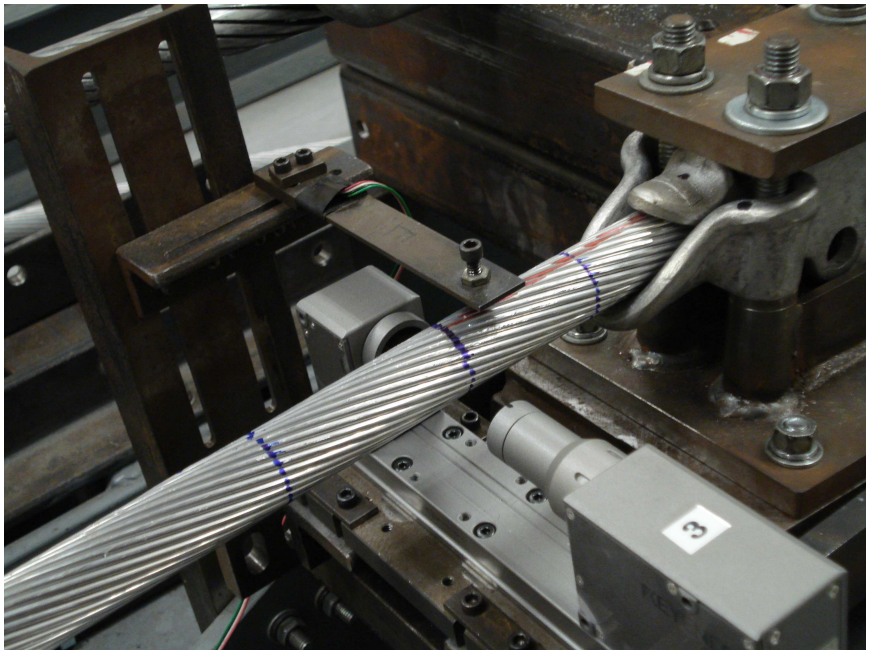

Figure 4.9: ACSR conductor, images of the span after the first failure

4.4.2 Failures of the ACSR conductor

In total, three failures on the external layer of the ACSR conductor were detected during the tests. The fretting zone (where the crack was initiated) was located in the lower part of the clamp for all of them. As can be seen in figure 4.9, each of these three failures caused the longest remaining part of the broken wire to move of approximately 2.5mm towards the centre of the span (instead of 5mm for the AAAC conductor). The difference probably comes from the higher wire cohesion in the ACSR conductor.

The signal recorded by the Hall sensor is also very different than that recorded during the previous failures. One can see that the angular position changes more slowly and without counter-rotation or de-spin (figure 4.9). The signal levels between failures 1 and 2 are consistent (about -0.1V), but there is a significant increase between failures 2 and 3 (from -0.4 to -0.3V). This time, the change in signal is believed to be caused by one or more failure(s) of the second internal layer. Such failures have been confirmed by the dissection. Moreover, the records show that a failure of the external layer causes the signal of the hall sensor to decrease. Due to the difference in lay direction between layers, a failure in the internal layer just under the external layer would logically cause an increase in the Hall signal.

Unfortunately, during all the tests preceding the second failure (see figure 4.11), the accelerometers measuring the vertical acceleration were saturating. The time left between the first and second tests was too short to

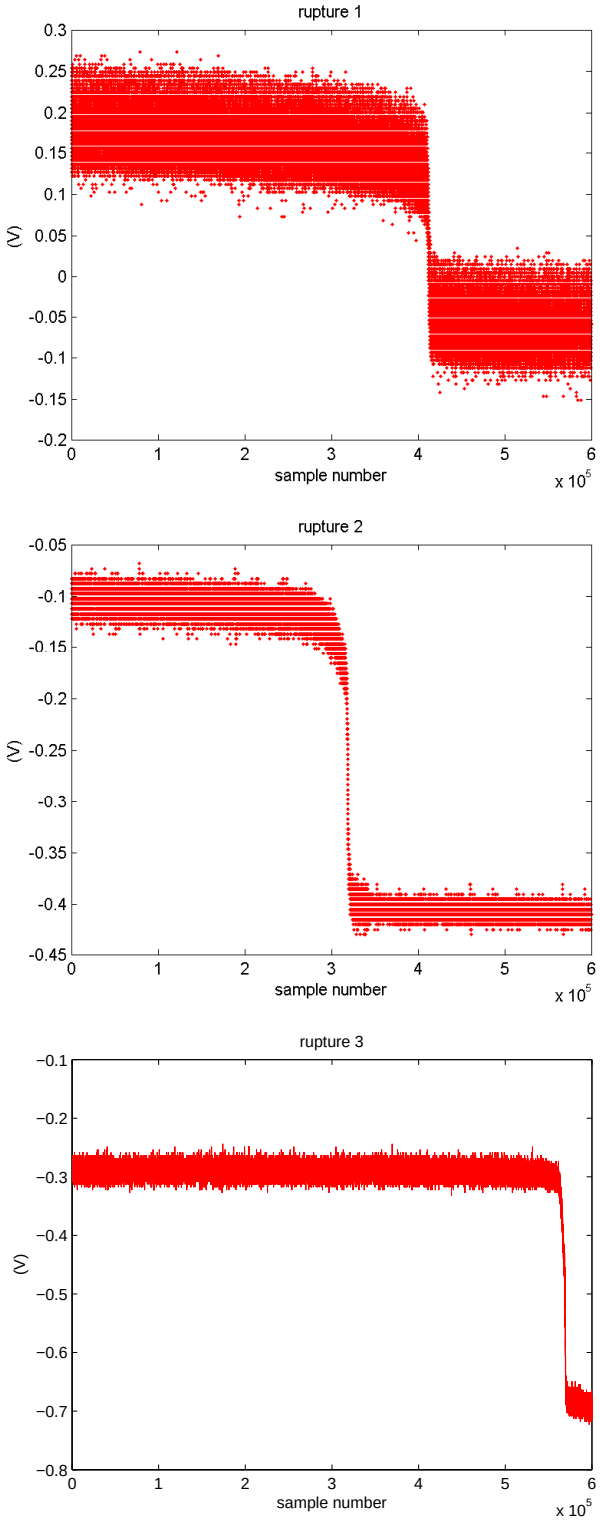

Figure 4.10: ACSR conductor, signal recorded by the Hall sensor during the first failure (top), second failure (middle), third failure (bottom)

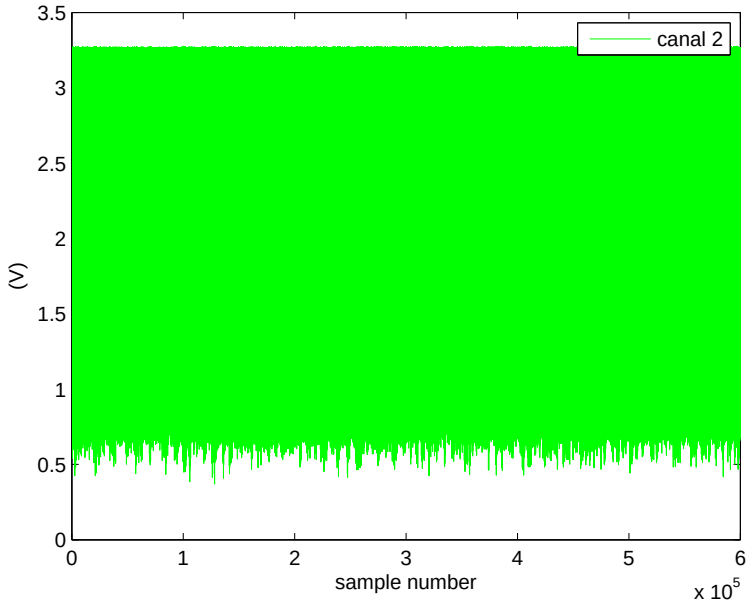

Figure 4.11: ACSR conductor, acceleration measured along the Z axis- saturation before the first failure

analyse the data recorded but just enough to perform a few impact tests. It is only after the second failure that the saturation was underlined. The saturation of the Z_i (vertical) axes unfortunately jeopardizes the analysis of the conductor rotation during the first two failures.

During the dissection of the conductor, three (additional) failures were detected on the second layer of the conductor. Unlike for the external failures, it is not possible to tell their order of happening. It is probable that these failures remained undetected during the tests because the corresponding change in the signal recorded by the Hall sensor was too small. Unlike for the AAAC conductor, there was little wax on the wires. The detailed results of the dissection are in appendix B.

Some typical failure faces can be seen in figure 4.12 (courtesy from Claude Jolicoeur).

4.5 Detection of the failures

4.5.1 Overview

The investigations to detect a failure using data recorded by the accelerometers were performed according to three aspects.

- The rotation motion which characterizes a wire failure incentivized us to perform an analysis of the rotational acceleration signal.

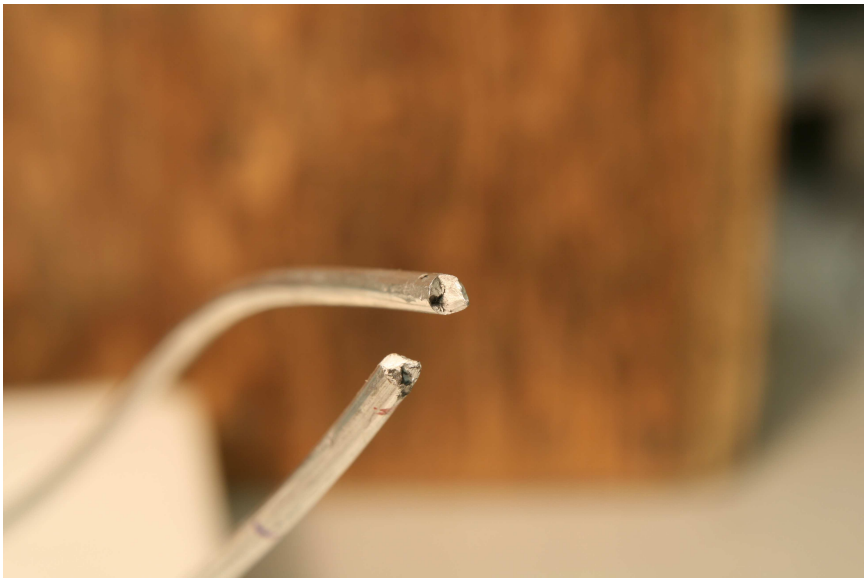

Figure 4.12: ACSR conductor, faces of the first detected failure (left)

- Every failure of the external layer was followed by a wire displacement. The longitudinal acceleration was therefore studied too.

- Last, the evolution of the eigen frequencies after each failure was deduced from some impact tests.

Both the rotational and longitudinal signals have been examined with different time scales. When far from a failure, within a time frame of a few seconds, the signal amplitude is steady. Increasing the time interval to a few hours, amplitude modifications of the order of a few percents could be noticed. For this reason, the detection of a failure using the first two aspects was definitely performed on a short time interval (a few seconds to a few tens of seconds).

4.5.2 Eigen frequencies

Gremca fatigue test spans can certainly be considered as short spans. The tests have been performed at rather high tension levels. The parameter M presented in [50] (which accounts for coupling inside a span and between spans of symmetric modes) is inferior to 0.001. The correction due to this factor (on vertical and torsional frequencies) can be neglected. Nevertheless, the conductor average bending stiffness may have some impact on the vertical and transversal frequencies. It was of course taken into account in the analysis hereunder.

Vertical frequencies

The relationships giving the eigen frequencies of a cable span as a function of its average bending stiffness can be found in e.g. [25, 58].

$$\omega_{v,k} = 2\pi f_{v,k} = \sqrt{(\frac{k\pi}{L})^2 * \frac{T}{m} * (1 + (\frac{k\pi}{L})^2 \frac{EI}{T})}$$

In the frame of these tests, the vertical frequencies could also easily be deduced from the tests performed (see e.g. figure 4.26 and 4.27), so that the previous formula was used for another purpose: assessing the conductor average bending stiffness (see appendix E).

Torsional frequencies

According to [32], the differential equation of a rod element subjected to end torques is

$$\frac{\partial M}{\partial x} = \rho J \frac{\partial^2 \theta}{\partial t^2} \tag{4.1}$$

where J is the polar moment of inertia $[m^4]$. For a rod of circular cross section, J is equal to $\frac{\pi d^4}{32}$. In the case of a cable, J can be approximated by [50] $\frac{\pi d^4}{32} f_{strand}$ where f_{strand} accounts for the stranding and is usually close to 0.7. The relationship between the torque and the angle of twist is given by:

$$M = GJ \frac{\partial \theta}{\partial x} \tag{4.2}$$

where G is the shear modulus of the material $[N/m^2]$. According to [50], in the case of an overhead line cable, the product GJ may be approximated by $GJ \approx k_\tau k_{ageing} k_{constitution} d^4$ where $k_\tau = 0.00027$, k_{ageing} is a factor comprised between 1 and 3 and $k_{constitution}$ is equal to 1 for stranded conductors. The resulting governing equation of motion for a rod of circular cross section is

$$\frac{\partial^2 \theta}{\partial x^2} = \frac{\rho J}{GJ} \frac{\partial^2 \theta}{\partial t^2} \tag{4.3}$$

Assuming a solution of the form

$$\theta(x,t) = \theta(x) \sin(\omega t) \tag{4.4}$$

equation (4.3) can be rewritten as

$$\frac{\partial^2 \theta(x)}{\partial x^2} + \frac{\rho J}{GJ} \theta(x) \omega^2 = 0 \tag{4.5}$$

A solution to the previous differential equation is

$$\theta(x) = Ae^{i\lambda x} \tag{4.6}$$

where $\lambda = \frac{k\pi x}{L}$. Replacing $\theta(x)$ by its expression in (4.5), one obtains the equation which needs to be satisfied by the torsional eigen pulsation

$$\omega_{\theta,k} = \frac{k\pi}{L}\sqrt{\frac{GJ}{\rho J}} \tag{4.7}$$

The previous formula is valid for a single conductor. The torsional eigen pulsation of bundle conductors is given in [50], but one must note that in the case of a wire failure in a real bundle span, the torsional motion may take place in one conductor (only) and solely on one subspan.

Longitudinal frequencies

The longitudinal frequencies of a span can be found from the longitudinal differential equation of motion (second order terms are neglected).

$$\frac{d^2\zeta}{dt^2} = \frac{E}{\rho}\frac{d^2\zeta}{dx^2} \tag{4.8}$$

where E is Young's modulus of elasticity $[N/m^2]$ and ρ the linear mass $[kg/m]$.

The previous equation admits a solution of the form $\zeta(x,t) = \zeta(x) * sin(\omega t)$, giving

$$\frac{E}{\rho}\frac{d^2\zeta}{dx^2} + \omega^2\zeta = 0 \tag{4.9}$$

A solution to this equation is $\zeta(x) = A\mathrm{e}^{i\lambda x}$ where $\lambda = \frac{k\pi x}{L}$ to implicitly respect the boundary conditions $\zeta(0) = \zeta(L) = 0$. Substituting in 4.9, one obtains the expression of the eigen pulsations

$$\omega_{l,k}^2 = (\frac{k\pi}{L})^2\frac{E}{\rho} \tag{4.10}$$

The first eigen longitudinal, vertical and torsional pulsations have been computed for the AAAC and ACSR conductor under the same conditions as in the laboratory (see table 4.3)

The sampling frequency required to detect the first longitudinal mode is far beyond half the sampling frequency (the sampling frequency is equal to

Table 4.3: first eigen longitudinal, vertical and torsional pulsations computed for the AAAC and ACSR conductor

	AAAC	ACSR
$\omega_{v,1}[rad/s]$	$\approx 2\pi 12$	$\approx 2\pi 11$
$\omega_{\theta,1}[rad/s]$	$\approx 2\pi 85$	$\approx 2\pi 77$
$\omega_{l,1}[rad/s]$	$\approx 2\pi 13230$	$\approx 2\pi 15919$

1000Hz). In real life, the parameter L of equation 4.10 is the length of the entire line section and eigen frequencies of the order of 10^0 to 10^2 Hz are common.

The first vertical and torsional mode of the 7m span, though much higher than in real life, do fall within the detectable frequency range. Usually, basic vertical frequencies of the order of 10^{-1} Hz are met. The torsional basic frequency of a single conductor is about one order of magnitude higher than that.

4.5.3 Tracking tools: wavelet transform versus short time Fourier transform

Processing a signal with a fast Fourier transform (FFT), one will see whether it contains any or many oscillations at a given frequency. To know how the amplitude and frequency content of a signal evolves as a function of time, more sophisticated tools are required. In his book "Une exploration des Signaux en ondelettes" [55], S. Mallat presents the Short Time Fourier Transform and the Wavelet Transform as the two main examples of time-frequency decomposition tools. In the case of multiple frequency signals, some criteria need to be fulfilled to correctly detect the signal ridges. Let g be a symmetrical window which support is $[-1/2, 1/2]$ and norm is $\|g\| = 1$. Let $\widehat{g}$ be its Fourier transform. The bandwidth $\Delta\omega$ of $\widehat{g}$ is defined by $\mid \widehat{g}(\omega) \mid \ll 1$ for $\mid \omega \mid \geq \Delta\omega$. During the application of a transform, the window will be translated on the time axis. The coordinate of its centre on the time axis is denoted u. Let s be a scale factor (constant for the STFT and variable for the wavelet transform). Then, let us consider a real signal which contains two frequencies. Their instantaneous values are denoted $\phi_1'(t)$ and $\phi_2'(t)$. The latter will correctly be separated by the transform (wavelet or STFT) if for all u [55]

$$\widehat{g}(s \mid \phi_1'(u) - \phi_2'(u) \mid) \ll 1 \tag{4.11}$$

Given the specificities of each transform, the previous relationship can be rewritten [55]:

- for a STFT transform

$$\mid \phi_1'(u) - \phi_2'(u) \mid \geq \frac{\Delta\omega}{s} \tag{4.12}$$

- for a wavelet transform

$$\frac{\mid \phi_1'(u) - \phi_2'(u) \mid}{\phi_2'(u)} \geq \frac{\Delta\omega}{s} \tag{4.13}$$

$$\frac{\mid \phi_1'(u) - \phi_2'(u) \mid}{\phi_1'(u)} \geq \frac{\Delta\omega}{s} \tag{4.14}$$

Heisenberg's uncertainty principle states that it is not possible to obtain both a high frequency resolution and a high time resolution at the same time. If σ_t and σ_ω denote respectively the time and frequency variance, this principle can be written under the following mathematical form [55]:

$$\sigma_t \sigma_\omega \geq \frac{1}{2} \tag{4.15}$$

In the case of a short time Fourier transform (STFT), σ_t and σ_ω are constant whatever the time or frequency. In the case of a wavelet transform, the product $\sigma_t \sigma_\omega$ is constant, but the respective values of these factors varies with the scale s. A small scale s is suitable to detect the high frequencies of a signal, but unfortunately the corresponding frequency resolution will be poor.

Considering a real signal which content is made up of high frequency values, inequality (4.12) will be more easily satisfied than (4.13-14). This also means that the high frequencies will be more easily separated. Provided these high frequencies are almost constant with time, the analysis of this signal can advantageously be performed with a STFT. Considering a real signal which content is made up of low frequency values which vary a lot with time, the wavelet analysis will be the most suitable tool.

In the frame of this work, high eigen frequencies (at least several tens of Hertz) almost steady or with very small changes as a function of time are expected. In such situation, the natural choice is to use short time Fourier transforms rather than wavelet transforms to perform the signal analysis.

For all other information on the definition, domain and validity of the STFT and wavelets, one may refer to [55]. The code which has been used is a courtesy of B. Godard. Its complete description is given in [26].

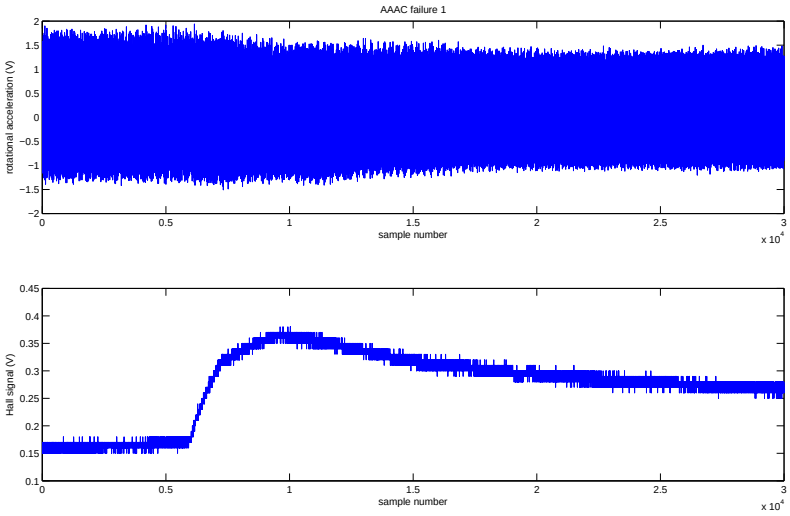

Figure 4.13: AAAC conductor, rotational acceleration and signal recorded by the Hall sensor during the first failure

4.5.4 Study of the rotational acceleration

The analysis is limited to the failures of the AAAC conductor and the third detected failure of the ACSR conductor (the accelerometers were saturating during the first two tests on the ACSR conductor). The rotational acceleration of the conductor can be deduced subtracting the signals recorded by the two accelerometers Z1 and Z2. The result is shown in figure 4.13 for the first AAAC failures as well as the Hall sensor signal.

The amplitude of the Z1-Z2 curve seems to be modified during the failures. Further analysis is required to confirm this feeling, starting with a fast Fourier transform of the signal (see figures 4.14 and 4.15 for a zoom on lower frequencies). Having used samples of 30000 data points acquired at a frequency of 1000Hz, the frequency resolution is equal to 0.033Hz. All peaks are narrow, which means that no significant change in frequency happens during the failures (potential changes are $< 1\%$). Four peaks are common to the figures, at about 60Hz, 120Hz, 180Hz and 300Hz. Within the range 0-50Hz there is nothing else but "noise", except for the second failure (figure 4.15) with a peak around 30Hz. The 60 Hz frequency coincides with the excitation signal and the other ones with its harmonics. The 30Hz peak corresponds to the third vertical frequency, which may have been excited at that moment and which may have contributed to the rotational signal by one of the mechanisms discussed in section 4.3.

A continuous wavelet transform, using Haar wavelet was applied on the same signals. It showed in a qualitative manner that the amplitude of some

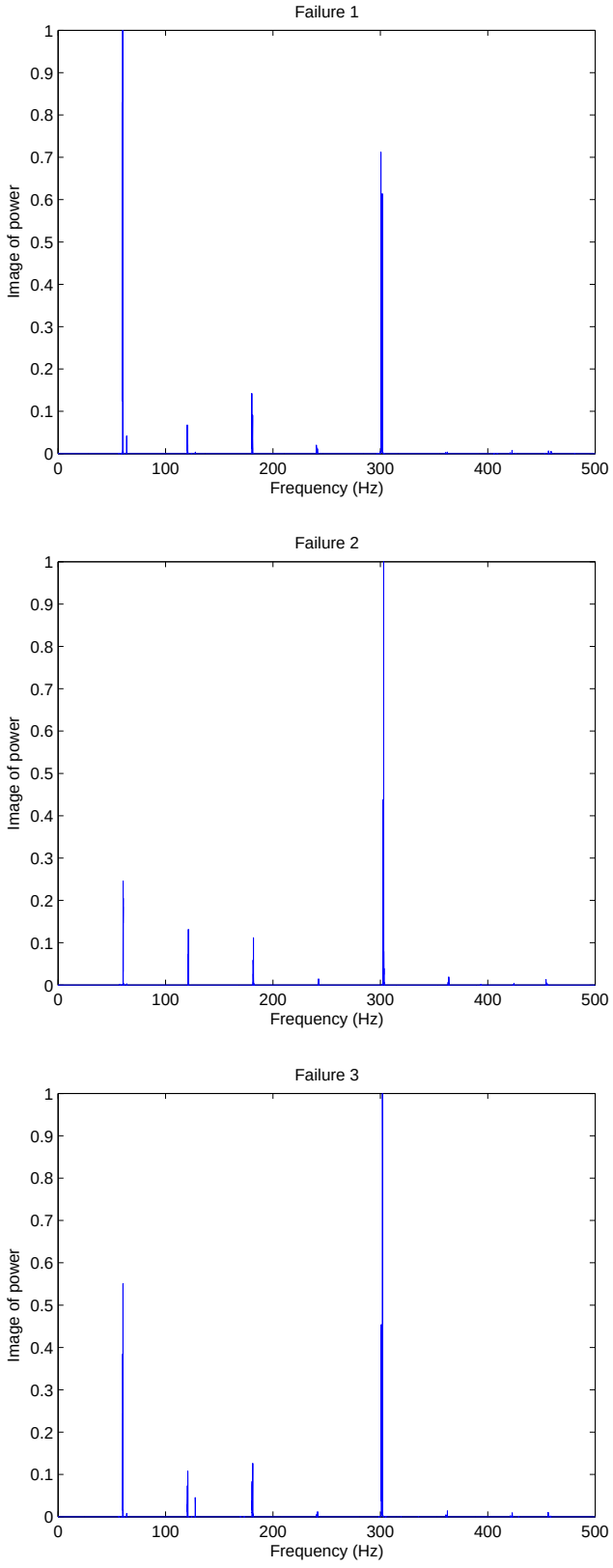

Figure 4.14: AAAC conductor, frequency content of the rotational acceleration during the first failure (top), second failure (middle), third failure (bottom). The vertical axis shows a non-dimensionnal image of the signal power.

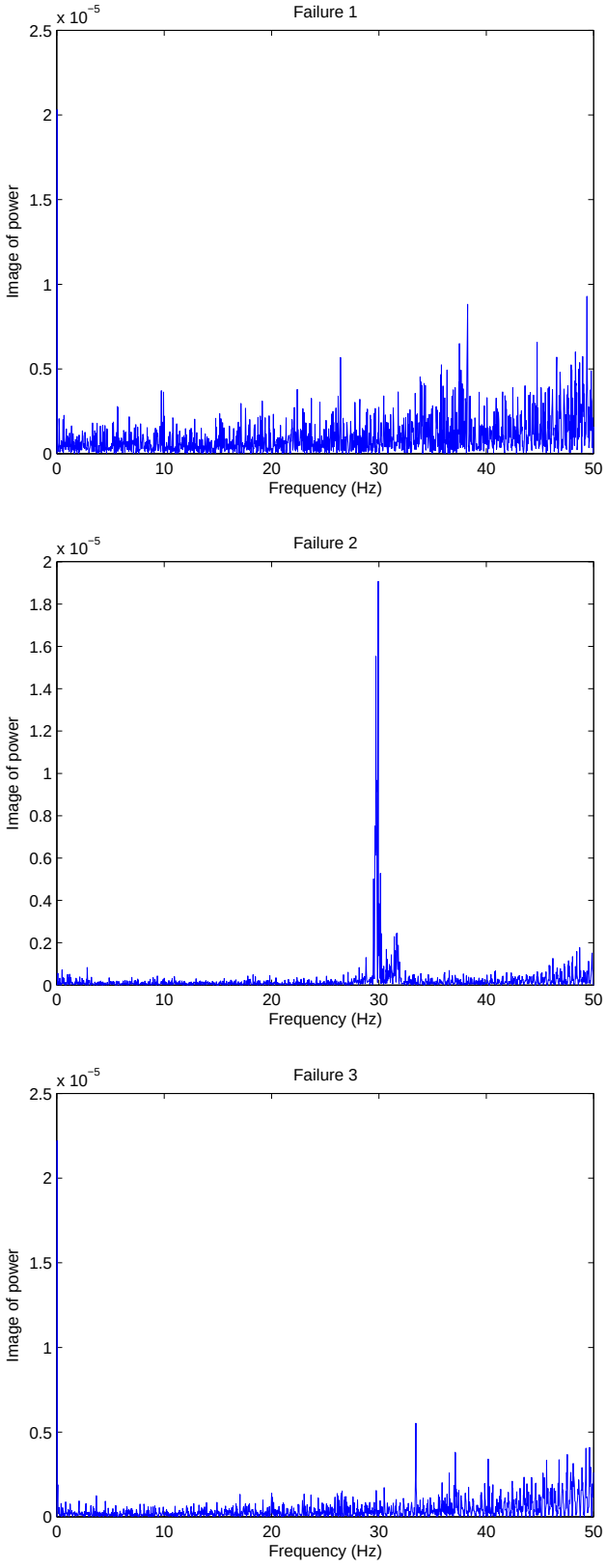

Figure 4.15: AAAC conductor, frequency content of the rotational acceleration during the first failure (top), second failure (middle), third failure (bottom), zoom on the lower frequencies. If X is the discrete fourier transform of the raw signal measured by the accelerometers, the vertical axis shows $(\frac{|X_k|}{N})^2$.

of the frequencies varied. To obtain quantitative information, the data was then processed through a short time Fourier transform algorithm written by B. Godard [26], which is able to detect the ridges of the signal [55]. The number of samples processed is 2^{14} (approximately 16.4 seconds) for the first two failures. For failure 3, due to some lack of memory problems, the maximum number of samples was 2^{13}, which corresponds to approximately 8.2 seconds. The size of the frame is 100 samples and the window inter spacing is 10 samples. The resolution in frequency is equal to about 10Hz. The results are shown in figures 4.16 and 4.17, with the evolution of the ridge amplitudes in the first figure and ridge frequencies as a function of time on the second one. The highest, the medium, and the lowest amplitudes correspond respectively to frequencies of about 300, 60 and 120Hz. As a comparison, figure 4.18 shows the evolution of ridge amplitudes outside a failure event. It can be deduced that the occurrence of a failure has an impact on the amplitudes of the rotational acceleration. As explained in the previous paragraph, the excitation frequency is approximately equal to 60Hz. The 120Hz peak is generated by tension fluctuations (at twice the excitation frequency). The presence of the 300Hz frequency may be due to some rotational eigen frequency of the cable. Similar observations can be made for the ACSR conductor. First, the fast Fourier transform confirms the presence of three peaks: at respectively 60, 120 and 180Hz (see figure 4.19). Then, the short time Fourier transform (performed on 2^{13} samples due to memory limitations) confirms that the amplitude of the 120Hz signal significantly decreases (see figure 4.20).

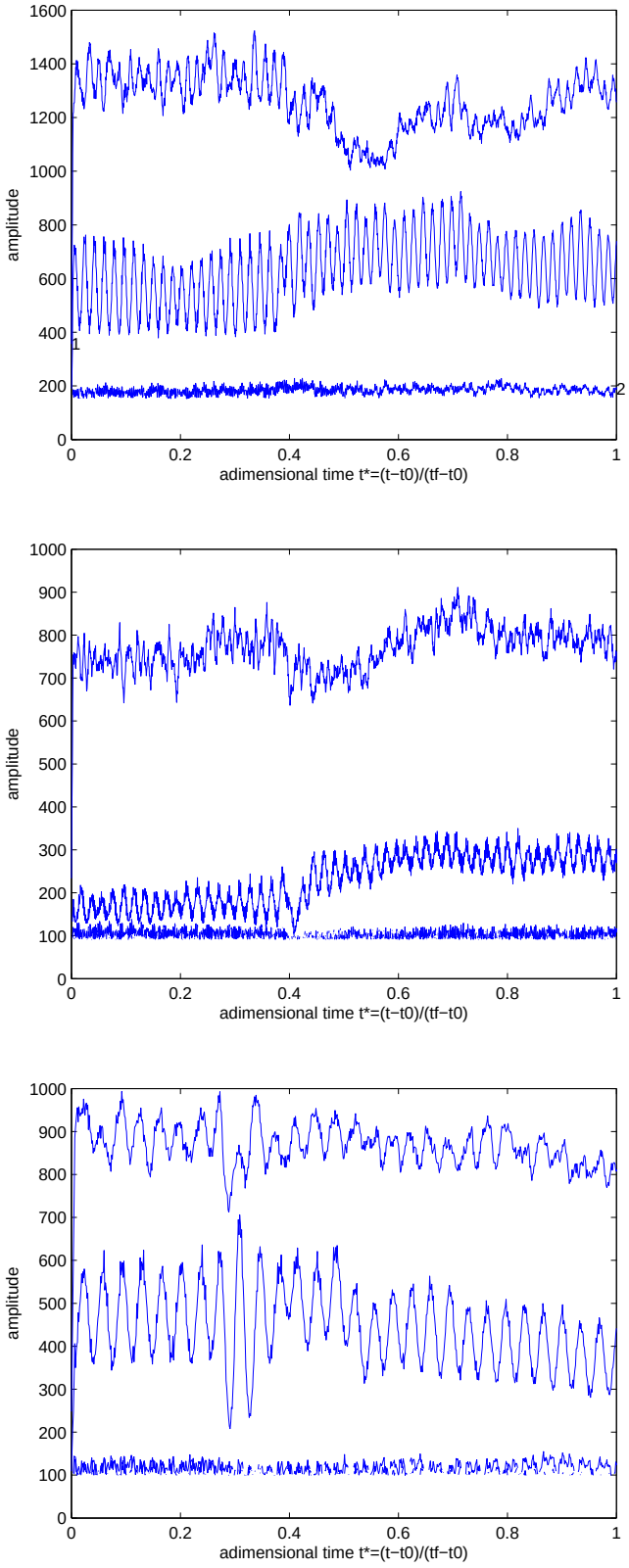

Figure 4.16: AAAC conductor, Short time Fourier transform of the rotational acceleration, amplitudes during the first failure (top), second failure (middle), third failure (bottom), ridge amplitudes

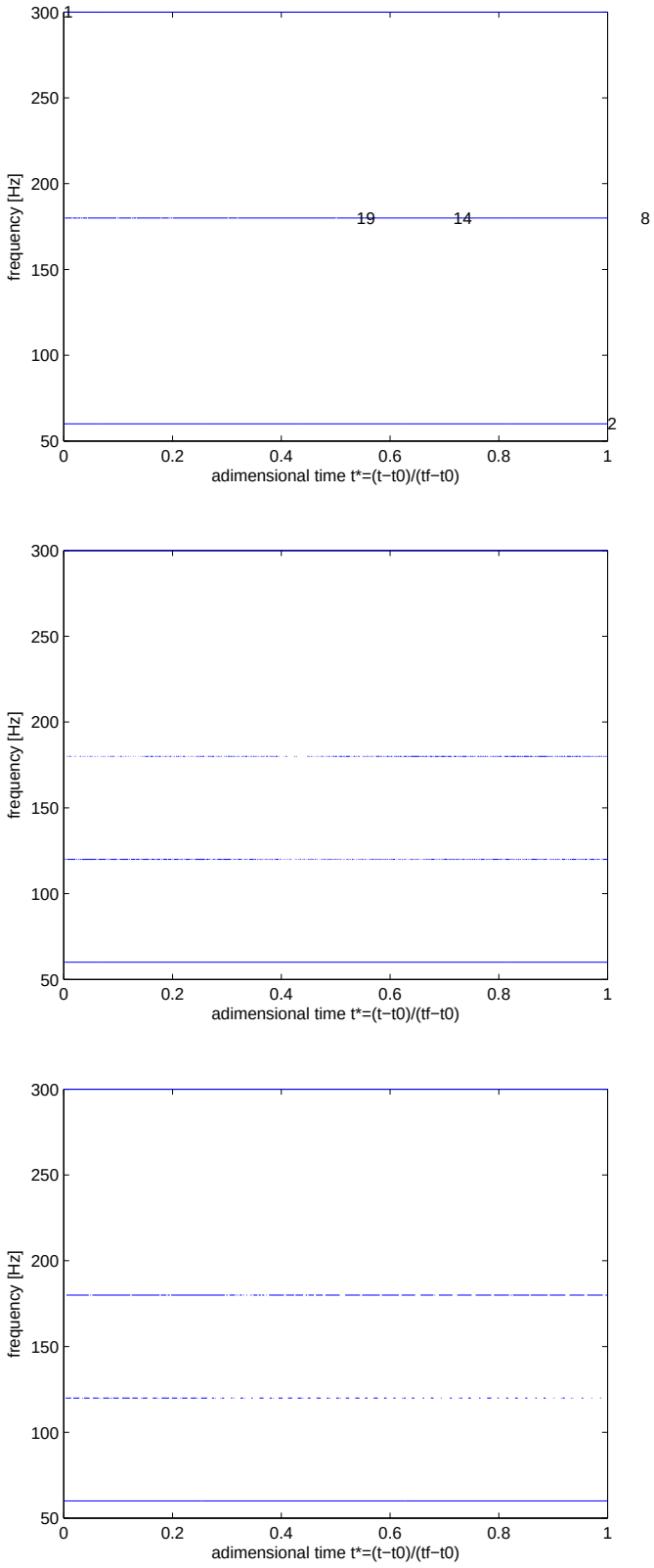

Figure 4.17: AAAC conductor, Short time Fourier transform of the rotational acceleration, frequencies during the first failure (top), second failure (middle), third failure (bottom), ridge frequencies

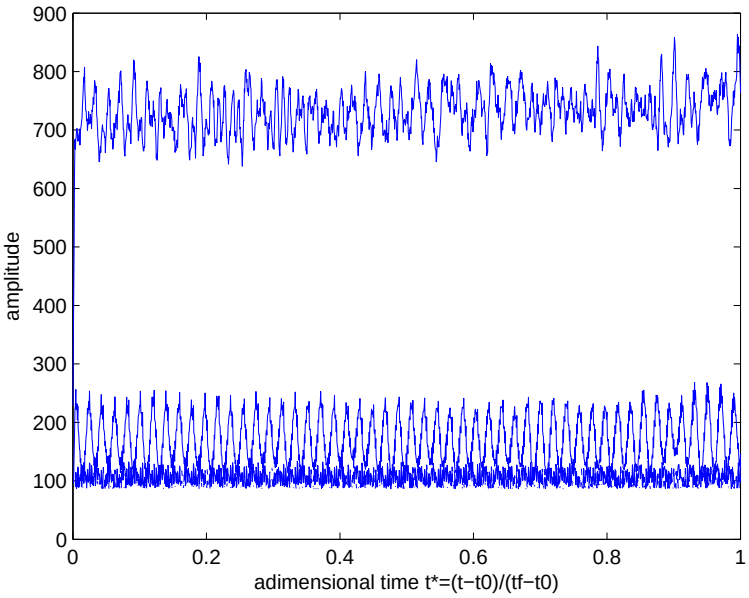

Figure 4.18: AAAC conductor, Short time Fourier transform of some typical rotational acceleration signal outside a failure event

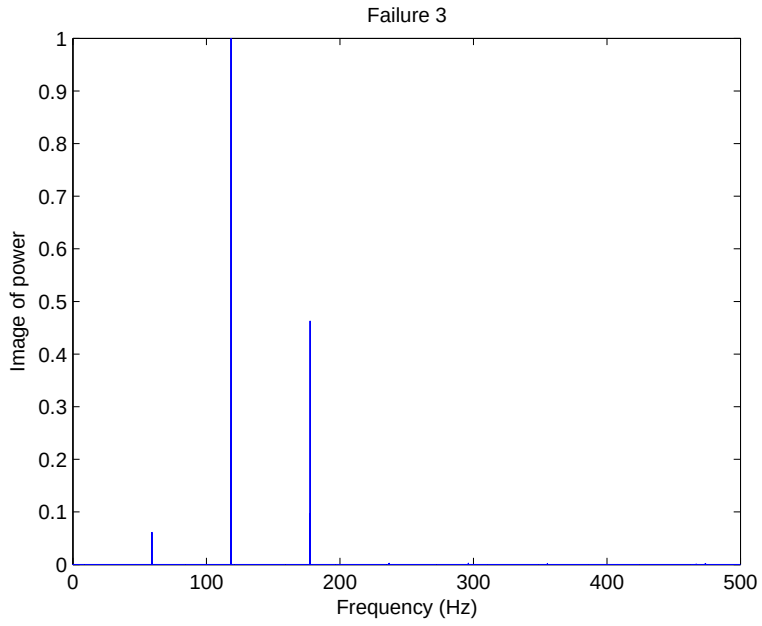

Figure 4.19: ACSR conductor, failure 3, fast Fourier transform of the rotational acceleration. The vertical axis shows a non-dimensional image of the signal power.

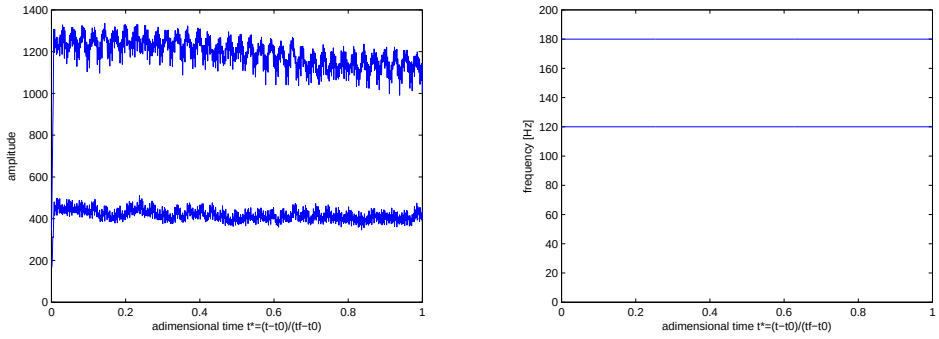

Figure 4.20: ACSR conductor, frequency content of the rotational acceleration during the third failure, ridge amplitudes (left) and ridge frequencies (right). If X is the discrete fourier transform of the acceleration signal, the vertical axis shows $(\frac{|X_k|}{N})^2$.

4.6 Axial acceleration of the conductor

Analysing the frequency spectra of longitudinal accelerations for both conductors, one will detect two peaks, one at 60Hz and the second one at twice that value (see figure 4.24). As could be expected for this 7m span, the contribution of changes in tension (120Hz) in the longitudinal signal is important. The data recorded by channel 1 has been processed with the short time Fourier transform routine described in the previous section. The computation parameters are similar as in the previous paragraph and so is the resolution (size of the frame equal to 100 samples, sampling frequency of 1000Hz, frequency resolution of 10 Hz). The results can be seen in figures 4.21 and 4.22 for the AAAC conductor and in figures 4.24 and 4.25 for the ACSR conductor. In figures 4.21, the highest amplitude corresponds to a frequency of about 60 Hz, while in 4.24 and 4.25, the highest amplitude corresponds to a frequency of about 120 Hz.

Some typical amplitude output outside a failure event can be seen in figure 4.23 (AAAC conductor). The comparison between figures 4.21-22 and 4.23 shows that during a failure event, the 60Hz signal amplitude significantly increases for the AAAC conductor. Note that even if the frequency resolution of the STFT is low, the same failure signals have also been processed with FFT (with a resolution of the order of 0.033 Hz), which has confirmed that no significant changes in the frequencies are to be expected during a failure (see e.g. figure 4.24, where the frequency peaks are narrow).

In the case of the ACSR conductor, both the 60Hz and the 120Hz amplitudes significantly decrease during the failure (see figure 4.25).

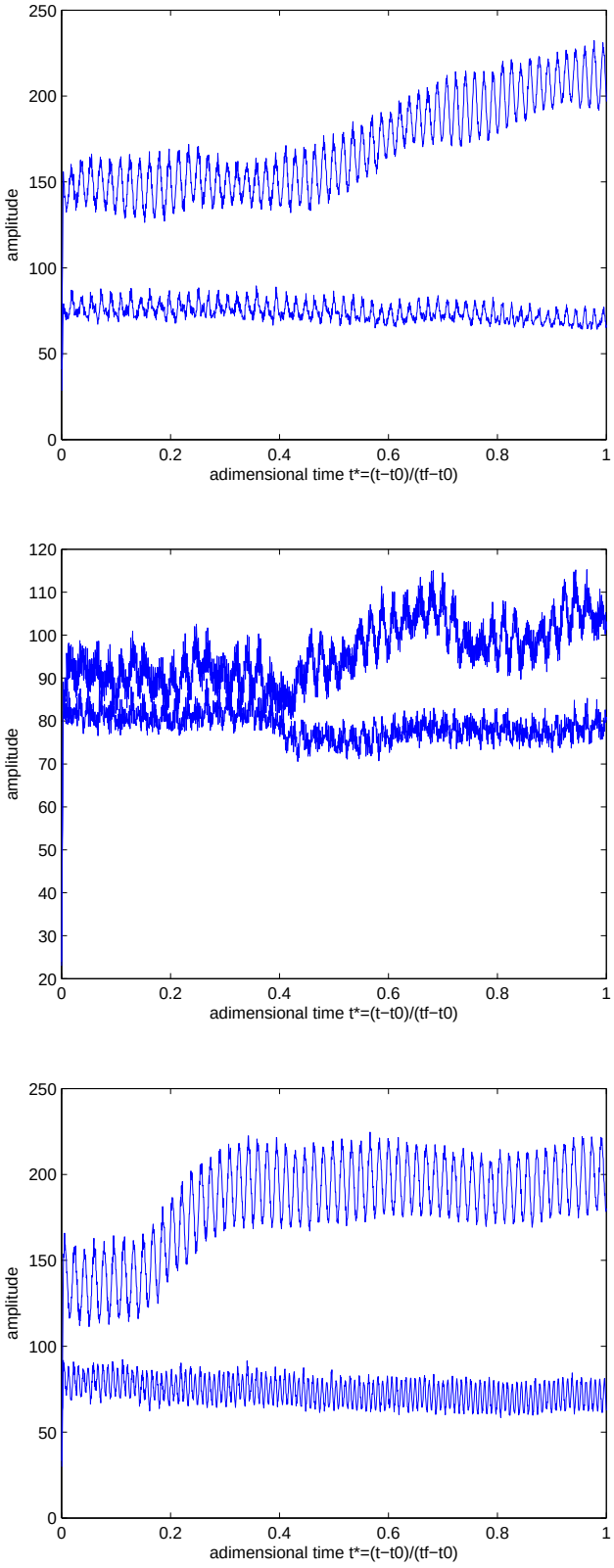

Figure 4.21: AAAC conductor, ridge amplitudes of the longitudinal acceleration deduced by short time Fourier transform during the first failure (top), second failure (middle), third failure (bottom)

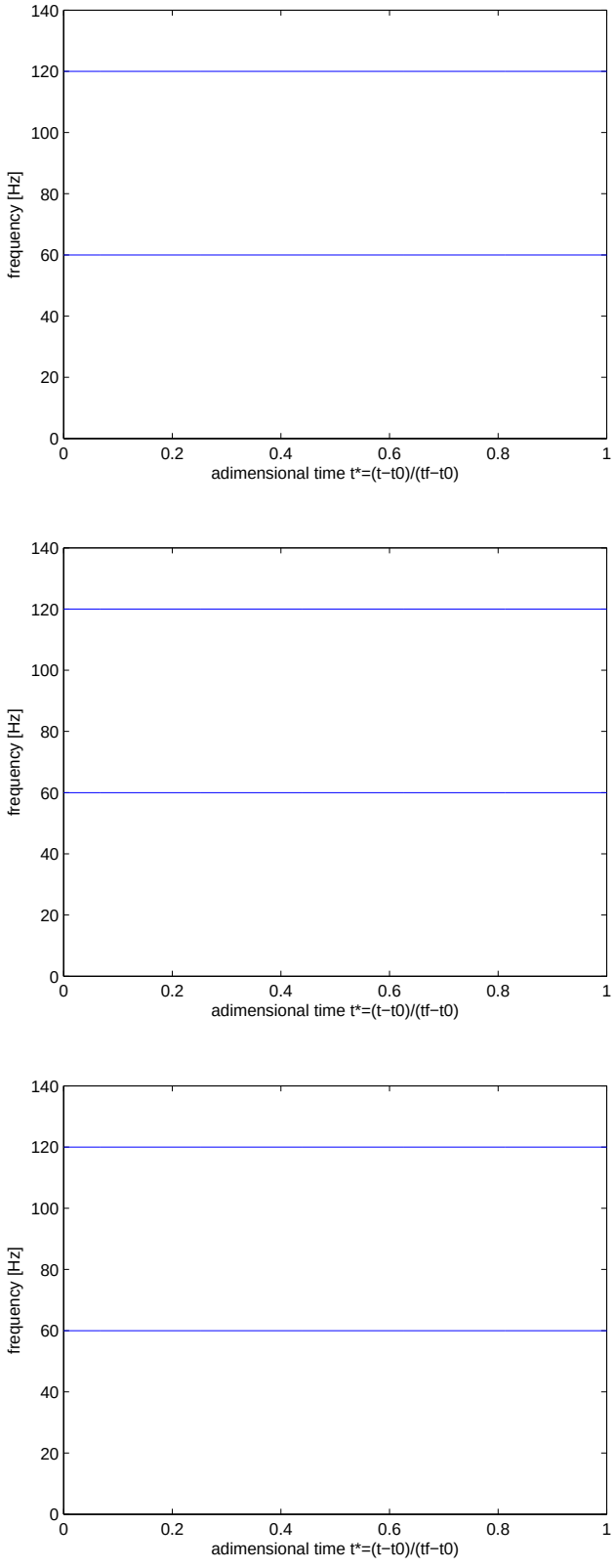

Figure 4.22: AAAC conductor, ridge frequencies of the longitudinal acceleration deduced by short time Fourier transform during the first failure (top), second failure (middle), third failure (bottom)

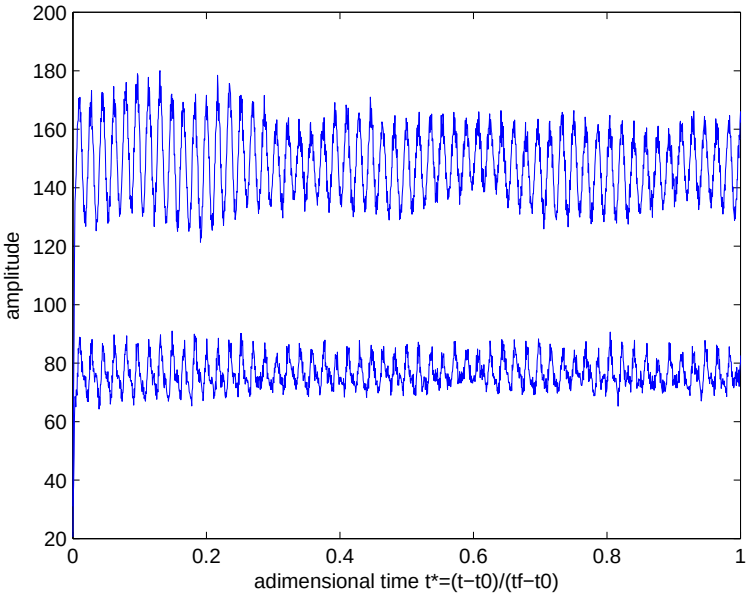

Figure 4.23: AAAC conductor, ridge amplitudes of the longitudinal acceleration deduced by short time Fourier transform outside a failure event

4.7 Evolution of the eigen frequencies as the number of failures increases

Generally speaking, the eigen frequencies of a conductor depend on several parameters among which its temperature. GREMCA's laboratory is located in a cellar without any window and all tests have been performed within a time interval of a few days. It seems reasonable to suppose that the maximum ambient temperature changes were of the order of one degree Celsius. The ruling span equations (which express the changes in conductor length due to changes in tension, temperature...see e.g. [6]) permit to estimate the impact of an ambient temperature change on the conductor length and hence on frequencies. It appears that a one degree Celsius change in ambient temperature would lead to a change in the first vertical eigen frequency inferior to 0.1Hz. Under this hypothesis, it was decided to study the evolution of the conductor eigen frequencies as the number of failures increased. It is also important to add that the conductors were not re-tensioned during the fatigue tests.

Impact tests using a hammer have been performed before and during the fatigue tests at the rate of one test after each (detected) fatigue failure. The recorded spectra have been processed with a fast Fourier transform algorithm to find the eigen frequencies. The frequency resolution of a FFT is equal to f_e/N, where f_e is the sampling frequency [Hz] and N is the number

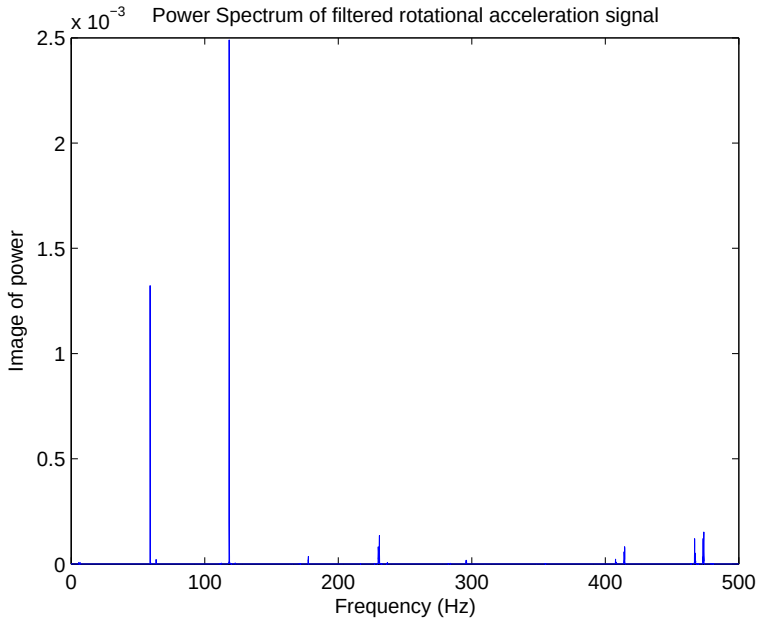

Figure 4.24: ACSR conductor, frequency content of the longitudinal acceleration during the third failure, amplitudes. If X is the discrete fourier transform of the raw signal measured by the accelerometers, the vertical axis shows $(\frac{|X_k|}{N})^2$.

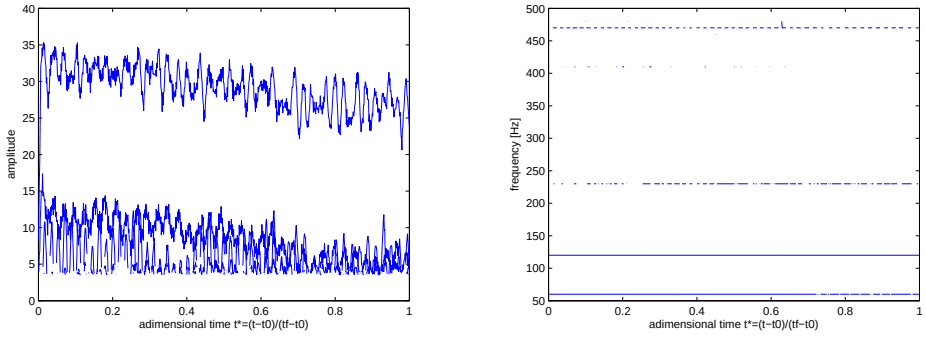

Figure 4.25: ACSR conductor, Short time Fourier transform of the longitudinal acceleration during the third failure, ridge amplitudes

of samples. The number of samples used for data processing is 30000 so that the resolution in frequency is 0.033Hz. The first four frequencies have then been tracked (figures 4.26 and 4.27). A steady decrease in the eigen frequencies is observed as the number of failures increases. Table 4.4 shows the slope of a linear fit on the data. As an example, for the AAAC conductor, the slope is -0.13 for the fourth mode, which means that in average, when a failure arises, the eigen frequency of the fourth mode decreases by 0.13 Hz. For the ACSR conductor, the decrease in frequency is inferior to the resolution in frequency, and no conclusions may be drawn from the frequency evolution analysis.

The table highlights that the impact of a failure is far more important for the AAAC than for the ACSR. In the case of the ACSR conductor, since the decrease in frequency is inferior to the resolution, nothing can be concluded.

One may not exclude that a change in ambient temperature may have had an impact on the vertical eigen frequencies (see the computation of order of magnitude performed two paragraphs earlier). Nevertheless, there is no particular reason for this impact to be such a steadily decrease. On the contrary, if the change in frequencies is a consequence of a wire failure, it is consistent with the relaxation which takes place after a failure and with the fact that the conductor was not re-tensioned between the failures.

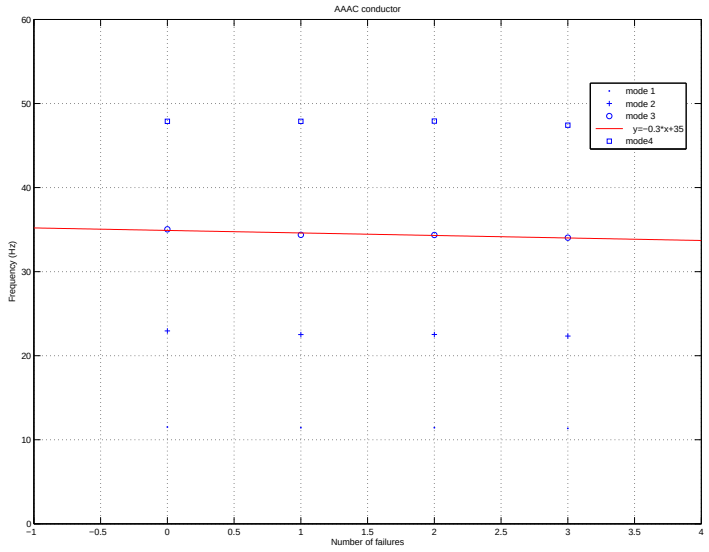

Figure 4.26: Evolution of the first four eigen frequencies as a function of the number of failures for conductor AAAC

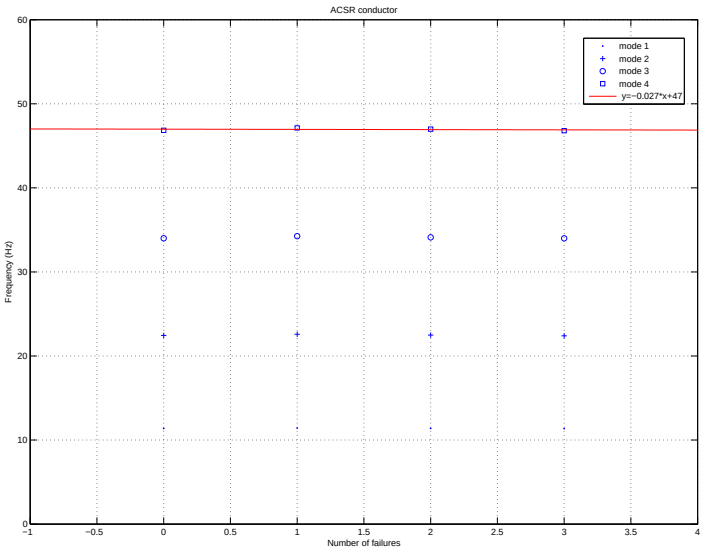

Figure 4.27: Evolution of the first four eigen frequencies as a function of the number of failures for conductor ACSR

Table 4.4: Slope of a linear fit on data presented in figures 26 and 27

mode number	slope AAAC fit	slope ACSR fit
1	-0.049	-0.0084
2	-0.18	-0.023
3	-0.3	-0.017
4	-0.13	-0.027

4.8 Conclusions

Considering a failure in the external layer, these are more easily detected on an AAAC than on an ACSR, probably due to a higher cohesion of the wires in the latter. The failure pattern may therefore vary from one type of conductor to another. Also, as could be expected, the failure of an external wire is easier to detect than an inner one because it produces a more important rotation of the conductor.

All aspects studied (rotational acceleration, longitudinal acceleration and eigen frequencies) have shown changes ensuing the occurrence of a failure.

- The occurrence of a failure has an impact in the amplitudes of the rotational acceleration signal measured on AAAC conductor. The amplitude of the 60Hz component increases for the first two failures and decreases in the last case. Some chaotic changes in amplitudes can also be noticed for the 300Hz component and nothing particular for the 120Hz component. The spectrum of the third ACSR conductor failure brings other information. Unlike the AAAC conductor, the amplitude of the 120Hz component is the highest and it steadily decreases during the failure event though the amplitude of vibration is maintained constant. This difference in behaviour could be explained as follows: The failure causes the conductor to rotate. The position of the accelerometer system is modified so that its capacity to measure some accelerations is either improved (AAAC conductor) or deteriorated (ACSR conductor).

- In all conductors, an analysis of the longitudinal acceleration signal shows that the 60Hz component is significantly modified during a failure event. The change is generally within the range 10-35%. For all AAAC failures, the amplitude systematically increases, and it decreases for the ACSR conductor. Once again, it is believed that the difference in amplitudes between the two conductors is due to the rotation ensuing the failure. In the case of the AAAC conductor, the axis of the longitudinal accelerometer coincides better with the cable's own longitudinal axis after the rotation. If these amplitudes decrease for the ACSR conductor, it is probably because its alignment is worse after the rotation.

- The occurrence of a failure on the AAAC conductor coincides with a decrease in the corresponding eigen frequency. This decrease ranges between 0.05 and 0.3 Hz. This decrease can probably be explained by a decrease in conductor tension.

In real life, the vibrational amplitudes of a conductor continually vary and so do the rotational accelerations. The impact of a failure on rotational

amplitudes of vibration may be flooded by these continual changes. This is specially true since the expected amplitude change in rotational acceleration due to a failure event is small compared to the normal vibration level.

The detection of a failure event studying the longitudinal acceleration of a cable may be more interesting. In particular because the "noise" level according to the conductor axis is much lower. The vibratory signature of a failure therefore represents a more important part of the nominal signal level. To further investigate this topic, one should study:

- whether the longitudinal frequencies are modified by the occurrence of a failure. Note that this study was not possible on a 7m span because the acquisition frequency was limited to 1000Hz, and the fundamental longitudinal frequency of such a short span is of the order of several kHz.

- how far from the failure location the longitudinal failure signal may propagate.

- how the continual (normal) changes in vibration amplitudes may modify the longitudinal acceleration signal via the conductor tension. In particular, one should check the time scale and amplitude of this phenomenon.

Provided the time evolution of influence parameters such as conductor temperature are known, the tracking of eigen frequencies could be of some use in the detection of failures for dead-end spans equipped with AAAC conductors. In the case of a line section, the mechanical coupling between suspension spans may make this task more difficult.

Part III

Modelling

Chapter 5

Basic model validation

5.1 Introduction

In the second chapter of this thesis, experiments carried out on IREQ´ s [1] laboratory cable test bench were described. One of the objectives of these experiments was to collect all the required data to validate the model of this cable test bench vibrating at its eigen frequencies. Near span ends, important variations of curvature as a function of time are expected. At that location, the influence of conductor bending stiffness is important. It is a well-known fact that, during bending, conductors show a variable bending stiffness [28, 65]. Under such circumstances, cable elements, where the bending strain energy of the cable is neglected cannot be used. Also, the mechanical behaviour of overhead line conductors is characterized by non linear damping. In the present chapter, basic simulation results are presented. To be more precise, the topics which are being worked out are: the shape of eigen modes, the computation of a time response with a forced excitation, a sensitivity analysis and the reproduction of observed phenomena when in-span line equipment is introduced. The strategy chosen to model these characteristics is described in the next paragraph.

5.2 Model description

The strategy followed is to use a beam element to obtain some bending stiffness. The finite element code used is Samcef V13.01 [2], and its non linear analysis module Mecano. There are two different non linear beam element formulations available in Samcef. The first one is the one from Cardona and Geradin [9]. The second one, which offers the opportunity to define users

[1] IREQ: Institut de Recherche dHydro-Québec, www.Ireq.ca

[2] Samcef is a trademark of Samtech Group, www.samtech.com or www.samcef.com, LIEGE science park, Rue des Chasseurs-Ardennais, 8, B-4031 Liège (Angleur), BELGIUM, Tel: +32 4 361 69 69, Fax: +32 4 361 69 80

materials and which was therefore used in the present model, is denoted 3D beams T022, and has the following characteristics:

- Beams have stiffness in extension, bending and shear in 2 planes and torsion,
- Beams can be curved. The initial curvature is treated by Arguerre's theory,

According to Samcef user manual [75], the two formulations converge towards the same solution when the mesh is refined. Several meshes were used to simulate the 63.5 m long span. One of them contains 330 elements, with a mesh refinement near the extremities of the span (see figure 5.1). For

Figure 5.1: One of the models used: 331 nodes along the 63.5m span, with mesh refinement near the span extremities

this first modeling attempt, conductor bending stiffness is kept constant and equal to the measured average conductor bending stiffness ($EI = 591.3N.m^2$ cf. [33]).

The integration scheme for time response is a Newmarks trapezoidal rule [60], with automatic time step. Integration parameters beta and gamma are chosen equal to respectively 0.25 and 0.5, so that there is no additional numerical damping introduced.

5.3 Shape of eigen modes

During the tests performed at IREQ´s laboratory cable test bench, two conductors were tested: a steel ground wire conductor (7 steel wires, diameter:

11.0mm, mass per unit length: 0.577kg/m, rated tensile strength (RTS): 86.7kN) and a Crow conductor (54 aluminium wires over 7steel wires, diameter: 26.3mm, mass per unit length: 1.369kg/m, RTS: 117.2kN). Those conductors were tensioned at approximately either 15 or 25% of their RTS (rated tensile strength). Their sag was measured on a daily basis. They have been tested at frequencies comprised respectively between 18 and 113 Hz and between 7 and 62Hz. For each frequency, tests were repeated with three different amplitudes which correspond to fy_{max} [3] values of 40, 80 and 160mm/s. This paper will focus mainly on tests performed on the Crow ACSR conductor on September 30th 2009, at a fy_{max} value of 80mm/s and a tension of approximately 24% RTS. The conductor was tested at frequencies of 20.4, 42.9 and 59.3Hz. During the tests, in order to collect information on mode shapes, especially near span ends, the position of the first three vibration nodes next to the span end opposite to the vibration shaker was measured for every mode excited. The position of another vibration node further in span was also measured, but for the purpose of assessing the conductor self damping properties. From the distance measured between adjacent mode nodes, it is possible to deduce the value of half the wavelength. As shown further in this paragraph, both the position of the first node and the distance between adjacent nodes of higher order (e.g. between the second and the third one) computed using the beam model of the span for vibration modes 19, 40 and 53 agreed well with measurements. This suggests that the excitation frequencies of 20.4, 42.9 and 59.3Hz correspond to eigen modes 19, 40 and 53 respectively. The sag of the finite element model has been tuned (using a virtual temperature change) so that both measured and computed sag coincide. Once the actual sag value of the span is obtained in the model, a modal analysis can be performed combining non linear matrices computed by Mecano with Dynam module for eigen frequency analysis. A comparison between measured frequencies, frequencies computed using a cable model, frequencies computed using a beam finite element model and frequencies computed with the following formula [25] (using the same tension values as in the model: 27.1kN for the beam and 29kN for the cable).

$$f_n = \frac{1}{2\pi}\sqrt{\left(\frac{n\pi}{L}\right)^2 \frac{T}{m_L}\left[1+\left(\frac{n\pi}{L}\right)^2 \frac{EI}{T}\right]} \tag{5.1}$$

The comparison between the beam and cable model is performed respecting an imposed sag value. Given this hypothesis, tension in the beam model is worth 27.1kN and 29kN in the cable model. A discussion of the difference between eigen frequencies computed with the beam model and observed ones is presented further in the text. The following tables (5.1-5.3)

[3] fy_{max} is the product of frequency [Hz] by zero-to-peak antinode amplitude of vibration y_{max} [mm], as defined in section 1.5

Table 5.1: Comparison between measured and computed frequencies for the beam and cable models

Mode	Obs. freq. [Hz]	Beam FE freq. [Hz]	Dif. %	Eq. (5.1) $591.3Nm^2$ [Hz]	Cable FE freq. [Hz]	Dif. %	Eq. (5.1) $0Nm^2$ [Hz]
19	20.4	21.06	+3.2	21.24	20.50	+0.5	21.76
40	42.9	44.46	+3.6	46.14	42.22	-1.6	45.82
53	59.3	61.74	+4.1	62.93	56.49	-4.7	60.71

Table 5.2: Comparison between measured half wavelength and computed half wavelength (for the beam and cable FE models)

Mode	Measured $\lambda/2$ [m]	Beam FE $\lambda/2$ [m]	Differ. %	Cable FE $\lambda/2$ [m]	Difference %
19	3.51	3.51	0.2	3.34	5
40	1.71	1.71	0.1	1.63	4.7
53	1.27	1.27	0.5	1.22	3.8

compare measured mode shape information versus values computed by a modal analysis, with a cable and a beam finite elements (FE) model of the span.

One can see that the beam model with the assumption of constant bending stiffness (taken equal to the average bending stiffness deduced from measurements) leads to good results. The position of node 1 is computed with a difference of a few % (against 10% for the cable model), which means that the mode shape in the vicinity of the span is correctly computed. The difference between computed and measured position of node 1 is minimum for the 53rd vibration mode (0.4%). Also, half the wavelength is computed with a difference much inferior to 1% (against about 5% for the cable model).

5.4 Time response with a forced excitation

On IREQ ´ s cable test bench, a vibration shaker was used to excite the cable. It was located at a distance of 1.68m of the span end opposed to the

Table 5.3: Comparison between measured and computed position of node 1 for the beam and cable models

Mode	Measured pos. of node 1	Beam FE pos. of node 1	Differ. %	Cable FE pos. of node 1	Differ. %
19	3.65	3.68	3 %	3.34	8.5 %
40	1.83	1.86	1.5 %	1.63	11 %
53	1.39	1.40	0.4 %	1.22	12.4 %

suspension clamp. Let us consider tests carried out on September 30th 2008 on Crow ACSR conductor tensioned at approximately 24% RTS. During those tests the conductor was excited at its 19th eigen frequency, with an amplitude fy_{max} equal to either 40, 80 or 160mm/s. The corresponding excitation forces imposed by the shaker were respectively 3.7, 13.2 and 40.67N (0-pk).

In our finite element model, the vibration shaker is modelled by a vertical harmonic force acting at the same distance from span end. The force amplitude introduced in the model is worth 26.4N 0-pk. This value therefore corresponds (in real world) to an fy_{max} amplitude comprised between 80 and 160 mm/s. The 19th eigen frequency computed by a modal analysis for the beam model is worth 21.15Hz. This means that there is a 3.6% difference between the computed value of the nineteenth frequency and the one measured in laboratory (20.4Hz). Such difference probably comes from one or several of the following reasons:

- no damping is considered for the present modal analysis; in reality, some damping is present, which will affect the values computed for eigen frequencies,
- the sag of the model has been tuned so as to coincide with the sag value deduced from measurements. To deduce that sag, the relative height of two points located at 50cm from the end of the span and of a third point located at the centre of the span was measured on a daily basis with a precision of the order of 0.1mm. Nevertheless, since information on the conductor shape between the span ends and 50cm further is not known, the precision on the sag value deduced from measurements is of the order of 1cm when transposed to the model. Moreover, a small sag variation during the day due to temperature change may not be excluded.
- the system used to excite the conductor is a vibration shaker which moving arm is connected to the conductor. The mass of this moving arm is not negligible and will impact conductor vibrations. Nevertheless, it is not taken into account in the present model. According to the data sheet of the vibration shaker, the armature weight of the vibration shaker is 9.1kg.
- the cable is a complicated system with layers, stranding angle, It is modelled here with a simple beam element,
- the spatial discretization of the span has an impact on the computed mass and stiffness matrices and hence on computed values of eigen frequencies.

Let us now consider the dynamic response of the cable when a forced harmonic excitation, with a frequency of 21.15 Hz and an amplitude equal to

26.4N (0-peak). The position of the third antinode (the first antinode being the one adjacent to the span end opposite to the shaker) as a function of time can be seen in figure 5.2. Note that the integration scheme used is Newmark with no numerical damping.

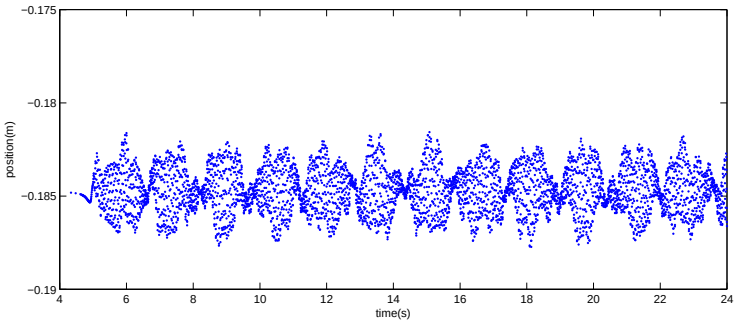

Figure 5.2: Position of the third antinode of eigen mode 19 at 21.15Hz

A beat is clearly visible. Its period is approximately 1.6 s. It may mean that the introduction of the vibration shaker in the model has an impact on eigen frequencies. The resonance can be visualised with a Lissajous curve, with position on one axis and excitation force on the other. At resonance, phase shift between acceleration and excitation force is 90°, which means that the Lissajous curve plotting either excitation force as a function of displacement, or excitation force as a function of acceleration is a circle (provided an appropriate scale is chosen for axes X and Y, else the plot will show an *unrotated* ellipse). Figure 5.3 shows a Lissajous curve (acceleration as a function of excitation) for an excitation frequency of 21.15Hz. One can see that the phase is not constant. Changing the excitation frequency to either 22 or 20.85Hz, it is possible to improve the phase stability, but not to completely get rid of beats (Figure 5.4).

The evolution of conductor tension during the same simulations is shown in figure 5.5. A frequency content analysis of the tension in the beam excited at 20.85 and 22Hz shows an important component at twice the excitation frequency (figure 5.6). These curves show that the introduction of an excitation force in the model induces tension variations. The interested reader can find further information on this double-frequency phenomenon in [66]. As long as tension continuously varies in the model, eigen frequencies will vary too. Therefore, with those continuously changing eigen frequencies, it is not possible to obtain a *perfect resonance* exciting the cable model at a fixed frequency. This is a plausible explanation to the beat phenomenon. The continuous tension fluctuations probably causes a continuous eigen frequency fluctuation, and even if no damping is introduced in the model, the *nodes* will be vibrating. This topic will be further investigated in chapter 6.

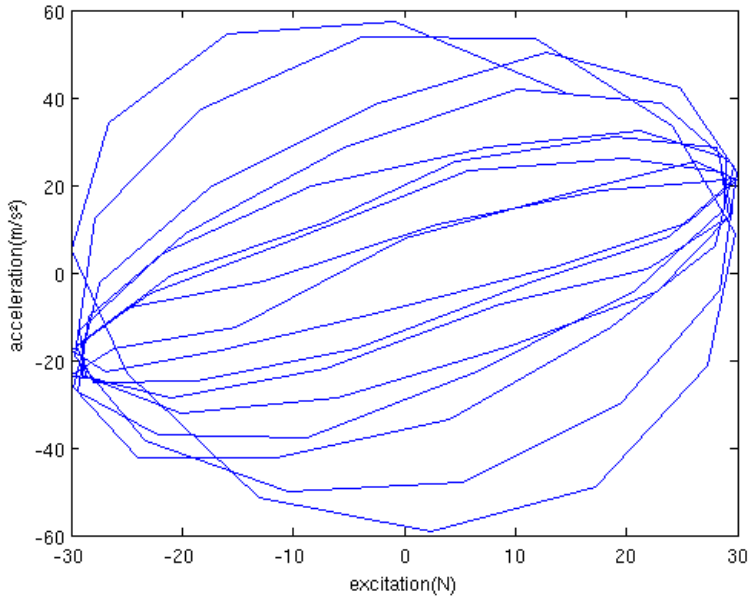

Figure 5.3: Lissajous curve (acceleration $[m/s]$ as a function of excitation $[N]$) at a frequency of $21.15Hz$.

5.5 Parametric study

As mentioned in the introduction of the present paper, the behaviour of overhead line cables is complex to model. The present parametric study aims at studying the impact of an inaccurate value of average bending stiffness on the one hand and of excitation force on the other hand.

Figure 5.7 shows the impact of a 10% change in the value of average bending stiffness used in the simulations. Three values of conductor bending stiffness are considered: the average one, as well as 90% and 110% of this average value. Also, the previous figure is drawn respecting a constant sag value and a frequency adjustment is performed for each case to get closer to resonance conditions. The previous figure shows that a bending stiffness change of 10% leads to an amplitude change comprised between 1 to 6%.

Another source of uncertainty resides in the knowledge of the excitation force. Figure 5.8 shows the results of a sensitivity analysis to the value of the excitation force. One can see that the sensitivity to the amplitude of the excitation force is low. Considering changes of 10% in the amplitude of the excitation force, corresponding changes in maximum amplitudes computed are of the order of 5%. Provided the value of the excitation force is of the order of a few tens of Newtons, the impact of a 1N error in the evaluation of the amplitude of the excitation force is negligible.

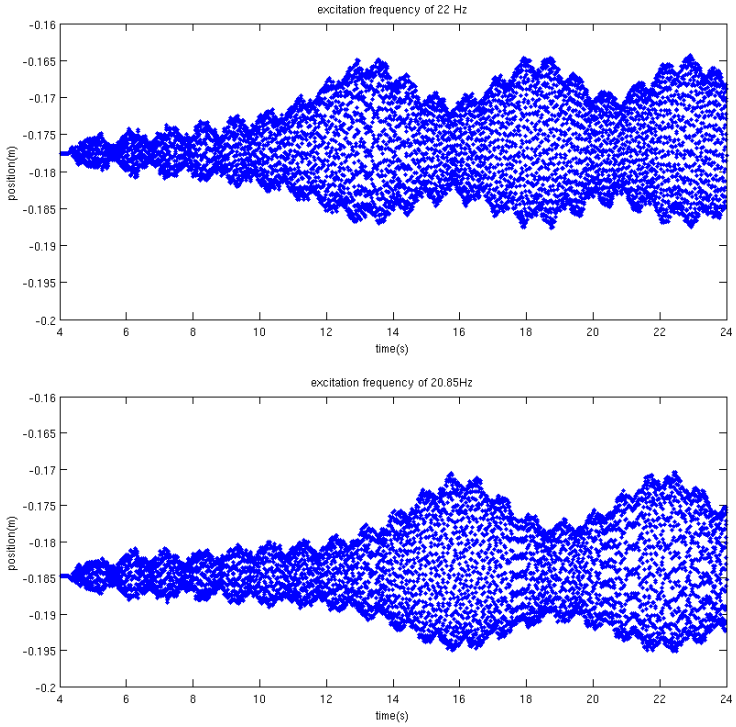

Figure 5.4: Position of the third antinode for eigen frequency of 20.85 Hz (top) and 22 Hz (bottom)

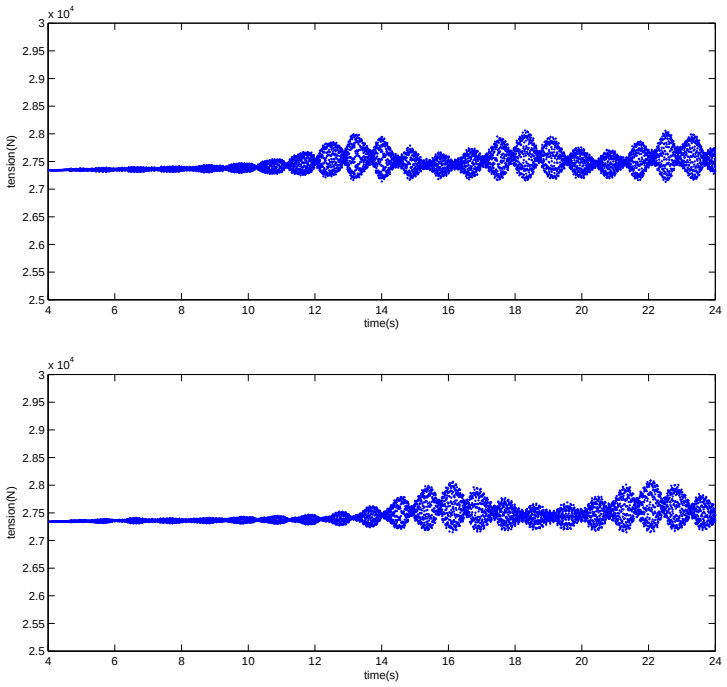

Figure 5.5: Evolution of tension in the model when the excitation frequency is 20.85 Hz (top) and 22 Hz (bottom)

5.6 Reproduction of observed phenomena when in-span line equipment is introduced

During some of the tests performed with line equipment installed in-span, higher amplitudes were observed on the subspan corresponding to the short portion of conductor between the line equipment and the suspension clamp, opposite to the shaker side. As further explained in this paragraph, it was possible to reproduce such phenomena with the beam model computing a dynamic time response of the span, but these higher amplitudes on the short portion of span can already be observed by modal analysis. Let us consider a vibration test made on October 27th 2008, with conductor Crow tensioned at approximately 23.5% RTS, a suspension clamp installed on the span extremity opposed to the vibration shaker, and monitoring device installed at approximately 6.2m from the suspension clamp. For an excitation frequency of 61.23Hz, amplitudes between the monitoring device and the suspension clamp (short subspan) were approximately 50% higher than amplitudes between the monitoring device and the shaker (long subspan). Modelling the monitoring device with a concentrated mass of 8kg, the 52nd mode shape which corresponds to a 59.44Hz eigen frequency is also characterized by higher amplitudes on the short portion of conductor between the

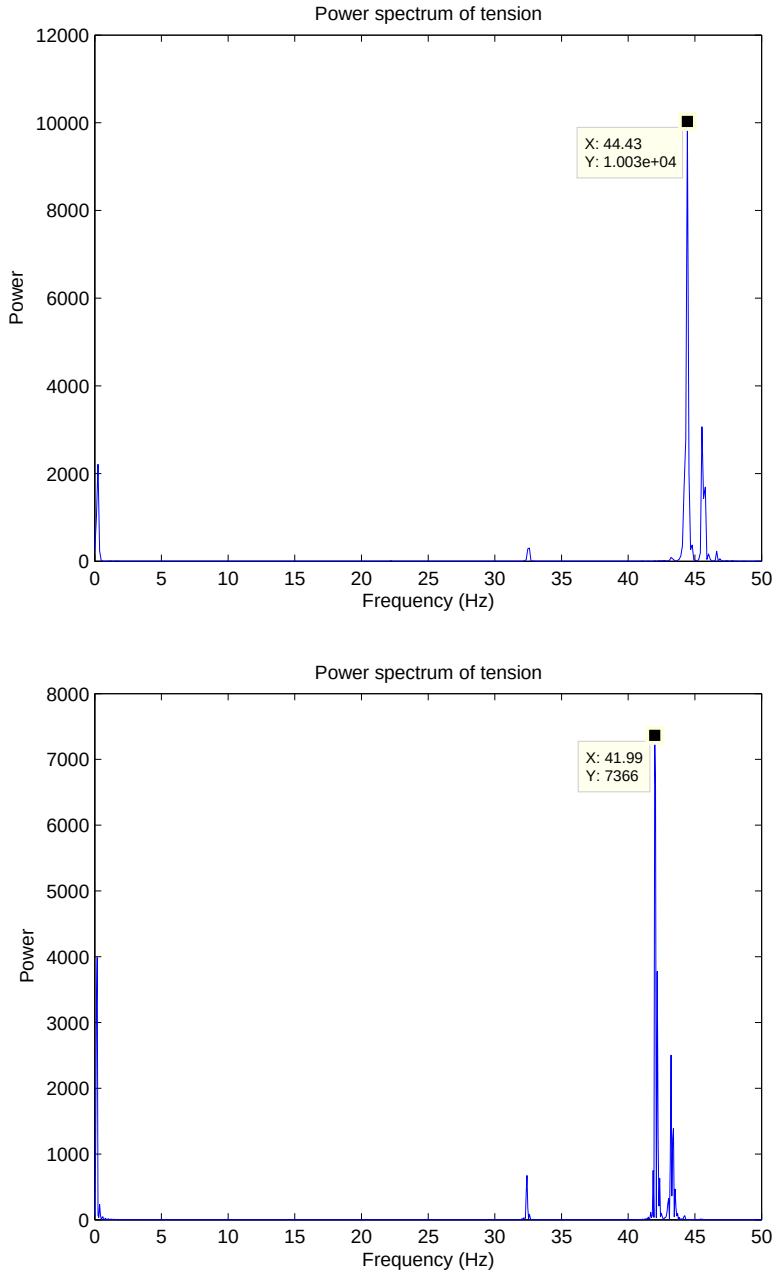

Figure 5.6: Frequency content of the tension in the beam for excitation frequencies of respectively 20.85Hz (top) and 22 Hz (bottom). If X is the discrete fourier transform of the tension signal, the vertical axis shows $(\frac{|X_k|}{N})^2$.

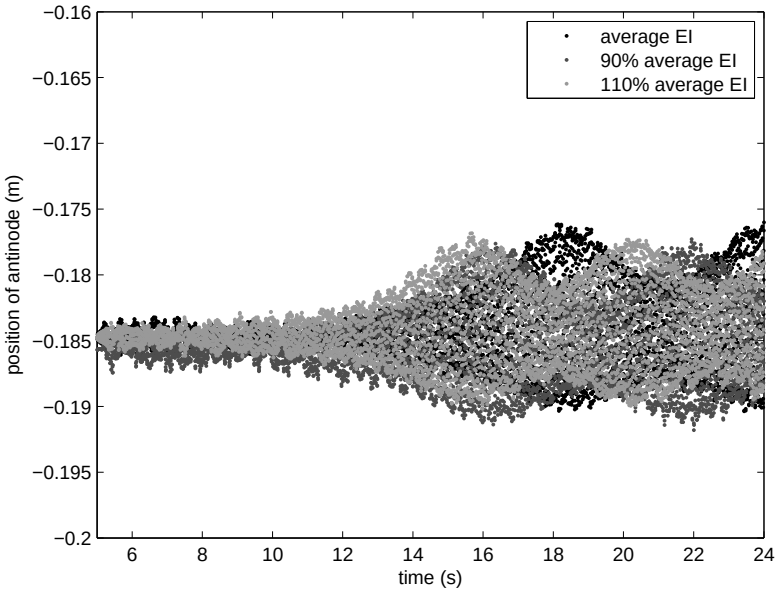

Figure 5.7: Sensitivity of the model to the value of average bending stiffness

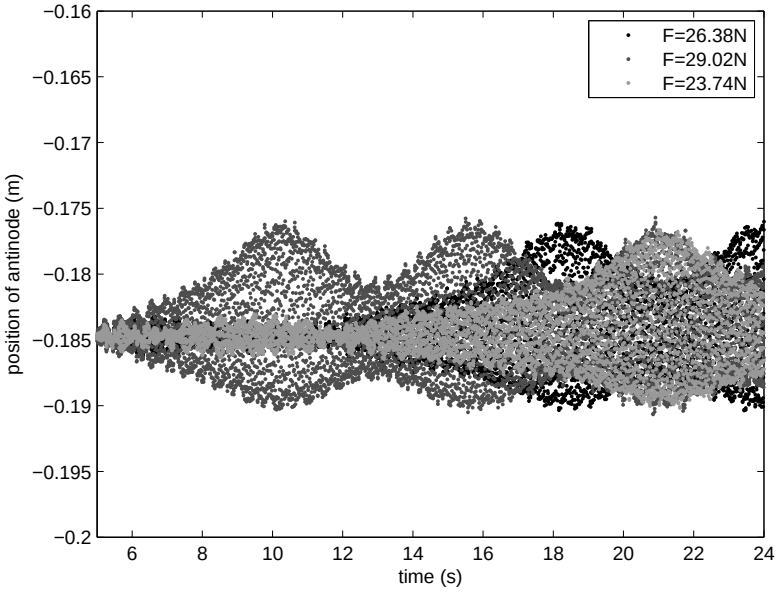

Figure 5.8: Sensitivity of the model to the value of excitation force

line equipment and the suspension clamp (see figure 5.9).

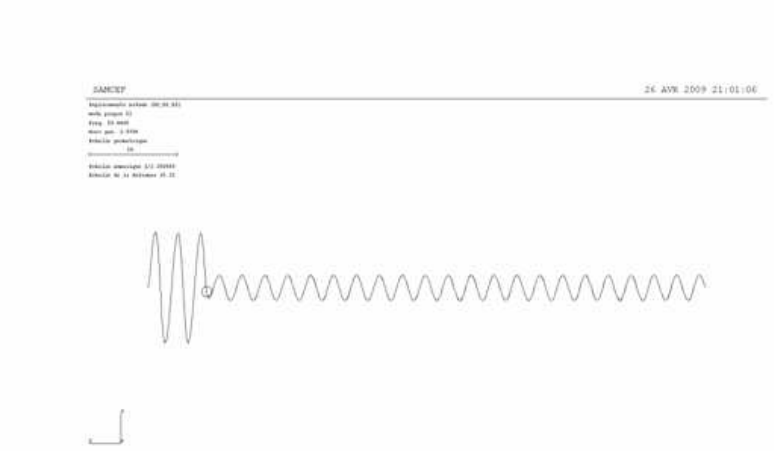

Figure 5.9: 52nd mode shape (eigen frequency of 59.44Hz), higher amplitudes are obtained on the short subspan

Investigating which conditions led to such higher amplitudes in the short subspan, the graph shown in figure 5.10 was drawn. The graph shows the ratio between antinode amplitude of the short subspan over antinode amplitude of the long subspan as a function of the ratio frequency/ fundamental frequency of the short subspan. Three series of data are shown: the first one with the real mass value of the line equipment (8kg), the second one with a lower mass value (5kg) and the last one with no mass at all (obviously leading to an antinode amplitude ratio equal to 1). From the previous graph, it is clear that amplitude ratios higher than 1 are met for excitation frequencies which correspond to a multiple of the fundamental frequency of the span portion between the line equipment device and the suspension clamp. Nevertheless for all other cases, the vibration amplitudes on the short portion of span are much lower than on the rest of the span. This amplitude amplification effect needs to be further investigated to determine the effect of subspan length ratios for example, but from this information, it is possible to predict when an amplitude amplification will occur.

5.7 Time response

The model used to compute the time response in the previous sections contains between 300 and 400 elements. With such discretization, it is possible to model adequately the time response at frequencies of the order of 20 Hz,

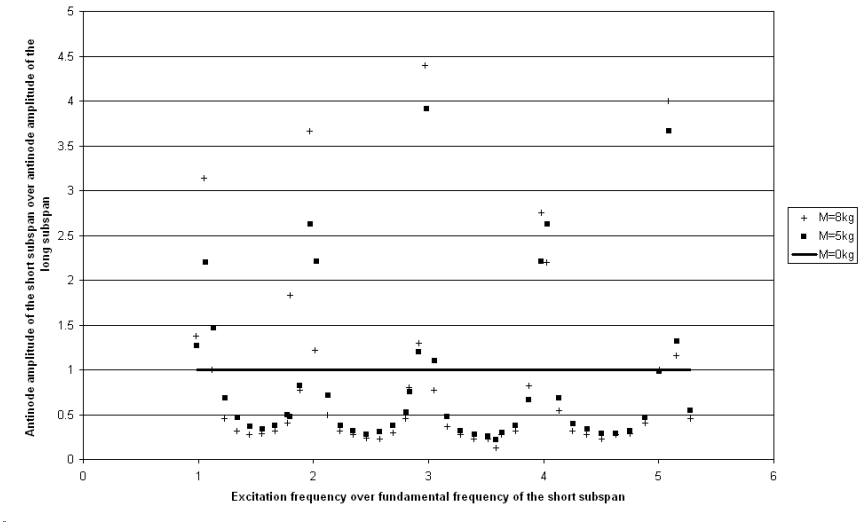

Figure 5.10: Effect of frequency on antinode amplitude of a subspan delimited by a concentrated mass

but for frequencies as high as 60Hz a mesh refinement is needed. In order not to increase the number of elements too much, it was decided to compute the time response of the beam under forced excitation at a lower frequency, trying to obtain higher amplitudes on the short portion of span. The model used contains 382 elements, and a case of higher amplitudes on the short portion of span was obtained for an excitation frequency of 23.075Hz.

On the short portion of span, the antinodes of mode 21 vibrate with a peak-to-peak amplitude of 25mm (see figure 5.11), while on the long portion of span, antinode amplitudes of the same mode reach only 13mm peak-to-peak. This observation is equivalent to a ratio of approximately 2 between the antinode amplitudes on the short and long portion of span, which is in agreement with the values of figure 5.10.

5.8 Conclusions

The shape of a conductor vibrating at its vibration modes in the vicinity of the span end is correctly reproduced by the beam element model.

Studying the time response of the conductor under forced excitation, it has been shown that tension fluctuations cannot be neglected in the observed phenomenon. A direct consequence is that the conductor eigen frequency fluctuates continuously, which makes it difficult to obtain a perfect resonance. The impact of tension fluctuations on the 63.5 m long span are much less important than for most other (shorter) laboratory tests spans. Still, even with its important length, vibration amplitudes on the 63.5m are

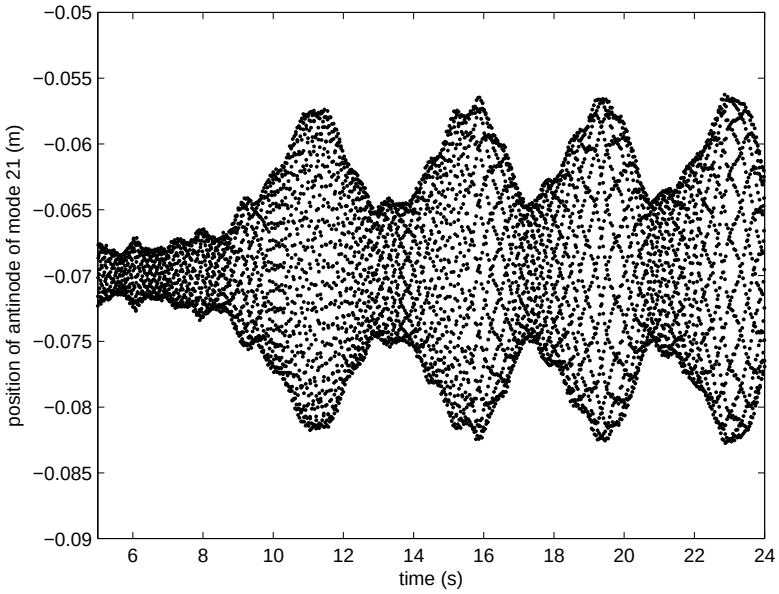

Figure 5.11: Amplitude at an antinode located on the short portion of span when the excitation frequency is 23.075 Hz

worth a significant sag percentage. The ratio amplitude of vibration/sag on the 63m laboratory test bench is of the order of 5%, while on a real span, the same ratio is of the order of 0.2%. Part of node displacement on the laboratory test span may be due to tension variations, and smaller tension variations may be expected on real spans during Aeolian vibration events. This potential contribution to node displacement will be investigated in the next chapters since it may invalidate the hypothesis of ISWR method, which is a widely used method to assess conductor self damping properties.

Considering a concentrated mass on the conductor, modal analysis with the beam model made it possible to understand which particular conditions led to higher amplitudes on the short portion of span (between the concentrated mass and the nearest span end in our experiment). Higher amplitudes on the short portion of span occur when the excitation frequency is a multiple of the short span fundamental frequency. For all other conditions, the amplitudes of vibration on the short portion of span are lower than everywhere else. This analysis must be further completed by a study using the propagation theory. Last, it was possible to reproduce these high amplitudes on the short portion of span with a dynamic time analysis for an excitation frequency of about twenty Hertz.

Chapter 6

Tension fluctuations and related consequences

6.1 Introduction

In the field of Cable Bridges, tension fluctuations are known to have a potential impact on vibration amplitudes, as is the case with the "parametric excitation" phenomenon. As explained in [14], the parametric excitation of cables is an instability phenomenon which consists of large amplitude transverse cable oscillations caused by the longitudinal component of the small periodic motion of the cable supports. More information on the subject can be found in [51] and [15].

An important amount of data was collected throughout the tests performed at Ireq in 2008 and 2009 (see chapter 3). In an attempt to model them, interesting phenomena have been highlighted (see section 5.4), which are believed to be linked to tension fluctuations. In order to confirm interpretation, one needs to go back to theory and cable equations.

6.2 Equations for vertical motion

Referring to [52, 50], the basic equation for vertical motion of a conductor can be written:

$$\frac{\partial^2 y}{\partial t^2} - \frac{T}{m}\frac{\partial^2 y}{\partial z^2} = \frac{f_e(z)}{m} \tag{6.1}$$

where m is the conductor mass per unit length [kg/m], T the conductor tension [N], and $f_e(z)$ external forces [N]. Let l [m] be the conductor instantaneous length at a given time t. Considering a small perturbation in the equilibrium position of the cable ($T = T_0 + \Delta T$, $l = l_0 + \Delta l$), the previous equation becomes

$$\frac{\partial^2 \Delta y}{\partial t^2} - \frac{1}{m}[T_0\frac{\partial^2 \Delta y}{\partial z^2} + a\Delta T] = 0 \tag{6.2}$$

where a is the conductor curvature, equal to

$$a = \frac{\partial^2 y_0}{\partial z^2} = \frac{mg}{T_0} \tag{6.3}$$

under the hypothesis of parabolic catenary shape.

6.3 Figuring the change in tension

6.3.1 Simple formulation

The change in tension can be estimated thanks to Hooke's law

$$\Delta T = K_v \Delta l. \tag{6.4}$$

where K_v accounts not only for conductor axial stiffness, but also for tower anchoring stiffness (K):

$$\frac{1}{K_v} = \frac{L}{ES} + \frac{1}{K}. \tag{6.5}$$

Note that when the cable is fixed by two heavy metallic clamps, which are themselves tightly fixed to two heavy and highly rigid concrete blocks (which is the case for IREQ´s test span), the contribution of the anchoring stiffness system may be neglected.
The change in length Δl can be estimated thanks to the following equation [25].

$$\Delta l \simeq \frac{1}{2} \int_0^l [(\frac{\partial y}{\partial z})^2 - (\frac{\partial y_0}{\partial z})^2] dz. \tag{6.6}$$

Assuming both a small perturbation in the equilibrium position of the cable and the following modal decomposition for y

$$y_s = \sum_{k=1}^{N_{modes}} y_{s,k} \sin(\frac{k\pi z}{L_s}) \tag{6.7}$$

where s is the span index and k the mode number, one obtains the following equation for the change in tension:

$$\Delta T \simeq K_v \sum_{s=1}^{N_s} L_s \sum_{k=1}^{N_{modes}} (\frac{k\pi}{2L_s})^2 (y_{s,k}^2 - y_{s,k0}^2). \tag{6.8}$$

where $y_{s,k0} = \frac{4mgL^2}{(k\pi)^3 T_0}$ for k odd and zero for k even.

6.3.2 A more accurate formulation

Neglecting the conductor bending stiffness effect, the shape of a conductor can be represented by a hyperbolic function. Considering a level span and a set of axes located at one end of the span, this function is:

$$y_s = P\cosh(\frac{x - L/2}{P}) - P\cosh(\frac{L}{2P}), \tag{6.9}$$

where P [m] is the ratio of conductor tension [N] on weight per unit length [N/m].

When the conductor is vibrating at one of its eigen modes, if the conductor bending stiffness is still neglected, the shape of the conductor can be approximated by the following function:

$$y = y_s + y_e \tag{6.10}$$

where

$$y_e = A\,sin(\omega t)\,sin(\frac{k\pi x}{L}) \tag{6.11}$$

and k is the mode number.

Let y' be the first derivative of y with respect to abscissa x. The length of conductor between the two span extremities is found by the formula

$$s = \int_0^L \sqrt{1 + y'(x)^2}\,dx. \tag{6.12}$$

6.3.3 Comparison of the changes in tension computed analytically versus with a finite element model

The comparison of the change in tension computed using either the finite element model or one of the analytical formula has been performed under the following hypotheses:

- 63.5 m long span with infinitely rigid span ends,
- An ACSR Crow conductor is strung on the span at 26.5% RTS. The cable characteristics can be found in [25]: a total section of $409.4mm^2$, an aluminium section of $362.6mm^2$, 54 aluminium wires (diameter 2.92mm), 7 steel wires (diameter 2.92mm), a total diameter of 26.3mm, a linear mass of 1.3698kg/m and a rated tensile strength of 116.9kN [25]. The conductor extensional stiffness can be estimated from this data:
$$\frac{ES}{L} = \frac{68.3 * 10^9 * 409.4 * 10^{-6}}{63.5} = 4.4 * 10^5 N/m$$

Table 6.1: Comparison of the changes in tension computed from a simple formulation (see section 6.3.1), a more accurate formulation (see section 6.3.2) or with a finite element model

Method	mean dynamic tension $< T >$	σ (standard deviation)	$\frac{<T>-T_0}{T_0}$
Analytic 1 (see section 6.3.1)	31212.96N	156.60N	0.69%
Analytic 2 (see section 6.3.2)	31212.94N	156.58N	0.69%
Finite elements	31187N	203.26N	0.6%

- The cable vibrates at its 19^{th} eigen mode, with an amplitude $fy_{max} = 188.8mm/s$. The latter amplitude is slightly inferior to the endurance limit of ACSR conductors, which is about $200mm/s$ [25]. Higher fy_{max} values would hardly be met in reality.

The previous table not only confirms that the analytical formulae lead to a change in tension too, but it also highlights that the latter values are very similar to those computed by the finite element model. As an example, the mean dynamic tension differ from less than 0.1% and $\frac{<T>-T_0}{T_0}$ by less than 15%.

The results computed with the "more accurate analytical formulation" (see section 6.3.2) are further illustrated. In figure 6.1, one can see the initial and deformed shape of the conductor and in figure 6.2, the evolution of the total span length, which is characterized by a frequency equal to twice the excitation one.

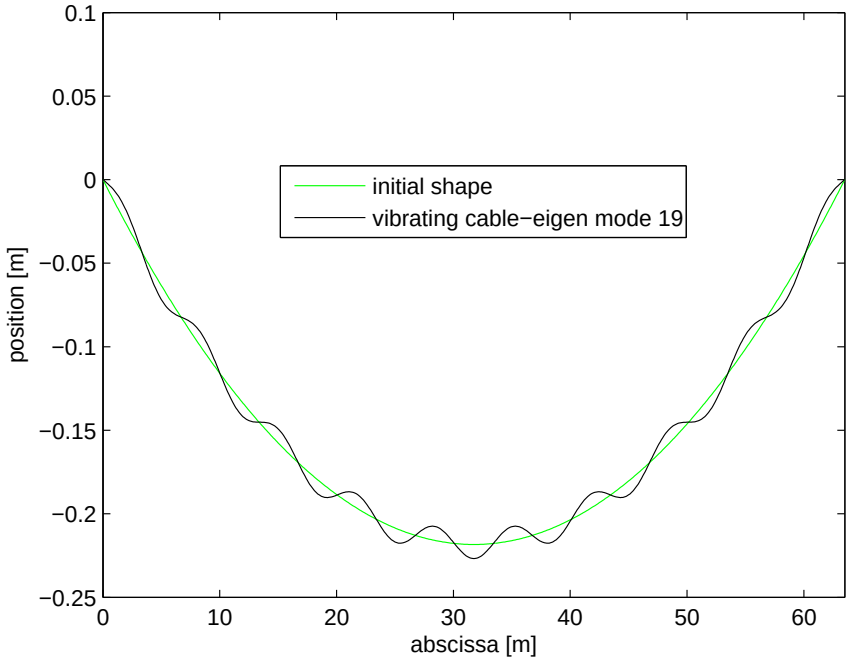

Figure 6.1: Initial and deformed shapes of the 63.5m span, as computed with the model presented in section 6.3.2

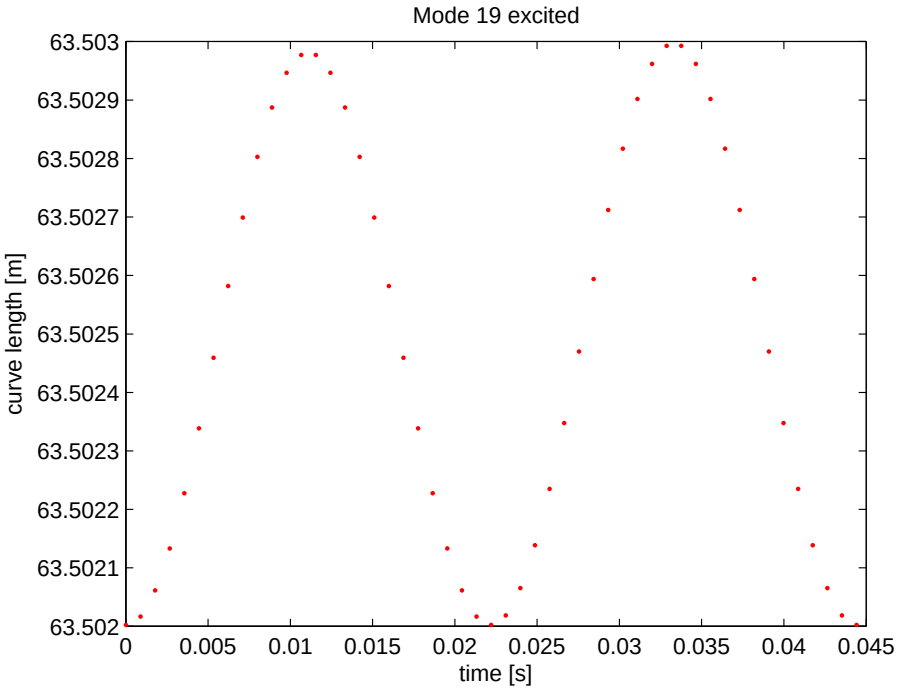

Figure 6.2: Evolution of the total span length over one period of vibration, as computed with the model presented in section 6.3.2

6.4 Tension fluctuations in real spans versus laboratory test spans

Since it is a common practice nowadays to assess the self damping properties of conductors on short laboratory dead end spans [1], it sounds relevant to ask ourselves whether tension fluctuations have a different impact on real spans versus laboratory ones.

In real life, it is commonplace to see single spans which length is of the order of a few hundreds of meters. In Cigré brochure TB396 [2], the maximum reported length for a single span is 5374m, in a fjord crossing in Greenland. In the present document, the vocable "long span" denotes spans with a length comparable to real ones (generally more than a hundred meters). Other spans which length represents a few tens of meters will be denoted "short spans".

Also, in real life configurations, line sections are common [2].

6.4.1 Changes in tension in a single dead end span versus a section span

Starting from equation (6.8), the potential changes in tension within a span can be estimated whatever its length or configuration. Let us assume that:

- a span of some overhead line section is vibrating at its k_{th} mode only (all other spans of the line section are supposed to be still),
- k is high enough so that its modal contribution to the initial sag is negligible, $(y_{sk}^2 - y_{sk0}^2) \approx \Delta y_{sk}^2$,
- the section ends are infinitely rigid.

If this vibrating span is the j_{th} span of a series of s suspension spans, the change in tension is

$$\Delta T \simeq K_v L_j (\frac{k\pi}{2L_j})^2 \Delta y_{j,k}^2 \tag{6.13}$$

Referring to (6.5), K_v satisfies

$$\frac{1}{K_v} = \frac{\sum_{s=1}^{N_s} L_s}{ES} + \frac{1}{K}$$

Since the section ends are supposed to be infinitely rigid, one obtains:

[1] The self damping power of an average to long span at a given frequency is generally estimated using data recorded on a short span, at the same amplitude and tension levels

[2] a section is a succession of suspension spans

$$K_v \simeq \frac{ES}{\sum_{s=1}^{N_s} L_s}$$

and equation 6.13 can be rewritten as:

$$\Delta T \simeq \frac{L_j}{\sum_{s=1}^{N_s} L_s} ES(\frac{k\pi}{2L_j})^2 \Delta y_{j,k}^2 \tag{6.14}$$

As a comparison, in the case of a single dead end span, the change in tension would be

$$\Delta T \simeq ES(\frac{k\pi}{2L})^2(\Delta y_k^2). \tag{6.15}$$

It means that all other things being equal (span length, mode number, vibration amplitude, etc..) the change in tension is much higher in a single dead-end span than in a line section (a realistic range for $\frac{L_j}{\sum_{s=1}^{N_s} L_s}$ is 0.1-0.3). Compared to single spans, their axial stiffness is of course much inferior.

6.4.2 The axial rigidity of span ends

Coming back to the rigidity of span ends, the anchoring stiffness of real spans will be completely different than in the case of a dead-end span "fixed by two heavy metallic clamps, themselves tightly fixed to two heavy and highly rigid concrete blocks". As a consequence, for real spans, the contribution of span ends should not be neglected in equation (6.5), leading to lower axial stiffness values.

This is another reason why in real life, changes in tension may be inferior to those existing on laboratory spans, even if similar vibration levels are considered.

6.4.3 fy_{max} (amplitudes times frequency) and changes in tension in single dead end spans

The fatigue indicator fy_{max} (defined in sections 1.4 and 1.5) is generally used to quantify the severity of vibrations on a power line in fatigue tests or self damping tests. It seems relevant: when strung at the same tension level, and excited at the same fy_{max} amplitude, two spans of different lengths will vibrate with a similar "loop pattern". Nevertheless, the corresponding changes in tension will only be similar in the case of single dead end spans, for which $\frac{k^2}{L^2} \simeq \frac{1}{\lambda_k^2}$ and $\lambda_k^2 \simeq \frac{T}{f_k^2 m}$, so that formula (6.15) can be further simplified in:

$$\Delta T \simeq (\frac{ES\pi^2 m}{4T})(f_k y_{max})^2 \tag{6.16}$$

This formula (6.16) has the following physical meaning: under the assumptions made, the change in tension in a (single) dead end span varies as the square of fy_{max}. Comparing two dead-end spans with exactly the same parameters and characteristics but length, vibrating with the same amplitude fy_{max}, at a high order vibration mode, no important difference in the computed changes in tension is to be expected.

6.4.4 Checking the hypotheses made

In case k is small and odd, the hypothesis of negligible contribution to the initial sag (which permits to approximate $(y_{sk}^2 - y_{sk0}^2)$ by Δy_{sk}^2) and to obtain (6.13)) may be violated. In order to check this out, some computations have been performed for a dead end span, using the " more accurate formulation " presented in section 6.3.2. Other hypotheses are identical as in section 6.3.3 except the amplitude which is worth exactly $fy_{max} = 200mm/s$. The results are shown in figure 6.3., where the change in tension (%) is given as a function of the span length. Four series of data are shown, each of them corresponding to a given mode (1, 3, 5 or 19) excited at an amplitude $fy_{max} = 200mm/s$. Analysing the curves, one can clearly see two things:

- for a fixed span length value, the influence of y_{k0} is stronger for mode 1. Yet, the difference between the computed changes in tension is inferior to 1% . For higher mode numbers, there is almost no scattering among the results.

- as the span length increase, for a fixed value of fy_{max}, the change in tension computed with a more accurate formula decreases. Nevertheless, the order of magnitude of this decrease is limited (e.g. for the case depicted in figure 6.3, less than 1% when the span length in increased from 100m to 200m).

All in all, the hypotheses made to deduce the simplified formulae (6.14) and (6.15) seem acceptable.

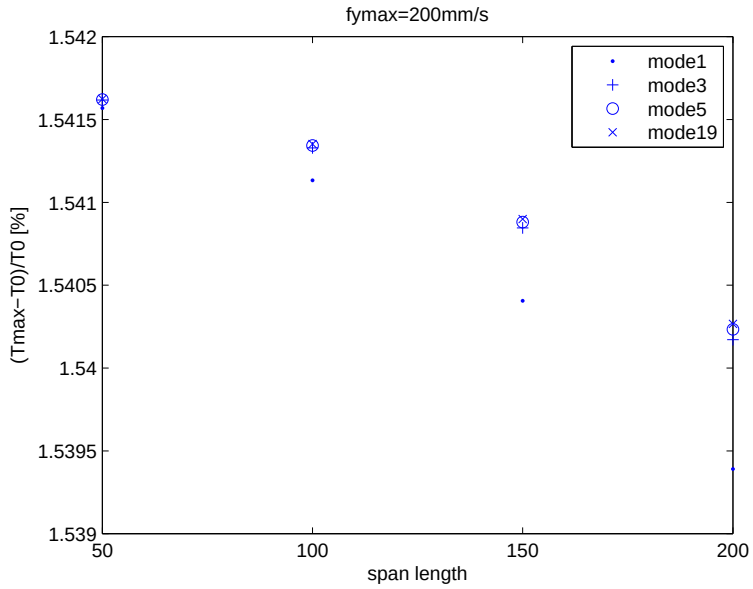

Figure 6.3: Maximum change in tension [%] computed analytically with the formulae presented in section 6.3.2 for several odd mode numbers and as the span length varies. The span length is in meters [m] and fy_{max} is taken equal to $200mm/s$. Other hypotheses are identical as those described in section 6.3.3

6.5 The effect of tension fluctuations on amplitudes

The previous section has demonstrated why differences in changes in tension may exist between a laboratory span versus a real span. A good understanding of the potential impact of tension fluctuations on the assessment of conductor properties is therefore of paramount importance. The aim of the present section is to qualify and quantify the effects of tension fluctuations. To do so, the solutions to two problems need to be compared. Considering the same amount of damping introduced, and the same harmonic excitation, a variable tension problem will be compared to a constant tension one.

6.5.1 Resolution of the constant tension problem

Modal solution

The equations of motion of a viscous string under forced transverse motion are:

$$m\frac{\partial^2 y}{\partial t^2} + c\frac{\partial y}{\partial t} = T\frac{\partial^2 y}{\partial x^2} + f(x,t) \tag{6.17}$$

where m is the linear mass $[kg/m]$, c is the viscous damping coefficient $[Ns/m^2]$, T is the string tension $[N]$ and $f(x,t)$ some transverse excitation $[N/m]$.

A solution to this problem can be sought as a "modal superposition", with the following form:

$$y(x,t) = \sum Y_i(x)\bar{q}_i(t) \tag{6.18}$$

where $\bar{q}$ are the generalized coordinates of the forced response solution and $Y_i(x)$ are the normalized mode shapes that satisfy the orthogonality properties

$$\int_0^l Y_i(x)Y_j(x)\,dx = 0,\ i \neq j \tag{6.19}$$

$$\int_0^l Y_i(x)Y_j(x)\,dx = \frac{l}{2},\ i = j \tag{6.20}$$

and the following equation,

$$\frac{d^2Y_i(x)}{dx^2} = -\lambda^2 Y_i(x) \tag{6.21}$$

with $\lambda_i = \frac{i\pi}{l}$.

Introducing (6.18) and (6.21) in (6.17), one obtains:

$$m\sum Y_i(x)\frac{\partial^2\bar{q}_i}{\partial t^2} + c\sum Y_i(x)\frac{\partial\bar{q}_i}{\partial t} = -T\sum {\lambda_i}^2 Y_i\bar{q}_i(t) + f(x,t) \tag{6.22}$$

Suppose the harmonic excitation is punctual and located at x=a. In other words, $f(x,t) = F_0\sin(\omega t)\delta(x-a)$

Multiplying the previous equation by Y_j and integrating it between 0 and L, one obtains

$$m\frac{l}{2}\ddot{\bar{q}}_i + \frac{cl}{2}\dot{\bar{q}}_i + \frac{\lambda^2 Tl}{2}\bar{q}_i = 2f_0\sin(\omega t)Y_i(a) \tag{6.23}$$

One can assume that a solution of this equation is

$$\bar{q}_i = A_i\sin(\omega t + \phi_i) \tag{6.24}$$

The solution to the initial problem is

$$y(x,t) = \sum A_i Y_i(x)\sin(\omega t + \phi_i) \tag{6.25}$$

where the mode shapes are given by $Y_i(x) = \sin(\frac{i\pi x}{L})$ so that the following boundary conditions are implicitly respected

$$y(L,t) = y(0,t) = 0 \tag{6.26}$$

Replacing the general coordinates $\bar{q_i}(t)$ by their values $A_i \sin(\omega_i t + \phi_i)$ in (6.21) gives:

$$-A_i\omega^2 \sin(\omega t + \phi_i) + \frac{c}{m} A_i \omega \cos(\omega t + \phi_i) + \tag{6.27}$$
$$\omega_i^2 A_i \sin(\omega t + \phi_i) = \frac{2f_0}{ml} \sin(\omega t) Y_i(a)$$

The previous expression can be rewritten decomposing the sinusoidal functions of a sum as a sum of products involving $\sin(\omega t)\cos(\omega t)$. Then, equating the coefficients of $\sin(\omega t)$ and $\cos(\omega t)$ in both members gives the following two equations:

$$A_i(\omega_i^2 - \omega^2)\cos(\phi_i) - \frac{c}{m} A_i \omega \sin(\phi_i) = \frac{2f_0}{ml} Y_i(a) \tag{6.28}$$

$$A_i(\omega_i^2 - \omega^2)\sin(\phi_i) + \frac{c}{m} A_i \omega \cos(\phi_i) = 0 \tag{6.29}$$

From the latter equations, it is possible to check that $\phi_i = \frac{\pi}{2}$ when the cable is excited at its ith resonance frequency (non trivial solution when $\omega_i = \omega$).

Numerical application

Assuming that a 63.5m span equiped with a cable of $1.369 kg/m$ tensioned to 28000N ($+-23\% RTS$), and that this cable is excited harmonically at its 19th excitation frequency at x=1.68m, with an amplitude of 30N (0-peak) then the contribution of mode 19 in the span motion is characterized by an amplitude $A_{19} = 0.007m$ and a phase lag $\phi_{19} = \frac{\pi}{2}$. The contributions of all other vibration modes under these conditions is far less important: e.g. $A_1 = 3.2 * 10^{-6} m$, $A_{18} = 3.71 * 10^{-4} m$, $A_{20} = 3.51 * 10^{-4} m$ with respective phase lags of -0.02, -2.9 and 3 degrees. The value of coefficient c may be changed, to introduce a different amount of damping. When c tends to zero, A_{19} tends to an infinite value. Considering c=0.01 and 0.1 the amplitude of the nineteenth mode equals respectively 0.7 and 0.07m respectively.

Self-damping computed via integration

The energy dissipated within the span per vibration cycle ($W_d[J]$) can be expressed as follows:

$$W_d = \int_0^L \oint f_d \, dy dx \tag{6.30}$$

The value of the previous integral can be computed once the damping force f_d is known. In the present case, it is worth:

$$f_d = c\frac{\partial y}{\partial t} \tag{6.31}$$

The energy loss per cycle in the span therefore amounts to

$$W_d = \int_0^L \int_0^{2\pi/\omega} c(\frac{\partial y}{\partial t})^2 dtdx \tag{6.32}$$

In the previous subsection, it has been shown that when the cable is excited at its kth eigen frequency and its motion decomposed according to its eigen mode shapes, the contribution of the kth mode shape was by far the most important. In a trial to estimate the self damping power in the cable, the motion will be approximated by:

$$y(x,t) = A_k Y_k(x)\sin(\omega t + \phi_k) \tag{6.33}$$

Since $\phi_k = \pi/2$, the previous relationship can be simplified:

$$y(x,t) = A_k Y_k(x)\cos(\omega t) \tag{6.34}$$

The derivative of y with respect to time is equal to

$$\frac{\partial y(x,t)}{\partial t} = -A_k Y_k(x)\omega\sin(\omega t) \tag{6.35}$$

Introducing the expression of $\frac{\partial y(x,t)}{\partial t}$ into 6.31 and assuming that $Y_k(x) = \sin(\frac{k\pi x}{L})$, one obtains

$$W_d = \int_0^L \int_0^{2\pi/\omega} c\omega^2 A_k^2 \sin^2(\frac{k\pi x}{L})\sin^2(\omega t)dtdx \tag{6.36}$$

Recalling that $\sin^2(a) = \frac{1-\cos 2a}{2}$, the previous integral gives

$$W_d = \frac{c\omega^2 A_k^2 \frac{2\pi}{\omega} L}{4} = \frac{\pi c\omega A_k^2 L}{2} \tag{6.37}$$

The power dissipated by the span is obtained multiplying W_d by the frequency.

Self-damping computed via ISWR

Several experimental methods exist to deduce the self-damping of a conductor [25]. Those have been described in the first chapter (Chapter 1, State of the Art). In the present section, the ISWR (Inverse Standing Wave Ratio) is used for a comparison with the result of the integration method. Its application requires the amplitudes of vibration at some nodes to be measured as well as an amplitude at an antinode. The method is derived from the work of Tompkins et al [85] and is based on principle that if there were no dissipation within the cable no motion at nodes would occur (because incident and reflecting waves are equal). The motion which occurs at vibration"nodes" hence reflects the damping within the conductor. Further explanation and all equations required to apply this method can be found in chapter 1 (section 1.10.3, equations 1.19-1.22).

Comparison of the self-damping computed via integration versus applying the ISWR method

Let us consider a span with the following characteristics:

- length of 63.5m,
- mass per unit length of 1.369 kg/m,
- tension of 31000N (26.5% RTS),
- harmonic excitation located at x=5m (amplitude of 43N and frequency equal to the nineteenth eigen frequency of the span),

The modal resolution of the constant tension problem leads to non-zero steadily decreasing amplitudes (as one moves away from the location of the excitation). This fact is illustrated in figure 6.4 for a constant c equal to 0.41. The corresponding value of the self damping coefficient ζ is 0.001 (see [25], formula 2.3-16)

The self damping power of the span can be computed using the two methods presented above (via Integration and via the ISWR method). The results are shown in figure 6.5, as well as the single antinode amplitude for different values of c. One can see that both methods lead to similar results. As the viscous damping coefficient c increases, the power dissipated by the span decreases. This result can be explained by the dependence of the energy dissipated per cycle as the square of antinode amplitudes. Any increase in the value of c will lead to lower antinode amplitudes and therefore lower dissipated power.

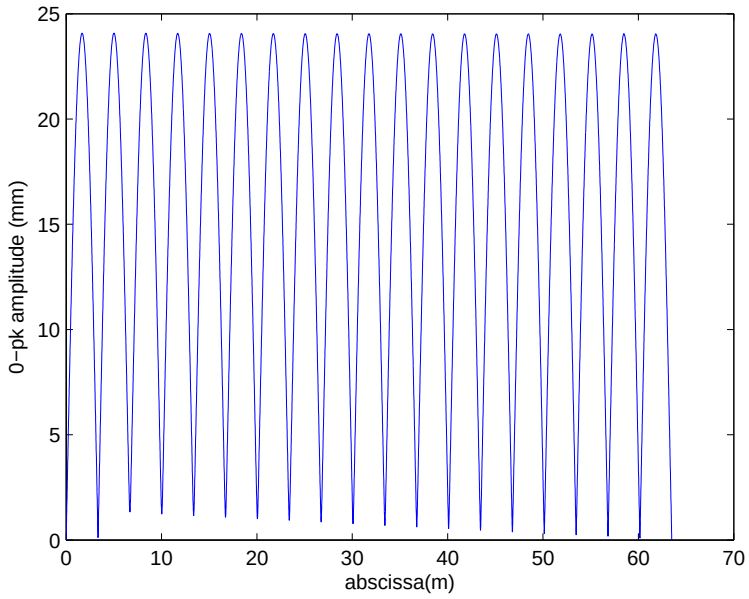

Figure 6.4: Evolution of the zero-to-peak amplitude along the span for a viscous damping coefficient (c) equal to 0.4 and an amplitude of the excitation force of 43N (0-peak)

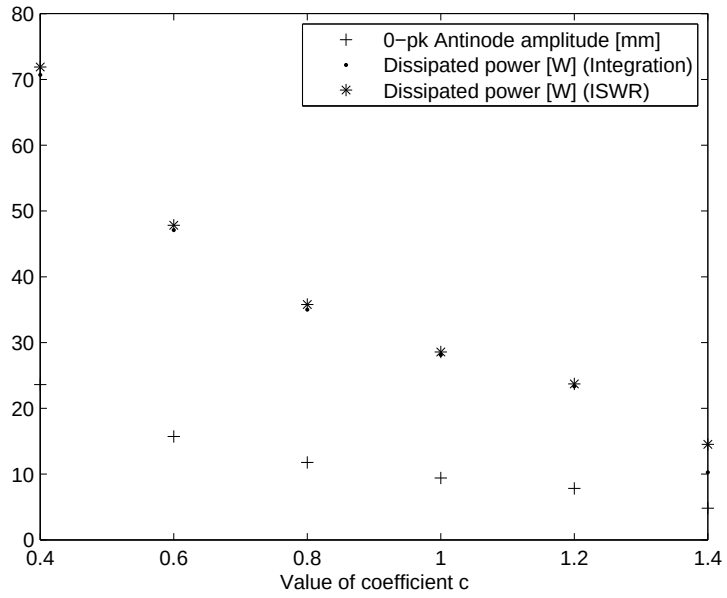

Figure 6.5: Evolution of the power dissipated by the span and single amplitude as the viscous damping coefficient c varies

6.5.2 Resolution of the variable tension problem

Introduction

As demonstrated in chapter 3, the effect of the conductor variable bending stiffness on the computed vibration shape is mostly concentrated near the fixtures, where the motion is hindered. No significant difference is to be expected at computed antinode amplitudes. This has been easily and duly confirmed by some simulations. The constant tension problem has been investigated using the string equation. For the sake of simplicity, the effect of changes in tension on the variable tension problem has been investigated using a cable finite element of the span. This also offers two advantages: the computation time is reduced and the comparison is performed under very similar conditions but non linearity.

Model and Computation strategy

As in chapter 3, a time resolution of the problem has been performed. The same finite element software is used (Samcef), with cable elements. Mesh refinement is introduced wherever and whenever needed:

- The slope of the vibrating conductor is maximum near vibration "nodes". A refined mesh is required to adequately estimate the amplitudes in these areas. Accordingly, the maximum element length used at the latter location is 10mm.

- The slope of the conductor near a vibration antinode is minimum. It seems useless to introduce mesh refinement in those areas. Given the excitation frequency (about 20Hz) and the corresponding wavelength (about 3m), a minimum element size of about 20cm is used.

The simulations are performed with a very small time step (of the order of 0.001s) during the first half second of dynamic simulation to ensure convergence. Afterwards, an automatic time-step is allowed. Its value is of the order of 0.005s, which is compatible with the excitation frequency of the order of 20Hz. As in chapter 5, the integration scheme is chosen in order not to introduce any numerical damping (Newmark trapezoidal rule with adequate integration parameter values).

Some viscous damping has been introduced in the model. To be more precise, this proportional damping has been introduced via a mass matrix coefficient. Since the latter matrix is constant, the equivalent viscous coefficient is constant too. A more complex model, able to cope with the variable bending stiffness and self damping properties will be presented in chapter 7.

Miscellaneous simulation results

Here is an illustration of some results, obtained under the following simulation conditions:

- excitation force of 30N (0-peak),
- excitation frequency of 20.98Hz (this value has been tuned with a parametric study so as to obtain maximum vibration amplitudes),
- span length equal to 63.5m,
- mass proportional damping coefficient equal to 0.1. This value was chosen for it leads to realistic amplitudes of vibrations (referring to the tests performed on Ireq's laboratory test span).

The evolution of the antinode amplitude during one minute is shown in figure 6.6. One can clearly see a transient in the establishment of the motion. At the end of one minute, the antinode amplitude still shows beats, but with a rather stable average zero-to-peak amplitude value, of the order of 5mm (0-peak). Given this result in the one hand and the considerable amount of data produced by such a simulation on the other hand, it was decided to base the analysis on data collected at the end of this one minute simulation (with corresponding time abscissae >40 seconds).

At each vibration cycle, the excitation force introduces some energy in the span. Its work can be visualised in a Lissajous curve, where the excitation force is plotted as a function of the cable position at the location of the excitation (see figure 6.7). The phase shift between the two signals continually varies around 90°. As an example, during the short time interval corresponding to figure 6.7, it is worth about 90.25°.

Because of the continual tension fluctuations, it is believed that the vibration nodes keep travelling during the simulation. Without any damping introduced in the model, both the location and magnitude of minimum amplitudes continually vary (see figure 6.8). The average amplitudes at vibration nodes 2 and 1 [3] are about 220 μm and 160 μm. Without damping, one can say that the "nodes" travel on a distance equal to a few centimetres along the span. When some damping is introduced in the model, the "nodes" still travel, but on a shorter distance and the amplitudes still vary, but in a lesser extent (see figure 6.9). The corresponding proportional mass damping coefficient of 0.1, which leads to realistic antinode and "node" amplitude values (e.g. 35 μm and 21 μm at two adjacent vibration nodes near the span end opposed to the excitation force). Such realistic amplitudes lead to a realistic loss factor ζ (defined in chapter 1) of the order of 0.001.

[3] The amplitudes at vibrations "nodes" increase as one goes near the excitation force (see figure 6.4 for example, where the excitation force is located at at an abscissa inferior to 10m). "Node 1" denotes the first vibration mode next to the span end opposed to the vibration shaker (the one with an abscissa of about 60m in figure 6.4)

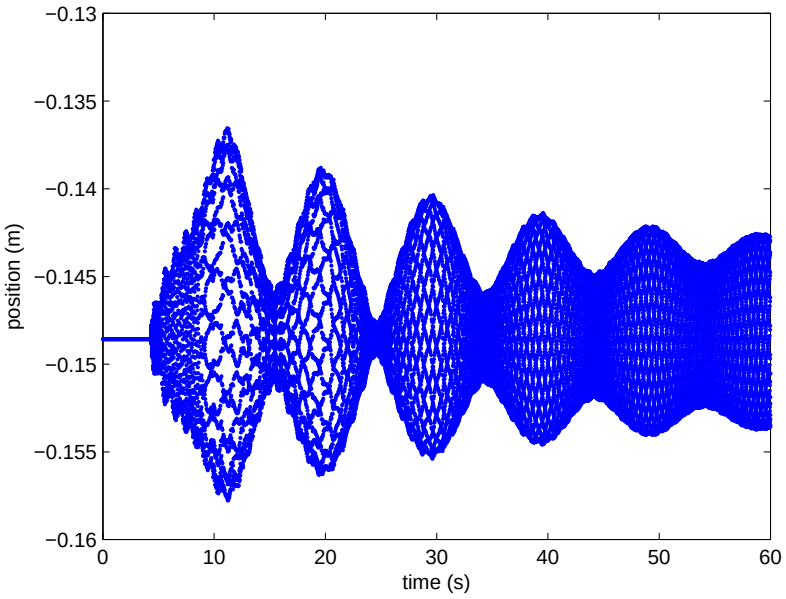

Figure 6.6: Variable tension problem. Time evolution of the antinode position for a mass proportional damping coefficient equal to 0.1, excitation frequency of 20.98Hz

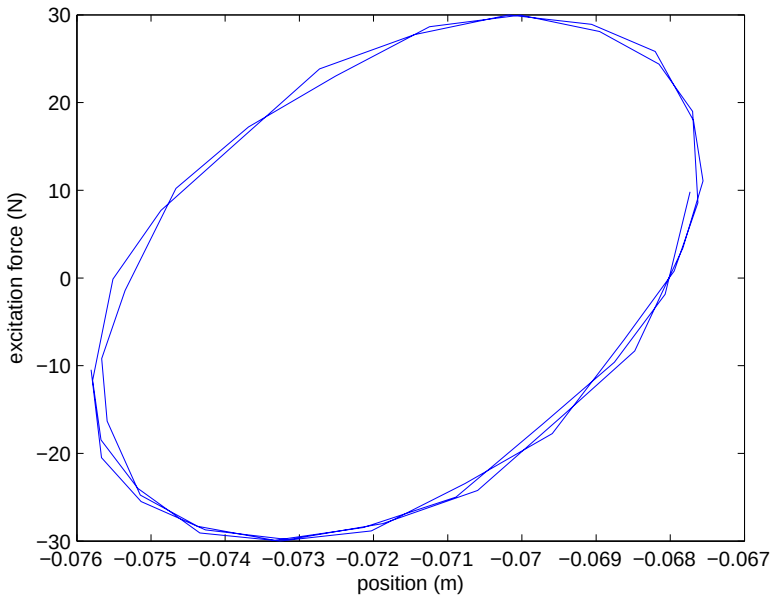

Figure 6.7: Lissajous curve of the excitation force versus cable position at the location of the excitation

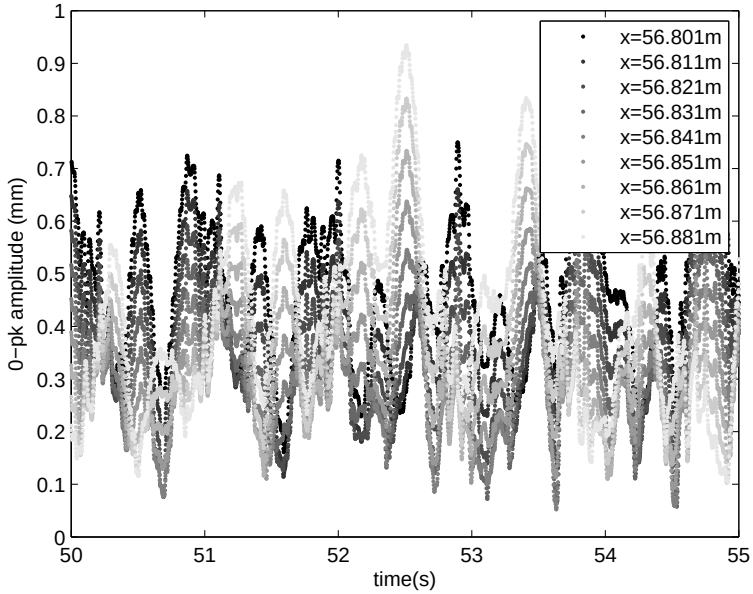

Figure 6.8: Variable tension problem 0-pk amplitude at several locations in the vicinity of the second vibration node without damping

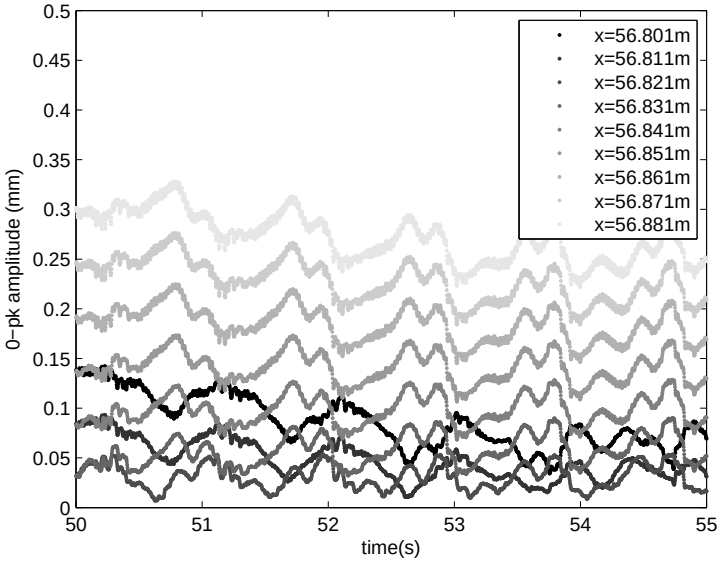

Figure 6.9: Variable tension problem 0-pk amplitude at several locations in the vicinity of the second vibration node with damping (the mass proportional damping coefficient is equal to 0.1)

As could be expected, a frequency content analysis of the displacement at vibration nodes shows that the main contribution (21.09Hz) is very near the excitation frequency (20.98Hz) (see figure 6.10).

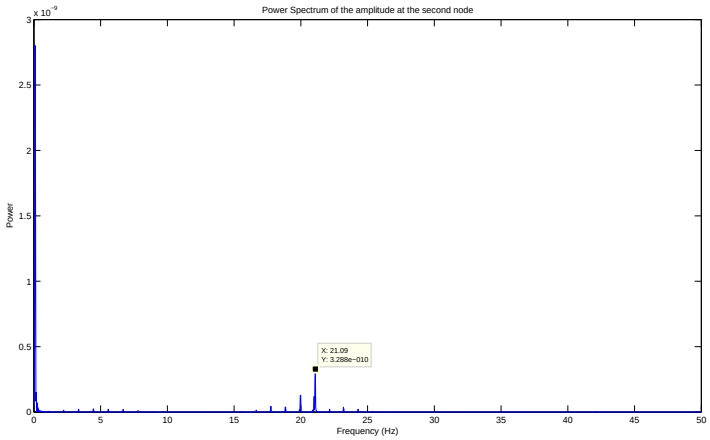

Figure 6.10: Variable tension problem. Frequency content of the antinode amplitude of vibration for a mass proportional damping coefficient equal to 0.1, excitation frequency of 20.98Hz. If X is the discrete fourier transform of the amplitude signal, the vertical axis shows $(\frac{|X_k|}{N})^2$.

A zoom on the frequency range comprised between 30 and 50Hz shows a second peak at twice the excitation frequency (42.18Hz, see figure 6.11). The presence of the latter can probably be explained by the influence of tension fluctuations. Note that in the validation part of this thesis (part III), some analyses of unfiltered data recorded at vibration nodes on a laboratory test bench show similar frequency peaks at twice the excitation frequency. Several smaller peaks separated by a frequency shift of 1.04Hz can also be noted. Since the fundamental frequency of the span is equal to 1.18Hz, it is plausible that these peaks are not numerical artefacts but have a physical origin.

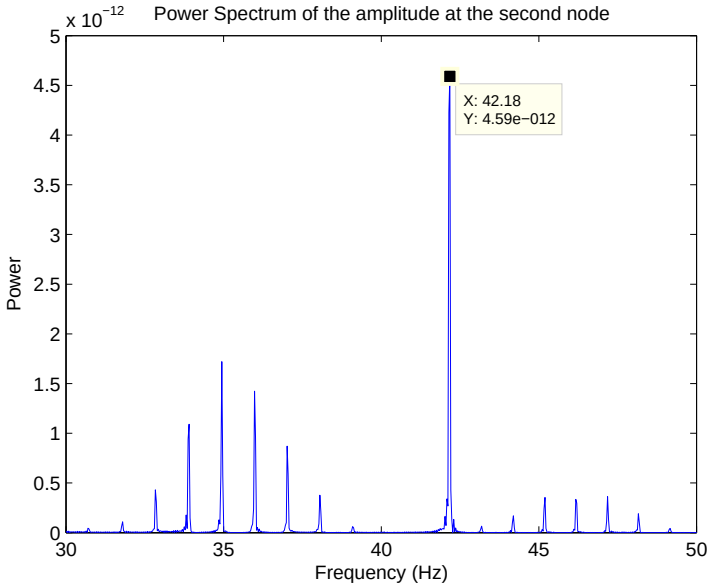

Figure 6.11: Zoom on the 30-50Hz range of the data shown in figure 6.10. Variable tension problem. Frequency content of the antinode amplitude of vibration for a mass proportional damping coefficient equal to 0.1, excitation frequency of 20.98Hz. If X is the discrete fourier transform of the amplitude signal, the vertical axis shows $(\frac{|X_k|}{N})^2$.

Table 6.2: Comparisons of the variable constant tension problem "without damping" versus reality

	Reality 1	Reality 2	T variable
Frequency [Hz]	20.4	20.4	20.9
0-pk excitation force [N]	13.2	40.7	26.4
0-pk antin. ampl. [mm]	3.92	7.84	5-10
0-pk ampl. at node 1 [μm]	31.51	93.21	≈ 160
0-pk ampl. at node 2 [μm]	24.18	81.04	≈ 220
0-pk ampl. at node 3 [μm]	38.54	111.38	
0-pk ampl. at node 14 [μm]	124.57	361.98	
ζ	0.0005-0.0015	0.0008-0.0015	
Elements size	not applicable	not applicable	1cm

6.5.3 Comparison of the variable tension problem without damping versus reality

In reality, it is of course impossible to suppress damping. This first comparison therefore aims at "identifying" and "qualifying" the damping effect of the conductor non-linearities. Some results of the variable tension problem without damping are illustrated in chapter 5. In those simulations, the conductor average bending stiffness is supposed constant and equal to the value deduced experimentally on Ireq's test-span (about 50% EI_{max}). Important difficulties have been faced while trying to "tune" a resonance without damping. Nevertheless, some resonance conditions have been approached. They correspond to the following experimental case: the tension in conductor Crow is about 25% RTS, the excitation frequency is worth about 20Hz and the excitation force is equal to 26.4 N (0-peak) (the conductor properties as well as the description of the test-span are supplied in chapter 5). The excitation frequency has then been adjusted to approach resonance conditions. In figures 5.4, 5.7 and 5.8, one can see that a variable antinode vibration amplitude is obtained, which amplitude varies between (about) 5-10mm 0-pk.

The amplitudes computed with the variable tension problem can be compared to what has been measured on Ireq's test-bench, under similar conditions but damping. The result is shown in table 6.2.

Even "without damping", the antinode amplitudes computed with the variable tension problem are similar to those measured on the laboratory test bench. Given the integration scheme is chosen in order to avoid artificial damping, this may mean that the damping effect of non linearities is very important.

The amplitudes measured in reality at the first "node" are not consistent with the ones measured at "node" 2: as can be seen in figure 6.4, "node" amplitudes should increase as the distance to the excitation force decreases

(which is the case for nodes 2, 3 and 14 in table 6.2). The amplitude at the second vibration "node" should be higher than at the first "node" one. Among the elements which could influence this anomaly:

- only the minimum amplitude value was kept in the records during the tests, and it often occurred that the amplitude at the vibration node varied (see also chapter 9),
- the measurement of each "node" requires some time (e.g. a few minutes each) to accurately locate the node, follow the time evolution of amplitude (to find its minimum value), etc.. Since the measurements are not simultaneous, some small differences in the corresponding test conditions may exist.

Can an equivalent self-damping coefficient be computed via the ISWR method for the variable tension problem without damping? According to this method, the difference in amplitudes between incident and reflected waves is an image of the power dissipation which takes place along the span. This method implicitly supposes that the wavelength of incident and reflecting waves are equal which is obviously not the case with the variable tension problem. Continual changes in tension will cause a continual change in wavelength. The conditions to apply the ISWR method are infringed. As an example, computing an equivalent value of the self-damping coefficient ζ from the simulations results of the variable tension model without damping, one obtains $\zeta \approx 0.4\%$. As will be seen in the next section, this value is higher than the self damping coefficient of the variable tension model where the mass proportional damping coefficient is taken equal to 0.1.! This result does not make sense.

Due to some memory limitations, it was not possible to perform computations with more than 1000 elements with the variable tension problem. The length of the mesh elements is worth about 1cm in the vicinity of vibration nodes and about 10cm elsewhere. In such conditions, the tuning of the excitation frequency can not be as fine as one would wish. As an example, for the present test conditions, a change of 0.1 in the eigen frequency corresponds to a change in the wavelength of the order of 5cm. The tuning of the excitation frequency with an finer accuracy than 0.1Hz is therefore illusory. A finer tuning of the excitation frequency could have led to different amplitudes of vibrations. It is nevertheless interesting to note that during the tests performed at Ireq in 2008, the resolution in the tuning of the excitation frequency was also limited to 0.1 Hz.

6.5.4 Comparison of the variable and constant tension problems without damping

Comparing the variable and constant tension problems without damping, a first difference can be seen in the phase lag between the excitation force and the cable position. In the constant tension problem (see equations 6.27 and 6.28) this value is constant. In the variable tension problem, the Lissajous curve of excitation versus cable position over several vibration periods shows a continually fluctuating phase.

Then, the amplitudes at antinodes fluctuate between about 5 and 10mm (0-pk) in the variable tension problem but tend towards an infinite value for the constant tension problem. In other words, the effect of the variable tension is similar to the introduction of some artificial damping. Figure 6.12 shows the amplitudes at the first two vibration nodes in the variable tension problem.

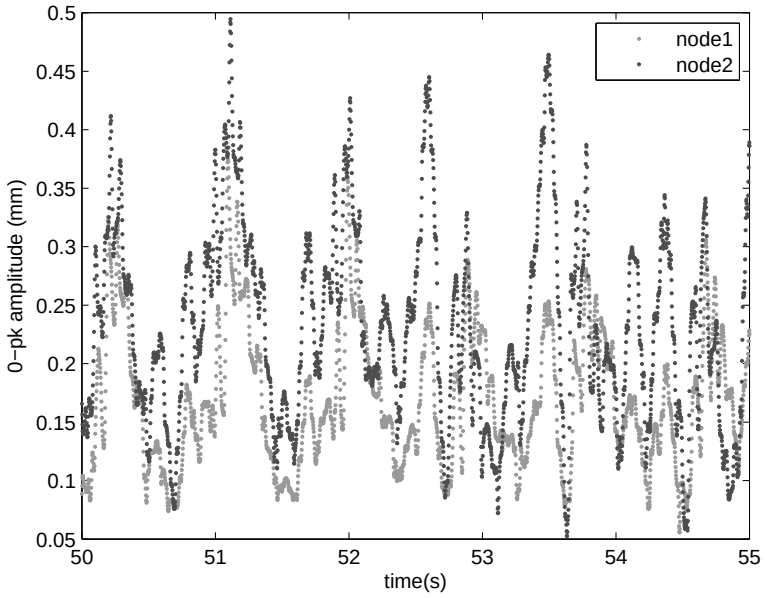

Figure 6.12: Variable tension problem- Time evolution of the amplitudes at the first two vibration nodes

Table 6.3: Comparisons of the variable and constant tension problems versus reality

	Reality 1	Reality 2	T Constant	T variable
Frequency [Hz]	20.4	20.4	22.5	20.98
ζ	0.0005-0.0015	0.0008-0.0015	0.001	0.0009
0-pk antin. ampl. [mm]	3.92	7.84	16.65	5
0-pk ampl., node 1 [μm]	31.51	93.21	52	21
0-pk ampl., node 2 [μm]	24.18	81.04	106	35
Injected power [W]	N.A.	N.A.	35.3	9
0-pk excitation force [N]	13.2	40.67	30	30
Elements size	not applicable	not applicable	1mm	1cm

6.5.5 Comparison of the variable and constant tension problems versus reality when damping is introduced

Data recorded on Ireq's cable test bench has been used as a reference for "reality" (the description of the test set-up can be found in chapter 2). Let us consider in particular the following case:

- Crow ACSR conductor with a tension equal to 25 % RTS,
- excitation frequency of 20.4 Hz.

Simulations under similar loss factor values have been performed with the constant and variable tension problems. The results are summarized table 6.3.

Analysing the results of table 6.3, the antinode amplitudes computed with the variable tension model agree better with reality than those deduced from the constant tension problem. To be more precise, the amplitudes computed with the constant tension are 2 to 3 times higher than real ones.

6.6 Conclusions

As a conductor vibrates, for example due to the presence of Aeolian vibrations, its length will vary and tension fluctuations will occur.

The analysis performed in this chapter shows that changes in tension computed from Hooke's law, using different approaches, are consistent with those obtained with the finite element model of the span.

Comparing the results of a constant versus variable tension model, it has been shown that non linearities obviously have an impact on vibration amplitudes (an undamped non-linear model leads to finite amplitudes of vibration near resonance while these amplitudes tend towards infinity for an undamped linear model). This influence probably comes from the interac-

tions between vertical and longitudinal motion. Changes in tension have an effect similar to the introduction of some artificial damping.

In section 6.4, several objective reasons are exposed which make believe that changes in tension in real spans could be inferior to those met on laboratory spans, even if similar vibration levels are considered. In reality, one will often find a succession of suspension spans (called a section), with a very low extensional stiffness. Also, unlike in laboratory test spans, the rigidity of real span ends cannot be neglected, leading to lower extensional stiffness values and lower changes in tension, all other things being equal.

It is a common practice nowadays to study the vibrational answer of average to long spans using self damping power laws deduced from tests performed on laboratory spans which length is of the order of a few tens of meters. The discussion highlights the need to check those changes in tension and to limit their potential impact on measurements. To do this, several kinds of solutions can be considered:

- Performing adequate non linear simulations may be of some help in separating the contribution of self damping due to non linearities versus conductor intrinsic self damping.

- As shown in chapter 5 and in the present chapter, changes in tension are characterized by a frequency equal to twice the vibration frequency. In the case of Ireq's laboratory, the displacements measured at vibration "nodes" are systematically processed through a passband filter with the middle of its range equal to the excitation frequency. This measure probably aims at limiting the impact of changes in tension on measurements.

- Another solution undoubtedly is to perform on-site self-damping measurements. Measurements on real spans permit to include all effects (e.g. span ends) and to avoid corrections for unwanted phenomena (e.g. "experimental" tension fluctuations different from real ones).

Chapter 7

Modelling conductor self-damping and bending stiffness

7.1 Introduction

Investigations to assess conductor self damping properties are generally carried out on laboratory test benches which length is of the order of a few tens of meters. The tests are carried out dynamically, using one of the self damping measurement methods described in chapter 1. Most of the time, the Inverse Standing Wave Ratio Method (ISWR) is used [1]. The outputs of these tests (expressed via the "power law") have been extensively discussed in chapter 3 and in particular the important discrepancies which exist between results provided by different authors. In the frame of this chapter, the focus will be drawn not only to the development of some realistic self damping model but also to potential improvements or facilitations to self damping measurement. Indeed, there are several reasons which make such conventional laboratory self damping tests somehow complicated:

- Because the amounts of self damping involved in a cable are so small, their measurement is a challenging task and requires very specific equipment, (using the ISWR method, "node" amplitudes of a few tens of micrometers have to be measured. With the Decay method, the excitation system must be disconnected from the vibrating cable without influencing the existing motion: as an example, any shock during the release may "pollute" the vibrating signal, et.),
- Self damping studies are expensive,

[1] This method is based on the hypothesis that when no damping is present, incident and reflected waves are equal. It therefore supposes that the motion of the vibration "nodes" is an image of the self damping which takes place within a conductor

- According to the previous chapter, higher tension fluctuations may be expected on a laboratory span than on a real span. In case the ISWR method is used, if no remedial measured is taken to limit their action, the changes in tension may have an impact on the measured "node" amplitudes and hence on the deduced self damping power.

The present chapter investigates the possibility of deducing power line conductor self damping properties from a series of tests performed on a short pre stressed conductor sample. Data recorded by Godinas [28] on 4m long pre-stressed conductor samples is used as an input. A formulation for the self damping per unit length is proposed as a function of the antinode amplitude of vibration, frequency, conductor tension, bending stiffness, mass per unit length plus a special parameter called β. The latter parameter has the dimension of an energy [J]. The present chapter also proposes :

- a comparison of the self damping power computed with this new formula versus the power law. It highlights a good agreement, in particular with Noiseux's exponents [62, 25].

- to use a viscoelastic model to take into account both the self damping behaviour and the variable bending stiffness of a conductor measured experimentally. Section 7.7 shows how the parameters of this model can be deduced from experimental data,

- a comparison of the "dynamic" variable bending stiffness deduced from the present research with the one computed using K. Papailiou's model [65, 64],

- a new method to deduce the self damping (and variable bending stiffness properties) of a conductor, which is far easier to apply than other conventional methods.

- a discussion of the results of chapter 3 "Self-damping evaluated in actual conditions", in light of the present new developments.

The interested reader will find a short state of the art on self damping in mechanical systems in appendix F (review of material damping, structural damping, etc.).

7.2 Relationship between curvature and moment versus conductor bending stiffness

In the flexure theory developed by Navier, the bending moment is proportional to the curvature ($\chi(x) = \frac{\partial^2 y(x)}{\partial x^2}$) and the proportionality coefficient between them is constant and equal to the bending stiffness EI (product of

Young's modulus by the area moment of inertia of the cross section). This theory is valid for an elastic structure and if the plane sections remain plane after flexure (Bernoulli's assumption).

$$M(x) = EI\chi(x) \tag{7.1}$$

In the literature, a maximum bending stiffness value is computed assuming that all wires act together as a solid [25]. This maximum bending stiffness is given by the product of the area moment of inertia of the section's wires (taking into account their distance to the neutral axis) by their Young's modulus of elasticity:

$$EI_c = \Sigma_{i=1}^{n_{wires}} E_i(I_{0i} + A_i d_i^2) \tag{7.2}$$

In the previous formula, I_{0i} is the area moment of inertia of an individual wire related to its own axis, A_i is the wire section, n_{wires} the number of wires and d_i the distance between the wire's axis and the bending's neutral axis. In [25], the latter distance is defined as a function of:

- r_i, the radius of a circle which centre is the conductor axis and which circumference contains the axes of the wires of the i_{th} layer
- α_i, the angle between the flexure neutral axis and an axis which passes by the conductor centre and the centre of the i_{th} wire, giving

$$d_i = r_i * \sin(\alpha_i)$$

A lower bound for this bending stiffness value is computed assuming that all wires act independently:

$$EI_c = \Sigma_{i=1}^{n_{wires}} E_i I_{0i} \tag{7.3}$$

Due to the bending of the cable, important stress differences exist between the concave and convex sides. Since the cable is made up of helically applied strands, the axial stress within one strand will also vary. The latter variation in turn creates friction forces between the different layers, which depend on the friction coefficient and the contact pressure. As explained by Godinas or Papailiou [28, 65, 64], in the case of cables, if the bending becomes large enough, the wires begin to slip against each other. From the moment when slipping occurs, the curvature is proportional not only to conductor curvature, but also to the tension force and the friction coefficient between the wires. The standard version of Navier's theory is no more applicable. Some authors, like K. Papailiou, have circumvented the fact Navier's law is not applicable when the wires begin to slip by introducing a dynamic bending stiffness [65, 64].

7.3 The Available data collected by Godinas

7.3.1 Presentation of the experiments

Between 1994 and 1999, in the frame of ARC convention 94/99-176, research was carried out in the field of cable damping at University of Liège. Experimental measurements of bending and damping properties of conductors were made by A. Godinas on 4 meter long cable samples. As described in [28], two aluminium alloy conductors were tested:

- AMS 621 (section $620.9mm^2$, 61 wires, $1.765kg/m$, conductor diameter $32.4mm$, wire diameter $3.6mm$, RTS 199950N, Young's modulus 54000 N/mm^2),
- AMS 298 (section $297.57mm^2$, 37 wires, $0.841kg/m$, wire diameter $3.2mm$, conductor diameter $22.4mm$, RTS 95850N, Young's modulus 56000 N/mm^2),

A complete description of the test set-up can be found in [28]. The cable samples were fixed on a rigid test frame and pre-stressed at different tension values. The tension ranges are not explicitly mentioned in [28] but in the *Experimental Results* section of the paper, one can see two test curves for AMS 621, respectively at 2.5% RTS and 17.5% RTS. More test curves are published in [27], some of which are shown in appendix A. They correspond respectively to tension values ranging from 2.5 to 10% RTS for AMS 621 and from 5 to 31 % RTS for AMS 228. In real life, conductors are generally strung between 15 and 30 % RTS. The tension range studied by Godinas certainly overlaps the latter interval for AMS 298. For AMS 621, one may infer that at least the lower range of realistic values was covered. During the tests, the cable motion took place in a horizontal plane. A coupling sleeve (which length is a=50mm and which is denoted *anchoring clip* in figure 7.1) is rigidly fixed on the conductor at mid length and a roller bearing is attached to it (see figure 7.1). A bending moment is applied at that location by means of a motor and the resulting bending rotation φ is measured (see figure 7.2).

7.3.2 Moment versus rotation angle curves

Having noticed that the moment versus rotation angle curve follows an asymptote for high values of φ, in [28], Godinas proposed to fit the moment versus rotation angle curve with the following equation:

$$M = \alpha N^{1/2}\varphi + \beta N^{1/2-\delta}[1 - \exp(-\gamma N^{\delta}\varphi)] \tag{7.4}$$

In the case of conductor AMS 621, the different coefficients proposed are :

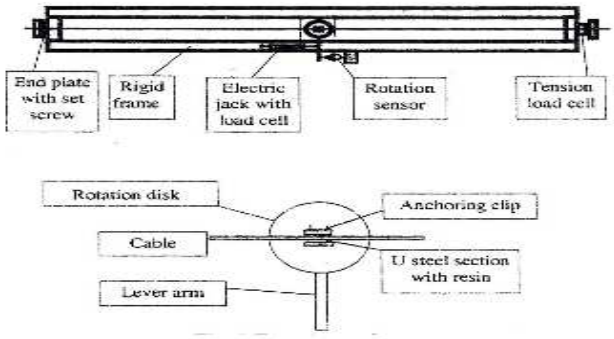

Figure 7.1: Experimental test set-up used by A. Godinas

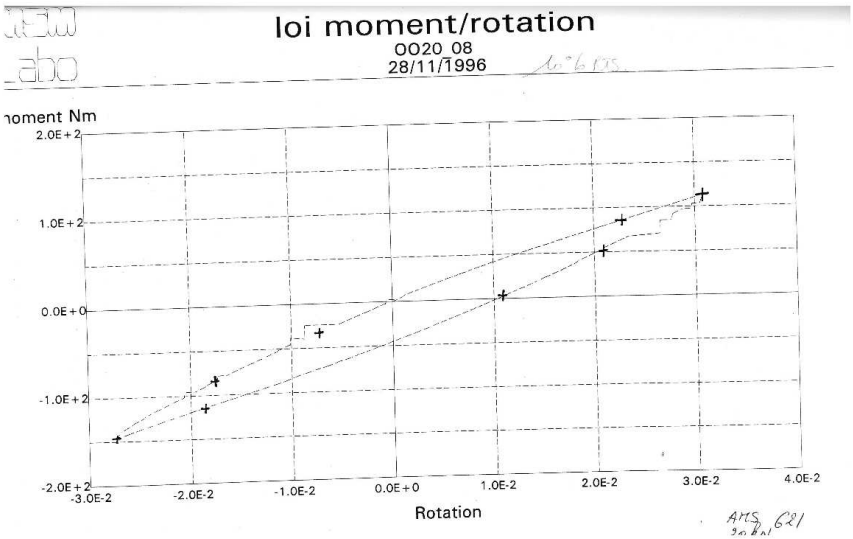

Figure 7.2: AMS 621, total moment versus rotation angle measured for a tension equal to 10%RTS

- $\alpha = 24$,
- $\beta = 5$,
- $\gamma = 5.8$,
- $\delta = 0.25$.

Note that equation 7.4 is written for a minimum rotation angle equal to zero and for a loading curve (as opposed to unloading). In case the minimum rotation angle is different from zero or in case of reverse loading , the axes and their origin need to be updated.

During his experiments, Godinas also noticed that the shape of the moment versus rotation angle curves was not influenced by the loading speed [28]. As a direct consequence, the experiment can be performed with the load being applied almost "statically".

Figure 7.3 illustrates the fit for conductor AMS621 at a tension of 10% RTS when the rotation angle varies between -0.03 and 0.03 radians. A good agreement with the curve measured experimentally is obtained (see figure 7.2).

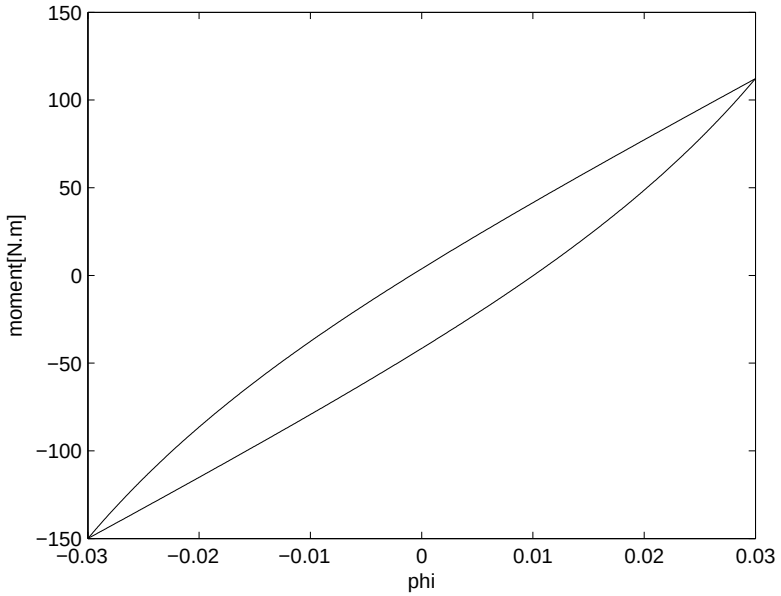

Figure 7.3: AMS 621, moment versus rotation angle curve computed from equation (7.4) for a tension equal to 10%RTS

7.4 Modelling strategy

7.4.1 Introduction

Here is the transition point between the description of the data collected by another author (Godinas) and the personal exploitation of the same data, performed in the frame of this thesis (from section 7.4 on).

The option followed to model the variable bending stiffness and self-damping properties of a conductor is to work with a beam finite element, where the relationship between "resultant efforts" and strains has been customized.

The "resultant efforts" are:

$$\begin{pmatrix} N \\ T_y \\ T_z \\ M_x \\ M_y \\ M_z \end{pmatrix}$$

and the strains:

$$\begin{pmatrix} \epsilon_x \\ \gamma_y \\ \gamma_z \\ \theta \\ \chi_y \\ \chi_z \end{pmatrix}$$

In particular, it is the relationship between moment and curvature which should be customized in order to reproduce the observed hysteresis curves. To achieve this aim, material damping has been used. To be more precise, the damping and variable bending stiffness have been introduced via a viscoelastic model of material. An introduction to material damping can be found in appendix F, and the main characteristics of the viscoelastic material model are given in the following section. The previous relationships, giving "resultant efforts" as a function of strains in a beam, consider separately M_x and M_y. In the case of an overhead line conductor, there is a rotational symmetry, and the bending stiffness properties remain unchanged if the neutral axis is rotated around a fixed point which is the centre of the section. To handle a situation of combined flexure (both M_x and M_y different from zero), the resulting moment and curvature need to be computed, so that the results do not depend on the reference axes. In the rest of the document, M and χ will represent the resulting moment and curvature.

7.4.2 Viscoelastic model

The visco-elastic model of a material is presented in appendix F. In such a model, the following relationships between stresses and strains are satisfied:

$$\sigma = \varepsilon E + E^*(\frac{d\varepsilon}{dt}) \tag{7.5}$$

The second term introduces some damping in the model via the parameter E^* $[Ns/m^2]$. Indeed, plotting stresses versus strains for a visco-elastic material, hysteresis curves are obtained. This model can be modified so that only the moment versus curvature relationship is damped (other relationships being elastic) giving:

$$M = A\chi + B\frac{d\chi}{dt} \tag{7.6}$$

Assuming

- harmonic bending:

$$\chi = \chi_0 \sin \omega t \tag{7.7}$$

$$\frac{d\chi}{dt} = \chi_0 \omega \cos \omega t \tag{7.8}$$

- A and B time independent

Integrating 7.6 over one period of vibration, the contribution of the first term vanishes, so that the area within the moment versus curvature curve is

$$\oint M d\chi = \oint B\frac{d\chi}{dt}d\chi = \int_0^{\frac{2\pi}{\omega}} B\frac{d\chi}{dt}\frac{d\chi}{dt}dt = \pi\omega B\chi_0^2 \tag{7.9}$$

From 7.6 and 7.9, it can be deduced that parameter A governs the conductor average bending stiffness and parameter B the amount of self damping introduced in the model.

7.5 Deducing moment versus curvature curves from experimental measurements on conductor AMS621

7.5.1 Introduction

According to the strategy developed in section 7.4, moment versus curvature curves need to be deduced. The bridge needs to be built between the

available moment versus rotation angle curves and required information (moment versus curvature curves). This task is not as simple as it might look at first. There are in fact three unknowns : the beam deflected shape, the beam variable bending stiffness and the variable conductor tension. Available data consists in the recorded applied moment, the rotation angle, the topology of the test-span and one equation: the beam equation of motion. The conversion was achieved in a first time by solving with a non linear finite element model the problem of the pre-stressed conductor elements undergoing bending on the 4 meter long test span. This permitted to deduce the conductor curvature and both a variable and average conductor bending stiffness. The finite element model of the span also permitted to check:

- that the moment value which appears in equation 7.4 does coincide with half the moment applied by the actuating system,

- the changes in tension. As an example, the latter amount to less than 0.5% at 20 % RTS. The results confirm that the conductor tension can be assumed constant and equal to the initial pre-stress value of the conductor (before tests start running)

Then the beam equation was solved analytically for the deflected shape of the conductor, providing a relationship between moment and curvature.

For future tests, the quality of the data could be improved by adding the variable conductor tension and the conductor deflected shape to the records.

7.5.2 Finite element model of the test-span

For symmetry reasons, there is no need to model the whole span length. Only half the test-span can be modelled, from one cable extremity to the centre of the rotation disk, but with only half the total moment supplied by the actuating system applied on the conductor.

324 elements have been used to model the 2m long section. The conductor is modelled with beam elements. Their bending stiffness is adjusted until results in agreement with the tests are met. The anchoring clip is modelled by beam elements which stiffness is 50 times higher than the beam maximum bending stiffness value. As boundary conditions,

- the left of the span is anchored (all degrees of freedom are fixed),

- all displacements are fixed at the centre of the rotation disk. So are the rotation around the cable axis (x) and the other in plane perpendicular axis (z). A bending moment M is applied according to the out of plane axis y.

7.5.3 The moment value of equation 7.4

Using equation 7.4, moment versus rotation angle curves can be plotted. Figure 7.5 shows such a curve for conductor AMS621 at a tension of 20 % RTS.

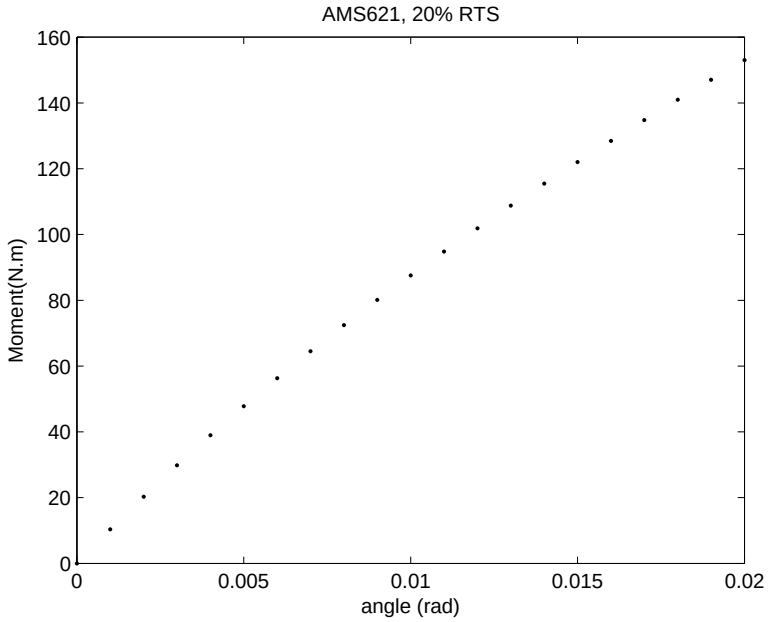

Figure 7.4: AMS 621, moment versus rotation angle computed from 7.4 for conductor AMS621 at a tension equal to 20% RTS

Let us assume in a first time that the M value which appears in 7.4 and in figure 7.5 corresponds to the total moment applied by the actuating system. In the finite element model, then only half this value should be introduced. Under the latter hypothesis, considering realistic amplitudes (for aeolian vibrations), the rotation angle measured experimentally can only be reproduced assuming a beam bending stiffness of the order of 10 to 15 $\%EI_{max}$.

In a second time, let us assume that the M value which appears in 7.4 is worth half the moment applied by the actuating system. In this case, considering amplitudes compatible with aeolian vibrations, the rotation angle measured experimentally can be reproduced assuming a beam bending stiffness ranging from 50 to 70 $\%EI_{max}$. Assuming a constant bending stiffness equal to 60 % EI_{max}, the amplitudes can be adequately estimated (with an error inferior or equal to 10 %) over the following realistic range of rotation angles: from 0.001 to 0.01.

As a comparison:

- the variable bending stiffness which can be deduced from K. Papailiou's model [65, 64] for conductor AMS621 (on the rotation angle range and hence curvature of aeolian vibrations) ranges between $50\% EI_{max}$ and EI_{max} for a friction coefficient equal to 0.5, or between $30\% EI_{max}$ and EI_{max} if the friction coefficient is equal to 0.2 (see figure 7.13).

- the average bending stiffness of ACSR Crow deduced experimentally on Ireq test span is worth 50% EI_{max} (see chapter 8),

- the average bending stiffness published in the literature is also of the order of 50% EI_{max},

It follows from the above that the first hypothesis should be rejected. It can be deduced that the M symbol which appears in 7.4 is equal to half the bending moment exerted by the actuating system and its values should be introduced as is in the model of half the test span.

7.5.4 How is the conductor tension affected by the tests?

The change in tension is of course maximum at the highest amplitudes of vibration. In the previous paragraph, it has been shown that the bending stiffness deduced from the tests was about 50% EI_{max} at the highest curvatures values. These maximum curvatures are met for $fy_{max} \approx 200mm/s$ and at the highest vibration frequencies. An upper limit to the maximum curvature is 0.1 m^{-1}. Let us consider conductor AMS621 at a tension of 20 % RTS. With this hypothesis, in Godinas's device, the maximum curvature value corresponds to a rotation angle of about 0.015 radians.

Introducing an adequate beam bending stiffness value in Samcef's finite element model (50 % EI_{max}), applying the required pre-stress value and exerting a moment equal to 115.5 N.m at the centre of centre of the rotation disk, a rotation angle of 0.014 radians is obtained. This result is in agreement with equation 7.4. The corresponding change in tension can be checked: it is worth less than 0.5 %. The change in tension would be inferior to that value for any other amplitude of aeolian vibration. It may be concluded from this investigation that the hypothesis of constant tension is reasonable.

7.5.5 From rotation angle to curvature

Referring to dimensional analysis, the conductor rotation angle may be seen as a dependent variable, which may be expressed as a function of the following independent variables: conductor tension N [N], conductor Young's modulus of elasticity E $[N/m^2]$, the area moment of inertia I $[m^4]$ and the curvature [1/m]. The relationship has therefore the form $\varphi = f(N, E, I, \chi)$ or $\varphi = \xi N^{a1} E^{a2} I^{a3} \chi^{a4}$, where $[\xi]$=1. The dimensional homogeneity requires

that

$$a1 + a2 = 0 \tag{7.10}$$

$$a1 - a2 + 4a3 - a4 = 0 \tag{7.11}$$

Assuming $a2 = a3$ and $a4 = 1$ (which is compatible with field experience and data), one obtains:

$$\varphi = \xi\sqrt{\frac{EI}{N}}\chi \tag{7.12}$$

The coefficient ξ was found solving analytically the problem of the pre-stressed beam, assuming that the cable of Godinas's set-up behaved like a beam of average bending stiffness equal to 60% EI_{max} (see previous section). Let us denote *extremity 1* one of the span end (e.g. the left one), and *extremity 2* the location where the conductor emerges from the coupling sleeve, on the same half span, (in this case, the left one). All these locations can be visualized in figure 7.1. Let a be the total length of the anchoring clip (see figure 7.1). The differential equation which characterizes the test span can be written:

$$EI\frac{\partial^4 y}{\partial x^4} - N\frac{\partial^2 y}{\partial x^2} = 0 \tag{7.13}$$

with the following boundary conditions:

$$y(extremity1) = \frac{\partial y}{\partial x}(extremity1) = 0 \tag{7.14}$$

$$y(extremity2) = -\frac{a}{2}\sin(\varphi) \tag{7.15}$$

$$\frac{\partial y}{\partial x}(extremity2) = \varphi \tag{7.16}$$

Note that $extremity2$ is the left side of the coupling sleeve. Solving the previous equation permits to obtain the shape of the cable in the vicinity of the left hand side of the coupling sleeve, which in turn permits to estimate the first and second derivatives of the shape, which correspond respectively to the rotation angle φ and the curvature χ. Introducing this information in (7.12) permits to deduce the value of coefficient ξ. It results that under the assumptions made, ξ is worth approximately 0.9.

As an illustration, figures 7.5 and 7.6 show the deflected shape and the curvature of the conductor obtained at a tension equal to 25 % RTS when the bending stiffness is equal to 50% EI_{max} and a rotation angle of 0.01 radians is imposed at the coupling sleeve.

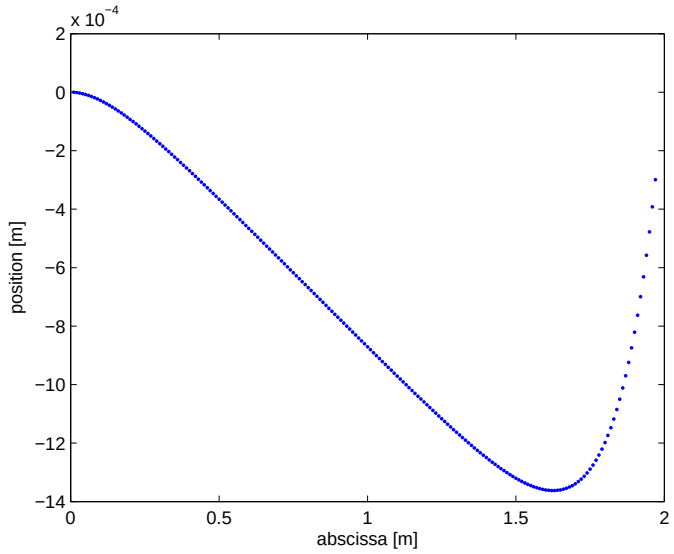

Figure 7.5: AMS 621 deflected shape obtained for a tension equal to 25 % RTS, when a rotation angle of 0.01 radians is imposed at the coupling sleeve

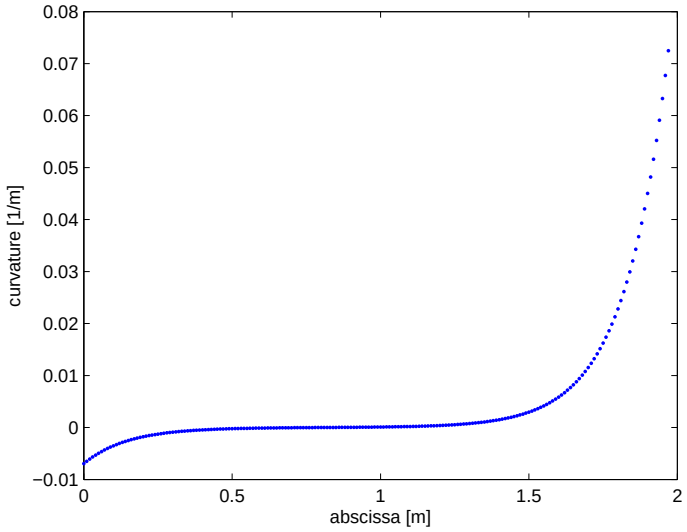

Figure 7.6: AMS 621, curvature computed for a tension equal to 25 % RTS, when a rotation angle of 0.01 radians is imposed at the coupling sleeve

7.5.6 The difference between rotation angle and curvature for a vibrating cable

For the test set-up described in section 7.3, near the coupling sleeve, the rotation angle is an image of the curvature, but it is not the case for a conductor vibrating at one of its eigen frequencies!

In a vibrating cable, the higher the curvature, the higher the dissipation. Therefore (as mentioned in the state of the art) important dissipation is expected near the span ends (where the conductor motion is hindered) and in the vicinity of vibration antinodes. The dissipation which occurs in span (as opposed to span end dissipation) and which is denoted by *free-field* by Noiseux [61] is the only contribution taken into account to estimate the self damping power per unit length in the literature. To be able to perform some comparisons, the present analysis has been limited to this *free field* contribution too: the *free field* shape of a vibrating conductor along half a wavelength has been approximated by a sine curve which amplitude and pulsation are defined once fy_{max}, frequency and tension are imposed. The curvature is therefore maximum at the antinode, while the rotation angle at that location is zero. Similarly, the curvature is zero at the vibration node, but the rotation is maximum at that place.

7.5.7 The dimensional homogeneity of the relationship between moment and curvature

Equation 7.12 permits to convert a rotation angle into curvature. Equation 7.4 furnishes a relationship between moment and rotation angle. One may expect all there is to do is to obtain an expression of the applied moment as a function of curvature is to introduce expression 7.12 into 7.4. It is only partially true. Another of our requirements is to respect the dimensional homogeneity of the equations, which is the case for 7.12 but not for 7.4. In order to make 7.4 dimensionally correct, the coefficient $C_\star$, which dimensions are $[M^{-1}L^{-1}T^2]$ [2] and which amplitude is 1 has been introduced. Assuming $[\alpha]=M^{\frac{1}{2}}L^{\frac{3}{2}}T^{-1}$, $[\delta=1]$, $[\gamma]=1$ and $[\beta]=ML^2T^{-2}$, 7.4 can advantageously be rewritten

$$M = \alpha N^{1/2}\varphi + \beta(C_\star N)^{1/2-\delta}[1-\exp(-\gamma(C_\star N)^\delta\varphi)] \tag{7.17}$$

which is dimensionally correct since the moment dimensions are ML^2T^{-2}, which is equivalent to kgm^2s^{-2} in the S.I system and commonly named "joule".

Once all corrections and substitutions are made, the relationship giving the bending moment as a function of curvature is:

[2] In dimensional analysis, M, L and T represent respectively the following base quantities: Mass (M), Length (L) and time (T)

$$M = \alpha\xi\sqrt{EI}\chi + \beta(C_\star N)^{1/2-\delta}[1 - \exp(-\gamma(C_\star N)^\delta \xi\sqrt{\frac{EI}{N}}\chi)] \qquad (7.18)$$

7.6 Formula giving the power dissipated per unit length

7.6.1 Introduction

The present section aims at deducing an expression of the self damping per unit length. This permits on the one hand to add value to the experimental results and on the other hand to compare them with other results published in the literature and generally expressed via the "power law".

7.6.2 The area within the moment versus curvature curve

It has been seen in section 7.4 that the area within M(χ) curves controls the power dissipated within a viscoelastic material. This will be our starting point.

If $\Delta\chi = \chi_{max} - \chi_{min}$ (i.e. the difference between the maximum and minimum curvatures of a vibrating cycle), the area within the moment versus curvature curve can be computed as

$$W_{cycle} = \oint M^t(\chi)d\chi^t = 2\int_0^{\Delta\chi} M^t(\chi)d\chi^t - M(\Delta\chi)\Delta\chi \qquad (7.19)$$

Introducing 7.18 into 7.19, one obtains that

$$\oint M^t(\chi)d\chi^t = \beta(C_\star N)^{\frac{1}{2}-\delta}[\Delta\chi(1 + \exp(-\gamma(C_\star N)^\delta \xi\sqrt{\frac{EI}{N}}\Delta\chi)) + \frac{2}{\gamma(C_\star N)^\delta \xi\sqrt{\frac{EI}{N}}}(\exp(-\gamma(C_\star N)^\delta \xi\sqrt{\frac{EI}{N}}\Delta\chi) - 1)] \qquad (7.20)$$

It is worth mentioning that in (7.20), $[\gamma]=[\xi]=1$ and the mantissa of the exponentials is (of course) non dimensional, so that the correct dimension of W_{cycle} (MLT^{-2} or J/m) is obtained combining

- β, which is dimensionally equivalent to an energy $[J]$,
- $\sqrt{\frac{EI}{N}}$, which is a characteristic length $[m]$,
- $\Delta\chi$, which is a curvature in $[m^{-1}]$.

7.6.3 Energy dissipated in a viscoelastic beam, under harmonic flexural loading

The equality between internal work (W_I) and external work (W_E) is valid for any continuous system. It can therefore also be used for any continuous dissipative system, provided the load history is taken into account [56]. Considering a viscoelastic beam under harmonic excitation, the energy dissipated along the beam during one cycle of vibration satisfies

$$W_{Ecycle} = \int \oint P^t d\Delta^t ds \tag{7.21}$$

where s is the curvilinear abscissa, P^t is the vector of external forces and Δ^t the vector of displacements (both P^t and Δ^t are a function of time). In case the cyclic motion is a cyclic bending, then $P^t = M^t$ (the bending moment) and $\Delta^t = \chi^t$ (the beam curvature). Equation (7.21) becomes

$$W_{Ecycle} = \int \oint M^t d\chi t ds \tag{7.22}$$

Making use of (7.19), the previous integral is worth

$$W_{Ecycle} = \int [2 \int_0^{\Delta\chi} M(\chi)^t d\chi^t - M(\Delta\chi)\Delta\chi] ds \tag{7.23}$$

or

$$W_{Ecycle} = \int \beta (C_\star N)^{\frac{1}{2}-\delta} [\Delta\chi (1 + \exp(-\gamma (C_\star N)^\delta \xi \sqrt{\frac{EI}{N}} \Delta\chi)) + \frac{2}{\gamma (C_\star N)^\delta \xi \sqrt{\frac{EI}{N}}} (\exp(-\gamma (C_\star N)^\delta \xi \sqrt{\frac{EI}{N}} \Delta\chi) - 1)] ds \tag{7.24}$$

From the previous equations, one can deduce that the area within the $M(\chi)$ curve has a physical meaning: it is the energy dissipated per unit length and per vibration cycle in the viscoelastic beam [J/m].

In order to compute the value of 7.24, an expression for $\Delta\chi(s) \approx \Delta\chi(x)$ has been obtained assuming a sinusoidal deflected shape for the vibrating conductor, giving:

$$\Delta\chi(x) = 2 y_{max} (\frac{2\pi}{\lambda})^2 \sin(\frac{2\pi x}{\lambda}) = E \sin(\frac{2\pi x}{\lambda}) \tag{7.25}$$

Let

$$A = \beta(C_\star N)^{1/2-\delta} \tag{7.26}$$

$$C = \gamma(C_\star N)^{\delta}\xi\sqrt{\frac{EI}{N}} \tag{7.27}$$

$$D = \frac{2\beta(C_\star N)^{1/2-\delta}}{\gamma(C_\star N)^{\delta}\xi\sqrt{\frac{EI}{N}}} \tag{7.28}$$

where $[A] = ML^2T^{-2}$, $[C] = L$, $[D] = MLT^{-2}$. The following power series expansion of the exponential (which is valid for $-\infty < x < \infty$) can be applied:

$$\exp(x) = 1 + x + \frac{x^2}{2!} + \frac{x^3}{3!} + ... \tag{7.29}$$

The value of 7.24 has been evaluated on half a wave length. Some numerical computations have been carried out. The results show that no significant improvement is obtained computing this integral with terms of higher order than $(\Delta\chi)^4$ in the integrand, so that:

$$W_{Ecycle}(\frac{\lambda}{2}) \approx (2A - CD)E\frac{\lambda}{\pi} + (\frac{1}{2}C^2D - AC)E^2\frac{\lambda}{4} + (AC^2 - \frac{1}{3}DC^3)E^3\frac{\lambda}{3\pi} \tag{7.30}$$

The power dissipated per unit length P_E ($[P_E]$=$MLT^{-3} = W/m$) can be obtained multiplying 7.30 by $(\frac{2f}{\lambda})$:

$$P_E \approx 2f[(2A - CD)\frac{E}{\pi} + (\frac{1}{2}C^2D - AC)\frac{E^2}{4} + (AC^2 - \frac{1}{3}DC^3)\frac{E^3}{3\pi}] \tag{7.31}$$

Limiting the analysis to the terms up to the order $(\Delta\chi)^3$ in the integrand, equation (7.31) can be further simplified as follows

$$P_E \approx \frac{1024}{9}\gamma^2(C_\star N)^{\delta+1/2}\xi^2\pi^5\beta y_{max}^3 m^3 f^7\frac{EI}{N^4} \tag{7.32}$$

As can be seen in figure 7.7, formula 7.32 provides a very good approximation at low frequencies whatever the amplitude, and also at high frequencies if the amplitudes remains limited (e.g. $fy_{max} = 50mm/s$).

7.6.4 Comparison of the self damping deduced from moment versus curvature curves and other results of the empirical power law

As mentionned in section 1.11, Noiseux has studied the possibility to predict the self damping for any ACSR conductor using a similarity law [61]. The

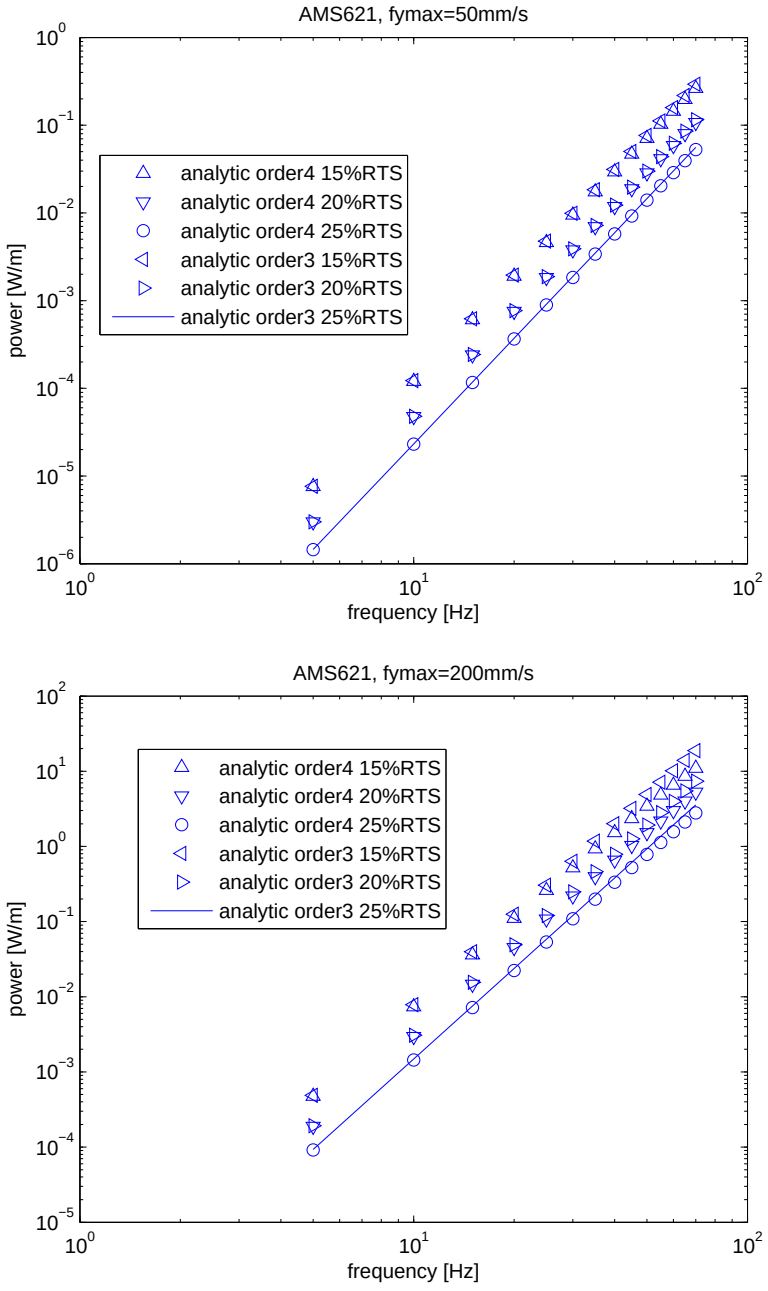

Figure 7.7: Comparison of the self damping power at $fy_{max} = 50mm/s$ (top) or $fy_{max} = 200mm/s$ (bottom), considering either the formula with terms up to $(\Delta\chi)^4$ or $(\Delta\chi)^3$. The conductor is AMS621, at 15,20 and 25% RTS

conductors used by Godinas during his tests are made of aluminium alloy (AMS). The latter will probably show a different damping behaviour than ACSR ones. Nevertheless, and since no set of coefficients is available to predict the self-damping of these AMS conductors using the power law, the results of the previous subsection have been compared to the self damping power values deduced from the power law (1.8) taking Noiseux's exponents (l=2.44, m=5.63, n=2.76) [25].

As can be seen in figure 7.8, there is a fairly good agreement between the curves, both in their trends and values.

To provide the reader another reference of comparison, figure 7.9 shows the self damping power computed from the empirical law (7.14), but with two sets of parameters coming from different authors (respectively Noiseux with l=2.44, m=5.63, n=2.76 and Politecnico di Milano with l=2.43, m=5.5, n=2). These sets of parameters have been obtained via the ISWR method [25]. It can clearly be seen in figure 7.9 that according to the set of coefficients used in the power law (Noiseux or Politecnico), there may be significant scattering within the results (one order of magnitude). Also, one may note that the self damping power deduced from formula 7.31 is comprised between Noiseux's and Politecnico's results.

7.7 Deducing the viscoelastic model parameters from measurements

7.7.1 Parameter A (which controls the slope of the hysteresis curve)

At a given frequency, tension and amplitude fy_{max}, the first parameter of the viscoelastic model "A" can be deduced from the average slope of the hysteresis loop. The latter was estimated from the knowledge of the maximum bending moment and the corresponding maximum curvature amplitude (combining equations 7.18 and 7.25). The results are shown in figure 7.10. One can see that for a fixed fy_{max} values, "A" decreases as the frequency increases. This result is logical: for a given vibration intensity fy_{max}, if the frequency increases, the wavelength decreases, and higher curvature levels are reached. In other words, a higher vibration frequency corresponds to a higher maximum curvature reached on the loading curve defined by equation 7.18. The corresponding hysteresis curve will have both a bigger area and a lower average slope value. This is illustrated in figure 7.11.

7.7.2 Parameter B (which controls the self damping via the area of the hysteresis curve)

At a given frequency, tension and amplitude fy_{max}, the value of B can be deduced from equation 7.9, provided the area within the $M(\chi)$ curve, and

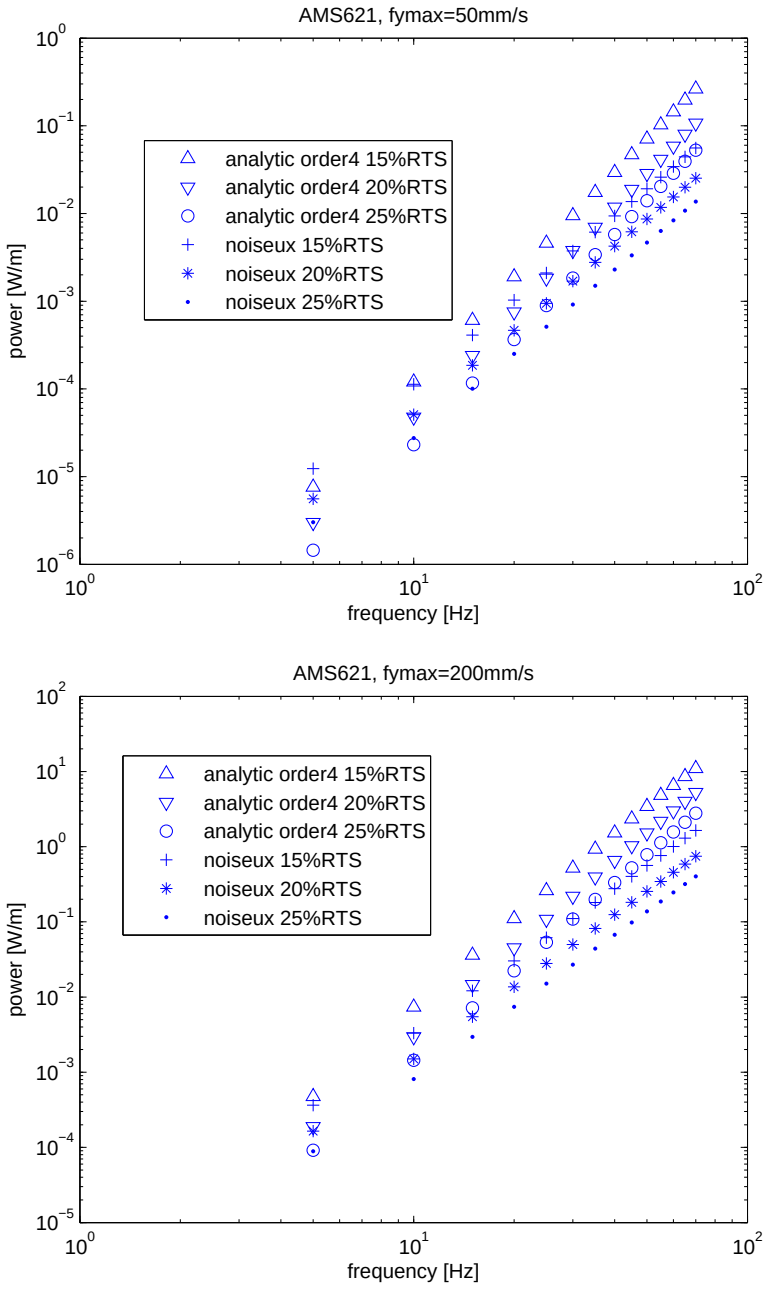

Figure 7.8: Comparison of the self damping power computed from formula 7.47 and from the power law (using Noiseux's coefficients: l=2.44, m=5.63, n=2.76) [25]. The conductor is AMS621, at 15,20 and 25% RTS. The top figure relates to $fy_{max} = 50mm/s$ and the bottom figure to $fy_{max} = 200mm/s$.

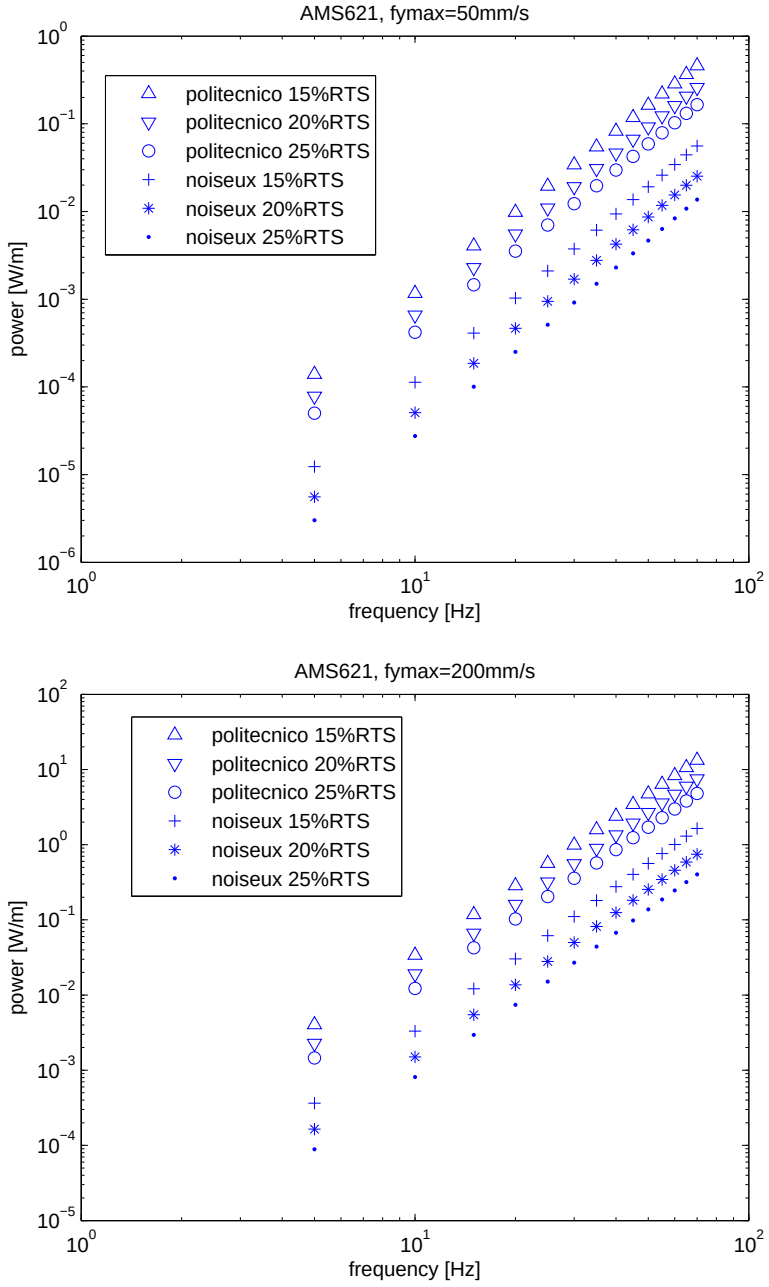

Figure 7.9: Comparison of the self damping power computed from the power law, using either Noiseux's coefficients (l=2.44, m=5.63, n=2.76) or Politecnico di Milano's coefficients (l=2.43, m=5.5, n=2) [25]. The conductor is AMS621, at 15,20 and 25% RTS. The top figure relates to $fy_{max} = 50mm/s$ and the bottom one to $fy_{max} = 200mm/s$

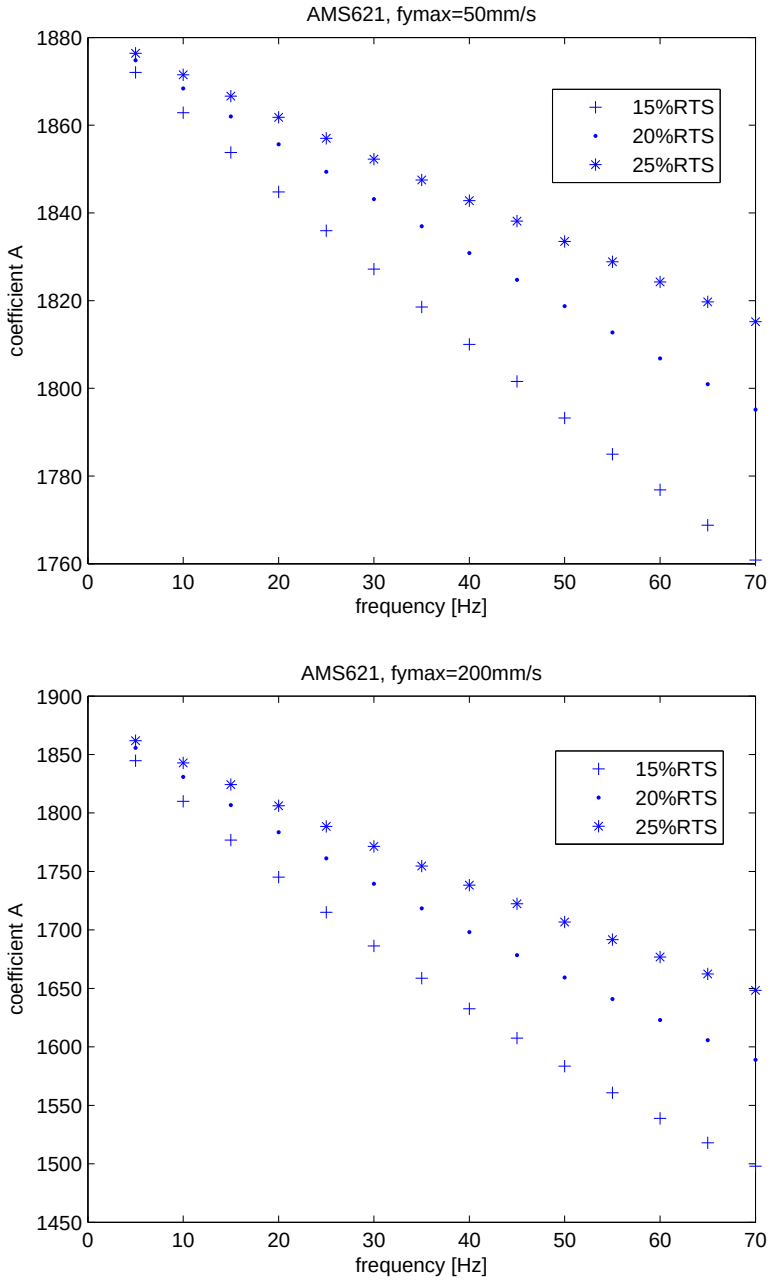

Figure 7.10: Comparison of the values of parameter A deduced from moment versus curvature curves. The top figure relates to $fy_{max} = 50mm/s$ and the bottom one to $fy_{max} = 200mm/s$

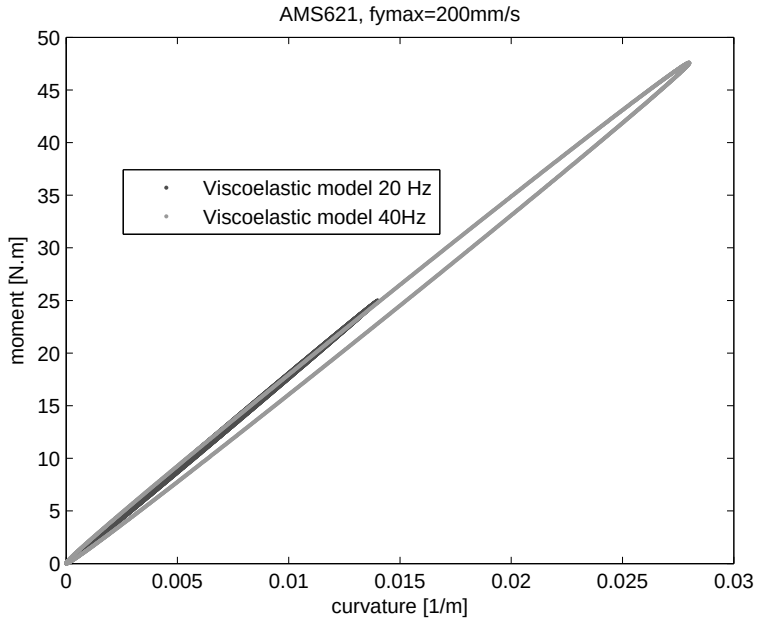

Figure 7.11: Viscoelastic hysteresis curves at the same vibration amplitude $fy_{max} = 200mm/s$, but at two frequencies (20 and 40 Hz)

the amplitude of curvature can be estimated. All this information has been gathered along the previous paragraphs. The results are presented in figure 7.12. Although the area within the $M(\chi)$ curve increases as the frequency increases (all other things being equal), the values of B are little affected by a change in frequency or even decrease. This may be explained by the fact that the area within the hysteresis curve is a function of the product $\omega B \chi_0^2$ and the resulting product increases with frequency. Also, more damping is expected if the tension level decreases. This is translated at the level of the viscoelastic model by a higher value of coefficient B.

In order to check the values deduced from parameters A and B of the viscoelastic model, the corresponding hysteresis curves have been plotted and compared to those deduced from measurements. An example is shown in figure 7.13 at 40Hz and $fy_{max} = 200mm/s$. One can see that both the area and the slope of the hysteresis curves agree well.

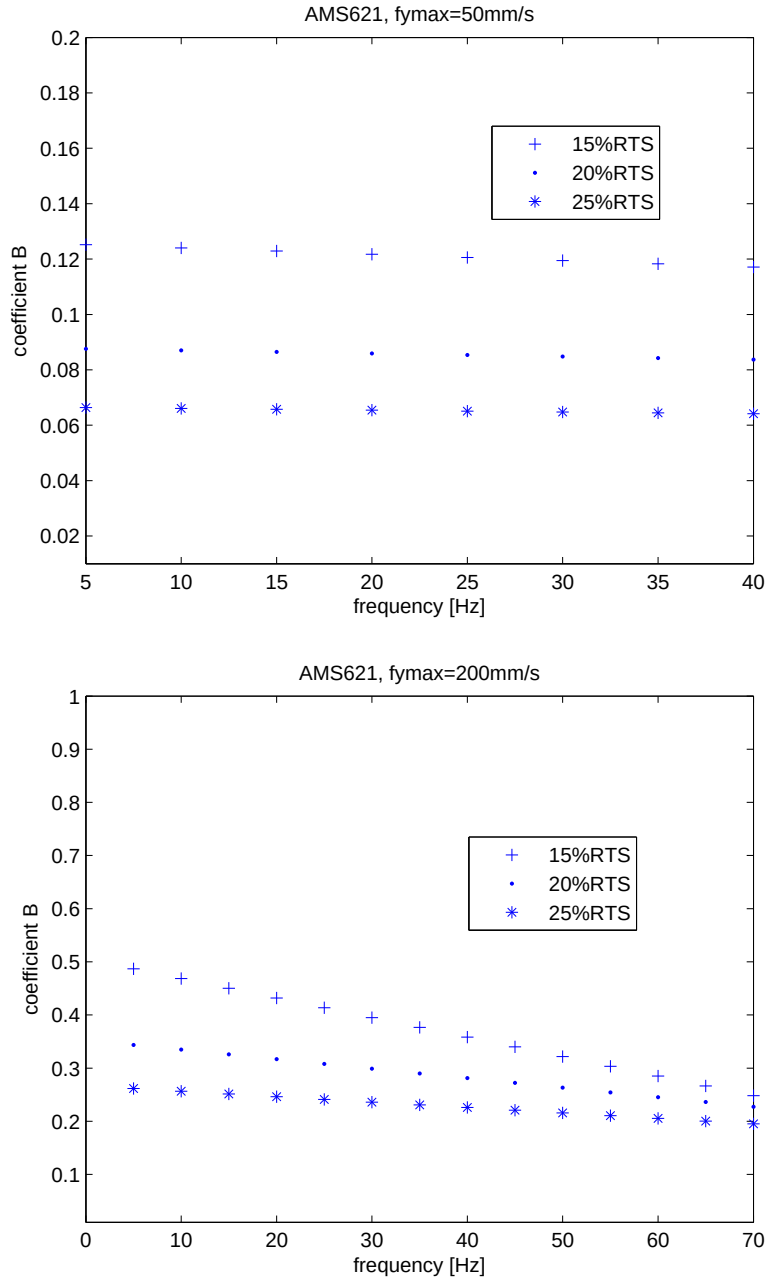

Figure 7.12: Comparison of the values of parameter B deduced from moment versus curvature curves using M. The top figure relates to $fy_{max} = 50mm/s$ and the bottom one to $fy_{max} = 200mm/s$

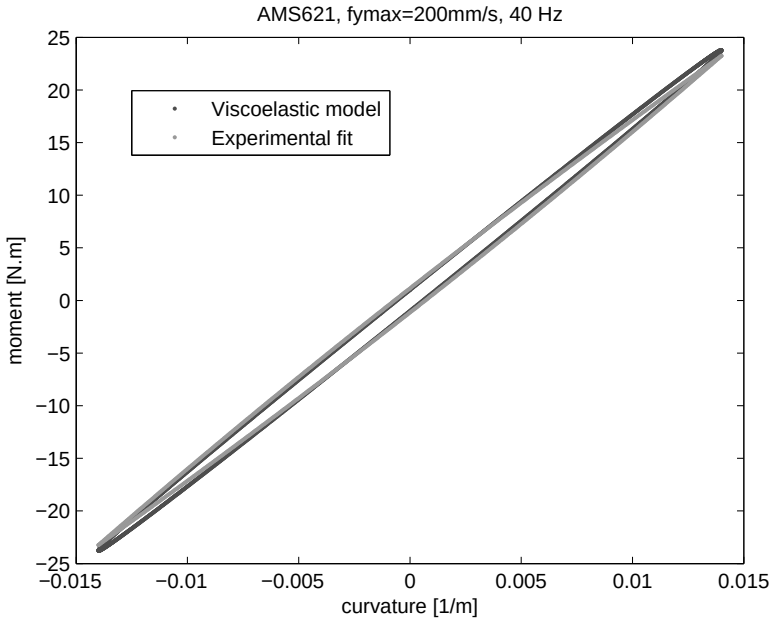

Figure 7.13: Comparison of the hysteresis curves of the viscoelastic model and deduced from measurements

7.8 Dynamic bending stiffness deduced from measurements

7.8.1 Slope of the moment versus curvature curve

The dynamic bending stiffness EI_{dyn} can be computed as the slope of the moment versus curvature curve. An expression of the dynamic bending stiffness can be obtained from the first derivative of 7.18:

$$EI_{dyn} = \alpha c\sqrt{EI} + \beta(C_\star N)^{1/2}\gamma c\sqrt{\frac{EI}{N}}\exp(-\gamma(C_\star N)^{\delta}c\sqrt{\frac{EI}{N}}\chi) \quad (7.33)$$

Note that the EI which appears in 7.18 and 7.33 is an average bending stiffness value, which has been deduced from available data in section 7.5.3 ($\approx 60\%EI_{max}$). Considering a realistic range for curvature ($\chi < 0.1$ $[1/m]$), a dynamic bending stiffness comprised between ≈ 50 and $90\%EI_{max}$ can be computed (see figure 7.14). The latter range is compatible with average bending stiffness values published in the literature (see chapter 8). Comparing the curve in figure 7.14 with the average bending stiffness values deduced on Ireq's test-span (see chapter 8, section 8.1):

- At high aeolian vibration amplitudes, the value of 50% EI_{max} is the same as the one deduced experimentally on Ireq's test-span,

- At lower aeolian vibration amplitudes, a value of 60% EI_{max} was deduced, which is compatible with figure (7.14).

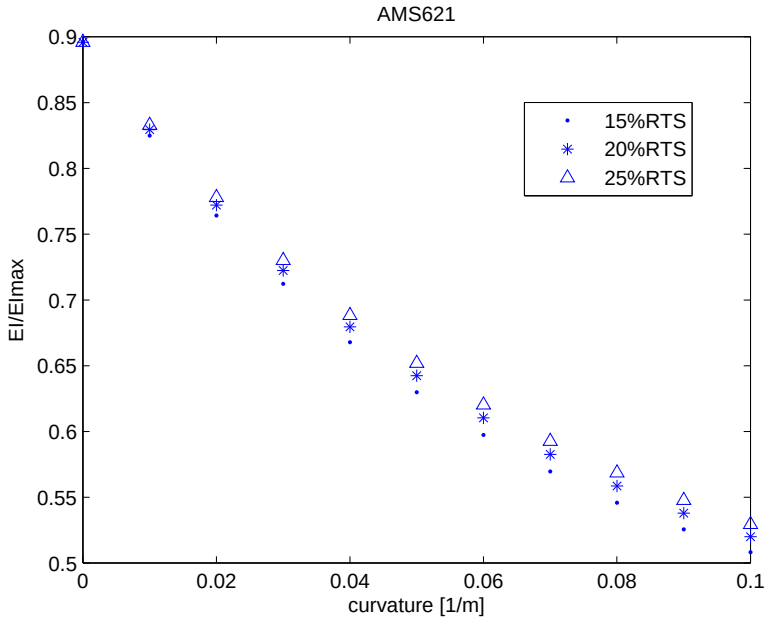

Figure 7.14: AMS 621, dynamic bending moment versus curvature (EI_{dyn}/EI_{max})

7.8.2 Comparison with K. Papailiou's model

In 1997, Papailiou published a model of variable bending stiffness [65]. The model gives the evolution of the bending stiffness with curvature for a single or multilayer conductor as a function of :

- the interlayer friction coefficients,
- the tension in the conductor,
- the modulus of elasticity of the wires
- the conductor's geometry (lay angle, wire diameter, angular position of the wires).

Both the geometry of a conductor and the modulus of elasticity of its wires are generally well known. Its tension can be measured or deduced easily. The friction coefficient is probably the most difficult data to obtain. This section aims at comparing K. Papailiou's model with the variable bending stiffness which can be deduced from the experimental curves collected

by Godinas, but first, it is necessary to recall that Godinas' records have been performed on established cycles of vibration. Therefore, to perform a correct comparison, one needs to assume repeated bending loads in K. Papailiou's model (in other words, a factor 2 needs to be introduced to compute the average slip curvature, see equation 35 of [65]). Introducing the data of conductor AMS621 in this model [3], assuming a tension equal to 20 % RTS and cyclic loading, and a friction coefficient equal to either 0.2 or 0.5, the curves shown in figure 7.15 are obtained.

Comparing these curves with the one shown in figure 7.14., one can say that within the curvature range which characterizes aeolian vibrations, both models predict a decrease in the bending stiffness in a ratio of about 2:1. Also, the orders of magnitude of the predicted dynamic bending stiffness are the same.

In Papailiou's model, the maximum bending stiffness value is in agreement with the theoretical maximum while in figure 7.14, it is worth 0.9 EI_{max}. Nevertheless, as can be seen in Appendix A, Godinas' moment versus curvature curves have probably been obtained with a low sampling frequency (less than 10 recorded points per cycle). The fit may therefore be improved increasing this sampling frequency, in particular where rapid changes in the slope of the hysteresis curve exist, i.e. at the lowest curvature values. Another improvement to the quality of the recorded data could be to record the conductor deflected shape, so that one does not have to deduce the relationship between rotation angle and curvature any more.

7.9 Proposal of a new method for the measurement of a conductor's self damping properties

As illustrated in figure 7.11 one single loading curve (giving $M(\chi)$) permits to deduce the viscoelastic self damping parameters of the beam. Also, according to Godinas [28, 27], this loading curve does not depend on the loading speed. Given these two facts, the measurement of both the conductor self damping properties could be considerably simplified:

- the loading curves could be measured (almost) statically,
- provided the maximum curvature level is reached, only one test per tension level would (theoretically) be required,
- the tests would provide information not only on the self damping properties, but also on the conductor variable bending stiffness.

Let us now review the test method in itself. The test frame on which the conductor is tensioned could be the same as in Godinas's experiments

[3] the Matlab code for Papailiou's variable bending stiffness model is a courtesy from B. Godard (ULg)

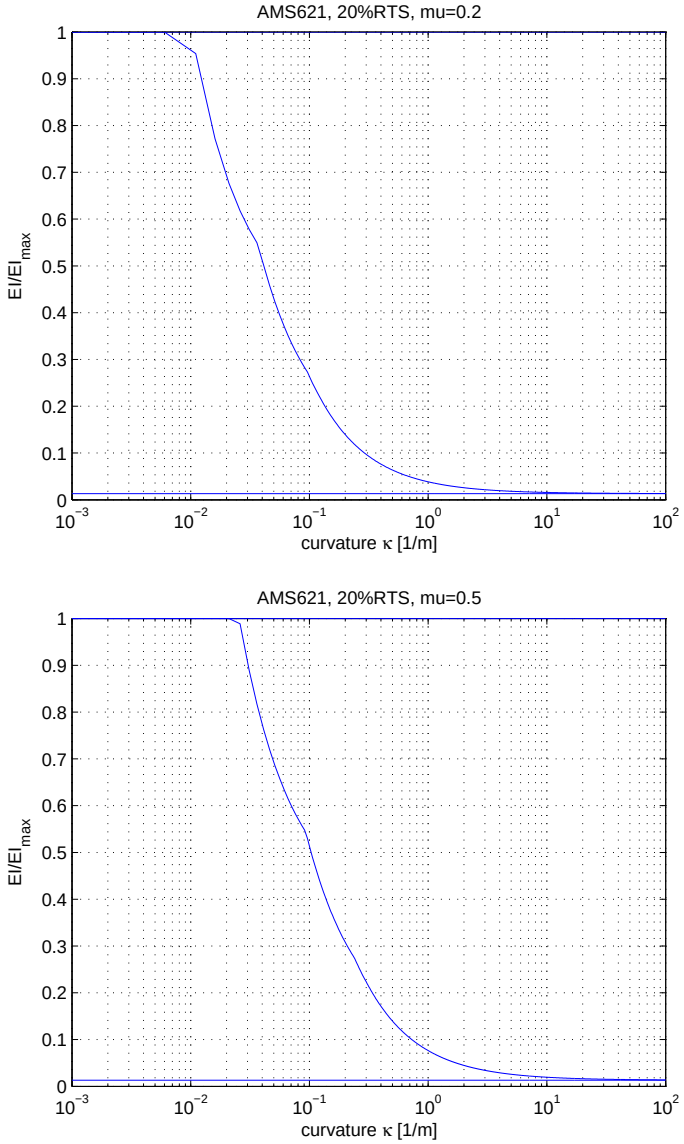

Figure 7.15: Variable bending stiffness computed from K. Papailiou's model [65, 64], assuming conductor AMS621 at a tension of 20% RTS and a friction coefficient equal to 0.2 (top) or 0.5 (bottom)

(see section 7.4). The following improvements could advantageously be implemented (to improve the quality of the data and/or to avoid re-deducing information from measurements, which is the case in sections 7.5.2 to 7.5.4):

- collect additional information on the cable deflection,
- increase the sampling frequency,
- record conductor tension during the tests.

It is certainly advised to:

- perform the tests within a tension range in agreement with reality,
- perform the tests at variable amplitudes.

Concerning the exact number and list of tests to be performed, this topic still needs to be further investigated. In a first approach, it seems reasonable to perform the tests at several realistic tension ranges (e.g.: 15, 20, 25% RTS). For each tension value, loading cycles covering the amplitude range $0 < \chi < 0.1$ should be conducted. Last, the observed independence of the loading cycle with respect to the loading speed should be checked. Eventually, having collected this information for a certain type of conductor, the parameters of the viscoelastic model could be deduced.

In order to better understand the loading cycles and curves, some tests at arbitrary loading patterns could be planned. In the context of rationalizing experimental costs and their duration, a study with the objective of comparing the quality of collected information as a function of the number of tests sounds worthwhile.

7.10 The implementation of the viscoelastic model

Once a curve giving the bending moment as a function of curvature and tension is available (7.18), the next step is to implement it in a finite element code. Let us consider the case of Samcef V13.01 [4] and the viscoelastic beam element. If the aim is to compute the response of a conductor at a particular tension, frequency and amplitude fy_{max}, a simple solution is to compute the corresponding values of the viscoelastic model A and B (see section 7.7) and to introduce them "manually" in the data file. If more complex computations are required, (for example under variable frequencies and/or amplitudes), an automatic adjustment of the viscoelastic parameters would be helpful. This implementation requires an advanced knowledge of the

[4] Samcef is a trademark of Samtech Group, www.samtech.com or www.samcef.com, LIEGE science park, Rue des Chasseurs-Ardennais, 8, B-4031 Liège (Angleur), BELGIUM, Tel: +32 4 361 69 69, Fax: +32 4 361 69 80

element code (as well as the authorization to have and modify the element code itself...), but is perfectly accessible. In fact, in a beam element, at each time step, "resulting efforts" are computed as a function of strains. The evolution of curvature (and of course tension) as a function of time is known by the software. Even though this information is not available among the standard post processing codes, an authorized user could read this information.

According to which case is being simulated and/or what information is made available in the code, several situations may arise. Here are a few examples an proposals to deal with them:

- Suppose the curves giving A and B as a function of tension and frequency are available via a "lookup table" and the evolution of the excitation frequency as a function of time is known. Keeping the maximum and minimum curvature values as well as the excitation frequency in the records, the values of the viscoelastic parameters A and B could be readjusted for each vibration cycle.

- Suppose the excitation frequency as a function of time is not known. Keeping the evolution of e.g. the cable position as a function of time in the records, the frequency of the motion could be approximated performing a FFT on a couple of vibration cycles. As can be seen in figures 7.10 and 7.11, the sensitivity of A and B with respect to frequency is low. A frequency resolution of the order of 1 Hz seems sufficient.

- Suppose the curves giving the viscoelastic parameters A and B as a function of tension amplitude and frequency are not available. Only the output of the tests is known (the relationship between moment and curvature). In such a case, the software first has to "learn" these parameters. Before random tests can be performed, a series of predefined tests have to be run, simulating different tension, amplitudes and frequencies so that "lookup tables" can be filled. As an example, after one of the predefined vibration cycles, the value of parameter A can be deduced from ΔM and $\Delta\chi$.

7.11 Another interpretation of the self-damping evaluated in actual conditions (chapter 3) in light of the present conductor self damping model

In chapter 3, on-site measurements performed on a "real" outdoor span have been used as an input to "fit" the exponents of the self damping power

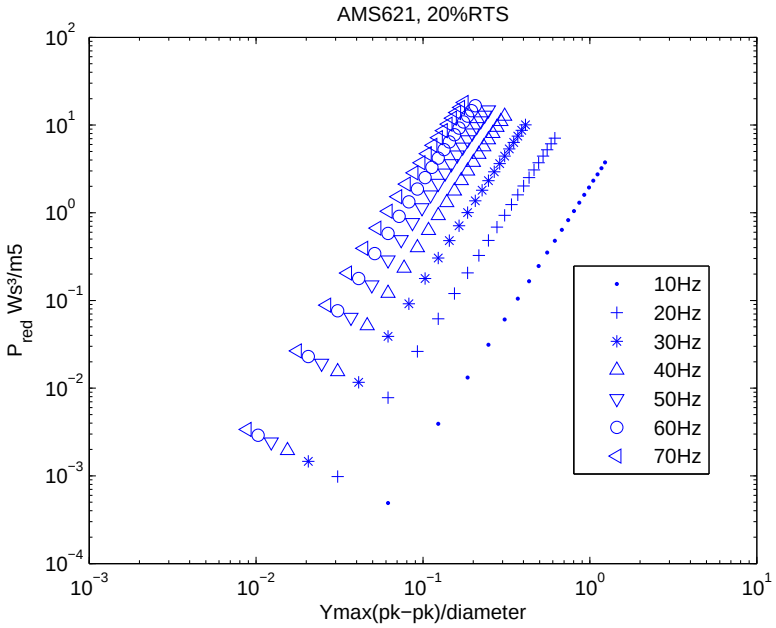

Figure 7.16: Curves of reduced power computed with formula 7.31 for conductor AMS621, at a tension equal to 20% RTS

law. The values of the tension exponent deduced was within the range given in the literature for conductors "Aster 570" and "Azalee 666" (their diameter is worth about 30mm), but was out of this range for the two smaller conductors "Aster 228" and "Azalee 261" (their diameter is about 20mm). In fact, higher values of the tension exponent were required to "fit" the data. Since the exponents of the power law are empirical values, not fully justified by the physics behind the damping phenomenon, one can hardly draw advanced conclusions on the relationship between self damping and conductor tension based on the power law.

The same analysis can be conducted with the self-damping formula given in 7.32. Using the exact set of parameters (β, δ and γ) found by Godinas for conductor AMS621, one obtains the curves in figure 7.17. One can see that the evolution of the predicted amplitudes as a function of frequency complies with the real one. The real maximum amplitudes are indeed smaller than those predicted with formula 7.32. Tuning the coefficients which specifically control the area within the hysteresis curve of the conductor (β, δ and γ) would permit to improve the compliance of the results. Figure 7.16 illustrates the adimensional self damping power curves which can be deduced using equation 7.31 for conductor AMS621, at a tension equal to 20 % RTS.

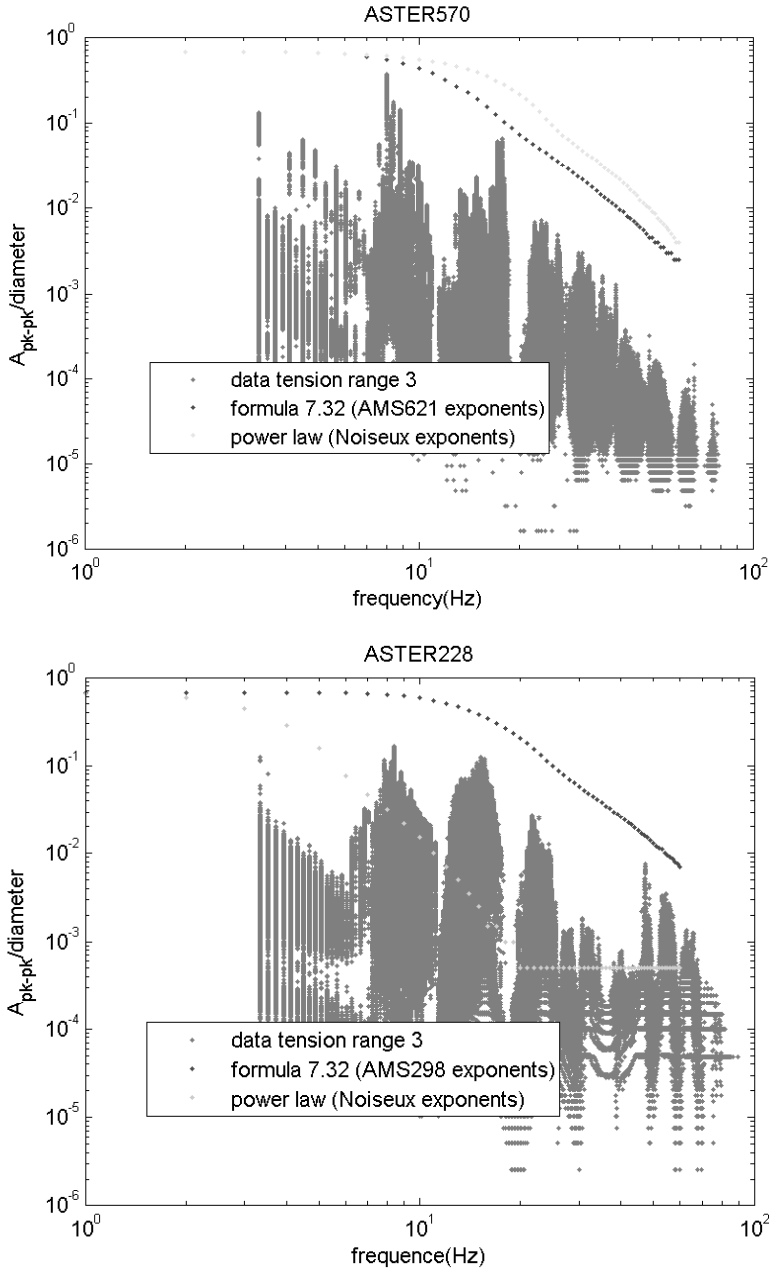

Figure 7.17: Comparison of the self damping power computed from formula 7.32 (using the exponents of AMS621) and the data recorded at Dead Water Fell on Aster570 and ASTER228 (see chapter 3). The self damping power which can be computed with the power law using Noiseux's set of exponents is also shown (note that Noiseux's exponents are valid for ACSR conductors only).

7.12 Conclusions

In this chapter, a new method is proposed to assess the self damping power of a conductor. Its main advantage is the simplicity to collect information: unlike the ISWR method, it does not require a fine tuning of eigen modes nor a measurement of amplitudes of vibration "nodes" nor dynamic loading. The latter advantage also means that the impact of tension fluctuations on amplitudes discussed chapter 5 is automatically circumvented.

Based on the recorded and processed data, a formulation for the self damping per unit length is proposed as a function of the antinode amplitude of vibration, frequency, conductor tension, bending stiffness, mass per unit length plus a special parameter called β. The latter parameter has the dimension of an energy [J]. Together with the conductor characteristic length $\sqrt{\frac{EI}{m}}$, tension and amplitude of strain (curvature in the case of a vibrating conductor), it characterizes the area of the moment versus curvature curve. It has been shown that a simplified version of this formulation permits to predict vibration amplitudes which are consistent with those measured in actual conditions (see chapter 3). The results could yet be improved by an appropriate tuning of the coefficients which characterize the area within the moment versus curvature curve. This simplified formulation also shows that the sensitivity of the self damping to the vibration amplitude, frequency and tension is comparable to that found by other authors, using another measurement technique, the ISWR method, but with the difference that in this case, the exponents for frequency, amplitude and tension are integers, fully justified by the physics behind the phenomenon of damping.

The present chapter also illustrates how this self damping formulation can be implemented in a finite element model via a viscoelastic material. This permits to take into account both the variable bending stiffness and the conductor self damping.

The perspective shown by this work is the following: knowing the conductor properties and the shape of some moment versus curvature cycles, the proposed complete formula would permit to estimate the conductor self damping in any kind of vibration frequency or amplitude without any dynamic testing.

Part IV

Model validation

Chapter 8

Validation of the variable bending stiffness model

8.1 Average bending stiffness values deduced from measurements on Ireq test span

In literature, formulae which express how the conductor natural frequencies depend on conductor bending stiffness can be found (e.g. formula 2.2 of [58]):

$$f_k = \frac{1}{2\pi}\sqrt{(\frac{k\pi}{L})^2\frac{T}{m_L}(1+(\frac{k\pi}{L})^2\frac{EI}{T})} \tag{8.1}$$

Knowing the value of several natural frequencies of vibration as well as their mode number for a constant amplitude of vibration fy_{max}, it becomes possible to estimate the conductor average bending stiffness value. Such information was collected on Ireq's cable test bench during experiments carried out in October 2008 and un July 2009 by Suzanne Guérard (ULg), Roger Paquette, Martin Gravel and Jacques Poirier (Ireq), under the supervision of Pierre Van Dyke (Ireq). Each data point which appears in figures 8.1 and 8.2 was obtained according to the following procedure:

- Tuning of the resonance. For a fixed amplitude of vibration (e.g. $fy_{max} = 40mm/s$ for the tests depicted in figure 8.2), the frequency was finely adjusted until the excitation force was minimum.
- The mode number was checked manually, counting the number of vibration loops (the trick was to count the vibration "nodes" which were fairly easy to detect manually).

Throughout the tests, a special attention was drawn to fy_{max} amplitudes of vibrations, which were kept as constant as possible. A first series

of test has been performed on an ACSR Crow conductor tensioned at approximately 22.7%RTS and a saddle metal-to-metal suspension clamp on the span extremity opposed to the shaker. These tests have been performed at a "high" fy_{max} value (the maximum fy_{max} value for aeolian vibrations is worth about $200mm/s$). An average value of $591N.m^2$ for conductor bending stiffness can be estimated. This value is obtained combining the data recorded during the experiment (see figure 8.1) with equation 8.1. This value is comprised between the conductor minimum and maximum bending stiffness values [25], respectively about 20 and 1200 $N.m^2$. It is close to 50% of EI_{max}.

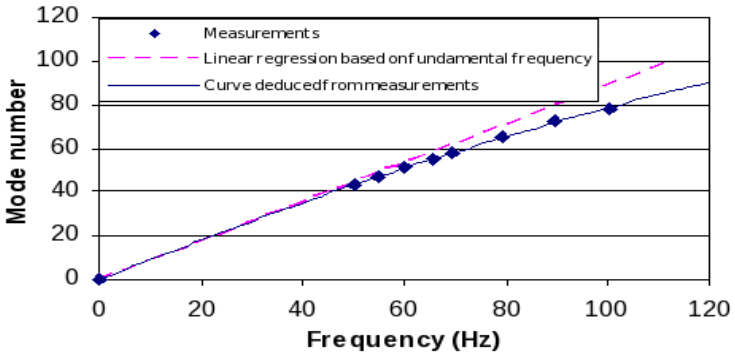

Figure 8.1: Evolution of frequency with mode number for test span equipped with conductor Crow and a suspension clamp at the extremity opposed to shaker, tension of 22.7% RTS

The information contained in the previous figure was complemented by other experimental data from tests at 15.7% and 21.2% RTS (see figure 8.2), but with other boundary conditions: the suspension clamp is removed and both span ends are very rigidly fixed. The amplitude of vibration fy_{max} is almost constant and equal to $\approx 40mm/s$ (see figure 8.2). The corresponding average bending stiffness values obtained at those tensions are respectively equal to $714N.m^2$ ($\approx 59\%EI_{max}$) and $734.5N.m^2$ ($\approx 61\%EI_{max}$). Due to some equipment limitations it was not possible to perform these tests at higher fy_{max} values for the whole mode number range. The higher average bending stiffness values are probably due to a lower excitation amplitude fy_{max} (and hence lower curvature values) than in the first series of tests. To summarize the results:

- at low amplitudes of vibration (around $fy_{max} \approx 40mm/s$), an average bending stiffness value of about 60 % EI_{max} is deduced,
- at "high" amplitude of vibration, an average bending stiffness value of about 50% EI_{max} is deduced.

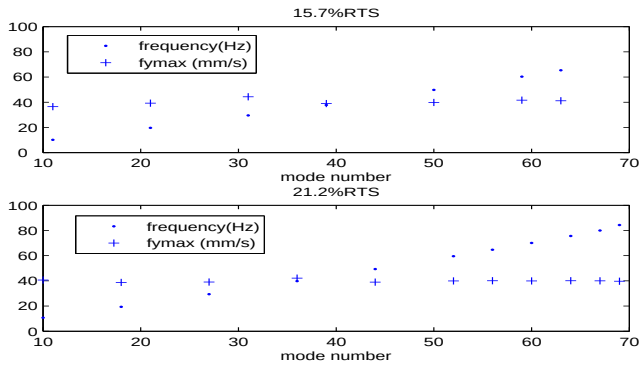

Figure 8.2: Evolution of frequency and amplitude ($fy_{max}(mm/s)$ with mode number for test span equipped with conductor Crow. Span ends are very rigidly fixed and tension is worth respectively 15.7% and 21.2% EI_{max}

8.2 Comparison with other average bending stiffness values given in the literature

In 1936, in a paper called "Cable and Dampers", R.G. Sturm published some results on conductor bending stiffness deduced from tests on two ACSR conductors [82]. As an example, for an ACSR 30/19 with a section of $403mm^2$ and a tension equal to 14% RTS, he deduces an average bending stiffness value of about 49% EI_{max} at "low" deflection values and down to 8.5%

EI_{max} at "high" deflection values. Nevertheless, "low" and "high" deflection values are not explicitely defined ("high" deflection values could be beyond the range of aeolian vibrations).

In 2003, Hardy and Leblond presented a paper entitled "On the Dynamic Flexural Rigidity of Taut stranded cables" [37]. A case study with an all-aluminium conductor is described in the paper. It predicts a "plateau" in the bending stiffness values, in the curvature range which characterizes aeolian vibrations. This plateau stands at about 60% EI_{max}.

An average bending stiffness value of the order of 50%EI_{max} was also deduced from experimental tests by Claren and Diana on the one hand and Scanlan and Swart on the other hand [76, 12].

8.3 Comparison with other variable bending stiffness models

Such a comparison has already been performed in section 7.8.2. For the sake of completion, one can mention that in 1997, Hagedorn presented a method to obtain the bending stiffness as a function of curvature [35].

8.4 Conclusions

Comparing the dynamic bending stiffness curve of the previous chapter (figure 7.14) with the average bending stiffness values deduced on Ireq's testspan, it has been shown that:

- At high aeolian vibration amplitudes, the values of bending stiffness found (50% EI_{max}) coincide,
- At lower aeolian vibration amplitudes ($fy_{max} \approx 40mm/s$), a value of 60% EI_{max} was deduced on Ireq's testspan, which is compatible with figure (7.14).

A good agreement is therefore obtained.

Also, the bending stiffness values deduced from Godinas'measurement complies with other average bending stiffness values published in the literature.

Chapter 9

Experimental attempts to reproduce resonance conditions

9.1 Introduction

Difficulties to perform the tuning of resonance with the non linear finite element model have been highlighted in chapter 5. These difficulties are believed to be the consequence of non linearities, mainly tension fluctuations and coupling between longitudinal and transversal motion. In order to further investigate this matter, Ireq has kindly accepted to support financially a new series of tests in July and Aujust 2009. Even if it was not possible to gather information on conductor tension, very interesting results related to the phase shift between excitation force and acceleration, to vibration amplitude near the "nodes", etc. have been collected. The latter show that the "theoretical resonance" is not so easy to reach in practice.

9.2 About the tests

The test set-up is the same as described in chapter 3, except that a new data acquisition system was available. This new system was inaugurated in July 2009. It is able to tune the excitation frequency with an accuracy of 0.01Hz (instead of 0.1Hz previously). It made continuous records at a frequency of 1000Hz and for a time length of 30 seconds possible. Among the data which could be recorded: shaker force, acceleration at the shaker place, antinode amplitude of displacement, and for some of the tests the displacement at the location of a vibration "node". Unfortunately, it was not possible to install strain gauges on the conductor to access to conductor tension information.

The displacement amplitude at the location of the node is often used by Ireq to assess the conductor self damping properties using the ISWR method.

In order to perform this node amplitude measurement, data is systematically processed through a passband filter with the middle of its range equal to the excitation frequency. In the frame of the present research, this filter was removed, so that all other components of the displacement at nodes could be recorded

Most of the tests have been conducted at an fy_{max} value of 40 mm/s.

9.3 Phase shift between excitation force and conductor acceleration

Resonance conditions are met (in theory) when the phase shift between force and acceleration is equal to $\pi/2$. Under these conditions, the excitation force needed to obtain a given amplitude of vibration is minimum. For a fixed value of the excitation force, the resonance can be found adjusting the excitation frequency until the antinode amplitude is maximum. As explained in chapter 5, a practical way to visualize the phase shift between two signals is to plot one of these signals as a function of the other, to obtain a Lissajous plot:

"The resonance can be visualised with a Lissajous curve, with position on one axis and excitation force on the other. At resonance, phase shift between acceleration and excitation force is 90°, which means that the Lissajous curve plotting either excitation force as a function of displacement, or excitation force as a function of acceleration is a "circle" (provided an appropriate scale is chosen for axes X and Y, else the plot will show an *unrotated* ellipse)."

The resonance frequency being set, the phase shift between acceleration and force often kept fluctuating (see e.g. figures 9.2 and 9.4). The corresponding conditions are respectively: a frequency of 13.85Hz and an fy_{max} value of 40mm/s for the first case and a frequency near 30Hz and an fy_{max} value of 80mm/s. Also, during the tests performed, it was noticed that for certain resonance frequencies, the force signal of the vibration shaker was "polluted" by harmonics, which made the tuning operation particularly difficult to perform. This "pollution" is illustrated in figure 9.1, which corresponds to the same test case as figure 9.2 (excitation frequency of 20.44 Hz, $fy_{max} = 40mm/s$, tension of 21.07% RTS). It can be observed that the amplitude of the excitation force also varies between 1 and 1.2N. To date, no satisfying explanation to the presence of harmonics in the force spectrum for some eigen frequencies has been found, but one may not exclude the possibility that the answer of the conductor to the excitation force contains harmonics which in turn are transmitted to the force sensor.

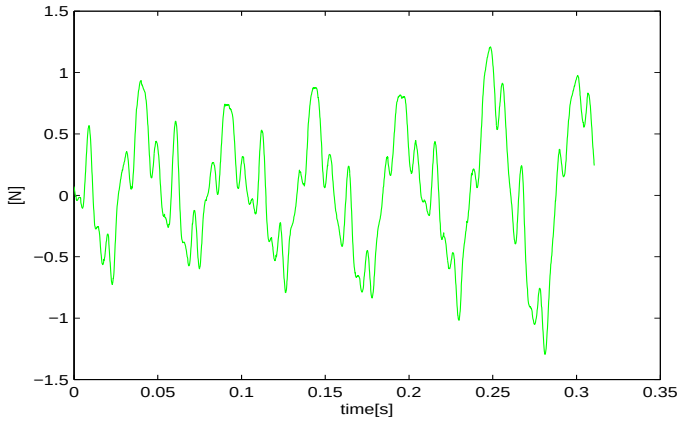

Figure 9.1: Force as a function of time for an eigenfrequency of 20.44Hz, an amplitude $fy_{max} = 40mm/s$ and at a tension of 21.07%RTS

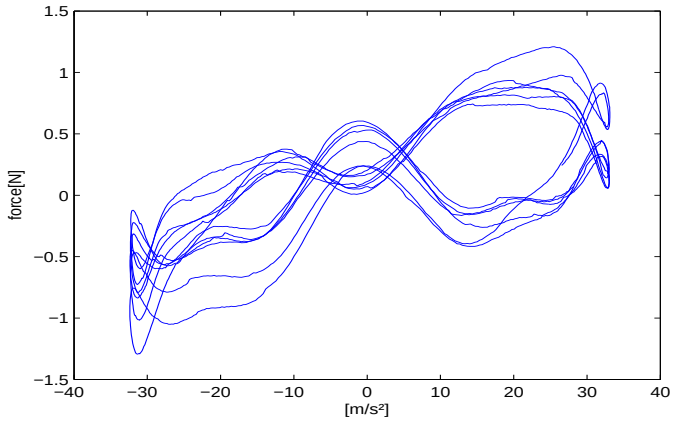

Figure 9.2: Lissajous curve of force versus acceleration for an eigenfrequency of 20.44Hz, an amplitude $fy_{max} = 40mm/s$ and at a tension of 21.07%RTS

Other experimental Lissajous curves are shown in figures 9.3-7. Except for the case at an amplitude of $fy_{max} = 160mm/s$ and a rather high excitation frequency (49.83Hz), which is characterized by a phase shift of 94 degrees, all Lissajous curves represent a phase shift remote from 90. This difficulty to obtain a perfect resonance experimentally may be due to the fact that there is little energy dissipation in the system, almost at low amplitudes of vibration: on the one hand the force sensor is able to measure within the range of +-4448N with a linearity of +-1% of full-scale and on the other hand:

- the present tests require an excitation force of the order of a few Newtons to a few tens of Newtons (0-peak),
- the frequency tuning is performed trying to detect a minimum in the excitation force.

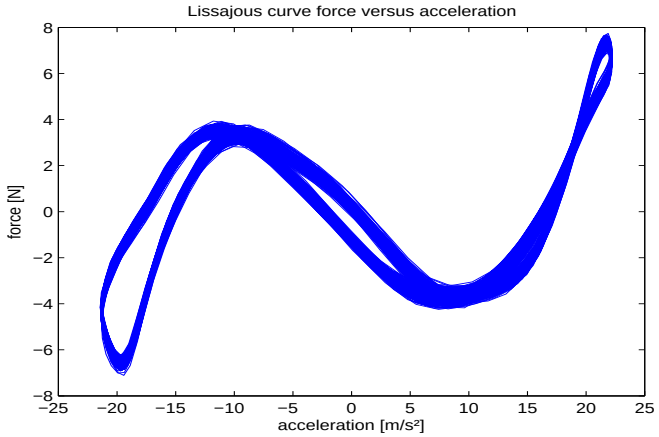

Figure 9.3: Lissajous curve of force versus acceleration m/s^2 for an eigenfrequency of 13.85Hz, an amplitude $fy_{max} = 40mm/s$ and at a tension of 15.32%RTS

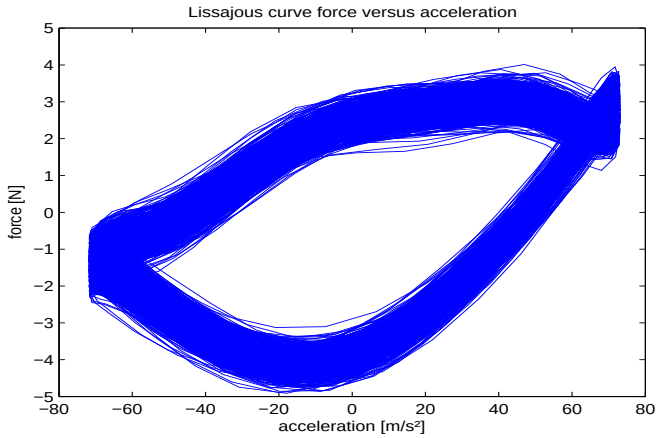

Figure 9.4: Lissajous curve of force versus acceleration m/s^2 for an eigenfrequency of 30.05Hz, an amplitude $fy_{max} = 80mm/s$ and at a tension of 24.1%RTS

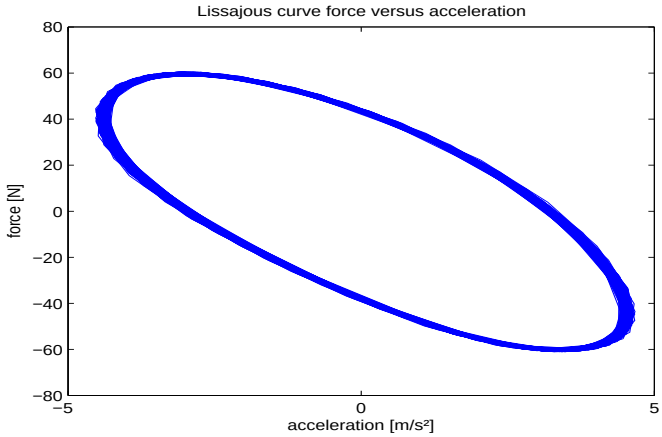

Figure 9.5: Lissajous curve of force versus acceleration m/s^2 for an eigenfrequency of 49.83Hz, an amplitude $fy_{max} = 40mm/s$ and at a tension of 24.%RTS

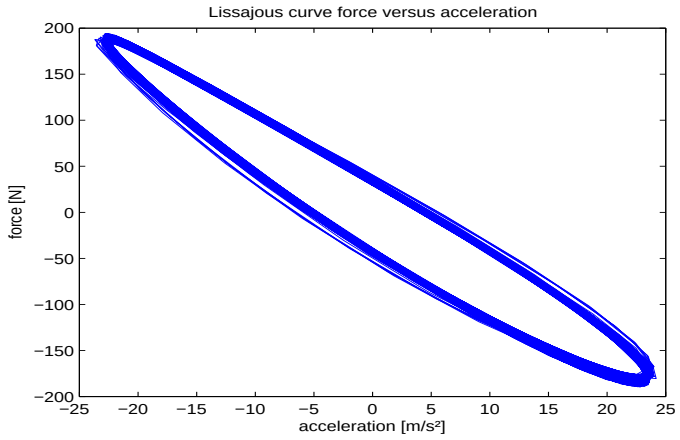

Figure 9.6: Lissajous curve of force versus acceleration m/s^2 for an eigenfrequency of 49.83Hz, an amplitude $fy_{max} = 73mm/s$ and at a tension of 24.%RTS

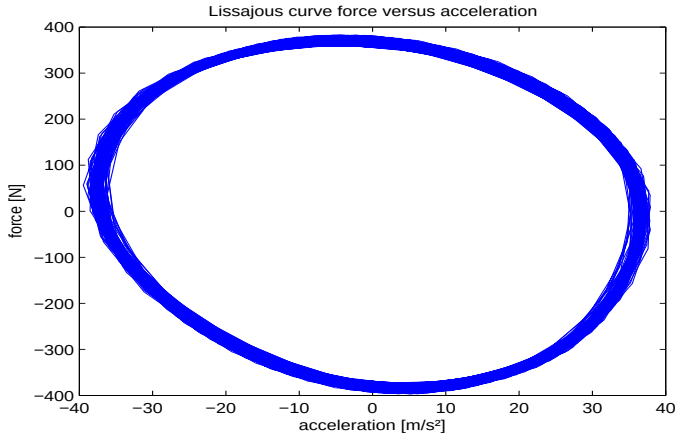

Figure 9.7: Lissajous curve of force versus acceleration m/s^2 for an eigenfrequency of 49.83Hz, an amplitude $fy_{max} = 161mm/s$ and at a tension of 24%RTS

9.4 Excitation force

Here are some example of curves of excitation force obtained during the tests. In some cases, particularly for low frequencies of vibrations (less than 30 Hz), the presence of harmonics 2 and 3 of the excitation force was very important (see e.g. figures 9.8).

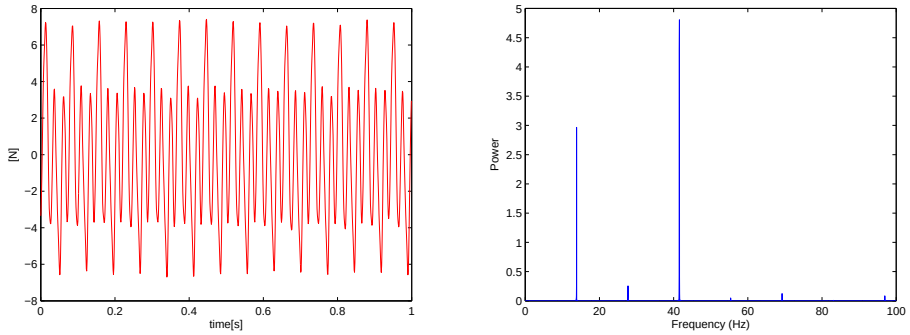

Figure 9.8: Force and frequency content of force for an excitation frequency of 13.85Hz, an amplitude $fy_{max} = 40mm/s$ and a tension of $15.32\%RTS$. If X is the discrete fourier transform of the force signal, the vertical axis of the right figure shows $(\frac{|X_k|}{N})^2$.

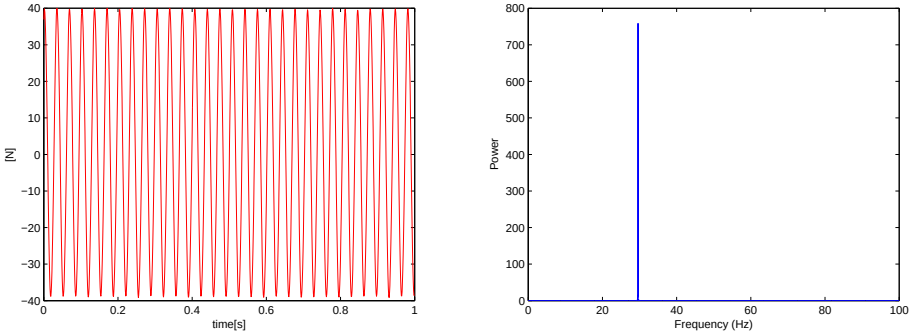

Figure 9.9: Force and frequency content of force for an excitation frequency of 29.6Hz, an amplitude $fy_{max} = 40mm/s$ and a tension of $15.32\%RTS$. If X is the discrete fourier transform of the force signal, the vertical axis of the right figure shows $(\frac{|X_k|}{N})^2$.

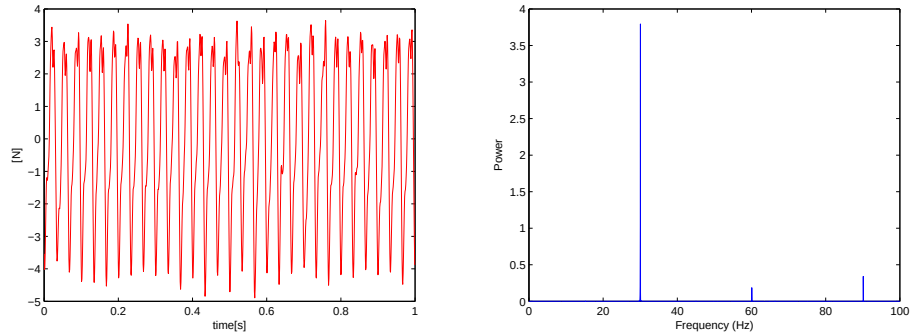

Figure 9.10: Force and frequency content of force for an excitation frequency of 30.05Hz, an amplitude $fy_{max} = 80mm/s$ and a tension of 24.1%RTS . If X is the discrete fourier transform of the force signal, the vertical axis of the right figure shows $(\frac{|X_k|}{N})^2$.

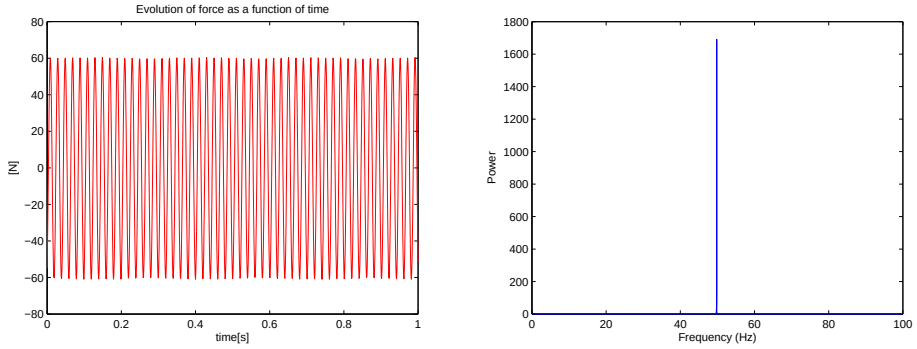

Figure 9.11: Force and frequency content of force for an excitation frequency of 49.83Hz, an amplitude $fy_{max} = 40mm/s$ and a tension of 24%RTS . If X is the discrete fourier transform of the force signal, the vertical axis of the right figure shows $(\frac{|X_k|}{N})^2$.

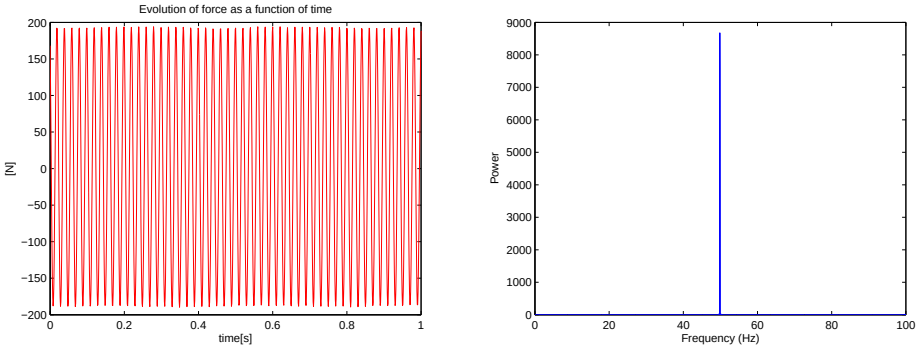

Figure 9.12: Force and frequency content of force for an excitation frequency of 49.83Hz, an amplitude $fy_{max} = 73mm/s$ and a tension of 24%RTS . If X is the discrete fourier transform of the force signal, the vertical axis of the right figure shows $(\frac{|X_k|}{N})^2$.

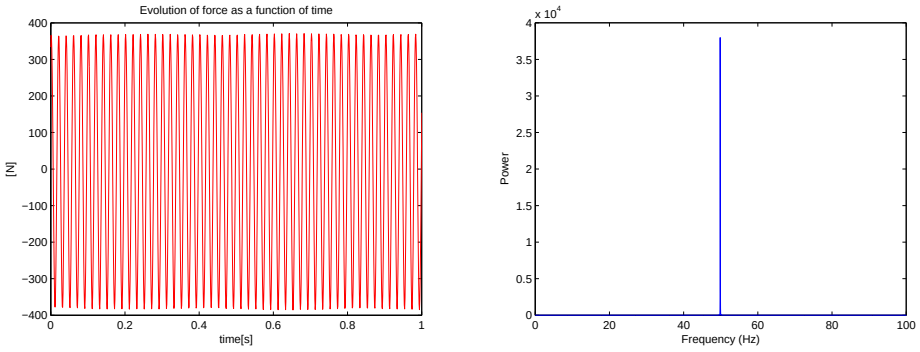

Figure 9.13: Force and frequency content of force for an excitation frequency of 49.83Hz, an amplitude $fy_{max} = 161mm/s$ and a tension of $24\%RTS$. If X is the discrete fourier transform of the force signal, the vertical axis of the right figure shows $(\frac{|X_k|}{N})^2$.

9.5 Amplitudes at "nodes" of vibration

Locating a vibration node requires much precision in order to collect valuable amplitude data, whereas a rough evaluation of the position of a vibration antinode leads to acceptable results. Physically, the difficulty to locate a vibration "node" has to see with the slope of the mode shape, which is maximum at a vibration "node" and minimum (close to zero) at a vibration antinode. Here are some examples of vibrations recorded at nodes and an analysis of their frequency content (figures 9.14-9.16):

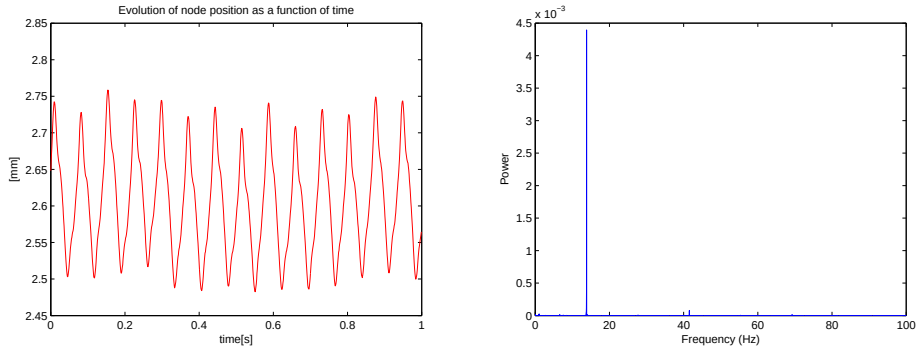

Figure 9.14: Evolution and frequency content of node amplitude for an excitation frequency of 13.85Hz, an amplitude $fy_{max} = 40mm/s$ and a tension of $15.32\%RTS$. If X is the discrete fourier transform of the node signal, the vertical axis of the right figure shows $(\frac{|X_k|}{N})^2$.

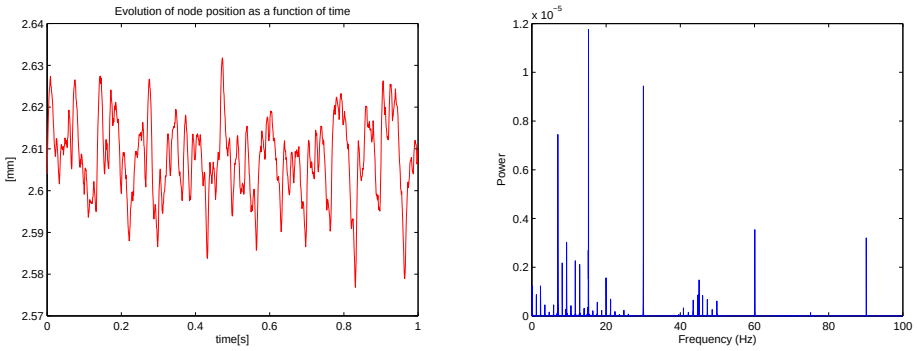

Figure 9.15: Evolution and frequency content of node position for an excitation frequency of 30Hz, an amplitude $fy_{max} = 80mm/s$ and a tension of 24.1%RTS . If X is the discrete fourier transform of the node signal, the vertical axis of the right figure shows $(\frac{|X_k|}{N})^2$.

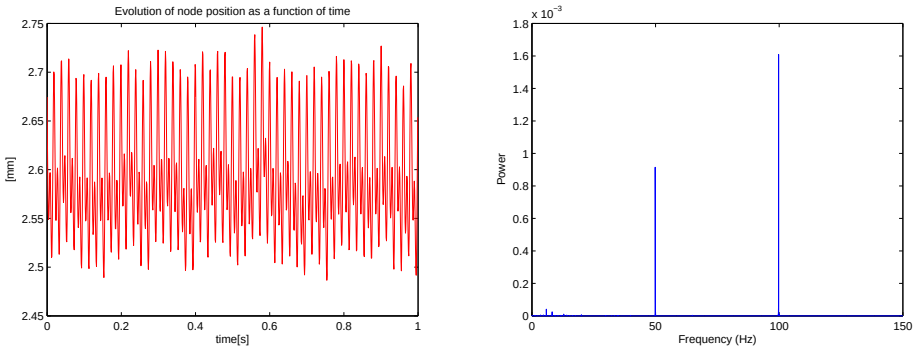

Figure 9.16: Evolution and frequency content of node position for an excitation frequency of 49.83Hz, an amplitude $fy_{max} = 160mm/s$ and a tension of 24.1%RTS. If X is the discrete fourier transform of the node signal, the vertical axis of the right figure shows $(\frac{|X_k|}{N})^2$.

According to these figures, the motion at vibration nodes contains other components than the excitation frequency. For the case at 30Hz, $fy_{max} = 80mm/s$ and a tension of $24.1\%RTS$, it has been seen in one of the previous paragraphs that the excitation force is not a pure sinusoid and this may explain the presence of other components in the vibration of nodes. But what is interesting to note is that for the case at 49.83Hz, $fy_{max} = 160mm/s$ and an tension of $24.1\%RTS$, a strong component at twice the excitation frequency is present, even if the excitation force is a pure sinusoid. This component could be due to tension fluctuations.

9.6 Amplitudes at antinode of vibrations

Amplitudes at antinodes of vibrations were systematically recorded. Here is a series of views (figures 9.17-19). These figures simply show that the main component of antinode vibrations is the same as the excitation frequency.

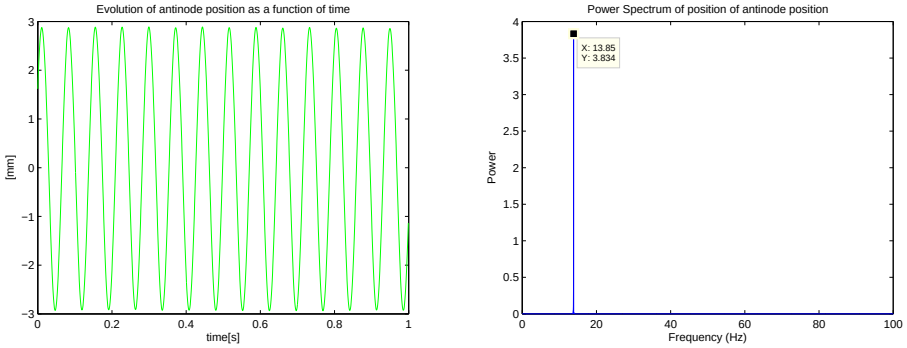

Figure 9.17: Evolution and frequency content of antinode position for an excitation frequency of 13.85Hz, an amplitude $fy_{max} = 40mm/s$ and a tension of $15.32\%RTS$. If X is the discrete fourier transform of the antinode signal, the vertical axis of the right figure shows $(\frac{|X_k|}{N})^2$.

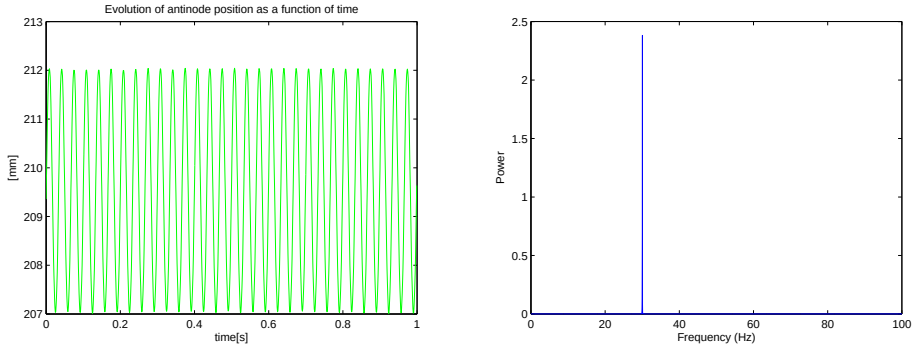

Figure 9.18: Evolution and frequency content of antinode position for an excitation frequency of 30Hz, an amplitude $fy_{max} = 80mm/s$ and a tension of 24.1%RTS. If X is the discrete fourier transform of the antinode signal, the vertical axis of the right figure shows $(\frac{|X_k|}{N})^2$.

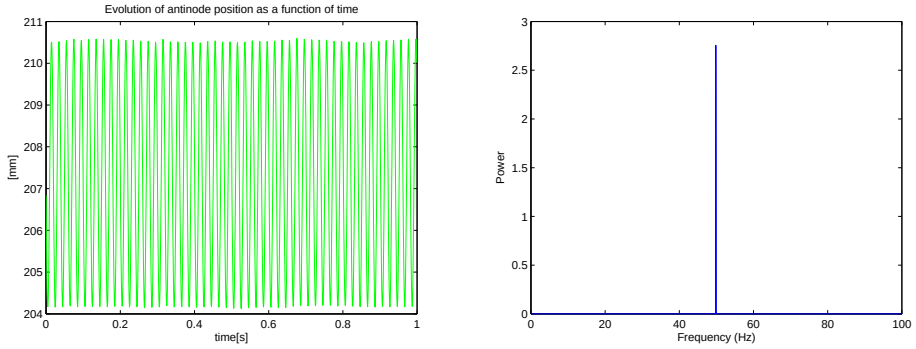

Figure 9.19: Evolution and frequency content of antinode position for an excitation frequency of 49.83Hz, an amplitude $fy_{max} = 160mm/s$ and a tension of 24.1%RTS. If X is the discrete fourier transform of the antinode signal, the vertical axis of the right figure shows $(\frac{|X_k|}{N})^2$.

9.7 Conclusions

The experimental curves of this chapter illustrate how difficult it is to perform a tuning operation on a 63.5m span. The Lissajous curves show that for some tests, the phase shift between force and acceleration keeps fluctuating. Most of the time, the phase shift between acceleration and excitation force is remote from 90 degrees, the expected value at resonance. Nevertheless, a case very near resonance is obtained at a frequency of 49.83Hz, an amplitude $fy_{max} = 160mm/s$ and a tension of $24.1\%RTS$: the phase shift between acceleration of force is worth about 94 degrees. For this same case at $fy_{max} = 160mm/s$, a frequency content analysis of the vibration at a "node" shows an important contribution at twice the excitation frequency. Given the excitation force is a pure sinusoid for that case, this contribution at twice the excitation frequency may be due to tension variations.

Chapter 10

Potential impact of the "non linear damping" in the energy balance

10.1 Introduction

Some verifications of the computation results have already been performed within the "modelling part" of this thesis. As an example:

- changes in tension computed with the finite element software have been confirmed analytically (chapter 6).
- The self damping power per unit length deduced from Godinas' measurements has been compared to other results from the literature. A fairly good agreement has been obtained (chapter 7).

In the present chapter, the aim is to seize the potential impact of changes in tension within an energy balance of the vibrating conductor.

Since there is no accurate data available on the power injected within the span for the tests performed at Ireq's laboratory, those measurements cannot serve as a basis for an energy balance.

This is why simulation results are being used in this chapter.

Once the vibration is installed, one can assume that the input power only serves to compensate the losses. In the finite element model of the vibrating span, there is no aerodynamic damping, nor span-end losses. It is therefore believed that the damping consists in conductor intrinsic self damping and the damping effect of non linearities. Ideally, simulations should be performed with beam elements, where the viscoelastic material model presented in chapter 7 has been implemented. This option has been investigated. Unfortunately, it was not applicable using Samcef V13.0 because the prestress of the beam, imposed via a thermal stress, was not taken into account (yet) by the corresponding version of the viscoelastic material routine.

It was therefore decided to model the conductor self damping by means of the proportionnal damping described in chapter 6. To be more precise, a mass proportional damping coefficient equal to 0.1 was used: this value leads to realistic amplitudes of vibrations (referring to the tests performed on Ireq's laboratory test span).

The simulation conditions are similar as those of chapter 6:

- ACSR Crow conductor,
- Tension equal to about 25% RTS,
- Harmonic excitation force of 30N (0-peak),
- excitation frequency of 20.98Hz,
- span length equal to 63.5m.

10.2 Energy injected within the beam

The energy injected within the span W_{in} is given by $W_{in} = \pi F \mu \sin(\phi)$ [25] (formula 2.3-9), where F is the single-peak amplitude of the excitation force, μ is the single-peak amplitude at the location of the excitation, and ϕ is the phase shift between those signals. The amount computed by this formula therefore corresponds to the area within the Lissajous curve shown in figure 6.7. In the present case, $F = 30N$, $\mu = 0.0045m$, giving $W_{in} \approx 0.4J$. The power injected is obtained by multiplying the previous result by the excitation frequency, giving about $9W$.

10.3 Energy dissipated within the conductor

As already discussed in details in chapter 6, the estimation of the conductor self damping per unit length should be performed via a method which is not influenced by the conductor non linearities. As an example, it could be deduced with the new method proposed in chapter 7 provided the required data is available. Unfortunately, this is not the case for an ACSR Crow conductor. The amount of self damping per unit length has therefore been roughly estimated by means of the ISWR method, under the hypotheses described in chapter 1. From the time evolution of both the antinode and node amplitude of vibration (see figures 6.8 and 6.9), one can compute the "snapshot" inverse standing wave ratio and then the power dissipated within the span. The results are presented in figure 10.1.

The average dissipated power computed by ISWR is worth 5W which is inferior to the injected power. Its standard deviation value is 2W, which is an important amount. In the figure, one can see the important fluctuations of the ISWR power due to the fluctuations of the vibration node amplitude.

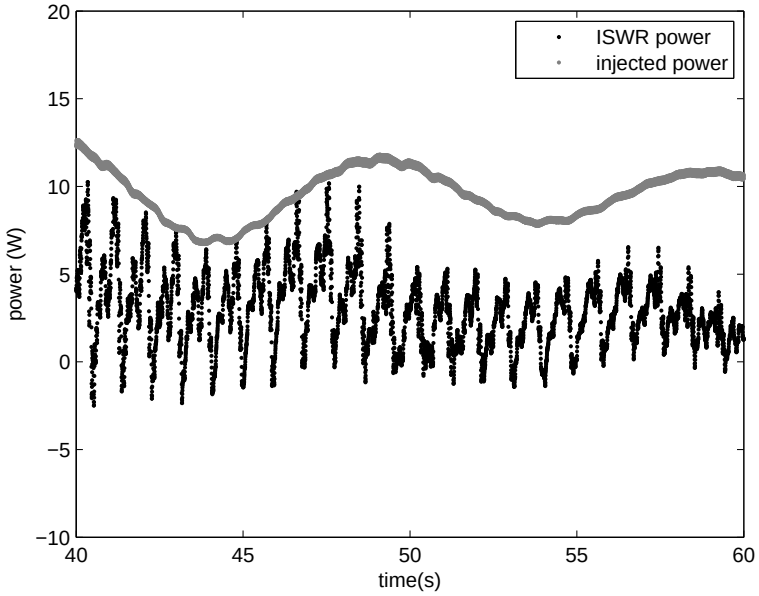

Figure 10.1: Variable tension problem. ISWR power dissipated within the span and injected power. The mass proportional damping coefficient is equal to 0.1, the excitation frequency to 20.98Hz and the excitation amplitude to 30N, $A/d = 0.2$

10.4 Axial strain energy

The instantaneous change in strain energy of the cable due to a change in the axial force $\Delta N(t)$ may be written :

$$W_g(t) = \int_0^L \Delta N(t)\varepsilon(x,t)dx \tag{10.1}$$

where $\varepsilon_x \approx \frac{1}{2}((\frac{\partial y}{\partial x})^2 - (\frac{\partial y_0}{\partial x})^2)$ (y_0 is the initial vertical coordinate)

It results that

$$W_g(t) \approx \frac{1}{2}\int_0^L \Delta N(t)((\frac{\partial y}{\partial x})^2 - (\frac{\partial y_0}{\partial x})^2)dx \tag{10.2}$$

Referring to section 6.3, $y_0(x)$ and $y(x,t)$ satisfy

$$y_0(x) = P\cosh(\frac{x - L/2}{P}) - P\cosh(\frac{L}{2P})$$

$$y(x,t) = P\cosh(\frac{x - L/2}{P}) - P\cosh(\frac{L}{2P}) + A_k \sin\frac{k\pi x}{L}\cos(\omega t)$$

Their derivatives are

$$\frac{\partial y_0}{\partial x} = \sinh(\frac{x - L/2}{P}) \tag{10.3}$$

$$\frac{\partial y}{\partial x} = \sinh(\frac{x - L/2}{P}) + A_k\frac{k\pi}{L}\cos\frac{k\pi x}{L}\cos(\omega t) \tag{10.4}$$

Introducing these values in the previous integral (10.1), the increase in length can be estimated. In the present case, its order of magnitude is $5 * 10^{-4}$m for the 63.5m span. Knowing that the value of ΔN is a few hundreds of Newtons (see figure 10.2), a strain energy value of the order of 0.05J can be expected. The order of magnitude of the average axial strain power is 1W.

10.5 Conclusions

For all the reasons discussed in chapter 6, linked to non-linearities, self damping measurements using dynamic testing is particularly challenging. In this chapter, the potential impact of changes in tension within an energy balance of the vibrating conductor has been studied. With the new self damping measurement method proposed in chapter 7, the potential impact of non linearities on measurements can be avoided. Unfortunately, no test data using this new method is available for the ACSR Crow conductor modelled in chapters 5 and 6. The self damping power has therefore been roughly estimated via the ISWR method. The results show that the computed ISWR power is systematically inferior or equal to the injected power.

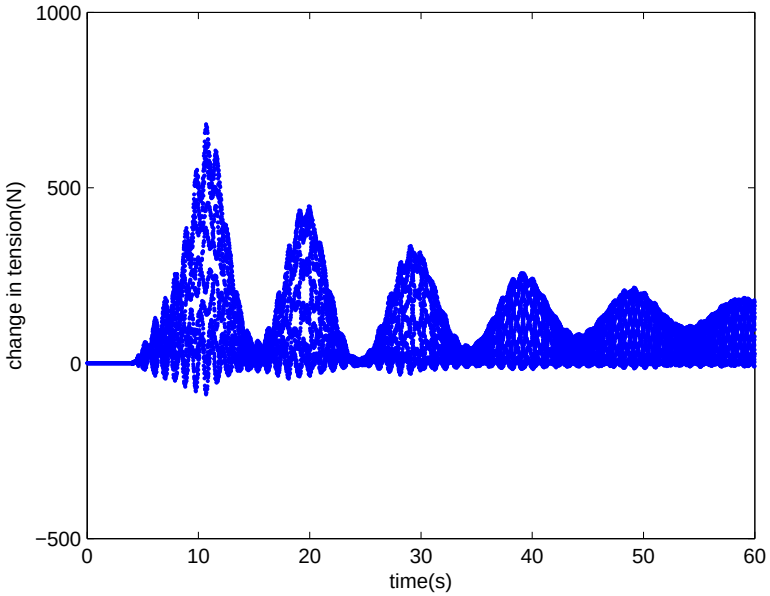

Figure 10.2: Variable tension problem. Change in tension for a mass proportional damping coefficient equal to 0.1, excitation frequency of 20.98Hz

Once the motion is initiated, the tension in the cable is higher (or equal) than at rest and keeps fluctuating (see figure 6.2). This continuous change in tension generates a continuous change in the axial strain of the cable and therefore consumes energy. As shown in section 10.4, the difference between the injected power and the ISWR power has the same order of magnitude than the power which could be dissipated in axial strains. Also, as demonstrated in section 6.4.3 for a single dead-end span, the higher the fy_{max} indicator, the higher the changes in tension and hence the corresponding power dissipation. In the present case, characterized by fy_{max} equal to 80mm/s, which is an average value for aeolian vibrations, the power dissipated by changes in tension may range from 10 % to a few tens of percents of the injected power.

Part V

General Conclusions

Chapter 11

General Conclusions

11.1 The new multi-tool strategy to assess conductor self damping

The core contribution of this thesis is the elaboration of a new strategy to correctly estimate the self damping of overhead power line cables. The strategy is a combination of three kinds of tools:

- laboratory quasi-static tests to measure hysteresis curves [1],
- the tuning of the parameters of a viscoelastic material model,
- on-site real time continuous measurements.

The laboratory tests are part of a new self damping measurement method which offers several advantages, the major one being the measurement of hysteresis curves can be performed quasi-statically [2], so that undesirable dynamic effects linked to changes in tension and coupling between longitudinal and vertical motion are automatically avoided. Moreover, only a limited number of tests are required: provided the whole curvature range corresponding to aeolian vibration is covered by the tests, only one moment versus curvature curve is required per conductor tension level. Also, the test procedure is simple.

The moment versus curvature hysteresis curves collected in laboratory are used to tune a viscoelastic material model. Even though the latter model is able to reproduce the observed behaviour of the conductor in all its complexity, it still remains simple and manageable. Once implemented in a non-linear beam finite element, it permits to predict on-site amplitudes.

[1] In fact, moment versus curvature curves. The area within the hysteresis represents the conductor self damping and the slope the hysteresis its variable bending stiffness.

[2] Experimentally, it has been observed that the shape of the hysteresis curves was not influenced by the loading speed. In other words, the same hysteresis curves will be recorder, whether the tests are performed dynamically or quasi-statically.

Other achievements have been managed processing adequately the laboratory data. A formulation for the self damping per unit length has been proposed by the author. The predicted power values are consistent with those deduced from the widely used *Power law*, using Noiseux's exponents [62, 25]. A simplified formulation has permitted to show that the sensitivity of the self damping to the vibration amplitude, frequency and tension is comparable to that found by other authors, using another measurement method. The main advantages of the new proposed formula are that it is dimensionally correct and also that the exponents of frequency, amplitude, and tension are integers, fully justified by the physics behind the damping phenomenon. Last, the conductor variable bending stiffness has been deduced from the quasi-static tests. The values found agree well with other experimental results or models.

11.2 Understanding the impact of non-linearities

Another interesting contribution concerns non-linearities linked to variable tension and coupling between longitudinal and transversal motion. Their potential impact has been highlighted, even though the amplitudes at stake are small [3]. This has led to some original developments to better understand the interaction of this non-linear effect with the aeolian vibration phenomenon. Several undesirable consequences have been demonstrated by the author, e.g.:

- The artificial damping effect of these non-linearities,
- Potential differences between changes in tension met on a laboratory span versus real spans.

Those changes in tension must be dealt with adequately so as to produce a correct estimation of the conductor self damping properties using dynamic tests. To remain constructive, here are some proposals:

- Use an adequate non-linear finite element model to separate the contributions of non linearities versus conductor intrinsic self damping,
- Use the new self damping measurement method proposed in chapter 7, which is proof against the dynamic impact of non-linearities,
- Perform real on-site measurements. As explained in chapter 3, the latter bring unique information on the effective self damping, which is a combination of among others span end effects, interactions between the cable and the air, cable self-damping. In suspended spans, the resulting amplitudes may also depend on the interactions between adjacent spans.

[3] Their order of magnitude may reach the conductor diameter.

In the "Validation part" of this work the power dissipated by the non-linearities (via the coupling between longitudinal and transversal motion) has been estimated via an energy balance for a given case study, at an average aeolian vibration amplitude ($fy_{max} = 80mm/s$). The amount found is significant. As explained in section 6.4, for a single dead-end span, the higher the fy_{max} value, the higher the amplitude of changes in tension (all other things being equal). Therefore, the amount of power dissipated via the non-linearities may be more important yet for a higher fy_{max} value ($fy_{max} = 200mm/s$ may be considered as a maximum for aeolian vibrations).

11.3 Superiority of real on-site measurements

Many results of this thesis also show the superiority and advantages of real on-site measurement.

The comparison of the widely used fatigue parameters Y_b and fy_{max} has shown that the study of the relative amplitudes in the vicinity of span extremities is only part of the vibration information: all span locations where the movement of the conductor is restrained may be at risk (near the clamp of vibration dampers, air warning markers, spacers, etc.). An adequate vibration risk analysis requires in-span measurements too.

As shown in chapter 3 and 7, based on real on-site self-damping measurements, it is possible to fit the coefficients of either the widely used power law or the new formulation presented in chapter 7 in order to adequately predict the real vibrational behaviour of a conductor.

Concerning the opportunities associated to the detection of wire failures thanks to on-site measurements, the following key information may be retained from chapter 4:

- The laboratory failures have been detected by the author using the rotational acceleration and longitudinal acceleration recorded by tri-axis accelerometers located in the vicinity of the span clamp.
- The failure pattern may vary from one type of conductor to another (e.g. from and ACSR conductor to an AAAC one),
- The failure is easier to detect when it takes place within external layers.

In real world, the vibrational amplitudes will continually vary. The impact of a failure may be flooded by those continual changes. For this reason, the author recommends to study the longitudinal accelerations, because the "noise" level according to the conductor axis is less than according to others. To improve real world failure detection, the author recommends to combine

acceleration measurements with the tracking of eigen frequencies and conductor average temperature. On the one hand, for the all aluminium alloy conductor, each failure concurred with a decrease in the eigen frequencies and on the other hand, it is important to distinguish the changes in frequencies caused by a wire failure from changes in frequencies caused by a change in conductor average temperature.

Last, the damping impact of non linearities is a valid motive to promote real on-site measurements.

For all those reasons, laboratory measurements and conductor modelling, though helpful, can not bring the same information as on-site studies. In the latter approach, the problem is studied as a whole, with all interactions and complexities taken into account. Performing on-site measurements also has a cost, but it brings the most complete picture of vibrational risks.

11.4 Future work

For future work, it would certainly be interesting to implement the viscoelastic material model within a non-linear beam finite element. Provided the material model is able to automatically adjust the viscoelastic parameters to follow the recorded moment versus curvature curve [4], this would permit to simulate the conductor answer in any kind of aeolian vibration. Both the variable bending stiffness and conductor self damping would be taken into account.

[4] only one curve has to be recorded per conductor tension level, provided it spans the curvature range of aeolian vibrations

Part VI

Appendixes

Appendix A

Experimental moment versus rotation angle curves recorded by Godinas

A.1 AMS 621

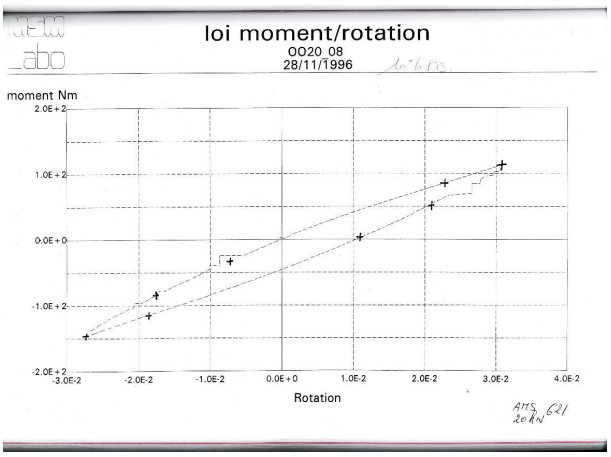

Figure A.1: AMS 621, Moment versus rotation angle for a tension equal to 20000N (10 % RTS)

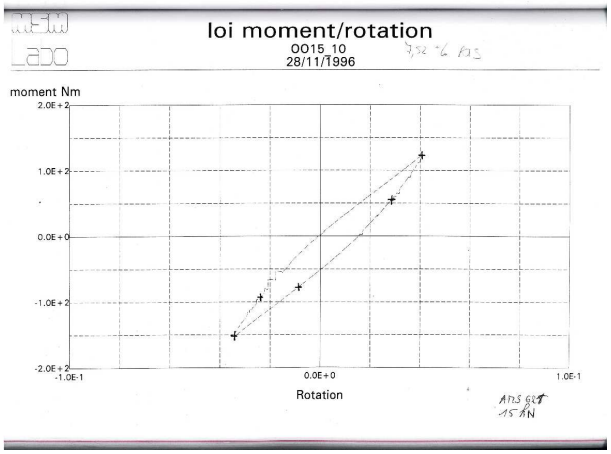

Figure A.2: AMS 621, Moment versus rotation angle for a tension equal to 15000N (7.5 % RTS)

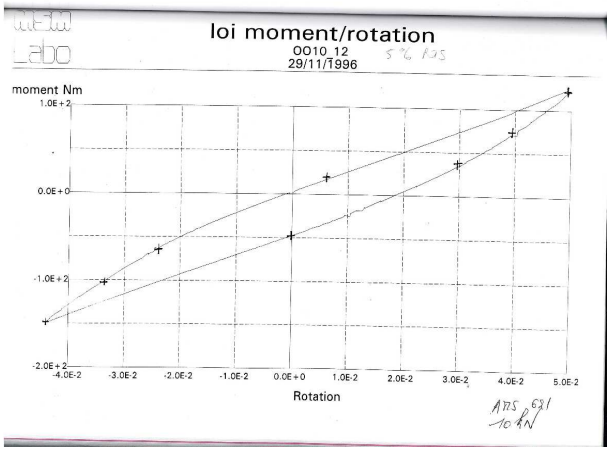

Figure A.3: AMS 621, Moment versus rotation angle for a tension equal to 10000N (5 % RTS)

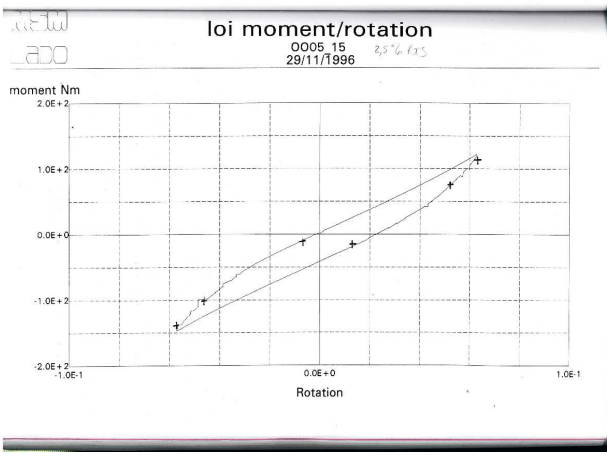

Figure A.4: AMS 621, Moment versus rotation angle for a tension equal to 5000N (2.5 % RTS)

A.2 AMS 298

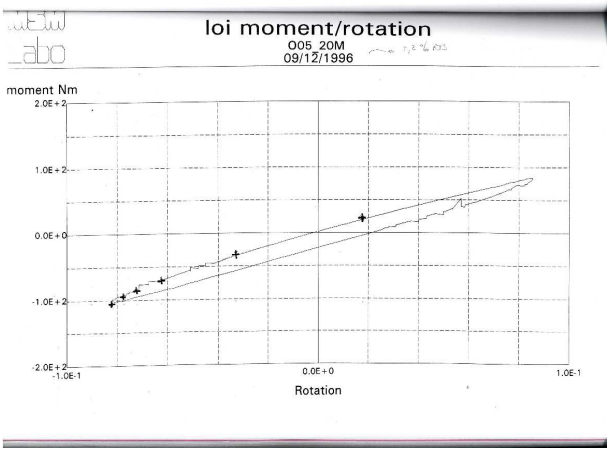

Figure A.5: AMS 298, Moment versus rotation angle for a tension equal to 5000N (5 % RTS)

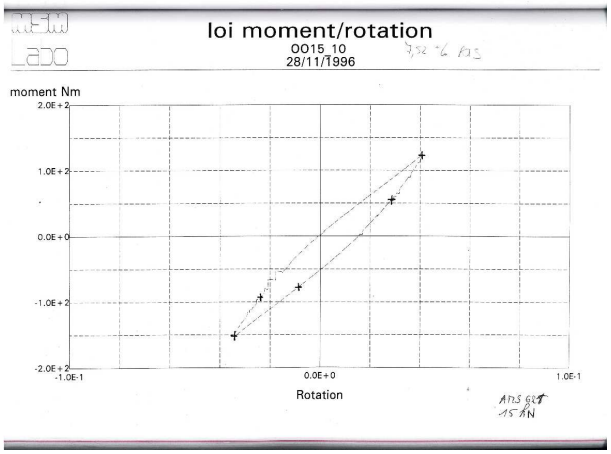

Figure A.6: AMS 298, Moment versus rotation angle for a tension equal to 10000N (10.4 % RTS)

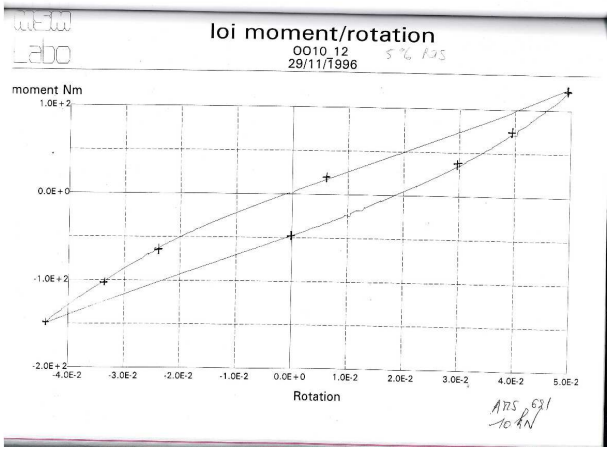

Figure A.7: AMS 298, Moment versus rotation angle for a tension equal to 20000N (20.9 % RTS)

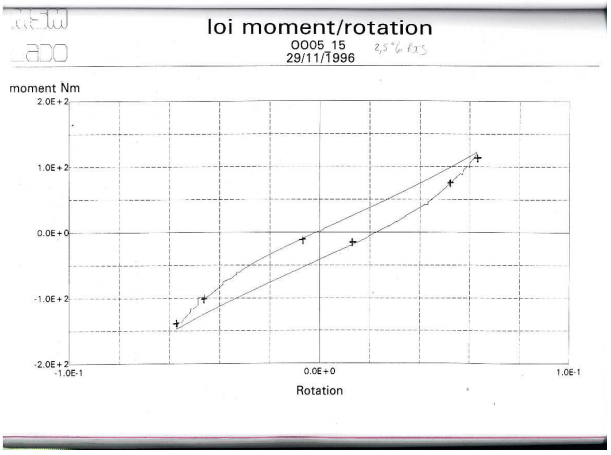

Figure A.8: AMS 298, Moment versus rotation angle for a tension equal to 30000N (31.3 % RTS)

Appendix B

Dissection reports

B.1 AAAC conductor

DISSECTION - ESSAI DE FATIGUE

Programme d'essais

Code : _____

Essai : _____

Y_b nominal : 0,7 mm

Date de la dissection : 25/05/2008 Par : Simon

Mesure de la traction (conducteur décroché) : T = 2,84 kN

Code des couleurs pour le marquage des fils :

- Point de mesure de l'amplitude, 89 mm du DPC (violet)
- Contrôle des ruptures (bleu - fin)
- Centre de la pince (vert)
- Position du DPC (rouge)
- Position du chapeau (orange)
- Ligne axiale indiquant le haut du conducteur (rouge)

Mesures axiales :

- Distance entre le centre de la pince et le point de mesure : 162 mm
- Distance entre le centre de la pince et le DPC : 73 mm
- Distance entre le DPC et le point de mesure (89 mm) 89 mm
- Position DPC du chapeau p/r DPC : -16 mm p/r centre : 57 mm
- Position des marques de contact avec la pince (p/r DPC) : -4 mm

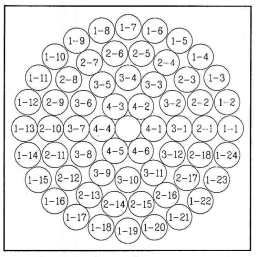

Section type du conducteur
Numérotation des fils au centre de la pince, en regardant vers la portée.

Ruptures :

Numéro du fil rompu	*Position angulaire de la rupture*	*Position axiale de la rupture*	*Marques de contact*	*Remarques*
1-15	1 - 13	- 14 mm	◯	
1-3	1 - 6	- 13 mm	◯	
1-4	1 - 7	- 17,5 mm	◯	
			◯	
			◯	
			◯	

Positions axiales des ruptures mesurées par rapport à : (DPC) *Centre de la pince / Point de mesure*
Valeurs positives vers la portée, négatives vers le centre de la pince

Remarques :

Le DPC du chapeau coïncide avec 2 ruptures, ce qui rend la mesure de ℓ_p très difficile

Figure B.1: Dissection report of the AAAC conductor

B.2 ACSR conductor

DISSECTION - ESSAI DE FATIGUE

Code : _____

Essai : _____

Y_b nominal : 0,65 mm et 0,6 mm pour la troisième rupture.

Date de la dissection : 1er juin 2005 Par : Simon

Pas de mesure de traction disponible, le système d'acquisition est à l'extérieur annuel

Code des couleurs pour le marquage des fils :

- Point de mesure de l'amplitude, 89 mm du DPC (noir)
- Centre de la pince (jaune)
- Position du DPC (rouge)
- Ligne axiale indiquant le haut du conducteur (bleu)

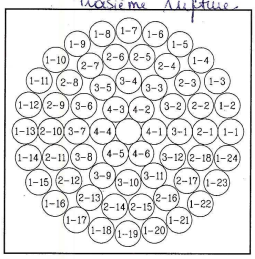

Section type du conducteur
Numérotation des fils au centre de la pince, en regardant vers la portée.

Mesures axiales :

- Distance entre le centre de la pince et le point de mesure : 175 mm
- Distance entre le centre de la pince et le DPC : 86 mm
- Distance entre le DPC et le point de mesure (89 mm) 89 mm
- Position du DPC du chapeau : -24,5 mm
- Position des marques de contact avec la pince : -5 mm

La zone de fretting ayant généré les ruptures est située hors de la pince pour différencier le chiffre, on se place dans cette section au milieu de la pince

Ruptures :

Numéro du fil rompu	*Position angulaire de la rupture*	*Position axiale de la rupture / DPC*	*Marques de contact (coupe dans brin)*	*Remarques*
1-1	1-13	-6,0	○	1e rupture est/ext
1-2	1-20	-3,8	○	2e rupture est/ext
1-3	1-21	-4,7	○	3e rupture est/ext
2-8	2-12	-6,1	○	?
2-9	2-13	-6,8	○	?
2-10	2-15	-2,8	○	?

Positions axiales des ruptures mesurées par rapport à : (DPC) / Centre de la pince / Point de mesure
Valeurs positives vers la portée, négatives vers le centre de la pince

on saute d'1 chiffre pour que les ruptures n'ont pas la même position axiale!

Remarques : Lors des essais, on constate des Δ du capteur à effet Hall (→ soupçons de glissements) beaucoup moins de casse que sur l'AAAC

En enlevant la 1re couche, on découvre 3 ruptures sur la 2e couche

Les ruptures internes sont probablement en lieu entre les ruptures externes

Dissection Crow.wpd 2 of 3

Figure B.2: Dissection report of the ACSR conductor

Appendix C

Calibration of the Hall sensors

C.1 AAAC conductor (testbench 6)

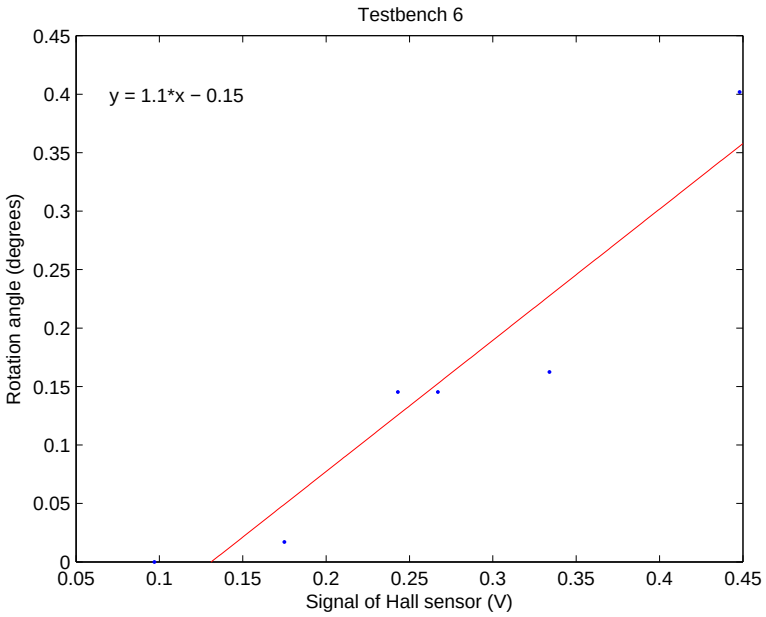

Figure C.1: Calibration of the Hall sensor of test bench 6

C.2 ACSR conductor (testbench 3)

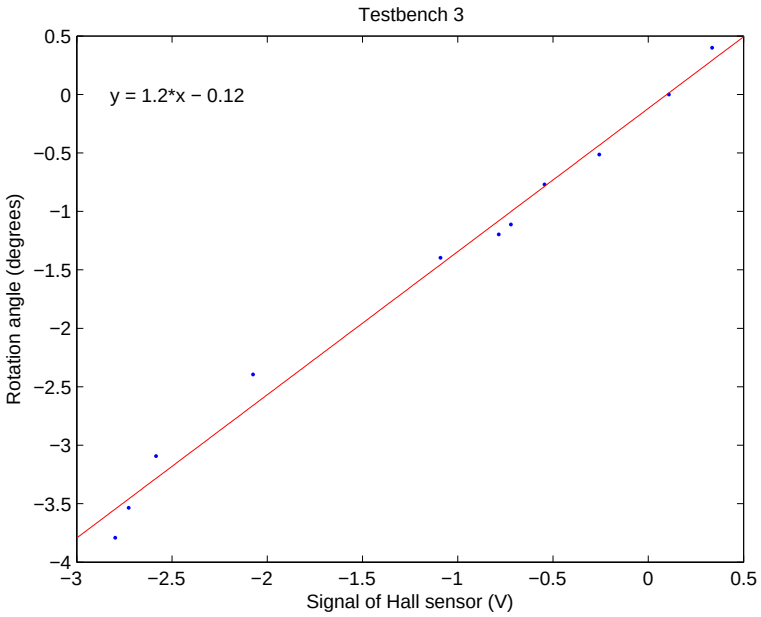

Figure C.2: Calibration of the Hall sensor of test bench 3

Appendix D

Data acquisition: matching between the accelerometer axes and the channels of the acquisition system

- X1 is connected to channel 4,
- Y1 is connected to channel 5,
- Z1 is connected to channel 6,
- X2 is connected to channel 1,
- Y2 is connected to channel 3,
- Z2 is connected to channel 2.

Appendix E

Average bending stiffness of the AAAC conductor

This test was solely possible on the AAAC conductor since some maintenance and update was scheduled on the test bench where the ACSR was tested right after the fatigue tests.

The relationships giving the eigen frequencies of a cable span can be found in e.g. [25, 58]. They permit to estimate the average bending stiffness of the conductor.

$$f_n = \frac{1}{2\pi} * \sqrt{(\frac{n\pi}{L})^2 * \frac{T}{m} * (1 + (\frac{n\pi}{L})^2 \frac{EI}{T})}$$

Given the upper limit of the vibration shaker (80Hz) only the modes 2 to 6 could be excited on the AAAC conductor. It was not possible to excite the first vibration mode.

The following figure shows the evolution of the eigen frequencies as a funtion of their order.

The data collected can be assimilated to an overdetermined system. Its solution leads to a bending stiffness value of $1260 N.m^2$.

A maximum bending stiffness value of $1800 N.m^2$ can be computed using the formula given in the literature ([25]). In the present case, the deduced average bending stiffness value represents approximately 70% of this maximum value. As a comparison, at Ireq's 63.5m laboratory test span, the average bending stiffness deduced from the data represented a little less than 50% of its maximum value for the ACSR Crow conductor strung at 25 % RTS.

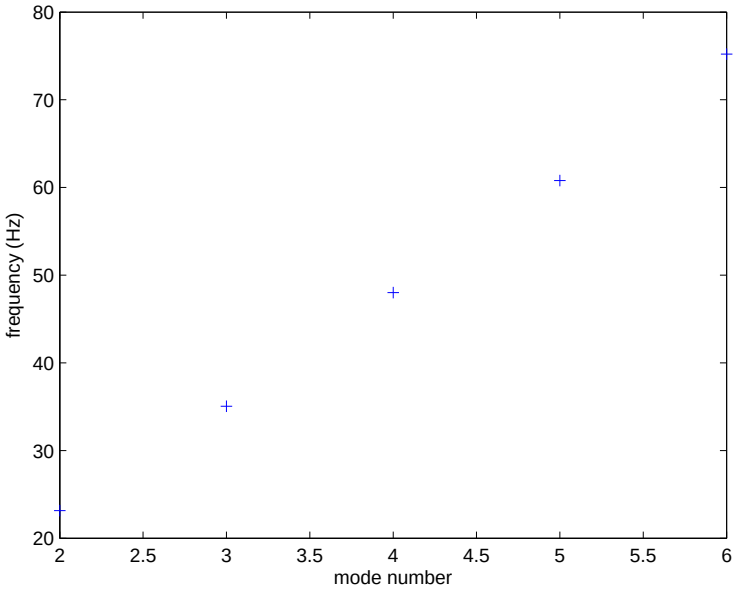

Figure E.1: Evolution of the eigen mode frequencies as a function of their order

Appendix F

Self damping in mechanical systems

F.1 Introduction

Self damping in a real mechanical system can be categorized in three primary categories of energy dissipation: material damping, structural damping and fluid damping. All these categories are present in a cable. The material damping corresponds to the energy dissipation that takes place in the micro-structure; in the case of a conductor, this takes place within a wire. The structural damping involves rubbing friction between components of the mechanical system and contacts at the joints. In the case of a conductor cable, such friction takes place at the contacts between wires or between wires and clamps. Then, the fluid damping results from the interactions between the conductor and the fluid in which it is plunged.

F.2 Material damping

As explained in reference books such as [80], the material damping corresponds to the energy dissipation that takes place in the micro-structure. This primary category can be further classified into viscoelastic and hysteretic damping.

F.2.1 Viscoelastic damping

An example of viscoelastic model is given by the "Kelvin-Voigt" Model in which the relationship between stress and strain is a linear differential equation with respect to time, with constant coefficients:

$$\sigma = \varepsilon E + E^*(\frac{d\varepsilon}{dt}) \tag{F.1}$$

For this model, the damping capacity of a material is frequency dependant (see equation 7.9).

F.2.2 Hysteretical damping

A second model of material damping is named Hysteretical damping. In fact, all types of internal damping produce an hysteresis loop, but the word "hysteretic" in this case means that the stress strain relationship satisfies:

$$\sigma = \varepsilon E + \frac{E'}{\omega} * (\frac{d\varepsilon}{dt}) \tag{F.2}$$

The damping capacity of a Hysteretical material is frequency independent [80].

F.3 Structural damping

Then, structural damping is an energy dissipation mechanism which involves rubbing friction between components of the mechanical system and contacts at the joints. The Coulomb model for example is able to represent the energy dissipation by rubbing:

$$f = c * sgn(\dot{q}) \tag{F.3}$$

where f is the damping force, q is the relative displacement at the joint and c is a friction parameter.

F.4 Fluid damping

The last category, fluid damping is produced when a body is in relative motion with respect to a fluid. The drag force satisfies:

$$f_d = \frac{1}{2} * C_D * \rho * d * \dot{q}^2 * sgn(\dot{q}) \tag{F.4}$$

in which $\dot{q}$ is the relative velocity $[m/s]$, C_D the drag coefficient [1], ρ the fluid density $[kg/m^3]$ and d the conductor diameter [m].

In the case of a vibrating overhead cable, material damping exists within any wire, structural damping at any contact between e.g. two wires, and the interactions between the vibration cable and the fluid in which it is immersed result in fluid damping.

F.5 Viscous damping

The section " material damping" showed relationships between stresses and strains which are defined at the microscopic level of a structure. In the case of a complete mechanical system, characterized by n degrees of freedom, it is more convenient to use a macroscopic damping representation rather than a microscopic one. A simple way to do so is to use an equivalent viscous damping. Let x be the vector of generalized coordinates, K the stiffness matrix of the system, M its mass matrix and f(t) the forcing function vector. The idea contained in the concept is to represent the damping capacity of a system by a so called equivalent viscous damping which is a function of $\dot{x}$ (only) and is characterized by the same amount of damping per cycle as the real one. This linear viscous damping can be introduced in the model by means of the damping matrix C $[Ns/m]$, so that the adapted equations of motion become:

$$M\ddot{x} + C\dot{x} + Kx = f(t)$$

If proportional damping is used, the damping matrix C is a linear combination of the mass and stiffness matrices:

$$C = c_m M + c_k K$$

Bibliography

[1] Alcoa. *Overhead Conductor Vibration*. Aluminum Company of America, 1961.

[2] Cigre W.G. B2.08. Large overhead lines (ovhl) crossings, tb396. Technical report, CIGRE, October 2009.

[3] U. Cosmai (Cigre TF B2.11). Assessment of vibration severity on actual lines. Technical report, Cigre, 2005.

[4] Cigre TF B2.11.01. Modelling of aeolian vibrations of a single conductor plus damper: assessment of technology. *Electra*, (223):28–36, 2005.

[5] Cigre Task Force B2.11.04. Overhead conductor safe design tension with respect to aeolian vibrations. Technical report, Cigre, 2005.

[6] Cigre Task Force B2.12.3. Sag-tension calculation methods for overhead lines. Technical report, Cigre, 2007.

[7] M.O. Bolser and E.L. Kanouse. Type HH cable in vibration and bending. Technical Report 215, Cigre, 1948.

[8] D. Brika and A. Laneville. A laboratory investigation of the aeolian power imparted to a conductor using a flexible circular cylinder. *IEEE Transactions on Power Delivery*, 11(2), April 1996.

[9] A. Cardona. *An integrated approach to mechanism analysis*. PhD thesis, Université de Liège, Faculté des Sciences appliquées, 1991.

[10] A. Cardou, L. Cloutier, and S. Goudreau. Fretting fatigue under spectrum loading- application to overhead electrical conductors (a literature review). Technical report, GREMCA, November 2002.

[11] C. Y. Chin, J. Mitchell, and P. R. Ukrainetz (Cigre SC22-70(SC)-03). On the measurement of conductor vibration. Technical report, August 1970.

[12] R. Claren and G. Diana. Dynamic strain distibution on loaded stranded cables. *IEEE Transactions*, (41), November 1969.

[13] L. Cloutier, C. Dalpe, A. Cardou, S. Goudreau, and C. Hardy. Studies on conductor vibration fatigue tests, flexural stiffness and fretting behavior. In *Third International Symposium on Cable Dynamics*, pages 197–202, 1999.

[14] A. Pinto Da Costa, J. Martins, and J.L. Lilien. Parametric excitation of cables of cable stayed bridges. volume 2, 1994.

[15] A. Pinto da Costa, J. A. C. Martins, F. Branco, and J.L. Lilien. Oscillations of bridge stay cables induced by periodic motions of deck and/or towers. *Journal of Engineering Mechanics*, 122, 1996.

[16] Cigre Comité d'études 6. Vibrations de petite amplitude. *Electra*, (201), 1950.

[17] O. D. Zetterholm (Comité d'Etudes 6). Conducteurs nus et calcul mécanique des lignes aériennes. Technical Report 223, Cigré, 1960.

[18] G. Diana, F. Cheli, F. Fossati, and A. Manenti. Aeolian vibrations of overhead transmission lines, computations in turbulence conditions. *JWE and IA*, (46 and 47):639–648, 1993.

[19] G. Diana, G. Di Giacomo, and R. Claren. An approach to vortex shedding under turbulent air-flow on a single vibrating cylinder. *IEEE SM*, (A79 529), 1979.

[20] C.B. Rawlins (Cigre SCB2-WG11-TF7-04-13 document). A perspective on the interpretation of field recordings of overhead conductor vibration with respect to fatigue. Technical report, Cigre, May 2004.

[21] P. Van Dyke, R. Paquette, and M. St-Louis. Design and test of a new aeolian vibration damper. In *Fourth International Symposium on Cable Dynamics*, May 2001.

[22] A.T. Edwards and J.M. Boyd. Ontario hydro live-line vibration recorder for transmission line conductors. *IEEE Transactions*, 82, June 1963.

[23] M.B. Elton, A.R. Hard, and A.N. Shealy. Transmission conductor vibration tests. *AIEE Trans. On Power Apparatus and Systems*, 78:528–537, August 1959.

[24] Epri, editor. *Transmission Line Reference Book: wind induced conductor motion*. Electric Power Research Institute, Palo Alto, California, United States, 1979.

[25] Epri, editor. *Transmission Line Reference Book: wind induced conductor motion*. Electric Power Research Institute, Palo Alto, California, United States, 2006.

[26] B. Godard. Traitement de signaux vibratoires par ondelettes. Master's thesis, University of Liège, 2006.

[27] A. Godinas. Projet ARC ICARE- amortissement dans les câbles-rapport annuel d'activites. Technical Report 22-70, ULG, 1997.

[28] A. Godinas and G. Fonder. Experimental measurements of bending and damping properties of conductors for overhead transmission lines. In *Third Cable Dynamics Conf. proceedings*, Trondheim (Norway), August 1999.

[29] S. Goudreau, F. Charrette, C. Hardy, and L. Cloutier. Bending energy dissipation of a simplified single layer stranded cable. *ASCE J. of Engineering Mechanics*, 124:811–817, August 1998.

[30] S. Goudreau, C. Jolicoeur, A. Cardou, L. Cloutier, and A. Leblond. Palmgren-miner law application to overhead conductor fatigue prediction. In *Fifth International Symposium on Cable Dynamics*, pages 501–508, Santa Margherita Ligure, Italy, 2003.

[31] S. Goudreau, F. Levesque, and A. Cardou. Analysis of variable loading fatigue tests on overhead conductor using palmgren-miner rule. In *Sixth International Symposium on Cable Dynamics*, Charleston, SC, 2005.

[32] Karl F. Graff. *Wave Motion in Elastic Solids*. 31 East 2nd Street, Minneola, N.Y. 11501, 1991.

[33] S. Guérard, P. Van Dyke, and J.L. Lilien. Evaluation of power line cable fatigue parameters based on measurements on a laboratory cable test span. In *Eigth Cable Dynamics Conf. Proceedings*, Paris, September 2009.

[34] Cigre WG 11 H. J. Krispin. Comparison studies of dynamic behavior of vibration recorders. Technical Report CIGRE Document 22-93(WG11)-75, Cigre, 1993.

[35] P. Hagedorn and U. Gutzer. On the determination of the bending stiffness of conductors by a simple vibration experiment. In *Proceedings of the 2nd International Symposium on Cable Dynamics*, Tokyo (Japan), 1997.

[36] C. Hardy and P. Van Dyke. Field observations on wind-induced conductor motions. *Journal of Fluids and Structures*, pages 43–60, 1995.

[37] C. Hardy and A. Leblond. On the dynamic flexural rigidity of a taut stranded cable. In *Proceedings of the 5th International Symposium on Cable Dynamics*, Santa Margherita, Ligure (Italy), 2005.

[38] C. Hardy, A. Leblond, S. Goudreau, and L. Cloutier. Application of contact mechanics to cable self damping. In *Proceedings of the 3rd International Symposium on Cable Dynamics*, Trondheim (Norway), 1999.

[39] Hashin. A reinterpretation of the palmgren-miner rule for fatigue life prediction. *ASME Trans. Journal of Applied Mechanics*, 47:324–328, June 1980.

[40] R. C. Heics and D. G. Havard. Influence of vibration recorders on conductor vibration. *IEEE Transactions on Power Delivery*, 9:919–938, April 1994.

[41] R. Helms. Zur sicherheit der hochspannungs freileitungen bei hoher mechanischer beanspruchung. Technical report, VDI, Forschungsheft 506, Berlin, 1964.

[42] B. Hondalus. Comparative vibration fatigue tests 84/19 acsr chukar vs 61-strand 5005. *IEEE Transactions paper*, PAS-83:971–974, 1964.

[43] IEEE. Ieee guide for aeolian vibration field measurement of overhead conductors. Technical Report Std 1368 TM-2006, IEEE, 2006.

[44] K. L. Johnson. *Contact Mechanics*. Cambridge University Press, Cambridge, 1985.

[45] Z. Josiki, A. Kierski, K. Lewichi, and W. Lieszkowski. New overhead transmission lines in the polish network-service experience. Technical Report Cigre Report 22-05, Cigre, 1976.

[46] R.F. Steidel Jr. Factors affecting vibratory stresses in cables near the point of support. In *AIEE Transactions*, number 78, pages 1207–1212.

[47] F. Kiessling, P. Nefzger, J.F. Nolasco, and U. Kaintzyk. *Overhead Power Lines, Planning, design and construction*. Springer, Berlin, 2003.

[48] V. Lamacq, M.C. Dubourg, and L. Vincent. Crack path prediction under fretting fatigue- a theoretical and experimental approach. *Journal of Tribology*, 118/711, October 1996.

[49] A. Laneville. Experiments on vortex-induced vibrations of a long flex. cylinder vibrating freely in air flow: the crit. curve and the exist. of the 2p and 2s. In *4th Conference on Bluff Body Wakes and Vortex-Induced Vibrations*, 2005.

[50] J.L. Lilien. Galloping and compact line. In *Cigre Symposium on Compacting Overhead Transmission Lines, Report 200-01*, Leningrad, June 1991.

[51] J.L. Lilien and A. Pinto Da Costa. Vibration amplitudes caused by parametric excitation of cable stayed structures. *Journal of Sound and Vibration*, 174, 1994.

[52] J.L. Lilien, H. Dubois, and F. Del Maso. General mathematical formulation for overhead line galloping. In *AIM Study day on Galloping*, March 1988.

[53] J.L. Lilien, S. Guérard, J. Destiné, and E. Cloet. Microsystems array for live high voltage lines monitoring. In *CIGRE session B2 302 2006*, 2006.

[54] J. C. Little, D.G. Mac Millan, and J.V. Majercak. Vibration and fatigue life of steel strand. *AIEE Transactions*, 69:1473–1479, 1950.

[55] S. Mallat. *Une exploration des signaux en ondelettes*. Les Editions de l'Ecole polytechnique, 91128 Palaiseau cedex, 2000.

[56] Ch. Massonnet and S. Cescotto. *Mécanique des Matériaux*. Sciences et Lettres, Liège, 1980.

[57] M. A. Miner. Cumulative damage in fatigue. *ASME J. Appl. Mech.*, 12, 1945.

[58] P. M. Morse. *Vibration and Sound*. Mc Graw-Hill, NY, 1948.

[59] Y. Nakayama, T.Ikeya, K. Yamagata, J. Katoh, and T. Munakata. Vibration fatigue characteristics of 470mm2 aaac. Technical Report 22-70, CIGRE, 1970.

[60] N.M. Newmark. A method of computation for structural dynamics. *Proc. ASCE, J. Eng. Mech. Div. 85*, pages 67–94, 1959.

[61] D. U. Noiseux, S. Houle, and R. Beauchemin. Transformation of wind tunnel data on aeolian vibrations for application to random conductor vibrations in a turbulent wind. In *IEEE/PES*, SM. Mexico City, 1988.

[62] D.U. Noiseux. Similarity laws of the internal damping of stranded cables in transverse vibrations. *IEEE Transactions on Power Delivery*, 7(3), July 1992.

[63] Institute of Electrical and Electronics Engineers IEEE. Guide on conductor self-damping measurements. Technical Report IEEE Standard 563-1993, IEEE, 1978.

[64] K.O. Papailiou. *Bending of helically twisted cables under variable bending stiffness due to internal friction, tensile force and cable curvature*. PhD thesis, Eidgenossische Technische Hochschule Zurich, 1995.

[65] K.O. Papailiou. On the bending stiffness of transmission line conductors. *IEEE Transactions on Power Delivery*, 12(4), 1997.

[66] H.M. Pape. *Beanspruchung schwingender Drahtseile unter besonderer Berucksichtigung der Beanspruchungen an den Tragklemmen von Freileitungen*. PhD thesis, Bericht des Wohlerinstituts der Technischen Hochschule Braunschweig, Heft7, 1930.

[67] J. C. Poffenberger and R.A. Komenda. Long-term vibration study with the live-line recorder. In *IEEE Winter Power Meeting*, New York, 1971.

[68] J.C. Poffenberger and R.L. Swart. Differential displacement and dynamic conductor strain. *IEEE Transactions on Power Apparatus and Systems*, PAS 84, 1965.

[69] C. B. Rawlins. The long span problem in the analysis of conductor vibration damping. *IEEE Transactions on Power Delivery*, 15:770–776, April 2000.

[70] C.B. Rawlins. Wind tunnel measurement of the power imparted to a model of a vibrating conductor. *IEEE Transactions on Power Apparatus and Systems*, PAS-102, 4, 1983.

[71] C.B. Rawlins. An efficient method for measuring dissipation by dampers in laboratory spans. *IEEE Transactions on Power Delivery*, 3(3), July 1988.

[72] C.B. Rawlins. Model of power imparted to a vibrating conductor under turbulent wind. Technical Report Technical note N° 31, Alcoa, 1998.

[73] C.B. Rawlins. Flexural self-damping in overhead electrical transmission conductors. *Journal of Sound and Vibration*, 323:232–256, 2009.

[74] IEEE Committee Report. Standardization of conductor vibration measurements. *IEEE Transactions on Power Apparatus and Systems*, PAS-85(1):10–20, 1966.

[75] Samtech s.a. *Samcef V13.0 User s Manual*, 2008.

[76] R.H. Scanlan and R. L. Swart. Bending stiffness and strain in stranded cables. In *IEEE Conference*, number C 68 43-PWR, 1968.

[77] W. Schutz and P. Heuler. Miner' s rule revisited. *Jahrg. 42, MP Materialprfung*, pages 245–252, 2000.

[78] T. Seppa. Dynamic behavior of the suspension clamp. Technical Report CSC 6-68-14, CIGRE, May 1968.

[79] T. Seppa. Effect of various factors on vibration fatigue life of acsr ibis. Technical Report 22-69, CIGRE, 1969.

[80] C. W. Silva. *Vibration Fundamentals and Practice*. CRC Press CLC, Boca Raton, Florida, 2000.

[81] C. W. Smollinger and R.B. Siter. Influence of compressive forces on the fatigue performance of bethalune strand wire. In *IEEE Conference*, number C 65237.

[82] R.G. Sturm. Vibration of cables and dampers. *Electrical Engineering*, May and June 1936.

[83] G.B. Tebo. Measurement and control of conductor vibration. *AIEE, Transactions*, (60):1188–1193, 1941.

[84] Cigre SC22 WG11 TF1. Modelling of aeolian vibrations of single conductors: Assessment of the technology. *Electra*, (198):53–69, 1998.

[85] J.S Tompkins, L.L. Merrill, and B. L. Jones. Quantitative relationships in conductor vibration damping. *IEEE Apparatus and Systems*, pages 879–896, October 1956.

[86] L. Vincent, Y. Berthier, and M. Godet. Mechanics and materials in fretting. *Wear*, (153):135–148, 1992.

[87] L. Vincent, Y. Berthier, and M. Godet. Testing method in fretting fatigue: A critical appraisal. *ASTM*, (1159):33–48, 1992.

[88] O. Vingsbo and D. Sodeberg. On fretting maps. *Wear*, (126):131–147, 1988.

[89] R. B. Waterhouse. *Fretting Corrosion*. Pergamon, Oxford, 1972.

[90] R. B. Waterhouse. *Fretting Fatigue*. Elsevier Applied Science, London, 1981.

[91] Cigre SC22 WG04. Endurance capability of conductors, final report. Technical report, Cigre, 1988.

[92] K. Yamagata, M. Fukuda, and Y. Nakayama. Vibration fatigue characteristics of overhead line conductors. Technical Report 22-69, CIGRE, 1969.

[93] R.Z. Zhou. *Fissuration induite en Petits Débattements: Application au cas d' Alliages d Aluminium Aéronautiques*. PhD thesis, Ecole Centrale de Lyon, 1992.

[94] Z.R. Zhou and L. Vincent. Cracking induced by fretting of aluminium alloys. *Transactions of the ASME*, (119), 1997.

List of Figures

1.1 Angle through which the conductor is bent at the clamp by the vibration, courtesy of EPRI [25] 12
1.2 Wind power input curves measured for different reduced velocities, courtesy from EPRI (A is the peak-to-peak displacement/2) [25] 21
1.3 Maximum wind power input coefficient in case of a single conductor, A is the peak-to-peak displacement (courtesy from[25], based on [8]) . . . 21
1.4 Recommended Safe Design H/w values for single unprotected conductors, Cigré 22.11 TF4 2005 24
1.5 Recommended safe design tension for single conductor lines. H: initial horizontal tension; w: conductor weight per unit length, L: actual span length, D: Conductor diameter and m: conductor mass per unit length [5]. 25
1.6 Fatigue tests of three-layer ACSR, courtesy from EPRI [EPRI2006]. . . 27
1.7 Cigré safe border line 28

2.1 IREQ 63.15m long laboratory test span 35
2.2 (a) Span end opposed to the shaker equipped with a rigid clamp embedded in a concrete block; (b) Span end opposed to the shaker equipped with a suspension clamp; (c) aeolian vibration damper ; (d-e) real time monitoring device; (f) non-contact sensors located at 89 and 178mm from the last point of contact with the metallic clamp in order to measure relative displacements 36
2.3 Evolution of the ratio of Y_b over fy_{max} as a function of frequency for $fy_{max} = 40mm/s$ (top), $fy_{max} = 80mm/s$ (middle) and $fy_{max} = 160mm/s$ (bottom), left column corresponds to no device installed in-span, right column corresponds to tests with devices installed in-span . . 38
2.4 Relative displacements (measured at 89mm from the last point of contact between conductor and suspension clamp) at span end with and without the presence of a suspension clamp 39
2.5 Comparison of relative displacements measured at 89mm from suspension and dampers clamp, Crow conductor tensioned at 23.8 %RTS . . . 41
2.6 Comparison of ratios of relative displacements measured at 89mm and 178mm from the suspension and real time monitoring device clamp, Crow conductor tensioned at 23.8%RTS 41

3.1 Section of an AZALEE666 conductor with Z shaped wires in its external layer 46
3.2 Dimensionless anti-node amplitude of vibration vs frequency. AZALEE666. Measured data is classified in three tension ranges (Table 3.3) and is fitted by a value of coefficient n equal to 2.7 52
3.3 Dimensionless anti-node amplitude of vibration vs frequency. AZALEE261. Measured data is classified in three tension ranges (Table 3.3) and is fitted by a value of coefficient n equal to 4 53
3.4 Checking of the fit based on data recorded in 2007 as a result of data recorded in 2006 -example of conductor ASTER570. 53
3.5 Reduced wind power input versus relative anti-node amplitude. In red, experimental dots based on self dissipation obtained using best fit coefficients for dissipation. In dashed and continuous lines, wind power input at 1 and 20% turbulence respectively, following Rawlins [71] 54

4.1 Resonance fatigue test bench, GREMCA laboratory 58
4.2 The two accelerometers are placed diametrically opposed on the conductor. In the figure, the shaker side is on the left and the clamp side on the right 59
4.3 View of the test settings on the clamp side of the span, the Hall sensor is located between the clamp and the accelerometers 60
4.4 Evolution of the X_i, Y_i and Z_i signals (respectively top, middle and bottom), when the AAAC conductor is vibrating with an amplitude Y_b=0.7mm. The vertical axis gives a value in volts [V] and the horizontal one the sample number. 62
4.5 Frequency content of the X_i, Y_i and Z_i signals (respectively top, middle and bottom) presented in figure 4.4, when the AAAC conductor is vibrating with an amplitude Y_b=0.7mm. The vertical axis shows a non-dimensionnal image of the signal power. 63
4.6 AAAC conductor, images of the span after the first failure 65
4.7 AAAC conductor, signal recorded by the Hall sensor during the first failure (top), second failure (middle), third failure (bottom) 66
4.8 AAAC conductor, faces of the second failure (courtesy from Claude Jolicoeur) 67
4.9 ACSR conductor, images of the span after the first failure 68
4.10 ACSR conductor, signal recorded by the Hall sensor during the first failure (top), second failure (middle), third failure (bottom) 69
4.11 ACSR conductor, acceleration measured along the Z axis- saturation before the first failure 70
4.12 ACSR conductor, faces of the first detected failure (left) 71
4.13 AAAC conductor, rotational acceleration and signal recorded by the Hall sensor during the first failure 76

4.14 AAAC conductor, frequency content of the rotational acceleration during the first failure (top), second failure (middle), third failure (bottom). The vertical axis shows a non-dimensionnal image of the signal power. . . . 77
4.15 AAAC conductor, frequency content of the rotational acceleration during the first failure (top), second failure (middle), third failure (bottom), zoom on the lower frequencies. If X is the discrete fourier transform of the raw signal measured by the accelerometers, the vertical axis shows $(\frac{|X_k|}{N})^2$. 78
4.16 AAAC conductor, Short time Fourier transform of the rotational acceleration, amplitudes during the first failure (top), second failure (middle), third failure (bottom), ridge amplitudes 80
4.17 AAAC conductor, Short time Fourier transform of the rotational acceleration, frequencies during the first failure (top), second failure (middle), third failure (bottom), ridge frequencies 81
4.18 AAAC conductor, Short time Fourier transform of some typical rotational acceleration signal outside a failure event 82
4.19 ACSR conductor, failure 3, fast Fourier transform of the rotational acceleration. The vertical axis shows a non-dimensional image of the signal power. 82
4.20 ACSR conductor, frequency content of the rotational acceleration during the third failure, ridge amplitudes (left) and ridge frequencies (right). If X is the discrete fourier transform of the acceleration signal, the vertical axis shows $(\frac{|X_k|}{N})^2$. 83
4.21 AAAC conductor, ridge amplitudes of the longitudinal acceleration deduced by short time Fourier transform during the first failure (top), second failure (middle), third failure (bottom) 84
4.22 AAAC conductor, ridge frequencies of the longitudinal acceleration deduced by short time Fourier transform during the first failure (top), second failure (middle), third failure (bottom) 85
4.23 AAAC conductor, ridge amplitudes of the longitudinal acceleration deduced by short time Fourier transform outside a failure event 86
4.24 ACSR conductor, frequency content of the longitudinal acceleration during the third failure, amplitudes. If X is the discrete fourier transform of the raw signal measured by the accelerometers, the vertical axis shows $(\frac{|X_k|}{N})^2$. 87
4.25 ACSR conductor, Short time Fourier transform of the longitudinal acceleration during the third failure, ridge amplitudes 87
4.26 Evolution of the first four eigen frequencies as a function of the number of failures for conductor AAAC 88
4.27 Evolution of the first four eigen frequencies as a function of the number of failures for conductor ACSR 89

5.1 One of the models used: 331 nodes along the 63.5m span, with mesh refinement near the span extremities 96

5.2 Position of the third antinode of eigen mode 19 at 21.15Hz 100
5.3 Lissajous curve (acceleration $[m/s]$ as a function of excitation $[N]$) at a frequency of $21.15Hz$. 101
5.4 Position of the third antinode for eigen frequency of 20.85 Hz (top) and 22 Hz (bottom) 102
5.5 Evolution of tension in the model when the excitation frequency is 20.85 Hz (top) and 22 Hz (bottom) 103
5.6 Frequency content of the tension in the beam for excitation frequencies of respectively 20.85Hz (top) and 22 Hz (bottom). If X is the discrete fourier transform of the tension signal, the vertical axis shows $(\frac{|X_k|}{N})^2$. . 104
5.7 Sensitivity of the model to the value of average bending stiffness 105
5.8 Sensitivity of the model to the value of excitation force 105
5.9 52nd mode shape (eigen frequency of 59.44Hz), higher amplitudes are obtained on the short subspan 106
5.10 Effect of frequency on antinode amplitude of a subspan delimited by a concentrated mass 107
5.11 Amplitude at an antinode located on the short portion of span when the excitation frequency is 23.075 Hz 108

6.1 Initial and deformed shapes of the 63.5m span, as computed with the model presented in section 6.3.2 113
6.2 Evolution of the total span length over one period of vibration, as computed with the model presented in section 6.3.2 114
6.3 Maximum change in tension [%] computed analytically with the formulae presented in section 6.3.2 for several odd mode numbers and as the span length varies. The span length is in meters [m] and fy_{max} is taken equal to $200mm/s$. Other hypotheses are identical as those described in section 6.3.3 118
6.4 Evolution of the zero-to-peak amplitude along the span for a viscous damping coefficient (c) equal to 0.4 and an amplitude of the excitation force of 43N (0-peak) 123
6.5 Evolution of the power dissipated by the span and single amplitude as the viscous damping coefficient c varies 123
6.6 Variable tension problem. Time evolution of the antinode position for a mass proportional damping coefficient equal to 0.1, excitation frequency of 20.98Hz 126
6.7 Lissajous curve of the excitation force versus cable position at the location of the excitation 126
6.8 Variable tension problem 0-pk amplitude at several locations in the vicinity of the second vibration node without damping 127
6.9 Variable tension problem 0-pk amplitude at several locations in the vicinity of the second vibration node with damping (the mass proportional damping coefficient is equal to 0.1) 127

6.10 Variable tension problem. Frequency content of the antinode amplitude of vibration for a mass proportional damping coefficient equal to 0.1, excitation frequency of 20.98Hz. If X is the discrete fourier transform of the amplitude signal, the vertical axis shows $(\frac{|X_k|}{N})^2$. 128
6.11 Zoom on the 30-50Hz range of the data shown in figure 6.10. Variable tension problem. Frequency content of the antinode amplitude of vibration for a mass proportional damping coefficient equal to 0.1, excitation frequency of 20.98Hz. If X is the discrete fourier transform of the amplitude signal, the vertical axis shows $(\frac{|X_k|}{N})^2$. 129
6.12 Variable tension problem- Time evolution of the amplitudes at the first two vibration nodes 132

7.1 Experimental test set-up used by A. Godinas 139
7.2 AMS 621, total moment versus rotation angle measured for a tension equal to 10%RTS 139
7.3 AMS 621, moment versus rotation angle curve computed from equation (7.4) for a tension equal to 10%RTS 140
7.4 AMS 621, moment versus rotation angle computed from 7.4 for conductor AMS621 at a tension equal to 20% RTS 144
7.5 AMS 621 deflected shape obtained for a tension equal to 25 % RTS, when a rotation angle of 0.01 radians is imposed at the coupling sleeve 147
7.6 AMS 621, curvature computed for a tension equal to 25 % RTS, when a rotation angle of 0.01 radians is imposed at the coupling sleeve 147
7.7 Comparison of the self damping power at $fy_{max} = 50mm/s$ (top) or $fy_{max} = 200mm/s$ (bottom), considering either the formula with terms up to $(\Delta\chi)^4$ or $(\Delta\chi)^3$. The conductor is AMS621, at 15,20 and 25% RTS 152
7.8 Comparison of the self damping power computed from formula 7.47 and from the power law (using Noiseux's coefficients: l=2.44, m=5.63, n=2.76) [25]. The conductor is AMS621, at 15,20 and 25% RTS. The top figure relates to $fy_{max} = 50mm/s$ and the bottom figure to $fy_{max} = 200mm/s$. 154
7.9 Comparison of the self damping power computed from the power law, using either Noiseux's coefficients (l=2.44, m=5.63, n=2.76) or Politecnico di Milano's coefficients (l=2.43, m=5.5, n=2) [25]. The conductor is AMS621, at 15,20 and 25% RTS. The top figure relates to $fy_{max} = 50mm/s$ and the bottom one to $fy_{max} = 200mm/s$ 155
7.10 Comparison of the values of parameter A deduced from moment versus curvature curves. The top figure relates to $fy_{max} = 50mm/s$ and the bottom one to $fy_{max} = 200mm/s$ 156
7.11 Viscoelastic hysteresis curves at the same vibration amplitude $fy_{max} = 200mm/s$, but at two frequencies (20 and 40 Hz) 157
7.12 Comparison of the values of parameter B deduced from moment versus curvature curves using M. The top figure relates to $fy_{max} = 50mm/s$ and the bottom one to $fy_{max} = 200mm/s$ 158

7.13 Comparison of the hysteresis curves of the viscoelastic model and deduced from measurements 159
7.14 AMS 621, dynamic bending moment versus curvature (EI_{dyn}/EI_{max}) . 160
7.15 Variable bending stiffness computed from K. Papailiou's model [65, 64], assuming conductor AMS621 at a tension of 20% RTS and a friction coefficient equal to 0.2 (top) or 0.5 (bottom) 162
7.16 Curves of reduced power computed with formula 7.31 for conductor AMS621, at a tension equal to 20% RTS 165
7.17 Comparison of the self damping power computed from formula 7.32 (using the exponents of AMS621) and the data recorded at Dead Water Fell on Aster570 and ASTER228 (see chapter 3). The self damping power which can be computed with the power law using Noiseux's set of exponents is also shown (note that Noiseux's exponents are valid for ACSR conductors only). 166

8.1 Evolution of frequency with mode number for test span equipped with conductor Crow and a suspension clamp at the extremity opposed to shaker, tension of 22.7% RTS 172
8.2 Evolution of frequency and amplitude ($fy_{max}(mm/s)$ with mode number for test span equipped with conductor Crow. Span ends are very rigidly fixed and tension is worth respectively 15.7% and 21.2% EI_{max} 173

9.1 Force as a function of time for an eigenfrequency of 20.44Hz, an amplitude $fy_{max} = 40mm/s$ and at a tension of 21.07%RTS 177
9.2 Lissajous curve of force versus acceleration for an eigenfrequency of 20.44Hz, an amplitude $fy_{max} = 40mm/s$ and at a tension of 21.07%RTS 177
9.3 Lissajous curve of force versus acceleration m/s^2 for an eigenfrequency of 13.85Hz, an amplitude $fy_{max} = 40mm/s$ and at a tension of 15.32%RTS 178
9.4 Lissajous curve of force versus acceleration m/s^2 for an eigenfrequency of 30.05Hz, an amplitude $fy_{max} = 80mm/s$ and at a tension of 24.1%RTS 179
9.5 Lissajous curve of force versus acceleration m/s^2 for an eigenfrequency of 49.83Hz, an amplitude $fy_{max} = 40mm/s$ and at a tension of 24.%RTS 179
9.6 Lissajous curve of force versus acceleration m/s^2 for an eigenfrequency of 49.83Hz, an amplitude $fy_{max} = 73mm/s$ and at a tension of 24.%RTS 180
9.7 Lissajous curve of force versus acceleration m/s^2 for an eigenfrequency of 49.83Hz, an amplitude $fy_{max} = 161mm/s$ and at a tension of 24%RTS 180
9.8 Force and frequency content of force for an excitation frequency of 13.85Hz, an amplitude $fy_{max} = 40mm/s$ and a tension of 15.32%RTS. If X is the discrete fourier transform of the force signal, the vertical axis of the right figure shows $(\frac{|X_k|}{N})^2$. 181
9.9 Force and frequency content of force for an excitation frequency of 29.6Hz, an amplitude $fy_{max} = 40mm/s$ and a tension of 15.32%RTS. If X is the discrete fourier transform of the force signal, the vertical axis of the right figure shows $(\frac{|X_k|}{N})^2$. 181

9.10 Force and frequency content of force for an excitation frequency of 30.05Hz, an amplitude $fy_{max} = 80mm/s$ and a tension of 24.1%RTS . If X is the discrete fourier transform of the force signal, the vertical axis of the right figure shows $(\frac{|X_k|}{N})^2$. 182

9.11 Force and frequency content of force for an excitation frequency of 49.83Hz, an amplitude $fy_{max} = 40mm/s$ and a tension of 24%RTS . If X is the discrete fourier transform of the force signal, the vertical axis of the right figure shows $(\frac{|X_k|}{N})^2$. 182

9.12 Force and frequency content of force for an excitation frequency of 49.83Hz, an amplitude $fy_{max} = 73mm/s$ and a tension of 24%RTS . If X is the discrete fourier transform of the force signal, the vertical axis of the right figure shows $(\frac{|X_k|}{N})^2$. 182

9.13 Force and frequency content of force for an excitation frequency of 49.83Hz, an amplitude $fy_{max} = 161mm/s$ and a tension of 24%RTS . If X is the discrete fourier transform of the force signal, the vertical axis of the right figure shows $(\frac{|X_k|}{N})^2$. 183

9.14 Evolution and frequency content of node amplitude for an excitation frequency of 13.85Hz, an amplitude $fy_{max} = 40mm/s$ and a tension of 15.32%RTS . If X is the discrete fourier transform of the node signal, the vertical axis of the right figure shows $(\frac{|X_k|}{N})^2$. 183

9.15 Evolution and frequency content of node position for an excitation frequency of 30Hz, an amplitude $fy_{max} = 80mm/s$ and a tension of 24.1%RTS . If X is the discrete fourier transform of the node signal, the vertical axis of the right figure shows $(\frac{|X_k|}{N})^2$. 184

9.16 Evolution and frequency content of node position for an excitation frequency of 49.83Hz, an amplitude $fy_{max} = 160mm/s$ and a tension of 24.1%RTS. If X is the discrete fourier transform of the node signal, the vertical axis of the right figure shows $(\frac{|X_k|}{N})^2$. 184

9.17 Evolution and frequency content of antinode position for an excitation frequency of 13.85Hz, an amplitude $fy_{max} = 40mm/s$ and a tension of 15.32%RTS. If X is the discrete fourier transform of the antinode signal, the vertical axis of the right figure shows $(\frac{|X_k|}{N})^2$. 185

9.18 Evolution and frequency content of antinode position for an excitation frequency of 30Hz, an amplitude $fy_{max} = 80mm/s$ and a tension of 24.1%RTS. If X is the discrete fourier transform of the antinode signal, the vertical axis of the right figure shows $(\frac{|X_k|}{N})^2$. 186

9.19 Evolution and frequency content of antinode position for an excitation frequency of 49.83Hz, an amplitude $fy_{max} = 160mm/s$ and a tension of 24.1%RTS. If X is the discrete fourier transform of the antinode signal, the vertical axis of the right figure shows $(\frac{|X_k|}{N})^2$. 186

10.1 Variable tension problem. ISWR power dissipated within the span and injected power. The mass proportional damping coefficient is equal to 0.1, the excitation frequency to 20.98Hz and the excitation amplitude to 30N, $A/d = 0.2$ 191
10.2 Variable tension problem. Change in tension for a mass proportional damping coefficient equal to 0.1, excitation frequency of 20.98Hz 193

A.1 AMS 621, Moment versus rotation angle for a tension equal to 20000N (10 % RTS) 203
A.2 AMS 621, Moment versus rotation angle for a tension equal to 15000N (7.5 % RTS) 204
A.3 AMS 621, Moment versus rotation angle for a tension equal to 10000N (5 % RTS) 204
A.4 AMS 621, Moment versus rotation angle for a tension equal to 5000N (2.5 % RTS) 205
A.5 AMS 298, Moment versus rotation angle for a tension equal to 5000N (5 % RTS) 205
A.6 AMS 298, Moment versus rotation angle for a tension equal to 10000N (10.4 % RTS) 206
A.7 AMS 298, Moment versus rotation angle for a tension equal to 20000N (20.9 % RTS) 206
A.8 AMS 298, Moment versus rotation angle for a tension equal to 30000N (31.3 % RTS) 207

B.1 Dissection report of the AAAC conductor 210
B.2 Dissection report of the ACSR conductor 212

C.1 Calibration of the Hall sensor of test bench 6 213
C.2 Calibration of the Hall sensor of test bench 3 214

E.1 Evolution of the eigen mode frequencies as a function of their order . . 218

List of Tables

1.1 Range of the exponents l, m, n of the self damping power law 19

3.1 Conductor properties 47
3.2 Test campaign (2007, 550 hours of recording), tension ranges used for the tuning of "n" self damping coefficient 50
3.3 Test campaign (2007, 550 hours of recording), tension ranges used for the tuning of "n" self damping coefficient 51
3.4 Test Campaign (2007, 550 hours of recording), best coefficient combinations to fit low frequency (lower than 20-30 Hz) amplitudes 51

4.1 Failures on the AAAC conductor 64
4.2 Failures on the ACSR conductor 64
4.3 first eigen longitudinal, vertical and torsional pulsations computed for the AAAC and ACSR conductor 74
4.4 Slope of a linear fit on data presented in figures 26 and 27 . . 89

5.1 Comparison between measured and computed frequencies for the beam and cable models 98
5.2 Comparison between measured half wavelength and computed half wavelength (for the beam and cable FE models) 98
5.3 Comparison between measured and computed position of node 1 for the beam and cable models 98

6.1 Comparison of the changes in tension computed from a simple formulation (see section 6.3.1), a more accurate formulation (see section 6.3.2) or with a finite element model 112
6.2 Comparisons of the variable constant tension problem "without damping" versus reality 130
6.3 Comparisons of the variable and constant tension problems versus reality 133